PROBING BACTERIAL SIGNALING AND CELL ENVELOPE ASSEMBLY WITH CHEMICAL REPORTERS

By

Heather L. Hodges

A dissertation submitted in partial fulfillment of

the requirements for the degree of

Doctor of Philosophy

(Chemistry)

at the

UNIVERSITY OF WISCONSIN–MADISON

2018

Date of final oral examination: 01/08/2018

The dissertation is approved by the following members of the Final Oral Committee:
Laura L. Kiessling, Professor Emeritus, Chemistry and Biochemistry
Helen E. Blackwell, Professor, Chemistry
Douglas B, Weibel, Professor, Biochemistry, Chemistry, and Biomedical Engineering
Andrew Buller, Assistant Professor, Chemistry

PROBING BACTERIAL SIGNALING AND CELL ENVELOPE ASSEMBLY WITH CHEMICAL REPORTERS

Heather L. Hodges

Under the supervision of Professor Laura L. Kiessling

At the University of Wisconsin–Madison

The bacterial cell envelope is a dynamic structure that forms an essential barrier between the bacterial cytosol and the environment. This cell surface is comprised of species-specific lipids, glycans, enzymes and signaling pathways. Here, I exploited unique molecular building blocks of the mycobacterial cell envelope and molecules that can influence bacterial signaling pathways in *E. coli* to develop chemical reporters.

First, I explored formation and signaling of the *E. coli* chemotaxis array, a pathway that is crucial for bacterial motility. We assessed how chemotaxis array architecture is altered by modulating the composition of the three core proteins that comprise the chemotaxis array. We observed intriguing intermediates that reveal insights into array assembly and architecture (Chapter 2). Next, I developed of an analog of the chemotaxis ligand aspartate, which binds to a chemotaxis array receptor protein. Multivalent polymers functionalized with this aspartate analog are effective activators of chemotaxis signaling. The modular design of this synthetic polymer presents an opportunity to investigate how multifold engagement of chemotaxis receptors by polymers can affect signaling (Chapter 3).

Additionally, I have developed small molecule probes to investigate the biosynthesis and dynamics of the mycobacterial cell envelope. This core, termed the

mycolylarabinogalactan, is a lipoheteropolysaccharide critical to the survival of mycolated bacteria. In this work an analog of the donor monosaccharide for the arabinan was developed. This arabinan monosaccharide probe presents a scaffold to tailor the arabinan with reporter groups and represents a new delivery strategy to manipulate arabinan structure and investigate arabinan biosynthetic enzymes (Chapter 5). I also demonstrate the utility of a fluorogenic mimic of a trehalose glycolipid to localize activity of the enzymes that generate the mycolic acid portion of the mycobacterial cell wall during growth (Chapter 4). This probe functions in live cells to report on mycolic acid assembly in real time and revealed that mycolyltransferase activity was localized throughout the cell cycle. This probe was employed as a diagnostic to identify mycolic acid containing bacteria in mixtures of cells. This work builds a toolbox of novel glycolipid donor probes to provide access to mycobacterial cell wall biosynthesis.

Acknowledgements

There are no words that can do justice to the enormous sacrifices my grandparents have made to allow me to be here and achieve this goal. I am eternally grateful to them and the choices they made to ensure that I could have this opportunity and their unending support of me has been a privilege. I hope to have made them proud.

I was fortunate to have great labmates who filled my work days with joy. I am thankful for the people that contributed to the work presented herein, Dr. Margaret Wong, Dr. Robert Brown, John Crooks, Phillip Calabretta, Cassie Jarvis, Professor Ariane Briegel, Professor Grant Jensen, Dr. Run-Zi Lai and Professor Sandy Parkinson.

I am thankful to the NSF-NCGRS advanced opportunity fellowship, UW–Madison Chemistry and Biology Interface Training Grant and the National NIH NRSA for financial support and a stimulating environment that has provided me countless opportunities to advance my training. I would also like to thank the Chemistry department and the Biochemistry department for their support.

Thank you to my thesis committee; I thank Professor Helen Blackwell for her enthusiastic support of my time here. I thank Professor Doug Weibel for his friendship and for providing me a home to finish my work. I thank Professor Andrew Buller for participating in my thesis review. I would also like to thank my thesis advisor Laura L. Kiessling who has been a tremendous source of knowledge, encouragement and understanding.

Table of Contents

List of Figures

List of Schemes

List of Tables

List of Abbreviations

ADA	azido-D-ala
ADC	albumin-dextrose-catalase
AG	arabinogalactan
Ag85	antigen 85 complex
aib	alpha-amino-iso-butyrate
Ara*f*	arabinofuranose
AraT	arabinofuranosyltransferase
ATP	adenosine-triphosphate
AU	airy unit
BHI	brain-heart infusion
BHIS	brain-heart infusion + sucrose
BOC	tert-butyloxycarbonyl
Boc-Fl	Bocillin, fluorescent penicillin
BSA	bovine serum albumin
CFPs	culture filtrate proteins
CFP	cyan fluorescent protein
CPS	capsular polysaccharide layer
CuAAC	copper catalyzed azide-alkyne click chemistry
CWG	cell wall glycan
DC	dendritic cell
DMSO	dimethyl sulfoxide

DNA	deoxyribonucleic acid
DOSY	diffusion-ordered nmr spectroscopy
DPA	decaprenyl-phospho-d-arabinofuranose
DTT	dithiothreitol
ECL	electrochemiluminescence
ECT	electron cryo-tomography
EDA	ethynyl-D-alanine
EDC	1-ethyl-3-(3-dimethylaminopropyl)carbodiimide
EDTA	ethylenediaminetetraacetic acid
EM	electron microscopy
ESI	electrospray ionization
ETALM	enzymatic-turnover-activated localization microscopy
ex/em	excitation/emission
FDAA	fluorescent D- amino acid
FPA	farnesylphosphoryl d-arabinose
FPLC	fast protein liquid chromatography
FRAP	fluorescence recovery after photobleaching
FRET	fluorescence resonance energy transfer
Gal*f*	galactofuranose
GalNAc	n-acetylgalactosamine
GFP	green fluorescent protein
GlcNAc	n-acetylglucosamine

GT	glycosyltransferase
HADA	hydroxy coumarin-carbonyl-amino-d-alanine
HEPES	4-(2-hydroxyethyl)-1-piperazine-ethanesulfonic acid
His_6	hexahistidine
HMBC	heteronuclear multiple bond correlation
HPLC	high performance liquid chromatography
HRMS	high resolution mass spectrometry
HRP	horseradish peroxidase
HSQC	heteronuclear single quantum correlation
IFE	inner filter effect
IPTG	isopropyl-β-D-thiogalactopyranoside
$K_{1/2}$	half-maximal fret response concentration
k_{cat}	turn-over number
k_{cat}/K_M	catalytic efficiency
KDO	3-deoxy-D-*manno*-oct-2-ulosonic acid
K_M	michaelis-menten constant
LC-MS	liquid chromatography mass spectrometry
Ldt	L,D-transpeptidases
LPS	lipopolysaccharide
LTA	lipoteichoic acid
mAGP	mycolyl-arabinogalactan-peptidoglycan
mDAP	meso-2,6-diaminopimelic acid

MS	mass spectrometry
MurNAc	n-acetylmuramic acid
NADA	4-chloro-7-nitrobenzofurazan-3-amino- d-alanine
NaS	sodium salicylate
NHS	n-hydroxysuccinimidyl
NMR	nuclear magnetic resonance
NPA	nerylphosphoryl d-arabinose
OD_{600}	optical density at 600 nm
PAGE	polyacrylamide gel electrophoresis
PALM	photoactivated localization microscopy
PBP	penicillin-binding protein
PBS	phosphate buffered saline
PC	phosphorylcholine
PCR	polymerase chain reaction
PDB	protein data bank
PE	phosphoethanolamine
PEG	polyethylene glycol
PG	peptidoglycan
PG	phosphorylglycerol
Pgc	propargyl choline
PMSF	phenylmethylsulfonyl fluoride
pRpp	phosphoribosyl pyrophosphate

PVDF	polyvinylidene fluoride
px	pixel
QTF	quencher-trehalose-fluorophore
RFU	relative fluorescence units
ROMP	ring opening metathesis polymerization
SD	standard deviation of the mean
SDS	sodium dodecyl sulfate
SEM	standard error of the mean
SIM	structured illumination microscopy
SPAAC	strain promoted azide-alkyne cycloadditions
SR	super resolution
STORM	stochastic optical reconstruction microscopy
TA	teichoic acids
TADA	tetramethylrhodamine-3-amino-d-alanine
TAT	twin-arginine translocase
TB broth	tryptone broth
TBS	tris-buffered-saline
TCEP	tris(2-carboxyethyl)phosphine
TDM	trehalose dimycolate
TEM	transmission electron microscopy
TFA	trifluoroacetic acid
THF	tetrahydrofuran

THL	tetrahydrolipstatin
TMM	trehalose monomycolate
TOCSY	total correlated spectroscopy
TOF	time of flight
TP	transpeptidase
Tris	tris(hydroxymethyl)aminomethane
Van-Fl	fluorescent vancomycin
w/v	weight by volume
WTA	wall teichoic acid
YFP	yellow fluorescent protein

Chapter 1

Fluorescent Probes of the Bacterial Cell Envelope

1.1 Abstract

Assembly and maintenance of the bacterial cell envelope determine bacterial survival, antibiotic susceptibility, and evasion of host defenses. Given these functions, the bacterial cell envelope is an important therapeutic target. However, as a result of increasing antibiotic resistance and a diminishing pipeline of available drugs, there is an urgent need to identify and validate new targets. While a significant number of components and proteins involved in bacterial cell envelope construction have been identified there are still many enzymes and strain-specific macromolecules that have not been identified. Mechanistic concepts governing cell envelope homeostasis are still emerging. In particular, a more complete understanding of cell envelope component localization, interaction and function in real time to construct the cell envelope would accelerate the discovery of new therapeutic targets. To address these issues, chemists are developing a toolbox of fluorescent probes to visualize cell envelope assembly. This chapter highlights the fluorescent small molecule probes available for investigating bacterial cell envelope biogenesis, and the important insights they have provided. Additionally, I describe the continuing advances in microscopy and bioconjugation chemistries that can be incorporated into cell envelope probe development to enable observation of cell envelope construction in real time.

1.2 Introduction

Successful microbial pathogens must navigate complex environments and effectively respond to a wide range of external stimuli. Consequently, bacteria possess a cell envelope structure that forms a barrier between the bacterial cytosolic components and its environment. This dynamic and complex cell surface is comprised of species-specific compositions of lipids, glycans, lipoglycans, and glycoproteins. The architecture and molecular composition of the cell envelope determine bacterial susceptibility to antibiotics, host defenses, and tolerance to environmental variation (1). The cell envelope has many attributes that have positioned its biosynthesis as a central target for the development of antibacterial agents: The cell envelope is essential, it is composed of compounds often absent from mammals, and it is constructed from the action of a plurality of biosynthetic enzymes that can, therefore, serve as drug targets. For example, β-lactam antibiotics, which target the bacterial cell wall, comprise some of the most successful antimicrobial compounds to treat human pathogens (2). However, there is an urgent need to validate new targets and to develop new inhibitors. Increasing resistance to antibiotics has diminished the clinical efficacy of existing drugs, a problem that is compounded by a dwindling antibiotic pipeline. Evolving research on the roles of bacteria in human health and disease is also providing impetus to develop narrow-spectrum agents to target specific bacteria (3).

As will be highlighted, the bacterial cell envelope can reveal unique entry points to such targeted therapies. Chemists are addressing this issue through the development of fluorescent small molecule probes that are improving understanding of cell envelope biosynthesis and assembly. Synthetic probes are ideal means to access non-proteinaceous macromolecules in

the highly glycosylated cell envelope, and fluorescent probes offer the ability to visualize cell envelope processes in live cells. Such probes also provide new opportunities to develop high throughput screens and identify antibiotic leads, evaluate antibacterial modes of action, and develop bacteria-specific diagnostics. This chapter will highlight the structure, design, and utility of fluorescent small molecule probes to study bacterial cell wall biogenesis by microscopy.

1.3 Bacterial Cell Envelopes

Bacteria have traditionally been classified into Gram-negative and Gram-positive based on staining, the results of which depend on the architecture of their cell envelopes. Here, I have categorized mycobacteria separately, as they do not fit neatly in either group (**Figure 1-1**).

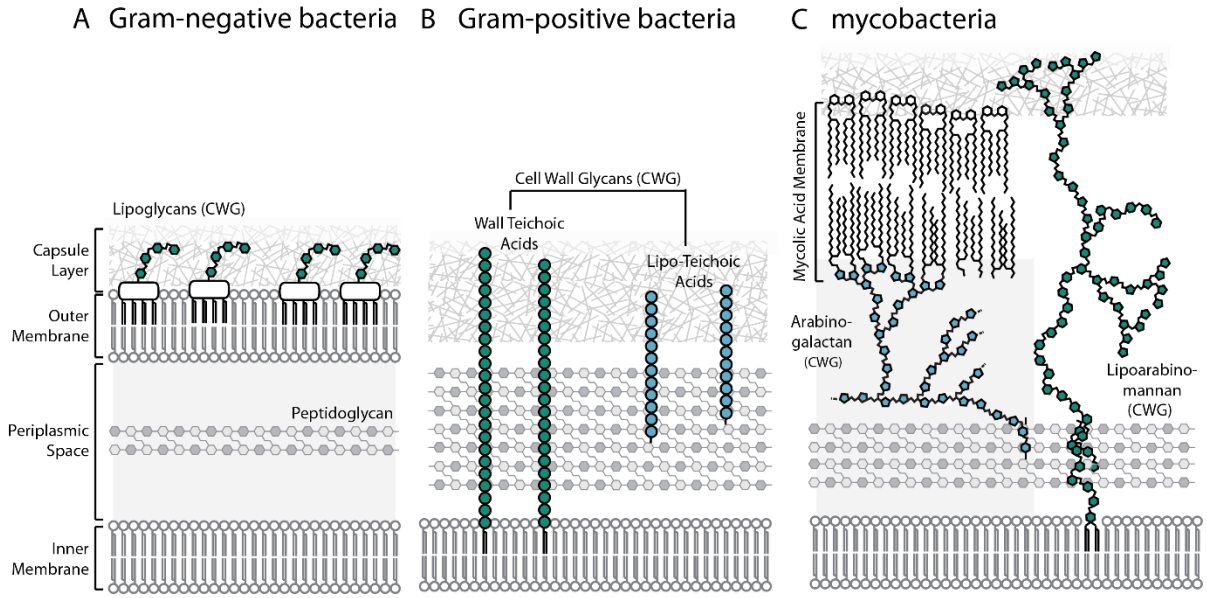

Figure 1-1. Schematic of bacterial cell envelope architecture (A) Gram-negative bacteria (B) Gram-positive bacteria (C) mycobacteria.

Gram-negative bacteria most notably possess both an inner and outer membrane, as well as a periplasmic space that also contains a vital structural polysaccharide, the peptidoglycan (PG). Displayed from the outer membrane are unique lipoglycans, lipopolysaccharides (LPS), and an associated capsular polysaccharide layer (**Figure 1-1A**). Gram-positive bacteria have a PG layer, which is thicker than that in Gram-negative bacteria, a CPS layer, and possess only an inner membrane. Gram-positive bacteria display teichoic acids as their cell wall glycans (**Figure 1-1B)**. Teichoic acids can be anchored to the PG or lipidated and displayed from the inner membrane. Though bacteria from the Corynebacterineae suborder are technically classified as Gram-positive bacteria and also possess a thick PG, their cell envelope contains distinct cell wall glycans and lipids (**Figure 1-1C**). These include a PG-anchored branched polysaccharide, the arabinogalactan, and a membrane-anchored polysaccharide, the lipoarabinomannan. Covalently attached to the arabinogalactan are mycolic acids, which interact with trehalose-linked lipids to form an asymmetric bilayer. Furthermore, bacteria of these different classifications are coated with species-specific molecules including proteins, glycans, and lipids. The structural attributes of and biosynthetic strategies employed to generate these strain-specific molecules have the potential to be exploited to target or identify specific bacteria.

Essential drugs such as penicillin, amoxicillin, and vancomycin target the production of bacterial cell wall glycopolymers (2, 4-9). While such broad-spectrum antibiotics are an essential tool to treat bacterial infections, there is some concern that the overuse of such medications has enabled the current and evolving resistance crisis. Development of new leads has been hampered by narrow selection of available chemical classes and limited range of

targets and mechanisms (4-6, 10). Exploration of bacterial strain-specific molecules has the potential to generate efficacious narrow-spectrum agents that operate on unique targets. Indeed, strain-specific bacterial carbohydrates have formed the basis for serum antibody-based bacterial diagnostics in infections (11, 12), vaccination strategies (13-15) and antibiotic development (2, 7-9). Researchers are increasingly exploring bacteria-bacteria interactions to discover novel compounds and modes of action, especially those produced by commensal bacteria against invading pathogens (16, 17). Use of narrower spectrum agents would reduce off-target effects to the microbiome which is increasingly connected to positive patient outcomes (18).

In combination with uncovering the molecular composition of the cell envelope and subsequent biosynthetic enzymes as antibacterial targets, delineating the physical mechanisms by which the cell envelope is assembled and maintained can provide new opportunities to target bacteria therapeutically. For instance, inhibition of cell wall glycopolymers in *Staphylococcus aureus* (teichoic acids) is not lethal. However, loss of teichoic acids affects PG construction enzyme localization and renders these usually resistant bacteria sensitive to traditional PG targeting antibiotics (19). In a related finding, *S. aureus* exposure to inhibitors of lipid microdomain formation (statins) interfered with cell wall biosynthetic enzyme localization and potentiated the effects of antibiotics (20). Thus, understanding cell envelope assembly can reveal synergistic combinations of drugs that target bacteria. Fluorescent reporters that can be used to validate potential targets and mechanisms of action as well as facilitate high throughput screen to identify lead compounds can accelerate antibiotic discovery—especially the development of narrow-spectrum agents. To realize the

potential of narrow-spectrum antibiotics, improved point of care diagnostics are necessary to rapidly identify infections and initiate treatment. Fluorescent reporters of strain-specific molecules could function as diagnostic aids and decrease the time needed to identify and initiate treatment.

1.4 Fluorescent Dyes, Proteins and Probes of the Bacterial Cell Wall Envelope

Studies using genetically encoded fluorescent protein fusions of bacterial cell wall proteins have uncovered localization and revealed diverse growth mechanisms across different bacterial species (21). By fluorescent microscopy, proteins have been shown to assemble into multiprotein complexes for cell growth and division. Such fluorescent fusions have included intrinsically fluorescent proteins (e.g., green fluorescent protein, GFP) (22, 23), self-labeling enzymes that react with specific fluorescent substrates (e.g., Halo-tag and Snap-tag) (24-27), peptides that bind fluorophores (e.g., FlAsH or ReAsH) and peptides that can be enzymatically ligated with a fluorophore (e.g., biotin ligase or sortase) (28, 29). The molecular details of these systems have been reviewed elsewhere (30-32). Use of fluorescent fusion proteins necessitates genetic modification of each protein of interest and require that the organism in question be genetically tractable. The appendage of protein fusion tags also introduces the risk of perturbation to native protein function including localization, expression levels and enzymatic activity (31, 33, 34). This is especially crucial for proteins that compose larger multi-protein complexes or whose exact localization is key to their functional performance (35, 36).

Small molecule dyes or chemically reactive fluorophores have been used as fluorescent labels, environmental indicators, and cellular strains (37, 38). While important, these fluorescent tools broadly lack molecular specificity for cell envelope components but can be valuable in

combination with imaging tools targeting components of the cell envelope. Intercalating dyes of nucleic acids which have advanced our understanding of chromosomal dynamics during cell division and have been reviewed elsewhere (39, 40). Lipophilic dyes broadly have been used to generate fluorescent membranes or identify membrane environmental features, such as heterogeneity (e.g., rafts and distribution) and fluidity, and have been described elsewhere (41-44). Additionally, amine-reactive fluorophores have been used in pulse-chase imaging experiments or to label the bacterial cell surface and then observe the ingrowth of regions devoid of fluorescence to discern sites of cell wall insertion. This technique has demonstrated the unipolar growth mechanism of Gram-negative bacteria, *Agrobacterium tumefaciens,* and the asymmetric polar growth of *Mycobacterium smegmatis* (45, 46).

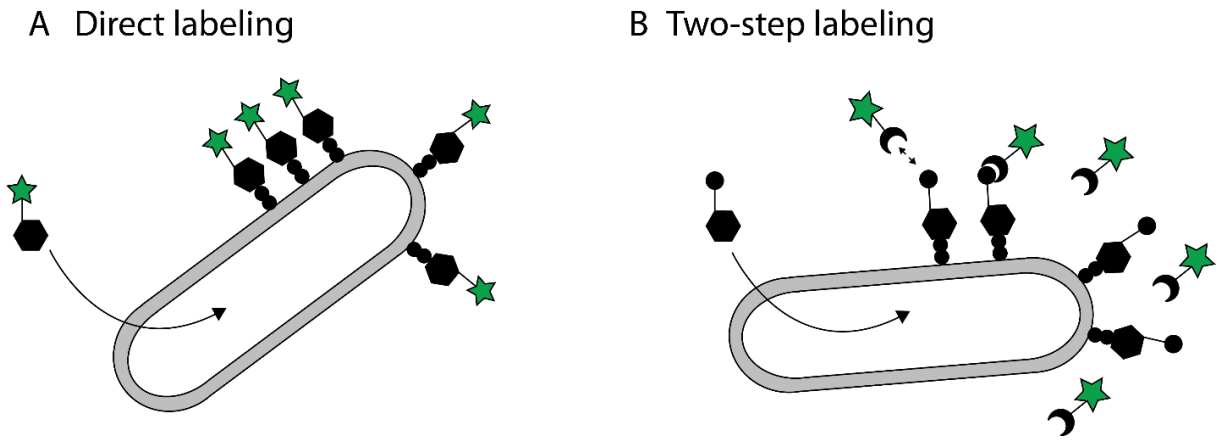

Figure 1-2. Labeling methods with small molecule probes of the cell envelope Probes can be incorporated extra- or intracellularly and rendered fluorescent either by being (A) Directly derivatized with a fluorophore and processed into the cell envelope or (B) derivatized with a reactive handle that facilitates selective conjugation of a fluorophore.

Fluorescent analogs of cell envelope components can overcome many of the disadvantages of genetically encoded protein fusions and generic fluorescent dyes. Indeed, small molecule fluorescent probes are enabling studies of localization and function in bacteria in ways that complement traditional genetic techniques. Derivatized inhibitors or structural

mimics of bacterial cell envelope substrates can be processed in place of their natural counterpart. To facilitate visualization, these compounds present either a fluorophore (**Figure 1-2A**) or a reactive handle that can be chemoselectively functionalized (**Figure 1-2B**). The advantages of chemical probes are multi-fold and include their ability to 1. label substrates that are not genetically encoded 2. function within genetically intractable systems and 3. act rapidly and be modulated as a function of dosage. These synthetic compounds can be tailored to act reversibly or covalently, through conserved broad targets (e.g., peptidoglycan), or via processes specific to distinct classes of bacteria. Fluorescent cell envelope analogs are therefore powerful and versatile tools to monitor cell envelope composition and elucidate mechanisms of cell envelope assembly and modification.

The large size of the appended fluorophore in directly fluorescent probes can hinder enzymatic processing or penetration. While fluorescent probes afford rapid visualization, and are compatible with live cells, they can require extensive washing steps to reduce background fluorescence. Probes bearing chemically reactive tags can be conjugated to a fluorophore in a two-step labeling process. This strategy can be limited by the small number of bioorthogonal reactions available to selectively label incorporated biomolecules and the slow rates of these reactions. Sluggish kinetic rates can necessitate usage of high concentrations of labeling substrates which can introduce potential off-target reactions and high background (30). Additionally, these reactions can require fixation, multiple reactants, or toxic catalysts, which can limit their use in living cells. In both labeling schemes, development of fluorogenic probes can improve contrast, reduce processing steps and facilitate real-time imaging to advance the ability to observe cell envelope construction as it is happening. Fluorogenic probes that only

display fluorescence either through enzymatic activity, environmental properties or a chemoselective reaction would enable access to increased information about cell envelope dynamics. Advances in this area are discussed in **section 1.7**.

1.5 Fluorescent Cell Envelope Substrate Probes and Their Use in Microscopy

1.5.1 Antibiotic-Based Fluorescent Analogs

PG is a peptide crosslinked glycan mesh that has been detected in virtually all bacteria. PG is a scaffold for many components of the bacterial cell envelope, responsible for bacterial shape and provides structural resistance to osmotic shifts in the environment (47, 48). A schematic depiction that illustrates the differences between PG in Gram-positive and Gram-negative bacteria is depicted in **Figure 1-1**. PG is constructed by polymerization of lipid II, a monomer composed of a disaccharide and pentapeptide chain (**Figure 1-3**). The disaccharide repeat unit consists of N-acetylglucosamine (GlcNAc) and N-acetylmuramic acid (MurNAc). The pentapeptide is appended to the C(3) hydroxyl of MurNAc. A common pentapeptide motif is L-Ala-D-Glu-meso-2,6-diaminopimelic acid (mDAP)-D-Ala-D-Ala (49). The disaccharides of lipid II are joined in a β-(1,4)-linked GlcNAc-MurNAc polymer by the activity of glycosyltransferase (GT) domains on membrane-bound PG biosynthetic enzymes, including penicillin-binding proteins (PBPs) and non-PBP GTs (e.g., RodA). PG is then further crosslinked by the pentapeptide chain through the activity of transpeptidase domains (TP) of PBPs and L,D-transpeptidases (Ldt) (**Figure 1-4A**&**B**). The molecular identity of the pentapeptide and the peptide cross-links can vary between species and these variations have been reviewed elsewhere (49, 50). PG is an important target for antibiotics due to its essential role, the uniqueness of the lipid II substrate and the plurality of enzymes involved in PG assembly (51).

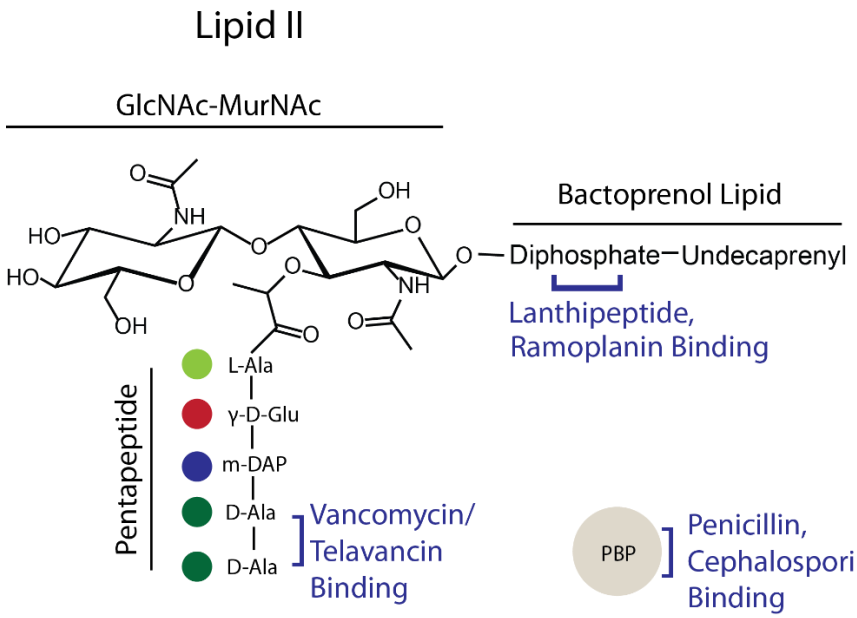

Figure 1-3. Lipid II inhibition Structure of lipid II highlighting GlcNAc-MurNAc disaccharide, pentapeptide, and lipid carrier, as well as, regions of antibiotic interaction.

Successful and important PG-targeted drugs function by two main modes: either targeting lipid II by sequestration (glycopeptide, lantibiotics) or inhibition of the activity of TG and GTs (β-lactams) (**Figure 1-3; Figure 1-5)**.

Scientists have leveraged the specific interactions of antibiotics and their targets to enable the visualization of their target by light microscopy and query their localization in the cell (**Table 1-1**). Examples of such reporters include fluorescent vancomycin (Van-Fl; commercially-available) (52), ramoplanin (Ram-Fl) (53), telavancin (54), penicillin V (Boc-Fl; commercially-available) (55, 56), cephalosporin C (CephC-Fl) (57) and the lanthipeptides (lacticin 481, haloduracin α, haloduracin β) (58). These probes have been used in a myriad of species, including, *Bacillus subtilis* (53, 57, 58), *Streptococcus pneumoniae* (52, 57), *S. aureus* (54, 59), *Streptomyces coelicolor* (52), *Corynebacterium glutamicum* (52, 60), *Caulobacter crescentus* (61) and *Lactococcus lactis* (62).

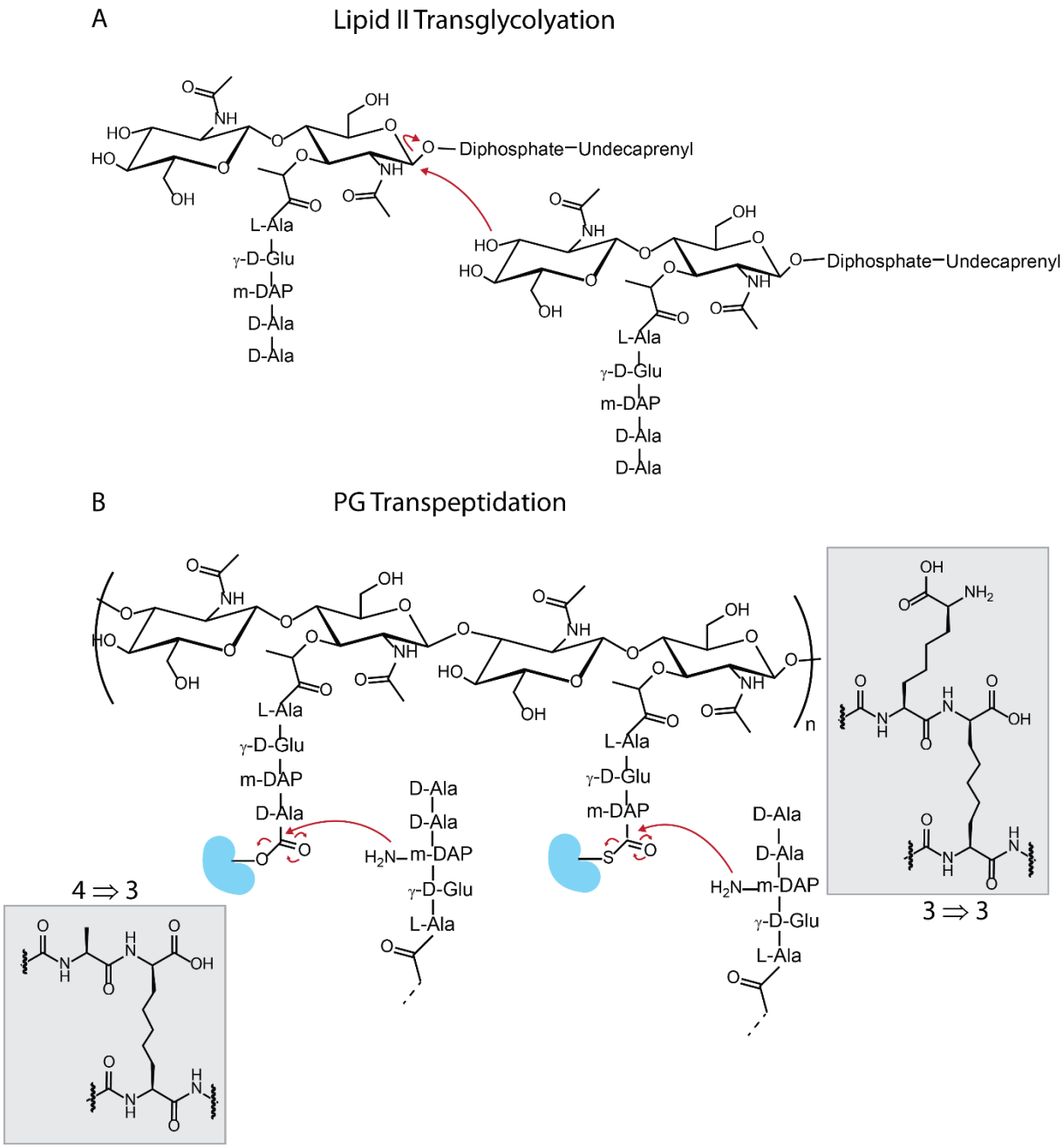

Figure 1-4. Lipid II processing Lipid II interaction with penicillin-binding proteins (PBPs). Including, transglycosylation (A) and transpeptidation (B) to form nascent and mature peptidoglycan (PG).

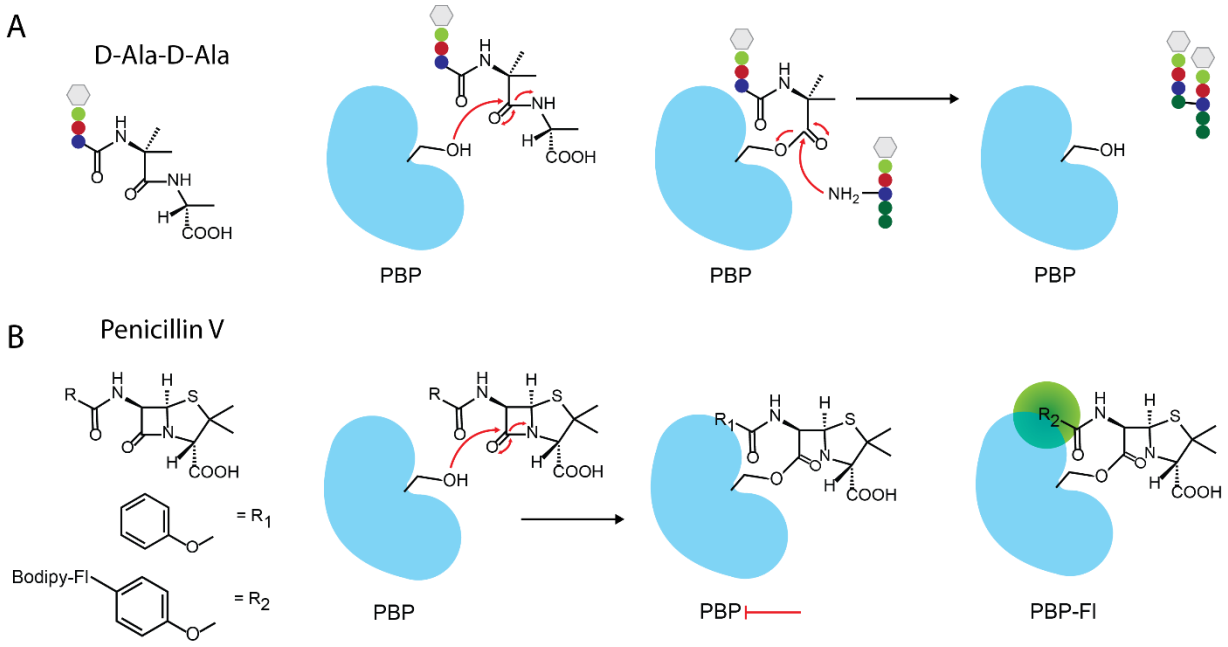

Figure 1-5. Lipid II labeling (A) D-Ala-D-Ala processing by PBPs. (B) Penicillin and other β-lactam antibiotics structurally mimic pentapeptide terminal D-Ala-D-Ala residues and are covalent inhibitors of PBPs. Processing of fluorophore-conjugated antibiotics can generate fluorescently labeled PBPs.

Vancomycin and telavancin bind to the terminal D-Ala-D-Ala residues of nascent Lipid II and inhibit further maturation and transpeptidation (63). Ramoplanin prevents lipid II maturation as well, but does so by binding to the MurNAc-diphosphate-lipid portion and inhibiting transglycosylation. This mechanism is analogous to that of lanthipeptide antibiotics. Fluorophore-labeled ramoplanin, vancomycin and telavancin label nascent. These probes give rise to similar staining patterns; therefore, the following section focuses on the use of Van-Fl, the more widely used probe likely due to its commercial availability. Van-Fl revealed helical staining patterns along the cylindrical side wall of *B. subtilis* (53). This novel observation about PG assembly indicated that biosynthesis was occurring in a continuous dispersed fashion, suggesting an underlying cytoskeletal scaffold (53). The helical pattern was abolished

in strains lacking the cytoskeletal protein Mbl but was stable in an MreB deletion (52). In *C. glutamicum*, a rod-shaped cell that lacks MreB and Mbl, Van-Fl staining was observed at the septum and poles highlighting separate elongation and division machinery and a divergent strategy to also generate a rod-shaped cell (52). In the spherical cell, *S. aureus* (which also lacks Mbl/MreB), Van-FL staining was observed at the division septum and found to be directed by the FtsZ dependent division machinery. Depletion of the septal protein, FtsZ, lead to the observation of diffuse fluorescence and PG synthesis throughout the cell instead of restriction to the septum (59). Researchers were able to follow these cells through the division process and found that remodeled PG in the form of septal discs could serve as a record of the prior division plane to spatially inform the location for subsequent division planes (64). Use of these probes has revealed the spatial organization of bacterial growth and division, and have been used to complement studies of fluorescently labeled proteins to investigate the role of PG enzymes and cytoskeletal proteins in PG synthesis.

Peptidoglycan is assembled by a suite of PBPs whose individual functions are difficult to determine because individual PBPs are frequently dispensable for growth. Due to the covalent mechanism by which PBPs function to link together PG stem peptides fluorescent derivatives of penicillin V (Boc-Fl), a beta-lactam antibiotic that inhibits PBP-TG domains, have been used to visualize PBP activity (**Figure 1-5**). Boc-Fl has mainly found applications as an activity probe in gel-based assays to examine PBP function and inhibition (60, 65-67). Boc-Fl has also sparingly been used to localize PBP proteins during cell growth by microscopy which can inform on the location of PG transglycosylation. Staining of *C. glutamicum* with Boc-Fl demonstrated polar and septal localization in agreement with earlier observations of Van-Fl localization of nascent

PG at the poles and septum (60). Boc-Fl staining of *B. subtilis* revealed strong signal at cell septa and diffuse staining of *S. pneumoniae (57).* Many PBP enzymes perform transglycosylation reactions and share overlapping substrates (PG stem peptides) and therefore similarly bind Boc-Fl. Since cells can contain 5-15 PBPs, this complicates the ability of Boc-Fl to dissect the roles of individual PBPs. Kocaoglu and Carlson therefore developed cephalosporin-C fluorescent analogs, which bind to a subset of PBPs in *B. subtilis* and *S. pneumoniae* (57). In fluorescence imaging by 3D-SIM, they observed differential and discrete localization of subsets of PBP enzymes generating a promising toolset to delineate the individual functions of seemingly redundant PBPs during cell wall construction. Other antibiotics have been derivatized, including, penicillin, cephalexin, cephalothin and used in *in vitro* gel based screens (66) but could inform specific PBP localization probes for microscopy applications.

Table 1-1. Examples of antibiotic-based fluorescent analogs
(black) natural substrate (green) substrate analog

	Natural substrate	Fluorescent antibiotic probe	Target	Ref.
1-1	Vancomycin	Fluorescent BODIPY FL conjugate of vancomycin, (Van-Fl)	Lipid II stem peptide (D-Ala-D-Ala)	(52)

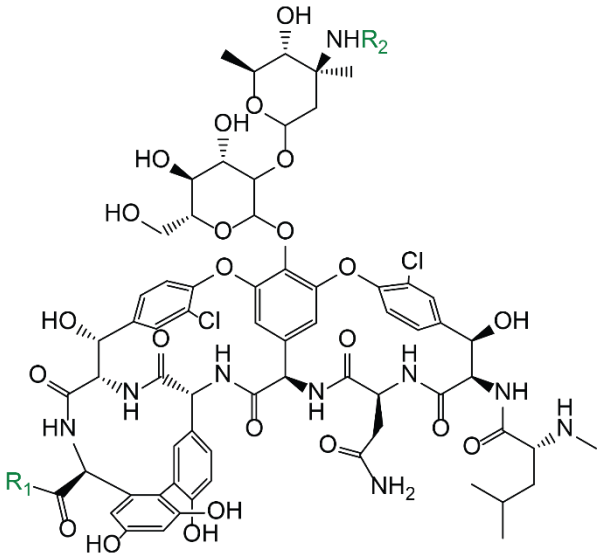

R1 = OH R2 = H
R1 = OH R2 = Bodipy-Fl
R1 = Bodipy-Fl R2 = H

1-2	Ramoplanin	Fluorescein conjugate of ramoplanin, (Ram-Fl)	Lipid II (diphospho-MurNAc)	(53)

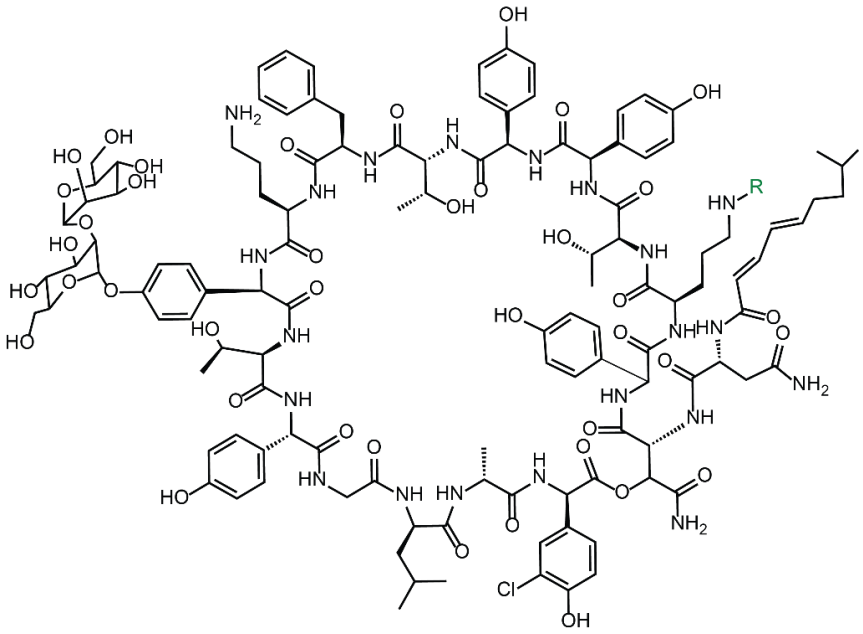

R = H

R = Fluorescein

1-3	Telavancin	Fluorescent BODIPY FL conjugate of telavancin, (TLV-FL)	Lipid II stem peptide (D-Ala-D-Ala)	(54)

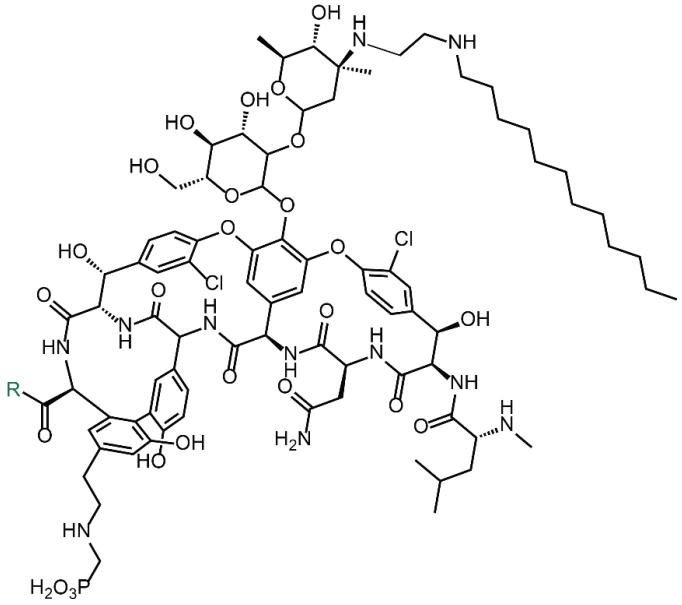

R = OH

R = Bodipy-Fl

1-4	Lanthipeptides (Lacticin 481, haloduracin α, haloduracin β)	Reactive N-terminal ketone substituted lanthipeptides	Lipid II (diphospho-MurNAc)	(58)

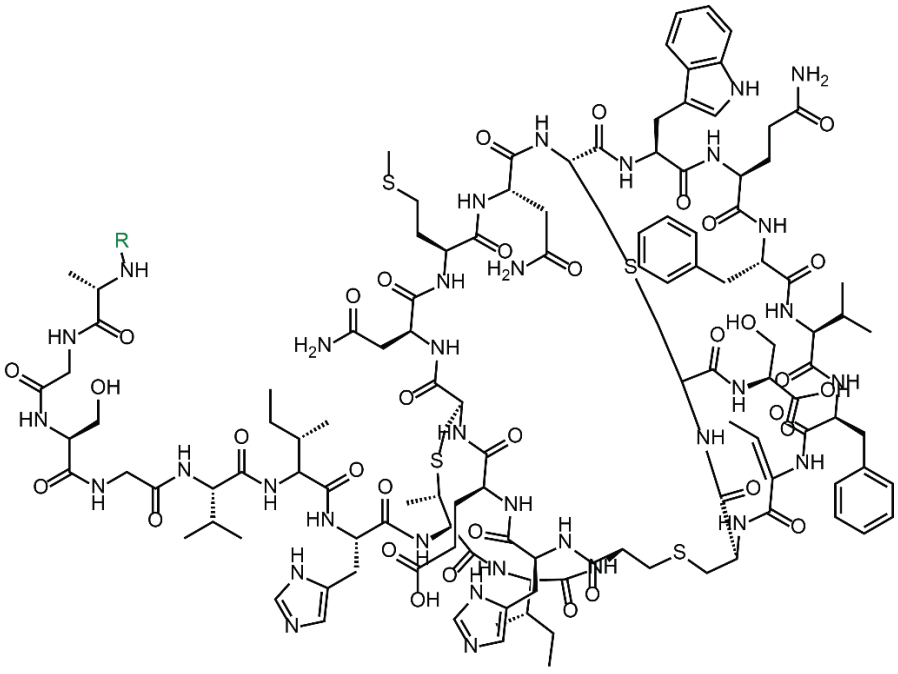

R = H

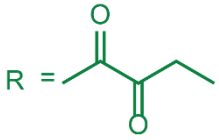

1-5	Penicillin V	Fluorescent BODIPY FL conjugate of Penicillin V, (Boc-Fl)	PBP (TG domain)	(55, 56)

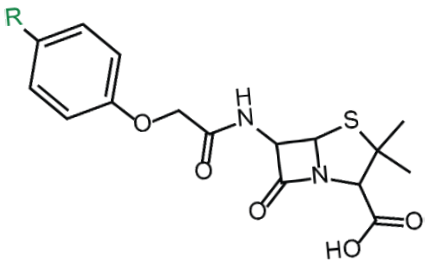

R = H

R = Bodipy-Fl

1-6	Cephalosporin C	Fluorescent TAMARA conjugate of Cephalosporin C, (CephC)	PBP (TG domain)	(57)

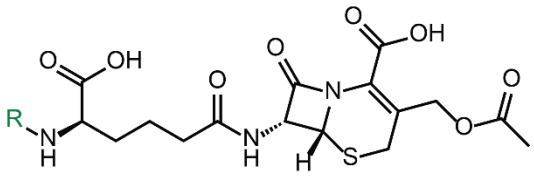

R = H

R = Fluorescein

(1-1) R_2 modified vancomycin is known commercially as BOC-Fl, R_1 modified vancomycin reported in reference (52).

(1-4) Lacticin 481 depicted.

1.5.2 Peptidoglycan-Based Fluorescent Analogs

Although fluorescent antibiotic conjugates have proven useful in labeling applications, they are inherently toxic to bacteria. Furthermore, these antibiotics are fairly large natural product analogs and suffer from some accessibility issues to reach and label their targets in Gram-negative bacteria. Therefore, to circumvent toxicity and permeability issues researchers have developed analogs of PG precursors (**Table 1-2**). Initial probes included fluorescent UDP-MurNAc pentapeptide (Fl-UDP-MurNAc) which is processed into lipid II and subsequently PG (68, 69). Incorporation of Fl-UDP-MurNAc rendered cells fluorescent and inspired the idea that the bacterial cell wall could be engineered. This concept informed future probes, including fluorescently labeled tripeptides (AeK-NBD), which revealed septal peptide processing dynamics in *B. subtilis* (69). Recent chemically reactive MurNAc derivatives developed by the Grimes research group were used in conjunction with high-resolution microscopy (70). Observations that MurNAc residues in mycobacteria and other Actinomycetes have modifications at the 2-*N* acetyl position of MurNAc directed the development of 2-azido-MurNAc (AzMurNac). AzMurNAc facilitated visualization of PG carbohydrate dynamics including the ability to interrogate the question of PG strand directional organization (helical or linear). Results thus far using fluorescent MurNAc analogs suggests circular networks or PG with the frequently observed helical component deriving from the peptide cross-links. The modular synthesis of the probes suggests that they may be able to be tailored for incorporation into specific strains of bacteria.

Surveys of the repertoire of bacterial lipid II pentapeptide sequences revealed that the terminal D-Ala residue could be substituted by various other D-amino acids. This observed

substitutional tolerance indicated that the terminal D-Ala might be able to be exchanged with a fluorescent derivative or a chemically reactive D-amino acid (FDAA) (71, 72). Substitution of the terminal D-Ala by an FDAA occurs via one of two distinct routes: intracellular or extracellular (**Figure 1-6**). Intracellularly, D-Ala-D-Ala ligase adds a D-amino acid at the fifth position of the PG stem peptide and may be involved in incorporation of chemically reactive D-amino acids (**Figure 1-6A**). Extracellularly, a D-amino acid is incorporated at the fourth or fifth position of the PG stem peptide via the enzymatic activity of Ldts or PBPs respectively and is likely involved in incorporation of fluorophore-conjugated D-amino acids and chemically reactive D-amino acids (**Figure 1-6B**) (73-75).

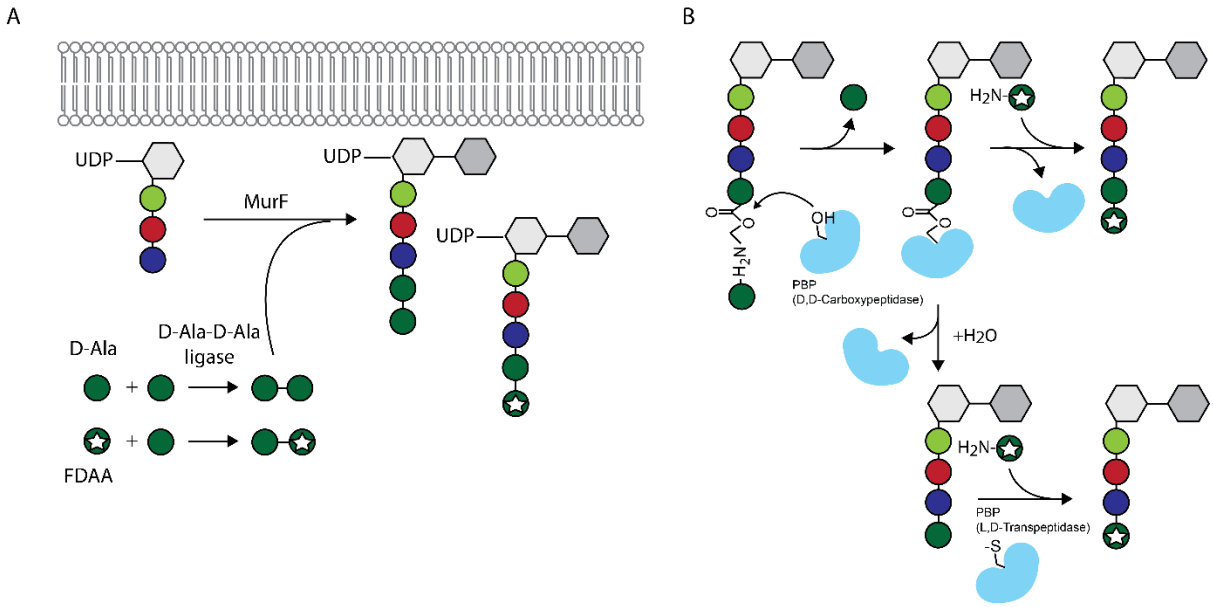

Figure 1-6. Incorporation routes for FDAA to label PG (A) intracellular FDAA incorporation occurs via D-Ala-D-Ala ligase and subsequent MurF processing. (B) Extracellular FDAA incorporation occurs via D-D-carboxypeptidases and L-D-transpeptidases.

A palette of direct fluorophore-conjugated D-alanine derivatives have been reported (e.g., 7-hydroxycoumarin-3-carboxylic acid-3-amino-d-alanine, HADA; 4-chloro-7-nitrobenzofurazan-3-amino- d-alanine, NADA; tetramethylrhodamine-3-amino-d-alanine;

TADA) (76, 77). Additionally, a toolbox of D-amino acids bearing a chemically reactive handle including, azido-D-ala (ADA), ethynyl-D-alanine (EDA), (R)-propargylglycine and non-alanine probes; D-amino carboxamide, D-Cys, and D-Lys (78). FDAA labeled cells can be visualized by subsequent conjugation with a fluorophore using bioorthogonal chemical reactions. The small size of these probes is advantageous for initial incorporation and broad utilization among bacteria. The two-step labeling process adds flexibility for the identity of the conjugation molecule and can facilitate multi-color labeling for fluorescent imaging of PG insertion. Short pulses of FDAAs covalently label nascent PG across the bacterial domain (73, 74). This includes dispersive and polar PG insertion in rod-shaped *Escherichia coli* and *B. subtilis*, polar and septal PG insertion in *Listeria monocytogenes*, polar and asymmetric PG insertion in *M. smegmatis* and *C. glutamicum*, septal and unipolar PG insertion in *Agrobacterium tumefaciens*, apical PG insertion in *Streptomyces venezuelae*, septal only PG insertion in *Lactococcus lactis* and *S. aureus*, and equatorial rings of PG insertion in *S. pneumoniae* (74). FDAAs were also used to resolve that obligate intracellular chlamydial species, which were believed to be absent of PG, possess functional PG (79). Collectively, these observations reveal that cell wall biogenesis in bacteria is achieved by a myriad of growth patterns. The use of FDAAs, therefore, provides a broad tool to examine the spatial dynamics of PG insertion in bacteria and have uncovered the growth mechanisms of diverse bacterial taxa. Given the uniqueness of D-Alanine and an exogenous route for incorporation, multiple species can be labeled in complex environments such as infections (73) or the spatial positioning of bacteria in the human gut (80).

Table 1-2. Examples of peptidoglycan-based fluorescent analogs
(black) natural substrate (green) substrate analog

	Natural Substrate	Fluorescent PG Probe	Target	Ref.
1-7	UDP-MurNAc pentapeptide	Fluorescent Fluorescein conjugate of UDP-MurNAc pentapeptide, (Fl-UDP-MurNAc)	Peptidoglycan (stem peptide)	(68)
	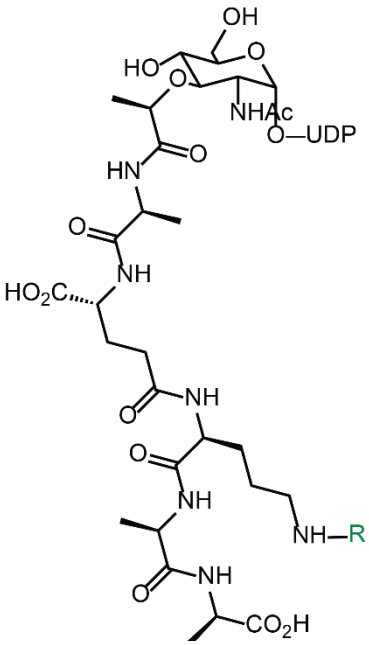			
	R = H R = Fluorescein			
1-8	L-alanyl-γ-D-glutamyl-L-lysine, (AeK)	Fluorescent NBD conjugate of AeK, (AeK-NBD),	Peptidoglycan (stem peptide)	(69)
	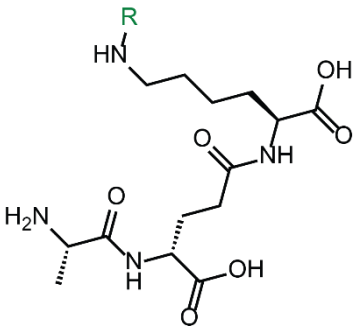			
	R = H R = NBD (nitrobenzoxadiazole)			

1-9	N-Acetylmuramic acid, (MurNAc)	Azido-2-MurNAc, (AzMurNAc)	Peptidoglycan (MurNAc)	(70)
	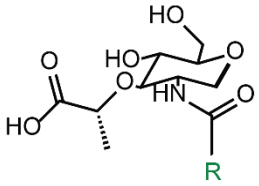			
	R = CH_3 R = N_3			
1-10	D-alanine	e.g.,7-hydroxycoumarin-3-carboxylic acid-3-amino-d-alanine (HADA)	Peptidoglycan (stem peptide)	(76, 77)
	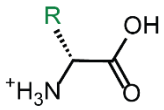			
	R = CH_3 R = 7-hydroxycoumarin-3-carboxylic acid, R = NBD, R = Bodipy (see (77))			
1-11	D-alanine	e.g., azido-D-ala (ADA), ethinyl-D-ala (EDA)	Peptidoglycan (stem peptide)	76
	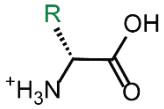			
	R = CH_3 R = N_3, R = alkyne			

1.5.3 Carbohydrate-Based Fluorescent Analogs

Bacterial cell envelopes are highly glycosylated and have been shown to be essential for the ability of pathogens to cause disease (81). As a result, bacterial glycans represent one of many intriguing cell envelope targets for antibiotic development. Bacteria use more than 700 monosaccharide building blocks to construct their glycans while mammalian cells use less than 25 monosaccharides (82). Bacterial usage of these monosaccharides varies; some are widely prevalent while others exist only in some orders or specific strains. Pathogenic bacterial classes can be clustered by shared monosaccharides thereby forming unique molecular signatures for exploitation as therapeutic or diagnostic targets (83-86). However, much work remains to uncover the biological roles of these glycans in bacteria. Therefore, tools that can facilitate discovery and access to bacterial glycans are needed to advance our understanding of glycan utilization and biological function in bacteria. Tools available to label proteins are not accessible to glycans which lack a genetic template and enzymatic activity. Glycans can be rendered susceptible to labeling using chemistry. Synthetic carbohydrate analogs bearing chemically reactive handles can be incorporated by cells in place of the natural sugar molecule through metabolic incorporation or synthetically modified *in situ* with chemically reactive groups to attach fluorescent reporters. Introduction of bioorthogonal chemical functionalities has its roots in eukaryotic glycoengineering but has seen minimal translation to bacterial systems. This is likely owing to the difficulty of carbohydrate synthesis, specificity of the carbohydrate enzymes and complicated interconnecting pathways of bacterial oligosaccharide processing. Bacteria can use a wide array of sugars as carbon sources and therefore it can be difficult in some systems to obtain specificity of molecular labeling through

cytosolic processing pathways. Nevertheless, glycans represent a rich source of strain-specific molecules to build imaging agents and develop therapeutics. The following examples will highlight recent advances in bacterial carbohydrate metabolic incorporation and fluorescent imaging applications. These probes have important applications as biological reporters and environmental or infectious diagnostics for important pathogens.

Analogs of Gram-negative LPS and Gram-positive teichoic acids have been developed and used to broadly label bacterial cell envelope glycopolymers in bacteria (see **Table 1-3**). LPS is an outer membrane glycolipid containing an inner polysaccharide core and an exterior O-antigen. The inner core contains an oligosaccharide of heptose and KDO. Gram-negative bacteria, including *E. coli*, *Salmonella typhimurium*, and *Legionella pneumophila* were shown to incorporate an azide-modified analog of 3-deoxy-D-manno-octulosonic acid (KDO) into LPS. Subsequent labeling with 8-azido-8-deoxy-KDO and a fluorophore enabled rapid detection of viable Gram-negative bacteria and did not label Gram-positive bacteria (87). KDOAz was effectively used in complex environments, including mouse intestines, to label Gram-negative bacteria along with Van-Fl to label Gram-positive bacteria and visualize bacterial class distribution within the mammalian gut (88).

Propargyl-choline (Pgc) was efficiently incorporated into teichoic acid (TA) polymers on the surface of the Gram-positive bacteria, *S. pneumoniae* (89). Pneumococci are known to incorporate choline into their teichoic acids, and loss of choline leads to decreases in virulence and resistance to the host immune system (90). Phosphorylcholine modification to glycopolymers, glycolipids or secreted proteins is also present in other pathogenic bacteria (91, 92). Subsequent labeling of Pgc modified TA polymers with a fluorophore allowed specific

detection of *S. pneumoniae*. Fluorescence image analysis also revealed TA assembly dynamics and that TA biosynthesis was localized to the cell septum, suggesting spatial coordination between TA and PG synthetic machinery. This tool can, therefore, inform on TA dynamics in *S. pneumoniae* or other bacteria that tailor glycans with choline.

Labeling strategies using shared bacterial and mammalian sugars (e.g., GalNAc) will be taken up by host cells and bacterial cells and metabolically incorporated into glycoproteins thereby limiting their application for *in situ* analysis of complex host processes. Nevertheless, these strategies can be useful for complex bacterial samples, as bacterial identification tools or to investigate bacterial cell envelope dynamics. *Bacteroides fragilis*, a human commensal Gram-negative bacterium, treated with D-GalNAz, an azido GalNAc analog, and a fluorophore generated fluorescent *B. fragilis* (93). D-GalNAz was incorporated into an abundant capsular polysaccharide, Polysaccharide A, comprised of repeating units of N-acetyl-galactosamine (GalNAc). GalNAz modified *B. fragilis* bacteria, and capsular polysaccharides were fluorescently labeled and tracked in a mouse host in real-time to examine bacterial distribution and colonization preferences (93). This demonstrated that cells could be labeled *in vitro* and introduced into complex systems, including infection models or microbial communities to circumvent the complications associated with a widely distributed monosaccharide.

Bacterial specific glycan probes of unique monosaccharides targeting glycolipids, capsular polysaccharides, protein N-glycosylation have been used in fluorescent-based detection applications. The human pathogen *L. pneumophila* is a Gram-negative bacterium and the causative agent of Legionaries disease. *L. pneumophila* has an LPS O-antigen that distinguishes its infectious serogroups. This O-antigen is composed of a repeating homopolysaccharide of

legionaminic acid (Leg5Am7Ac), a nonulosonic acid similar to 5-acetamido neuraminic acid. Researchers generated an azido derivative of a Leg5Am7Ac metabolic intermediate, 6-azido-2,4-diacetamido-2,4,6-trideoxy-d-mannopyranose. Metabolic incorporation of this sugar analog and subsequent fluorescent labeling allowed the specific labeling and detection of live *L. pneumophila* bacteria specifically and not other species of *Legionella* (94).

Campylobacter jejuni, a Gram-negative bacterium responsible for outbreaks of food poisoning that can require medical attention. Protein N-glycans and lipooligosaccharides (major glycolipids that are structurally similar to LPS) are known to include terminal GalNAc residues. The enzyme, galactose oxidase, was used to chemoenzymatically install a reactive aldehyde on these terminal GalNAc residues, GalNAc-6-Ald. Subsequent conjugation with an aminooxy fluorophore leads to the labeling of live *C. jejuni* glycoconjugates and exploration of *C. jejuni* glycoconjugates that include terminal GalNAc residues. (95). Additionally, this strategy should allow for identification of cell-surface glycoproteins and glycolipids from other bacteria that contain galactose or GalNAc-terminating glycans.

The mycobacterial cell envelope is unique from that of Gram-positive and Gram-negative bacteria (Figure 1-1). A notable feature is the presence of trehalose glycolipids that form an outer membrane. This membrane structure, the mycolic acid membrane, is vital for mycobacterial infection and recalcitrance to antibiotics. The uniqueness of the trehalose glycan, the accessibility provided by its location and extracellular processing route and importance to mycobacterial disease progression have inspired its development as a mycobacterial probe. A large library of substituted trehalose disaccharides was tested with a myriad of substitutions to determine the promiscuity of the mycolyltransferases that process

mycobacterial trehalose glycolipids. Using this information and published crystal structures of trehalose bound mycolyltransferases a fluorescein trehalose analog (96) and a suite of chemically reactive trehalose analogs have been developed (97-99). These probes have facilitated the examination of glycolipid function and dynamics in mycobacterial cells, revealing that trehalose metabolic products, TMM, and TDM, accumulate at cell poles and septum concurrent with the known polar growth model of mycobacterial species. The rapid and effective diagnosis of mycobacterial infections is crucial for treatment of this devastating disease. Existing diagnostic protocols center around a fairly laborious and insensitive acid-fast staining protocol. Therefore, these analogs have the inspired the formation of a simple fluorescent diagnostic. Indeed, these probes can selectively label mycobacterial cells and not other tested Gram-negative or Gram-positive bacteria (96). These probes would, however, label all bacteria that contain mycolic acids. The small size of FITC-trehalose allowed exogenous incorporation into TMM and TDM of infected macrophages (96). The result was later extended to the development of PET reporter labeled trehalose with the goal of monitoring *in vivo* infection progress of tuberculosis (96, 100).

Chemically reactive analogs of other rare bacterial sugars have been reported but have not been used in imaging-based applications. Such probes include pseudaminic acid derivatives that were incorporated into the flagellin protein of *C. jejuni* flagella (101), use of an azido modified GlcNAc to metabolically profile *Helicobacter pylori* glycosylation (102), alkyne-bearing fucose analogs have been metabolically incorporated into glycoproteins of Bacteroidales species for glycoproteomic analysis (103) and the O-antigen of *E. coli* LPS (104). These results

highlight the enormous potential present in bacterial glycans to interrogate the role of bacterial polysaccharides in bacterial fitness or for exploitation to detect bacterial strains.

Table 1-3. Examples of carbohydrate-based fluorescent analogs
(black) natural substrate (green) substrate analog

	Natural Substrate	Fluorescent Carbohydrate Probe	Target	Ref.
1-12	3-deoxy-D-manno-octulosonic acid	8-azido-8-deoxy-KDO (kdoAz)	Gram-negative/LPS	(87)
	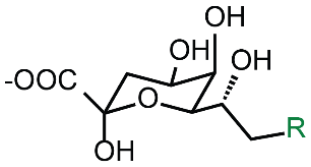 R = OH R = Alkyne			
1-13	Propargyl choline	Propargyl-choline	Gram-positive/Teichoic Acids	(89)
	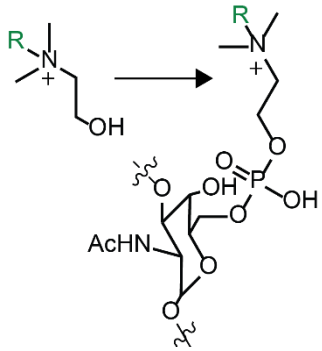 R = CH_3 R = Alkyne			
1-14	2,4-diacetamido-2,4,6- trideoxy-d-mannopyranose	6-azido-2,4-diacetamido-2,4,6-trideoxy-d-mannopyranose, (LegAz)	Gram-negative/LPS	(94)
	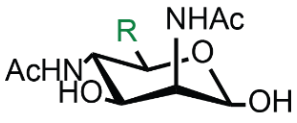 R = CH_3 R = Alkyne			

1-15	Galactose and N-acetyl-D-galactosamine (GalNAc)	C6-Aldehyde substituted Gal/GalNAc (Gal-6-Ald, GalNAc-6-Ald)	Gram-negative/Protein N-glycosylation	(95)
	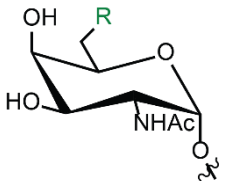			
	R = OH R = aldehyde			
1-16	GalNAc	GalNAz	Gram-negative/Capsular polysaccharide	(93)
	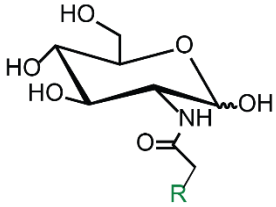			
	R = H R = N_3			
1-17	Trehalose (TMM, TDM)	Modified trehalose (TreAz, Tre-Fl)	Mycobacteria/mycomembrane	(96-99)
	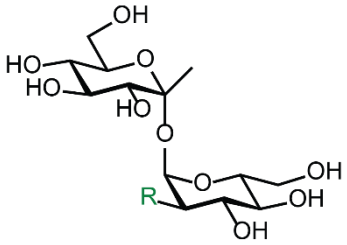			
	R = OH R = FiTC			
	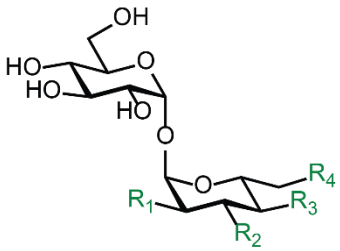			
	R_1, R_2, R_3, R_4 = OH R_1 = N_3 R_2, R_3, R_4 = OH R_2 = N_3 R_1, R_3, R_4 = OH R_3 = N_3 R_1, R_2, R_4 = OH			

1.5.4 Lipid-Based Fluorescent Analogs

Lipid composition varies widely across bacteria and can be modulated in different physical environments (105). Maintenance of bilayer composition is vital during cell division and to localize proteins properly (106). Control of fatty acid production is important both for energy storage, consumption and controlling pools of molecular precursors processed into the cell envelope (e.g., lipid II). The diversity of lipid structures raises questions relating to their function and recognition (107, 108). Commercially available synthetic fluorescent lipids are available for major bacterial lipids, such as phosphoethanolamine (PE), phosphorylcholine (PC) and phosphoglycerol (PG). Lipid probes are typically fluorescent at either their head group or acyl chain or contain chemically reactive groups at these locations. Early explorations suggested such fluorescent lipids could be used as markers of the unique lipid composition of mycolic acid membranes (109, 110). While many fluorescent small molecules are available (41-44), very few studies to date have used species-specific lipid analogs for imaging experiments of cell membrane dynamics (111). Relevant to cell envelope biosynthesis is the localization of the fluorescent small molecules dye nonyl acridine orange (NAO) to anionic lipids. NAO demonstrated coincident localization of membrane rafts and fluorescent flotillin fusion proteins (raft scaffold protein) and fluorescent penicillin-binding proteins (PBPs) that assemble *S. aureus* PG which generated a localization model for PBPs and lipid rafts (19). A cluster of efforts has focused on the development of fluorescent lipid analogs for the mycobacterial mycolic acid membrane (**Table 1-4**). This includes the use of fluorescent trehalose glycans (FiTC-6-Tre) metabolically incorporated into trehalose glycolipids where membrane fluidity features were assessed in mycolic acid-containing bacteria (97). Using fluorescence recovery

after photobleaching (FRAP) researchers were able to demonstrate that fluidity of the mycolic acid membrane was correlated with the length of the acyl chains of the trehalose glycolipids. The length of these glycoconjugates varies throughout species that contain mycolic acid membranes (112). Recently, the Swarts research group developed trehalose glycolipid mimics with an alkyne positioned at the terminus of the acyl chain (Alk-TMM) (113, 114). Alk-TMM was able to be attached to the arabinogalactan and therefore covalently label mycobacteria. Results with this probe reported that active arabinogalactan mycolylation occurs at the cell poles and septum. Recent observations that pools of certain lipids are enriched in bacterial rafts and can direct the location of PG biosynthetic enzymes (115) presents the opportunity to examine how different lipids are localized in bacteria, including pools of isoprenoid based lipids. Indeed, synthetic methods to assemble fluorescent bacterial isoprenoids have been reported but have not been evaluated microscopically (116). Also of interest are the many bacterial lipoglycans present in mycobacteria (117, 118) and other bacteria and how these lipids are flipped from the cytoplasm to the surface for enzymatic processing (119-121). Many of these flippases have yet to be identified owing to the difficulty associated with their transmembrane structure and complexity of their substrates. Fluorescent substrates would be efficacious to validate and localize these proteins. Indeed, many unique *in vitro* assays have been developed to validate flippases. However they are not broadly applicable owing to the unique nature of their substrates.

Table 1-4. Examples of lipid-based fluorescent analogs
(black) natural substrate (green) substrate analog

	Natural Substrate	Fluorescent lipid Probe	Target	Ref.
1-18	Trehalose (TMM, TDM)	Fluorescent fluorescein-conjugated trehalose (FiTC-6-Tre)	Mycobacteria/ mycomembrane	(97)
	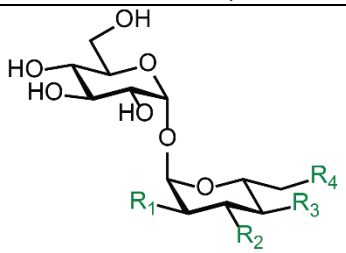 R_1, R_2, R_3, R_4 = OH R_1 = FiTC R_2, R_3, R_4 = OH R_2 = FiTC R_1, R_3, R_4 = OH R_3 = FiTC R_1, R_2, R_4 = OH			
1-19	Trehalose (mAG)	Alkynyl modified trehalose (Alk-TMM)	Mycobacteria/ mycomembrane	(113, 114)
	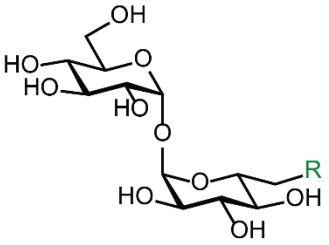 R = OH R = 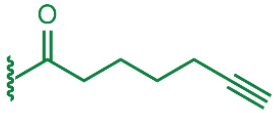			

1.6 Microscopy

Fluorescence microscopy of live microbial cells can enable illumination of the localization, dynamics, and interactions of cell envelope macromolecules. Conventional fluorescence microscopy, however, is hindered by the diffraction limit of light. The maximal lateral resolution of light microscopy is a few hundred nanometers (~250 nm) and given the small size of bacterial cells (1 to 10 microns) many important bacterial subcellular features are unable to be optically resolved. Fluorescence super-resolution microscopy (SR) techniques have been developed that function beyond the diffraction limit of light (**Figure 1-7**) (122, 123). This includes structured illumination microscopy (SIM) (~120 nm). SIM can be implemented on a conventional widefield microscope using a single laser, conventional fluorophores and is compatible with live samples. SIM, however, is restricted in resolution enhancement because the pattern frequencies used for illumination are themselves limited by the diffraction limit of the lens. Therefore, scientists have turned to techniques that instead exploit properties of the fluorescent molecules being detected which can circumvent diffraction limits to achieve higher resolutions.

Super-resolution techniques based on fluorophore properties include a strategy known as non-linear SIM, which can functionally achieve a lateral resolution of ~50 nm. Another technique which relies on specialized fluorophores is stochastic optical reconstruction microscopy (STORM) and photoactivated localization microscopy (PALM). STORM/PALM rely on special photo-switchable fluorophores; these are fluorophores that can be switched between a dark and bright state with separate lasers. In PALM/STORM, two lasers differentially antagonize a photoswitchable fluorophore or fluorescent protein (photoactivatable GFP) and

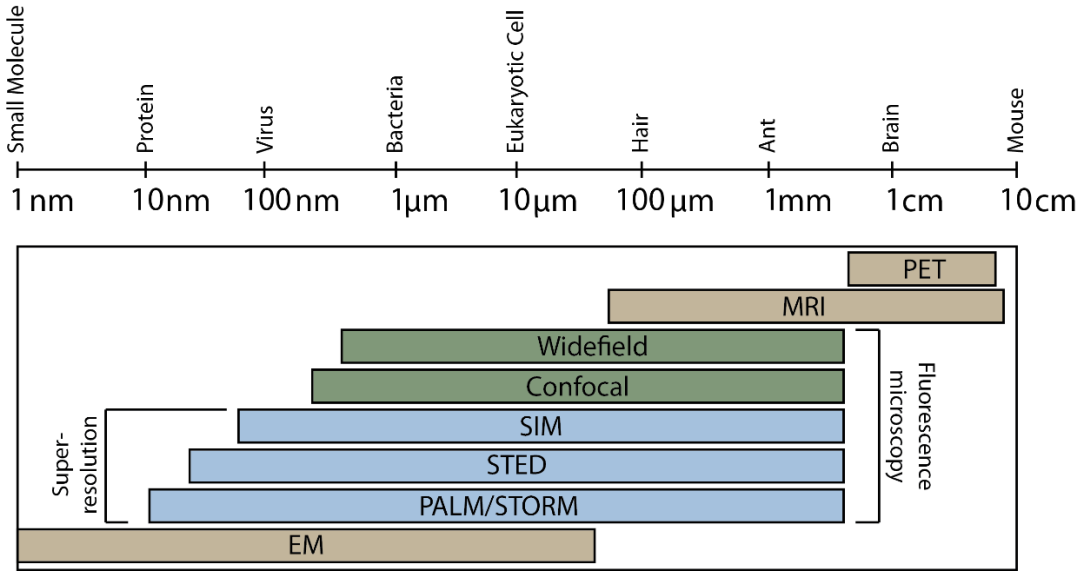

Figure 1-7. Spatial resolution of biological imaging techniques Adapted from (124)

collect a series of images, each containing only a handful of activated fluorophores. These images of individually activated fluorophores are later combined to generate the final fluorescent image. During each imaging cycle because only a small subset of fluorophores are activated they are unlikely to be overlapping. This strategy can achieve lateral resolutions of 20 nm. The physics of these techniques and their application to microbiology have been reviewed elsewhere (122, 123, 125-129). These techniques are also being combined with imaging capabilities of cryo-electron microscopy to image cellular structures at potentially Angstrom resolution (130).

The combination of fluorescent bacterial probes of cell envelope components and continually advancing microscopy techniques that function below the diffraction limit present opportunities to reveal important details about cell envelope nanoscale assembly processes. A probe of a cytosolic enzyme in *B. subtilis* was developed to function with a push-pull red-emitting fluorophore that generated fluorescence upon enzymatic processing. This process

(ETALM, enzymatic-turnover-activated localization microscopy) therefore provided a beacon to localize enzymatic activity by microscopy (131). As an SR technique, enzymatic turnover continuously generated new fluorophores thereby performing the photo-switching function. Probes of this class targeted at cell envelope enzymes would benefit from external accessibility and could inform on the specifics of extra-cytoplasmic cell envelope assembly. Cell envelope construction is performed by various enzymes that are frequently transmembrane and therefore difficult to examine *in vitro*.

1.7 Fluorogenic Probes

Properties of fluorescent molecules are particularly important for the ability to sufficiently image fluorescently labeled bacterial components especially regarding SR microscopy. The chemistry of these probes has been expertly reviewed elsewhere (132-139). Here I will highlight the development and need for fluorogenic probes which can improve contrast, reduce processing steps and facilitate real-time imaging to advance the ability to observe cell envelope construction as it is happening. Conventional fluorophores are fluorescent before and after incorporation which can necessitate washing or secondary labeling steps that can obscure fine spatial-temporal information. Fluorogenic probes that only display fluorescence either through enzymatic activity, environmental properties or a chemoselective reaction would enable access to increased information about cell envelope dynamics.

Fluorogenic probes can be generated using fluorophores whose structure is altered by their environment to induce fluorescence (solvochromatic dyes) or modified by an enzymatic reaction to generate fluorescence. The fluorescence emission intensities of solvochromatic dyes are sensitive to features of their local environment. This can be exploited to generate

fluorophore molecules that are responsive to hydrophobicity, for instance. One recent application of such a probe was the addition of a polarity sensitive fluorophore, 4-N,N-dimethylamino-1,8-naphthalimide (DMN), to trehalose. This enabled a change in fluorescence upon incorporation of trehalose into the mycolic acid membrane of mycobacteria. A probe of this class can, therefore, function to fluorescently label mycobacteria without washing and could for the basis for an effective diagnostic or to monitor mycolic acid membrane dynamics (140). Such a strategy could be employed for other cell envelope components that function near the inner or outer membrane. A similar strategy was used with the dye nile red and a genetically encoded protein tag (SNAP-tag) whereby conjugation of nile red to a membrane protein via SNAP-tag was induced to be fluorescent upon interaction with the adjacent membrane (141). The cell envelope is a rich source of enzymatic activity. Therefore, fluorophores could be designed with molecules that inhibit the aromaticity required for fluorescence emission until processing. Such examples were seen with ETALM described in **section 1.6** and in assays detecting esterase, sulfatase and β-lactamases activity *in vitro* (142-146). Probes could also be designed to encode a fluorophore-quencher pair that can separate upon specific enzymatic processing to reveal fluorescence and have been used in eukaryotic systems (147-150).

Secondary conjugation of a fluorophore to a metabolically incorporated cell envelope macromolecule requires a unique chemical functionality that should be absent from the system being studied. This functionality must also react in a selective and specific manner within the complex milieu of the cell envelope and its environment. Reactions that satisfy these requirements are referred to as biorthogonal (orthogonal to biology). Many biorthogonal

reactions have been used to label biomolecules under physiological conditions without background cross-reaction to functional groups of other cellular biomolecules, and have been thoroughly reviewed (30, 32, 151, 152). Imaging living systems in real time requires additional attributes beyond biorthogonality; 1. the reaction conditions must not be toxic to the cells, 2. the reaction should proceed with fast reaction kinetics, 3. the resultant conjugation should yield a stable linkage, and 4. the labeling should proceed with rapid induction to minimize processing and background. Fluorogenic probes that are dark until conjugated to the target molecule would satisfy this latter requirement. Chemoselective reactions that display biorthogonality, biocompatibility and selectivity in living systems have been identified, and used in bacterial imaging (**Figure 1-8)** and includes ketone, azide, and alkyne-based reactive handles. Here, I will briefly discuss these reactions and their use in fluorogenic labeling reactions.

Ketones have been used for selective transformations owing to their negligible size, stability and virtual absence from cell surface biomolecules. Ketones can undergo attack from the reactive amine of hydrazine and alkoxyamine fluorophores to form hydrazone or oxime adducts (**Figure 1-8A**). Due to the pH requirements of this reaction and presence of ketones in cytosolic intermediates, it is well suited for functionalization of molecules displayed on cell surfaces and the ability to achieve the necessary reagent concentrations (~5mM). This reaction has been used to label bacterial surfaces (68). However, ketone condensation reaction kinetics proceed quite slowly (**Figure 1-8D)**, and its functionalization conditions can limit its effectiveness in complex samples. Fluorogenic hydrazines have been developed that become fluorescent upon reaction with ketones or aldehydes (153, 154). However, the condensation

products suffer from aqueous stability issues and alternative reagents that could form more stable adducts are needed.

Alkyl azides are a particularly useful reactive handle; they are small, stable, absent from cellular molecules and relatively nontoxic. Alkyl azides can undergo unique reactions with phosphines and alkynes, two reactants that are also absent from biological systems. The terminal nitrogen of the azide reacts with a triarylphosphine to generate a stable amide bond in a reaction known as a Staudinger ligation (**Figure 1-8B**) (155). Drawbacks of this reaction, however, include slow reaction kinetics (**Figure 1-8D)** and the susceptibility of phosphine reagents to oxidation which necessitates high concentration of phosphine reagents which may generate a high background signal in imaging applications. This reaction has been used to label bacterial surfaces (156). Fluorogenic phosphines have been generated for the Staudinger ligation including, a Coumarin-based fluorogenic phosphine that takes advantage of oxidation to become fluorescent (**Figure 1-8A**) (157). However, phosphine oxidation can occur with ambient oxidation resulting in fluorescence. Another strategy uses a FRET-based fluorogenic phosphine that becomes fluorescent upon release of a quencher subsequent to the Staudinger ligation (**Figure 1-8B**) (154, 158). Non-specific oxidation is not an issue as the fluorescent phosphine remains dark as a result of the quencher.

Azides can also undergo [3 + 2] cycloadditions with alkynes to yield triazoles (**Figure 1-8C**) (159). This reaction is inherently very slow but was shown to undergo dramatic rate enhancement with a catalytic amount of copper, Cu(I), at physiological conditions (CuAAC, copper assisted azide-alkyne cycloaddition) (**Figure 1-8D)** (160, 161). The use of copper salts, however, has proven toxic in some biological systems. Therefore, strain-promoted

cycloadditions using cyclooctynes and azides to generate triazoles have been established (SPAAC, strain promoted azide-alkyne cycloadditions) (**Figure 1-8C)**. SPAAC has similar rates to the Staudinger ligation but is kinetically slower than CuAAC (**Figure 1-8D**). SPAAC has therefore found broad utility for imaging living systems where azide bearing probes have been incorporated owing to procedural simplicity and reduced toxicity (73, 98, 101, 103, 156). Strained cyclooctynes, however, can have off-target reactions with endogenous nucleophiles. Fluorogenic probes activated by CuAAC and SPAAC have been developed (**Figure 1-9C**&**D**). These probes take advantage of the electron lone pair of the proximal azide nitrogen to delocalize into the triazole thereby releasing its quenching ability. Fluorogenic alkynyl probes have been generated however their photophysical mechanisms have been more difficult to establish. The off-target reactions of strained cyclooctynes with endogenous nucleophiles have been reduced with the development of dibenzocyclooctyne (DIBO) and biarylazacyclooctynone (BARAC) cyclooctyne versions (162).

In summary, a wide array of bioorthogonal chemical reactions have been established for use in living systems and optimized for selectivity, stability, lack of toxicity and kinetics. The modularity and chemical potential of these reagents are poised to resolve bacterial nanoscale architectures especially as imaging and fluorophore technologies continue to advance. Microscopic imaging of dynamic living systems can be enhanced by the development of fluorogenic probes that limit the number of processing steps and enhance contrast while facilitating continuous image acquisition to capture spatial-temporal information (154).

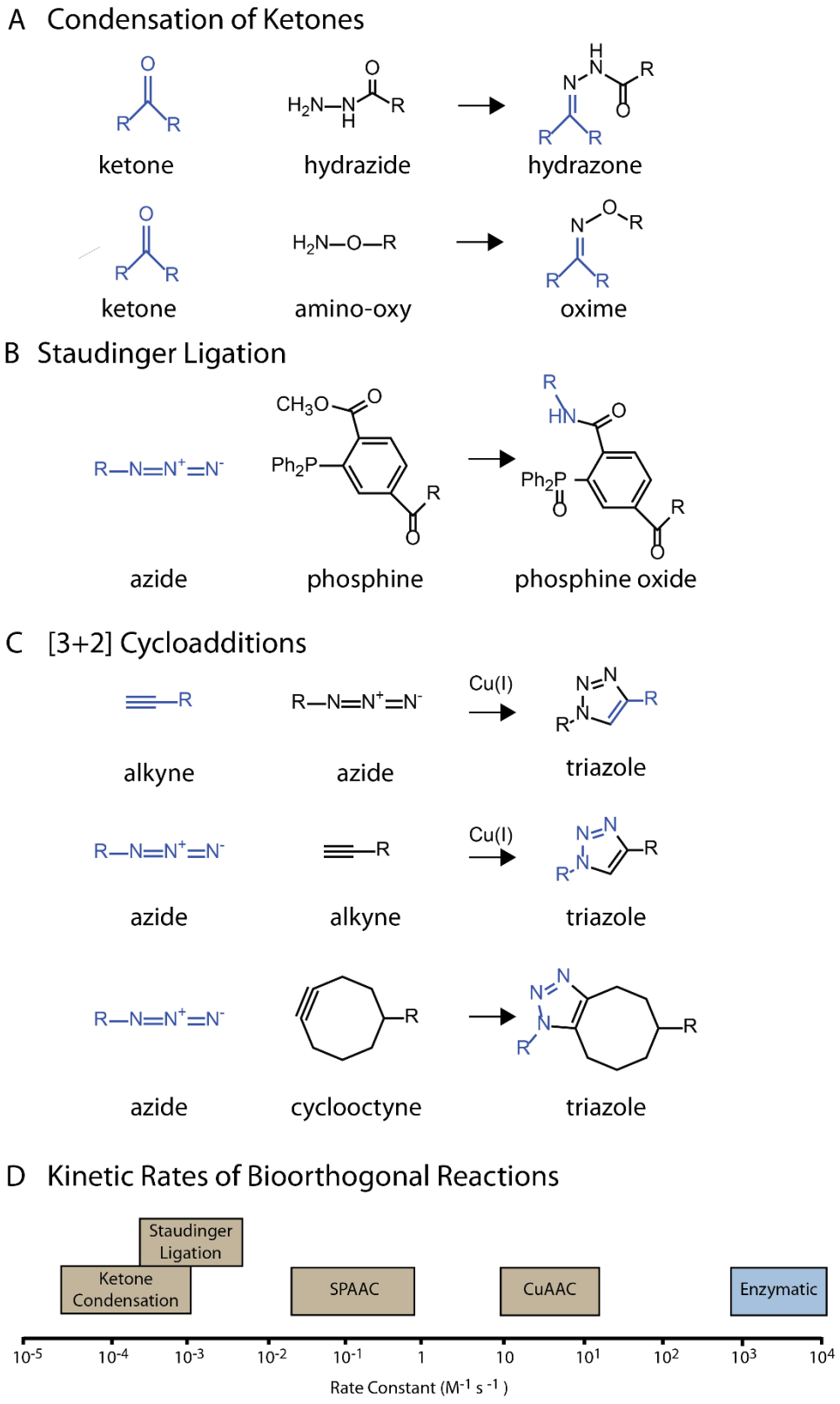

Figure 1-8. Referenced bioorthogonal reactions used to fluorescently label the bacterial cell envelope Adapted from (163), (32), (30).

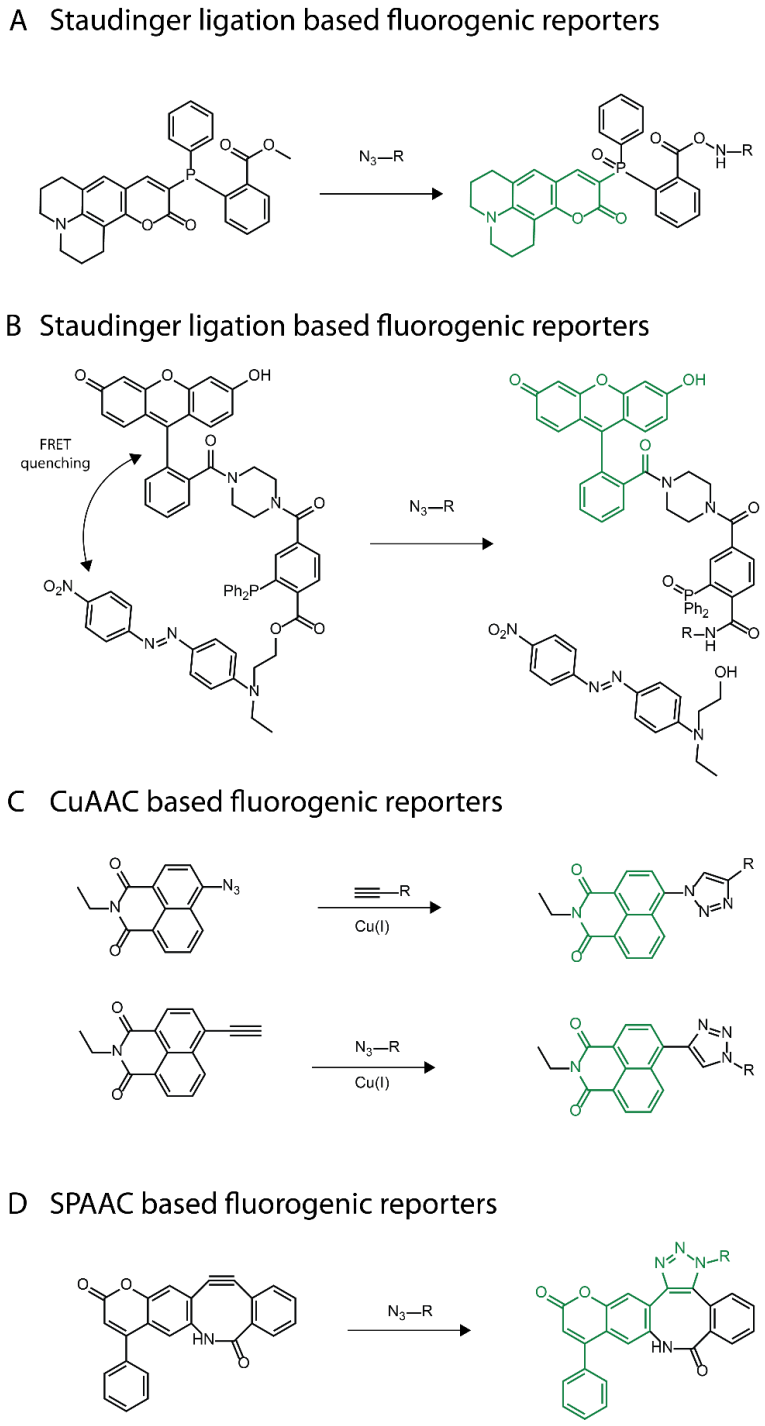

Figure 1-9. Fluorogenic bioorthogonal reporters Staudinger ligation based probes (A) activated by reaction with an azide to cleave an ester (B) ester cleavage releases a FRET-based quencher. (C) CuAAC (D) SPAAC fluorogenic reporters from triazole formation. Adapted from (163), (154).

1.8 Conclusions

The studies described above demonstrate that distinctive cell envelope molecular features can form the basis for fluorescent reporters to uncover bacterial cell envelope assembly. Synthetic methods present the opportunity to access nearly any component of the cell envelope. The probes highlighted herein have addressed important questions in microbiology by allowing researchers to watch biochemistry in action, including, how bacterial cell envelope construction and maintenance is controlled in three dimensions during the cell-cycle. The ability to observe cell envelope components and assembly machineries in the context of living cells is not possible by available conventional biological techniques alone. Continued development of fluorescent probes for bacterial glycans, lipids and enzymes offer an innovative approach that can inform on bacterial processes in either a broad- or narrow-spectrum manner in single cells or complex communities. The ability of these probes to target unique bacterial epitopes, including strain-specific features, presents the potential to discover or to validate novel acting antibiotics by forming the basis for high throughput or selective screening. These probes can also be used to develop clinical diagnostics as highlighted by the evolving development of trehalose based probes for mycobacterial infections. The specificity of these probes can visualize the distribution and fate of bacteria in host and infection models. Realization of the potential for these reporters requires continued development not only in synthetic access to increased bacterial cell envelope targets but also advances in fluorophore chemistry and imaging technologies. The generation of fluorogenic reporters would facilitate the ability to follow bacterial processes in real-time. Fluorogenic reporters could be accessed

through either turn-on or responsive fluorophores or fluorescent cell envelope probes that are activated by enzymes directly or through the release of FRET-based quenching.

1.9 Acknowledgements

Thanks to Alexander Justen for helpful discussions.

Chapter 2

Isolation and Reconstitution of Spatially Intact *Escherichia coli* Chemotaxis Arrays

Portions of this work have been published in:

Briegel, A., Wong, M.L., Hodges, H.L., Oikonomou, C.M., Piasta, K.N., Harris, M.J., Fowler, D.J., Thompson, L.K., Falke, J.J., Kiessling, L.L. and Jensen, G.J., 2014. New insights into bacterial chemoreceptor array structure and assembly from electron cryotomography. Biochemistry, 53(10), pp.1575-1585 (http://pubs.acs.org/doi/abs/10.1021/bi5000614)

2.1 Abstract

Bacteria have evolved sophisticated signaling pathways to generate adaptive responses to their environment. One of the best-characterized pathways is the chemotaxis system which controls cellular motility. Studies have revealed complex hierarchal arrangements of chemotaxis components. Transmembrane chemotaxis receptor dimers are arranged as clusters in extended hexagonal polar arrays. These clusters are connected into a signaling network by the histidine autokinase, CheA, and adapter protein, CheW. It is unclear how these proteins assemble to form extended arrays. Methods to reconstruct *in vitro* chemotaxis arrays with native architecture remains challenging. We used molecular biology and protein biochemistry to generate arrays of chemotaxis proteins under various conditions *in vivo* and *in vitro* which were imaged by electron cryo-tomography. We present details of assembly intermediates and the assembly mechanism of this macromolecular complex. Receptors were observed as clusters of trimers-of-dimers, indicating that this formation is a highly favored fundamental building block. Receptor trimers-of-dimers displayed versatility in their formations with each other and with other components of the signaling pathway in reconstituted arrays and but not in native arrays. Finally, CheA and CheW formed alternating CheA-filled and CheA-empty rings that linked receptor trimers-of-dimer units into a hexagonal lattice. While isolated native arrays yielded correct hexagonal order, CheA occupancy, however, was lower and less ordered, suggesting that temporal and spatial coordination of gene expression may be vital for full array connectivity. These results reveal insights into the assembly and architecture of the chemoreceptor array and present structural details of available *in vitro* preparations of reconstituted chemoreceptor complexes and those developed herein.

2.2 Introduction

Cellular membranes are complex protein-rich environments that form the interface between cells and their environment. Cellular signaling pathways within this crowded milieu have evolved as multi-protein complexes in order to achieve specific and sensitive responses to ligands (164). Indeed, many fundamental biological processes are mediated by spatially and dynamically organized transmembrane receptor complexes, including cell-cell recognition, immune responses, and signal transduction. Transmembrane receptor protein clustering is observed in many diverse signaling systems including B-cell and DC-Sign antigen processing (165-167), T-cell immunological and neuronal synapses (168, 169), epidermal growth factor receptors (170) and in bacterial chemotaxis (171) (**Figure 2-1**). Malfunctions in such pathways are known to underlie disease states (172, 173). Given the central role of multi-protein complexes in environmental signal integration and cell fate decision-making, development of techniques to elucidate their structure, assembly, and molecular mechanisms is essential to understanding their functions and generating therapeutics.

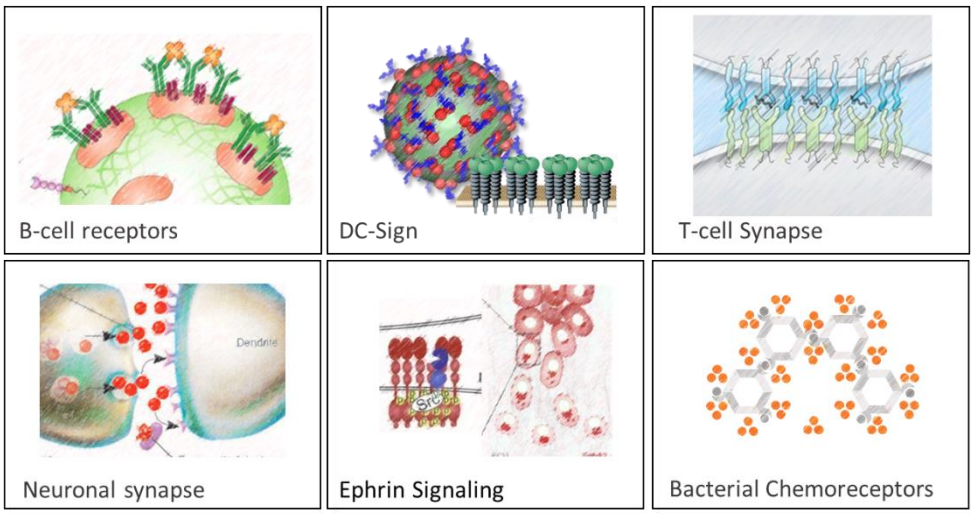

Figure 2-1. Multi-protein complexes are prevalent throughout biology

The multi-protein signaling cascade termed bacterial chemotaxis is a temporal sensing mechanism that controls the motility of relevant chemotactic bacteria in response to chemical changes in the environment (174-178). Chemotaxis is best understood in *Escherichia coli* (*E. coli)*. In this model system, conditions at the present location are compared with those in the immediate past (176, 178). Environments more favorable than those previously encountered reduce the rate of tumbling, thereby prolonging the time spent in favorable surroundings. Exposure to less favorable environments promotes re-orienting tumbles, which allow the bacteria to rapidly sample adjacent environments (179) (**Figure 2-2**). Temporal changes in environmental chemical concentrations are detected through a collection of mostly transmembrane chemoreceptors which act as sensitive naturally occurring biosensors (180). Each chemoreceptor responds to a unique subset of ligands that includes molecules that are either attractants or repellents and chemotactic bacteria encode 3-60 chemoreceptors. The substrate specificity for the vast majority of these chemotaxis receptors has not been determined. In *E. coli* attractant identity correlates to rates of amino acid consumption (181,

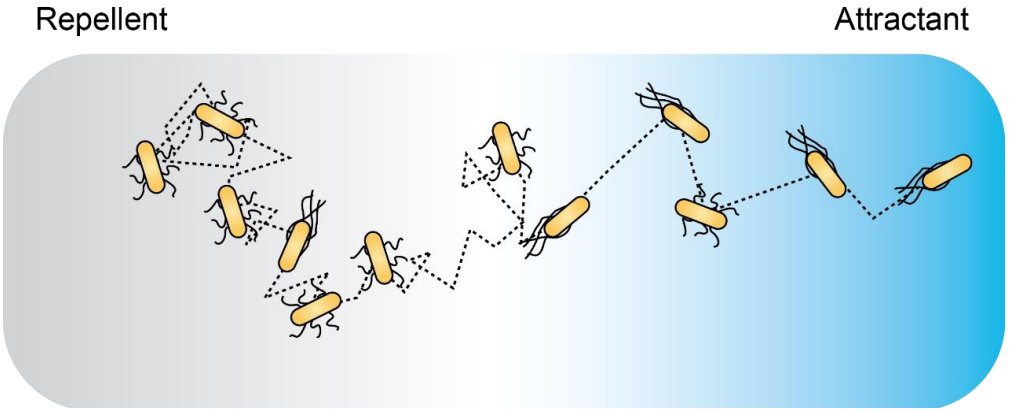

Figure 2-2. The bacterial chemotaxis pathway biases bacterial swimming toward attractants and away from repellents Attractant molecules induce a smooth swimming bacterial run. Repellent molecules cause bacteria to tumble and rapidly reorient in space.

182), though in other bacteria ligands have included energy sources and colonization factors (180). *E. coli* encode four transmembrane receptors (Tar, Tsr, Trg, and Tap) where attractants include sugars and amino acids and repellents are metals and hydrophobic amino acids. Chemoreceptors are elongated (~350 Å) stable homodimeric transmembrane four-helix bundles (183). Ligand binding to chemoreceptor extracytoplasmic domain dictates the signaling state of the distally associated kinase, CheA. CheA is a large, multi-domain dimer that associates with the cytoplasmic end of the transmembrane chemoreceptors through the adaptor protein CheW (184-188). CheA increases its autophosphorylation rate in response to repellent binding and inhibits phosphorylation when an attractant is bound. Activated CheA transfers its phosphorylation to the soluble receiver protein CheY which can interact with the flagellar motor complex (189, 190). In peritrichously flagellated bacteria, like *E. coli*, this pathway controls the rotational direction of the bacterial flagella resulting in runs and tumbles **(Figure 2-3**). This is a limited explanation of the chemotaxis system which also employs enzymes that are essential for the temporal control of chemotaxis signals including a phosphatase of phosphorylated CheY, CheZ and the receptor methylation and demethylation enzymes, CheR and CheB. These proteins along with those that comprise the flagella are beyond the scope of this work but have been expertly reviewed elsewhere (191, 192).

Traditional biochemical methods have been crucial to identify chemotaxis protein components, protein-protein interactions and to uncover the localization of chemotaxis proteins to the cellular poles. Advanced imaging techniques and protein crystallography have enhanced and refined our understanding of chemotaxis protein organization and the molecular basis for protein-protein interactions within the chemotaxis system. It has emerged

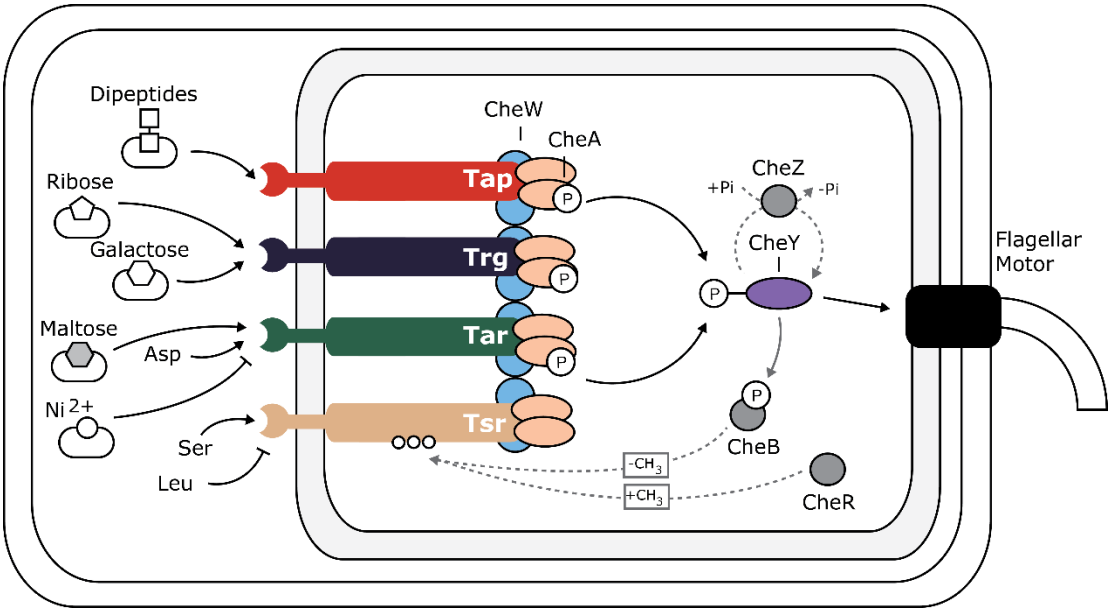

Figure 2-3. The *E. coli* chemotaxis machinery Repellents or attractants bind to polar arrays of transmembrane chemoreceptors in the periplasm. Ligand binding transduces a signal to the histidine kinase, CheA. CheA is localized at the cytoplasmic tip with the adaptor protein CheW. CheA controls the phosphorylation state of the receiver protein CheY and the demethylase, CheB. CheB removes CheR derived methylations on the chemoreceptors thereby facilitating adaptation. Phospho-CheY interacts with the flagellar motor to control its rotational direction and is modulated by its phosphatase, CheZ.

that the chemosensory complex of *E. coli* is composed of conserved higher-order assemblies. Transmembrane receptor homodimers are arranged as trimers-of-dimers (183) through interactions at their cytoplasmic tips and subsequently clustered in an extended polar localized array (**Figure 2-4A**) (175). Receptor trimers can contain mixtures of different ligand binding receptor types forming mixed signaling clusters (193). Moreover, the chemotaxis receptor polar arrays are arranged geometrically as a hexagonal lattice with 12 nm center to center spaced hexagonal units (**Figure 2-4B**) (194). This organization is conserved in bacteria and archaea that perform chemotaxis and express chemoreceptors (195). Despite decades of research and a wealth of biochemical, genetic and structural information about of virtually all of the major

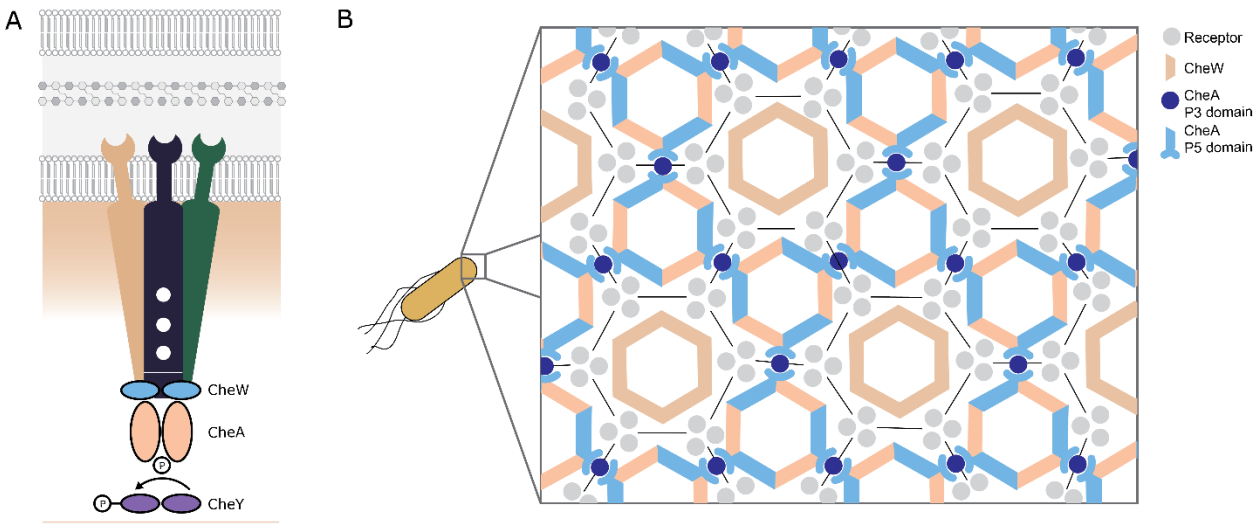

Figure 2-4. *E. coli* chemotaxis array (A) Basic architecture of chemotactic minimal unit, a trimer-of-dimers associated with a dimer of CheA and two CheW adapter proteins. (B) Expansion map of chemotaxis array protein connectivity interfaces.

component proteins, fundamental questions remain regarding the molecular mechanisms that underlie signal propagation and receptor array assembly.

A full understanding of how chemotaxis arrays function is important to understand how cells perceive and respond to their environments and has implications for human and plant health (182, 196). Bacterial chemotaxis is used by pathogenic or beneficial organisms to colonize animal and plant hosts. Chemotactic pathogens that affect animals notably include *Campylobacter* species, *E. coli, Salmonella, Helicobacter pylori, Borrelia burgdorferi, Vibrio cholerae and Pseudomonas aeruginosa.* Correct localization of chemotactic bacteria in specific host niches has proven vital to the effective establishment of infections (197, 198). Therefore, some platforms aim to develop therapeutics that interfere with fundamental processes like chemotaxis (199, 200). An antibacterial surface was developed that effectively lured

chemotactic bacteria using embedded chemoattractants and successfully functioned as a contact-killing surface (201).

Remarkable in these examples is the ability of these chemotactic bacteria to sensitively and selectively monitor unique chemicals in a complex chemical environment and to reconcile contradictory stimuli to perform productive colonization events. Indeed, a cell undergoing chemotaxis is highly sensitive to chemical changes in its environment. Chemotactic cells can respond to a gradient change equivalent to a difference of fewer than 10 molecules (202, 203). It has been demonstrated that the system demonstrates a signal gain, ligand binding to a single receptor is amplified by the system (204). Moreover, the system displays robust adaptation (203, 205, 206) and can precisely reset kinase activity to baseline in response to ambient chemoeffector concentrations that span five orders of magnitude (207). The molecular mechanisms by which the chemotaxis array accomplishes such remarkable properties is not yet known though it is emerging that array signaling features involves interconnected array components (171, 208, 209). Therefore understanding how arrays are arranged and assemble is crucial to address this issue.

There are a myriad of technological tools available to study multiprotein complexes, ranging from traditional biochemistry to advanced instrumental techniques, such as NMR, X-ray crystallography, and electron microscopy (EM). Insights into chemotaxis arrays have been obtained through these techniques though full characterization of the array and its assembly dynamics presents challenges to structural characterization. Namely, the chemotaxis array is a large, complex, multi-protein assembly with precise higher-order organization scaffolded by transmembrane receptors. Nevertheless, important details have emerged from these efforts.

Fluorescence microscopy of fluorescently labeled proteins or using fluorescently labeled antibodies have established that chemotaxis receptors and soluble proteins are localized to subcellular clusters of thousands of receptor proteins. (210) Traditional electron microscopy has observed large (~250nm) crystalline patches from cells (211). Studies of protein structure and protein-protein interactions have been effective to determine local features of the arrays. Cysteine cross-linking studies established that receptor dimers were arranged as mixed trimers-of-dimers (193). Conformational suppression studies showed that amino acid changes at trimer contact regions introduced signaling defects (212). Using multi-dimensional NMR , solution structures of chemotaxis proteins CheW and CheY have been determined (213-216). X-ray crystallography has obtained structural information on the individual chemotaxis proteins, including chemotaxis modulatory proteins CheR, CheB, and CheZ (217-219), High-resolution structures of chemoreceptor fragments are available (183, 220) as well as individual domains of CheA (221-224). Details of protein-protein interactions of chemotaxis signaling components have been revealed from co-crystal structures of CheY and CheZ (219) as well as truncated domains of CheA with CheY and CheW (221, 223, 225). A structure was solved that contained a receptor from *Thermotoga maritima* in complex with CheA domains P4-P5 and CheW to define the P5-receptor interface (186).

Much of the available structural details regarding the array core complex was obtained from investigations of domain truncations. High-resolution techniques that can visualize native biological samples are ideal for the extended localized clusters of the chemotaxis receptors. ECT provides an opportunity to study the structure of biological complexes at molecular resolution (4-8 nm) in three dimensions. ECT can image native biological samples without the

rigid preparation that is necessary for traditional electron microscopy and crystallography. Living cells are quickly frozen so that all the proteins remain in the same places they were in the living state. An electron microscope then takes sets of two-dimensional projections at different angles. These images are later reconstructed into three-dimensions (226-229). Using this technique, chemotaxis arrays have been demonstrated to form localized extended hexagonal lattices interconnected at their cytoplasmic tips by a baseplate of CheA and CheW proteins (194). Moreover, ECT showed that the basic architecture of the lattice is universally conserved throughout chemotactic bacteria (230). This geometric arrangement was different than what had been previously described by X-ray crystallography alone (225, 231). Combinations of ECT and X-ray crystallography have provided the most advanced understanding of array structure (232). The resolution achievable by ECT depends upon sample diameter. Initial ECT results of chemotaxis arrays were aided by the small size of *Caulobacter crescentus* cells and later by chemical techniques developed to reduce the thickness of *E. coli* cells. To yield higher resolution images from thinner samples and to generate a system where chemotaxis components could be varied researchers are in need of functional assemblies reconstituted *in vitro*.

Reconstitution of chemotaxis signaling complexes *in vitro* and in native membranes have been demonstrated. Use of these preparations have focused on defining the stoichiometry of the chemotaxis signaling unit, protein-protein interactions, array stability and the nature of signal propagation through the protein components of the array (233-240). Methods to generate these experimental systems generally consist of overexpressing a receptor of interest in *E. coli*, lysis of the bacteria and isolation of plasma membrane vesicles (239, 241). To these

membrane preparations, purified soluble chemotaxis proteins are then added at a predetermined optimal ratio to regenerate connectivity. While systems of this type can incorporate proteins and signal, it has been unclear if any thus far are organized such that the known array structure is maintained. Recapitulation of the conserved hexagonal order is likely crucial to the full investigation of the emergent signaling and cooperation properties of the chemotaxis array.

Herein, we set out to characterize the structures of existing preparations and to develop new methods to investigate the structural organization and assembly process of the chemotaxis system. Using molecular biology, protein biochemistry and electron cryotomography (ECT), we present details of assembly intermediates and the assembly mechanism of this macromolecular complex. The results of this work will aid our understanding of bacterial motility and organized transmembrane signaling. Discerning the dynamics of the chemotaxis array will impact our understanding of the role that higher order organization can play in signal regulation and the processes by which some macromolecular systems assemble.

2.3 Results

2.3.1 WT *E. coli* Chemoreceptor Arrays are Super-Lattices of Alternating CheA-filled and CheA-less Rings

In *E. coli* polar chemoreceptor arrays, dimers of CheA link adjacent trimers of MCP dimers. Based on the crystal structures of these components and their complexes, it is apparent that in the extended hexagonal lattice, not all hexagons can be occupied by three CheA dimers. Rather, a regular pattern was predicted in which CheA-filled hexagons alternate with CheA-empty hexagons (232). While this hypothesis was strongly supported by the demonstration that there

are two different kinds of array hexagons in a tomogram (“filled” and “empty”), the arrangement of these units was not reported (242).

Thanks to further advances in sample preparation (receptors locked in a single-state), data collection (thinner sample, direct detector), and processing (contrast transfer function correction), we are now often able to visualize CheA dimers individually in tomograms within intact arrays. This allowed us to confirm the order of the "super-lattice" of CheA-filled and CheA-empty hexagons directly. To do this, we analyzed tomograms of wild-type (WT) cells expressing serine-sensing receptors in the demethylated state (Tsr-EEEE). This modification state of the receptors promotes stable packing of the P1 and P2 domains of CheA (243), leading to a strong keel-like density that facilitates identification of CheA dimers in tomograms. We observed a layer of CheA below the MCP hexagons in tomograms, which appeared highly ordered, as confirmed by Fourier transform (**Figure 2-5**). Individual CheW molecules were not identifiable, likely due to their smaller size. We then used principal component analysis (PCA) to identify classes of hexagons in a tomographic slice on the basis of CheA occupancy. Only two classes of receptor hexagons were observed: one in which each pair of Tsr trimers is linked by a CheA dimer, and one in which none of them are (**Figure 2-5G**&**H**). When we forced more classes, only additional filled and empty classes resulted, confirming that there are very few if any partially-filled hexagons. These two classes were present in a roughly 2:1 ratio (117 filled rings; 64 empty rings). By mapping the classes back onto the tomographic slice, we found a strictly alternating pattern (**Figure 2-5I**), confirming that native arrays are a super-lattice: The trimers-of-receptor-dimers lie at the vertices of a hexagonal lattice with 12 nm spacing. Connected to the cytoplasmic tips of the receptors, the associated CheA (together with CheW)

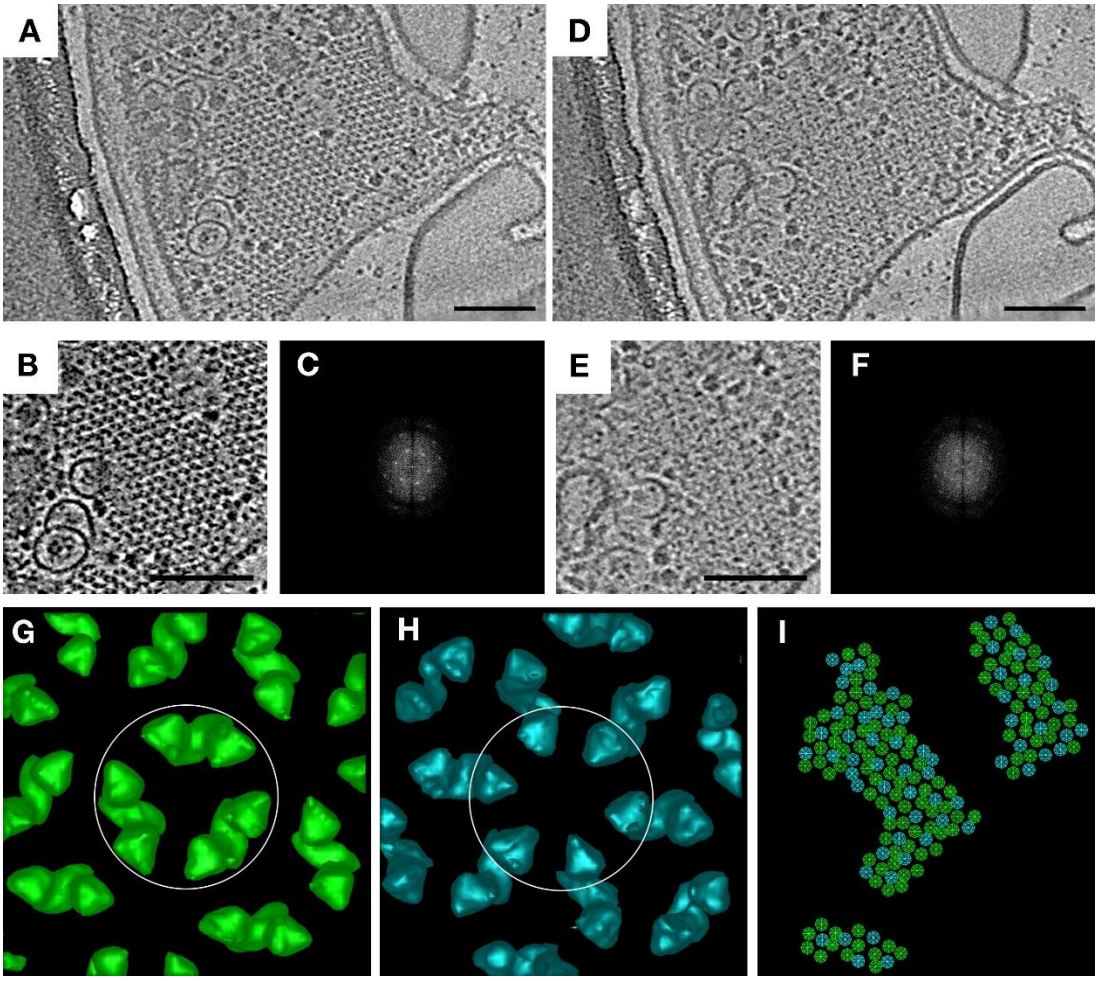

Figure 2-5. Classification of *E. coli* chemoreceptor array hexagons reveals ordered CheA occupancy (A) Tomographic slice through an array patch at the level of the chemoreceptors. (B) A cutout of the patch, and corresponding power spectrum (C), revealing hexagonal lattice. (D) Tomographic slice of the same array patch below the level of the chemoreceptors, showing CheA. (E) A cutout of the patch, and corresponding power spectrum (F), revealing ordered occupancy by CheA. (G-I) Classification by principal components analysis and k-means clustering of hexagons in the same array patch results in two distinct classes: hexagons linked by three CheA dimers (green symbols, subvolume average shown circled in G) and hexagons lacking CheA dimers (turquoise symbols, subvolume average shown circled in H). Organization of class averages is shown in (I). Scale bars 100 nm, power spectra not to scale.

forms another lattice. Here, the three CheA dimers linking one receptor hexagon lie at the vertices of a larger hexagonal lattice with a spacing of 12 nm. This results in a hexagonal array of receptors linked to a lattice of alternating CheA-filled and CheA-empty hexagon

2.3.2 Preparation of Native Membrane Vesicles

Various investigators have explored different protocols to characterize array structure and function, one of the earliest strategies was to simply overexpress receptors, often in the absence of CheA and CheW (244). Another strategy that has been used to reconstitute chemoreceptor systems *in vitro* is to add excess purified CheA and CheW to overexpressed receptors purified within their native *E. coli* membranes (236, 245). Guided by precedence for *in vitro* reassembly of chemotaxis signaling complexes and prior work in the Kiessling research group examining protein-protein interactions using native membranes (246) compelled us to employ these materials and preparations to examine their receptor lattice architecture. To generate a defined chemoreceptor array, we prepared native membranes containing a single chemoreceptor, Tsr. We chose the serine receptor Tsr as a model chemoreceptor because it exhibits highly cooperative signaling in reconstituted *in vitro* systems (236, 247). We overexpressed Tsr in an *E. coli* strain (HCB326) lacking all genes encoding chemotaxis signaling proteins (248). The isolated native membranes (249, 250) formed non-uniform sheets and vesicles, averaging ~100–400 nm in diameter (237 $\pm$ 62 nm average, n = 200) (**Figure 2-6A**). We measured the incorporation of CheA into signaling complexes with our native membranes using a membrane pull-down binding assay. CheA was found in the membrane preparations and enhanced when CheW was present. The addition of excess CheW effectively blocked CheA incorporation by occupying additional binding sites on the receptor and occluding

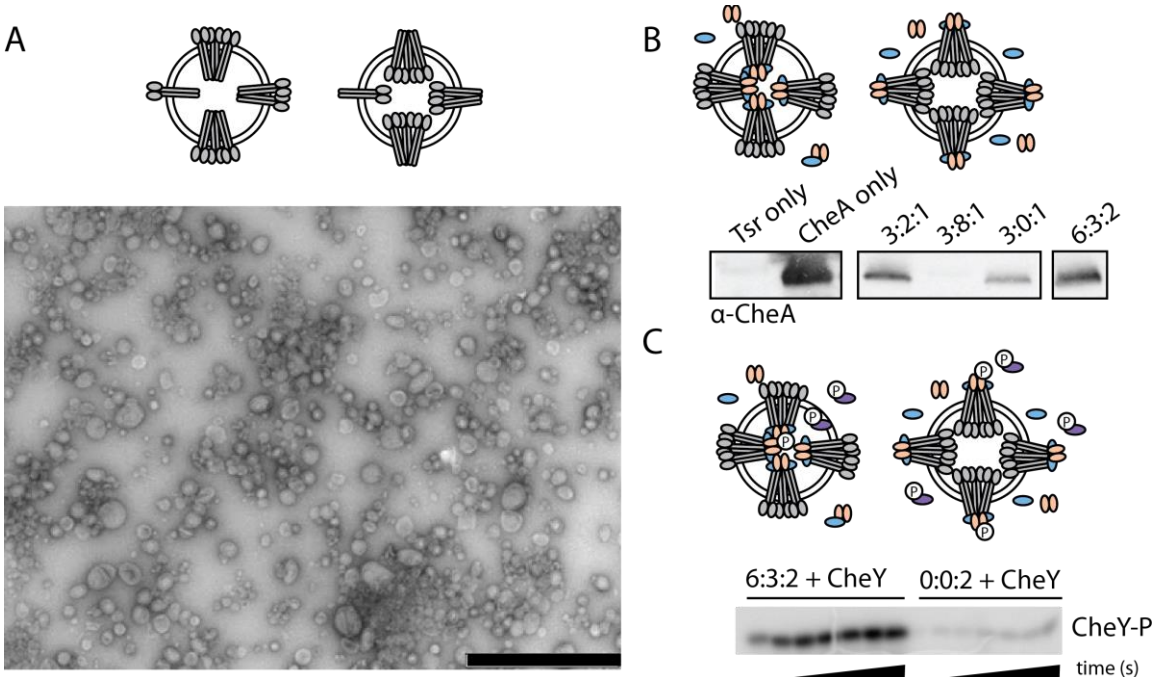

Figure 2-6. Characterization of native membrane preparations (A) TEM image of vesicles isolated from *E. coli* where Tsr has been overexpressed, average size: 100-400 nm . Scale bar is 2 μM. (B) Membrane pull-down assay to assess incorporation of soluble CheA and CheW into isolated membrane vesicles containing Tsr. Ratio is Tsr:CheW:CheA where 1 unit corresponds to 2 μM. Segmented images are lane selections for a contiguous western blot that was cropped for clarity. (C) Autoradiograph of phospho-CheY formation from soluble CheY and γ-^{32}P-ATP incubation with reconstituted signaling complexes (left) or soluble CheA (right). Timecourse: 4-98 s reactions.

incorporation of CheA (**Figure 2-6B**) (251, 252). These data indicate that formation of the full signaling complex requires all components in a physiologically relevant ratio (234). To demonstrate signaling complex function, we measured CheA autophosphorylation when incubated with CheY and γ-^{32}ATP as a soluble protein and when present in native membranes reconstituted with our predetermined ratio of CheA and CheW (Tsr:CheW:CheA, 6:3:2) (246). We observed a time-dependent increase in phospho-CheY production that was enhanced when incorporated into signaling complexes (**Figure 2-6C**). This is in agreement with previous reports increase CheA autophosphorylation rates when incorporated into signaling complexes (245). These results support that soluble signaling factors have access to the chemoreceptor

domains for ternary complex formation and CheY activation. With the biological-features of our reconstituted chemotactic complexes validated, we next utilized ECT to characterize the structural features of these chemotactic assemblies.

2.3.3 Overexpressed Chemoreceptors, in the Absence of CheA and CheW Form Zippers

We first analyzed membranes containing Tsr in the absence of CheA and CheW. It was unclear if the receptors were ill-defined aggregates or adopted any particular organization in the absence of the other signaling proteins. Highly overexpressed Tsr chemoreceptors are known to form non-native ordered arrays termed "zippers" in which two receptor layers interact with one another at their cytoplasmic tips which are normally occupied by the signaling proteins CheA and CheW. Zippers manifest as observable membrane invaginations in electron microscopy (211, 253-255). We investigated the structure of these zippers at higher resolution using a preparation of *E. coli* Tsr in purified inner membranes. Interestingly, we found that zippers survived cell lysis and membrane purification, indicating that the interactions between the kinase-binding domains of the MCPs at their membrane-distal tips are highly stable. Importantly, the fundamental building block in zippers was seen to be trimers-of-dimers, just as in native arrays, but when viewed from the top, zippers exhibited tighter packing, with triangular lattices at the top and bottom and a hexagonal pattern at midsection (**Figure 2-7**). This complicated pattern was the result of two layers of receptors linked in a hexagonal lattice with a center-to-center spacing of 9 nm at the midsection, with alternating trimers facing opposite directions (**Figure 2-7**). Chemoreceptors in the absence of their signaling proteins do not unfold and aggregate but rather form ordered macromolecular complexes that are not native yet highly stable.

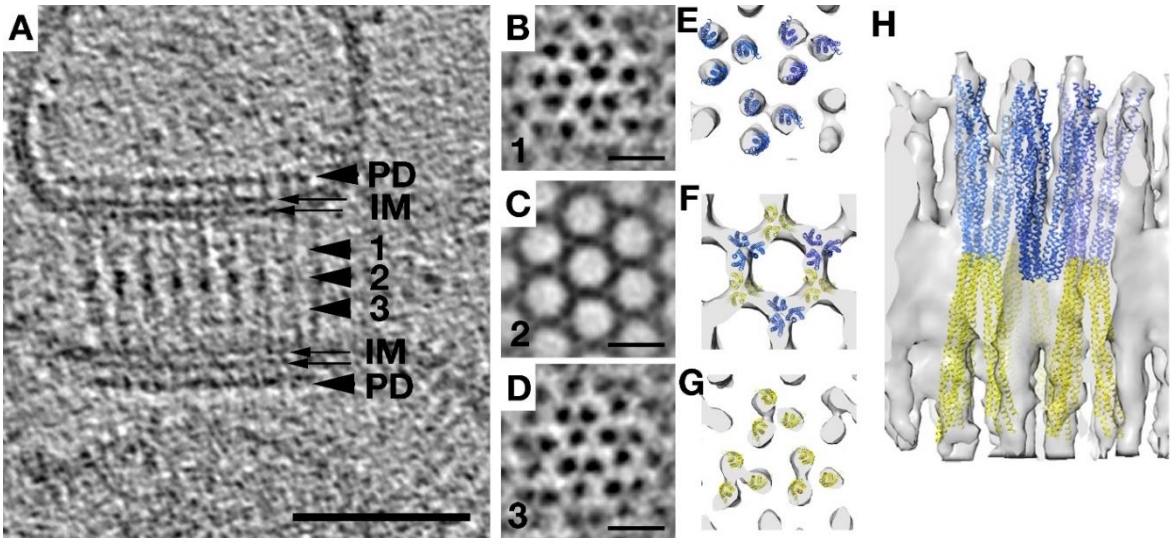

Figure 2-7. Overexpression of Tsr without sufficient CheA and CheW results in zippers (A) Side view of a receptor zipper reveals two layers of membrane-bound receptors interacting at their membrane-distal tips. PD: Periplasmic domains; IM: Inner membrane leaflets. Scale bar 50 nm. Arrows indicate relative positions of subvolume averages shown at right in (B-D). Scale bars 10 nm. (E-H) Model of receptor density from the subvolume average and manually fitted Tsr crystal structure from (183), in top view (E-G, levels roughly corresponding to B-D) and side view (H), showing arrangement of receptors. Blue and yellow colors indicate receptors of opposing orientation.

2.3.4 Chemoreceptor Structure in the Presence of CheA and CheW

Next, we examined reconstitution preparations (**Figure 2-6B-D**). This type of preparation is known to generate functional receptor-CheA-CheW units in which receptors bind attractant serine and regulate CheA kinase activity similar to *in vivo* bacterial chemotaxis systems (239, 256). ECT revealed Tsr zippers similar to those observed in Tsr inner membranes prior to addition of CheA and CheW, as well as large, loosely associated aggregates (**Figure 2-8**). The zippers likely formed within the cell and remained associated throughout lysis and addition of CheA and CheW. Inner membrane preps are known to yield an ~80:20 molar ratio of inside-out to right-side-out receptors (241). Both receptor orientations are observed in the images, and

the outward-pointing cytoplasmic tips dominate as expected (**Figure 2-8**) Besides the expected zippers, a range of assembly intermediates was observed, providing insight into the mechanism of array assembly. We also found partial or full Tsr hexagons, double hexagons, and small arrays formed from multiple hexagons. Individual receptor hexagons were fully occupied by three CheA dimers (**Figure 2-9**). No large, native-like arrays were detected, however, consistent with the low Hill coefficient, a measure of receptor cooperativity, observed for this type of prep (239).

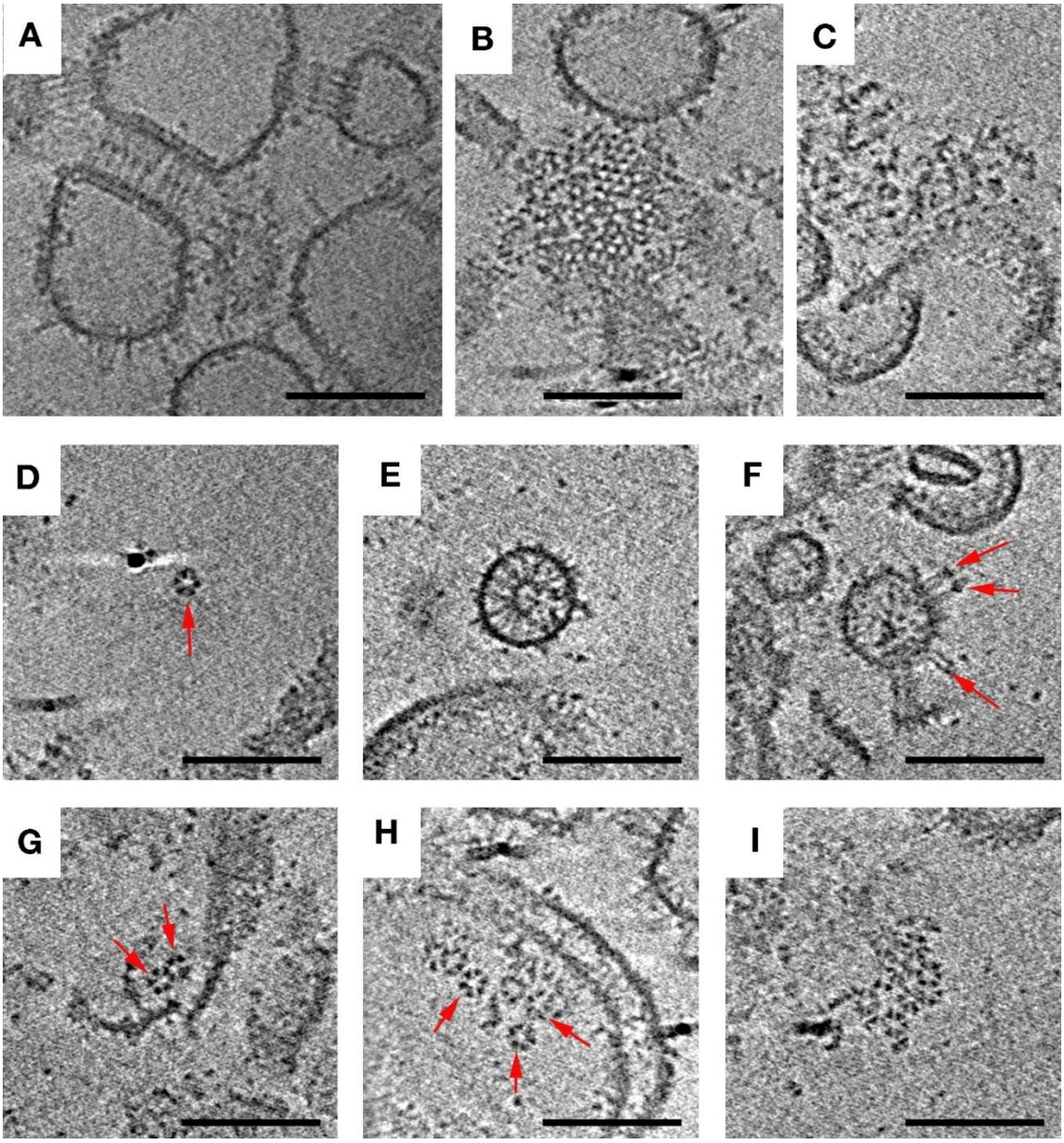

Figure 2-8. *In vitro* reconstitution of signaling complexes produces a variety of structures
Arrangements observed included receptor zippers with 9 nm center-to-center hexagonal spacing (side view, A; top view, B), loosely ordered aggregates (C), individual hexagons of six trimers-of-dimers (D), receptors oriented inwards (E) and outwards (F) from vesicles, linked hexagons (G), multiple unlinked hexagons (H), and the largest 12 nm hexagonal array patch observed (I). Arrows indicate structures of interest. Scale bars 100 nm.

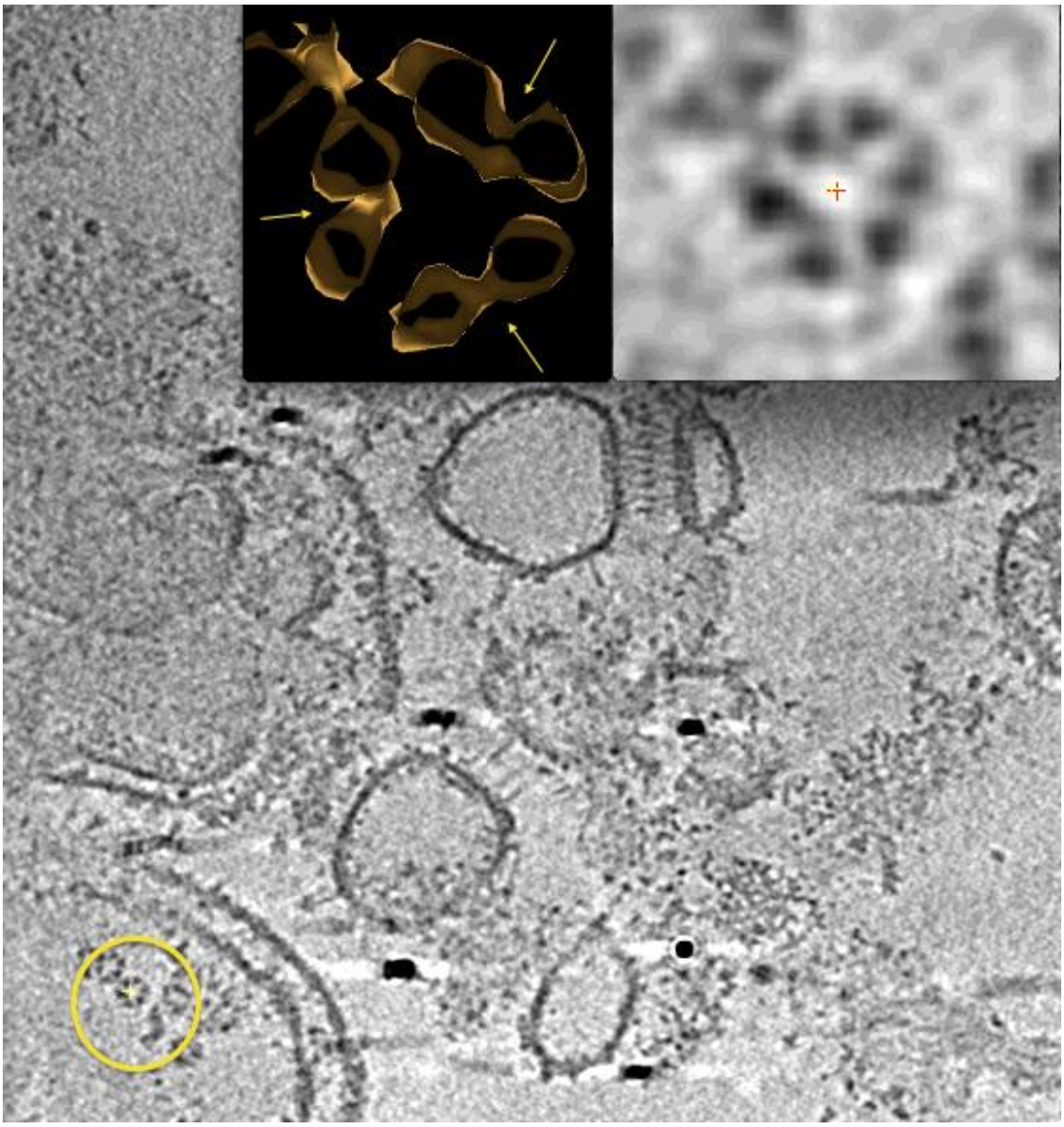

Figure 2-9. *In vitro* receptor hexagons are associated with three CheA dimers Tomographic slice of an *in vitro* preparation of Tsr in inner membrane vesicles following the addition of CheA and CheW. Isosurface representation (left inset) of a cut-out section at the level of the CheA/W ring from the receptor hexagon (right inset) highlighted by the yellow circle. Yellow arrows indicate densities corresponding to CheA dimers.

2.3.5 Characterization and Preparation of Tsr, CheA, and CheW Co-overexpression Cellular Arrays

Suspecting that optimal array formation may require the simultaneous production of receptors and CheA/W, some investigators have tried co-overexpression. Concomitant overexpression of CheA and CheW has been shown to produce large arrays without membrane invaginations (257). To establish the necessary experimental conditions to generate large arrays of concomitantly overexpressed CheA, CheW, and Tsr from separate plasmids we made use of the visual readout of swimming ability afforded by chemotactic cells in soft agar plates. Motile bacterial cells inoculated onto soft agar (~0.2-0.3% agar) prepared in bacterial growth media support the outward migration of cells as they swim up attractant gradients in the plate and consume the nutrients contained in the growth media. Non-concentric rings of migration from and are associated with ordered depletion of nutrients (258, 259). We examined swimming of a strain of *E. coli* expressing all chemotactic proteins except CheA and CheW (UU1607), and no spreading was observed. We also examined the swimming phenotypes of a strain lacking all chemoreceptors (RP8611) but containing a plasmid that can express the chemoreceptor Tsr from an inducible promoter (pJC3). High levels of Tsr expression inhibit bacterial swimming (>250 μM IPTG) (**Figure 2-10A)**. UU1607 with pJC3 and a plasmid with inducible expression of CheA and CheW (pPM25) was examined for the concentration of inducer needed to express CheA and CheW to rescue swimming inhibition as a result of Tsr overexpression. We observed a range of concentrations (1-10 μM sodium salicylate) that was able to restore bacterial spreading to the *E. coli* strain overexpressing Tsr (**Figure 2-10B)**. We used electron microscopy to visualize membrane morphology in these strains at our determined induction conditions. Receptor overexpression lead to significant membrane ruffling as was observed in the strain

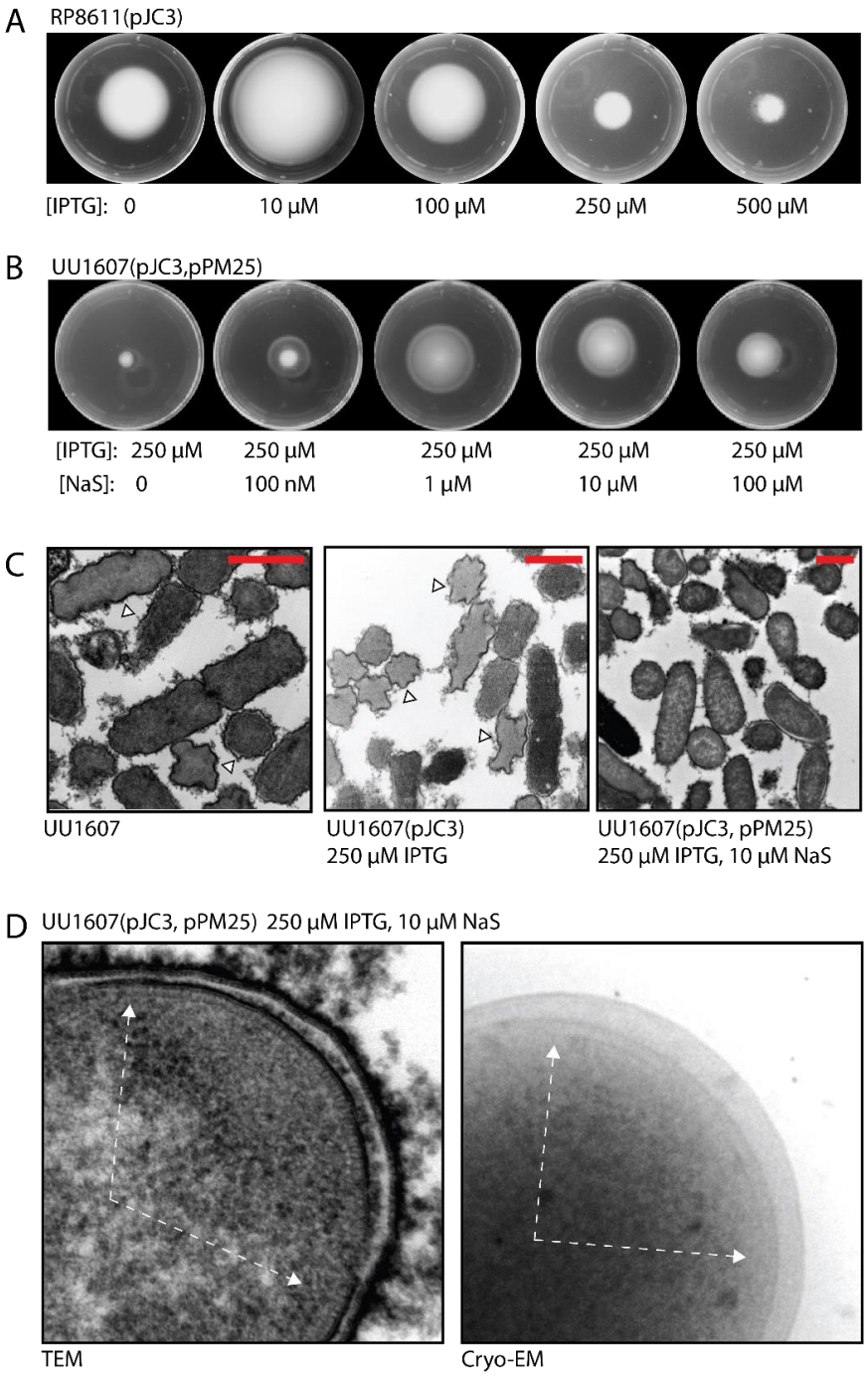

Figure 2-10. Characterization and preparation of Tsr, CheA and CheW co-overexpression cellular arrays (A) Swim plate phenotypes of an *E. coli* strain devoid of all transmembrane chemoreceptors differentially induced to express Tsr. (B) Swim plate phenotypes of an *E. coli* strain lacking CheA and CheW differentially induced to express CheA and CheW when Tsr is concomitantly being overexpressed. (C) TEM images of strain lacking CheW and CheA (UU1607), UU1607 overexpressing Tsr and UU1607 concomitantly expressing Tsr, CheA, and CheW. White arrows indicate regions of membrane ruffling caused

by Tsr overexpression. Scale bar is 1 μm. (D) TEM and ECT insets of enlarged arrays spanning the bacterial pole.

lacking CheA and CheW (Figure 2-10C). Simultaneous expression of CheA and CheW in a strain overexpressing the receptor Tsr corrects the membrane ruffling phenotype and generates large polar arrays (**Figure 2-10D)**.

2.3.6 Chemoreceptor Structure with Concomitant Expression of CheA and CheW

In cells overexpressing Tsr from one plasmid and CheA and CheW from another, we observed arrays with the native 12 nm hexagonal spacing (**Figure 2-11**). We used a Tsr variant (Tsr-A413T) that locks the P1 and P2 domains of CheA into an identifiable "keel" to investigate CheA occupancy (243). By immunoblotting, we determined that Tsr and CheA had been overexpressed to similar extents (25.5 and 26 times their WT levels, respectively; **Figure 2-12**), but classification of hexagons in tomograms revealed significantly lower, and less-ordered occupancy of CheA than in native arrays (**Figure 2-13**). Two major classes were observed with zero or two CheA dimers per ring. Direct observation of CheA dimers in the tomograms confirmed the lack of any super-lattice order of CheA-filled or CheA-empty rings.

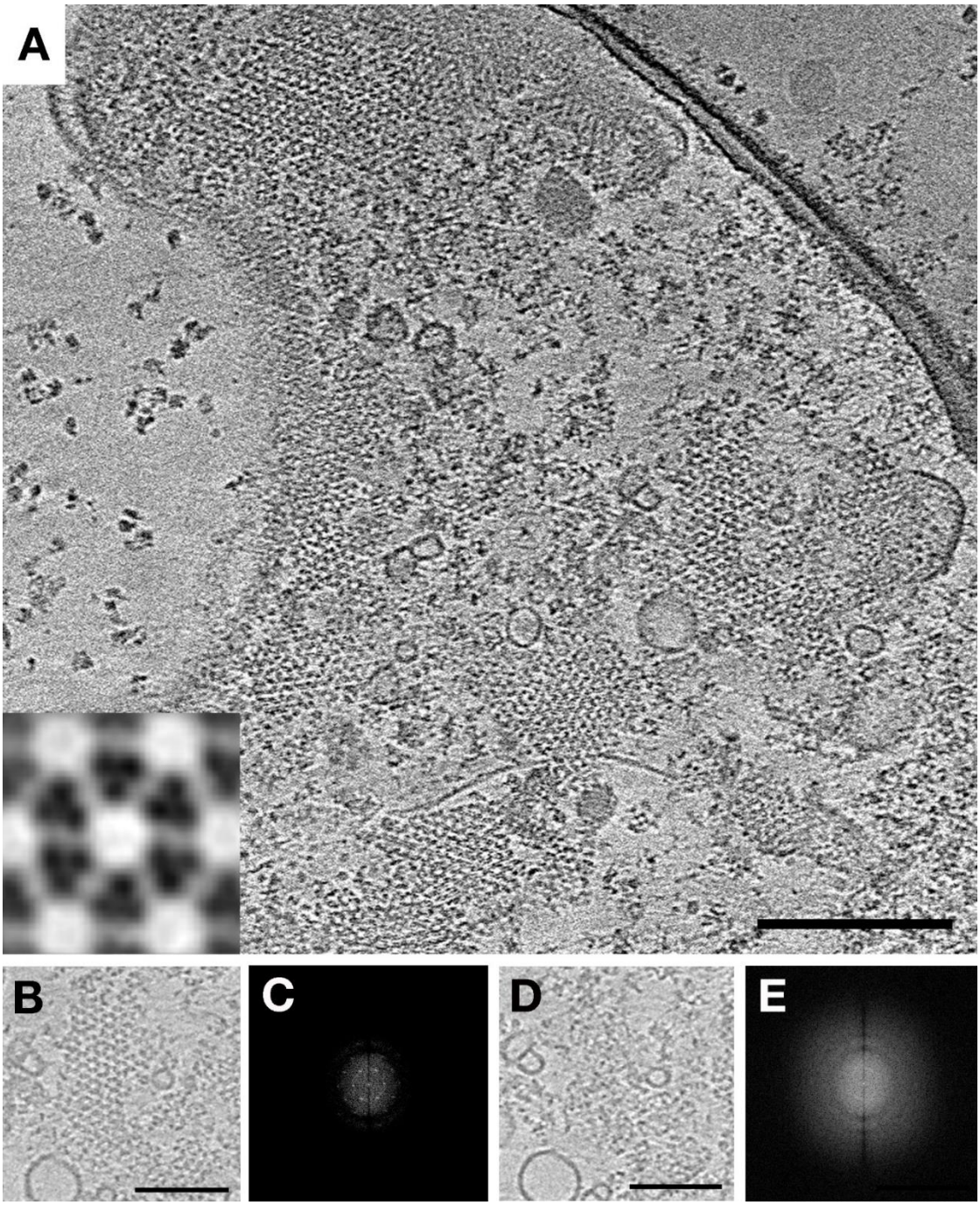

Figure 2-11. Co-overexpression of Tsr, CheA, and CheW restores WT array structure (A) Tomographic slice of a lysed *E. coli* cell overexpressing the chemotaxis proteins Tsr-A413T, CheA, and CheW reveals extended well-ordered hexagonal arrays with 12 nm center-to-center spacing. Inset: higher-magnification subvolume average is showing the top-view of a single hexagon. (B) Array patch at the level of the receptors, and corresponding power spectrum (C). (D) Same array patch at the level of CheA, and corresponding power spectrum (E) shows lack of order in CheA arrangement. Scale bars 100 nm, power spectra not to scale.

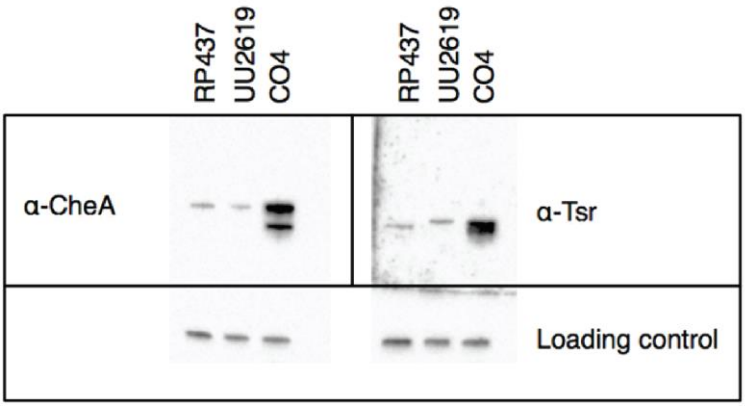

Figure 2-12. Relative protein levels of CheA and Tsr overexpression Western blot showing levels of CheA (top left), Tsr (top right), and a loading control (bottom; unknown protein detected by α-β-lactamase) in RP437, UU2619, and CO4. Quantification by densitometry gives the following overexpression levels: CO4/RP437 CheA 25.5, Tsr 26, CO4/UU2619 CheA 33.7, Tsr 15.5.

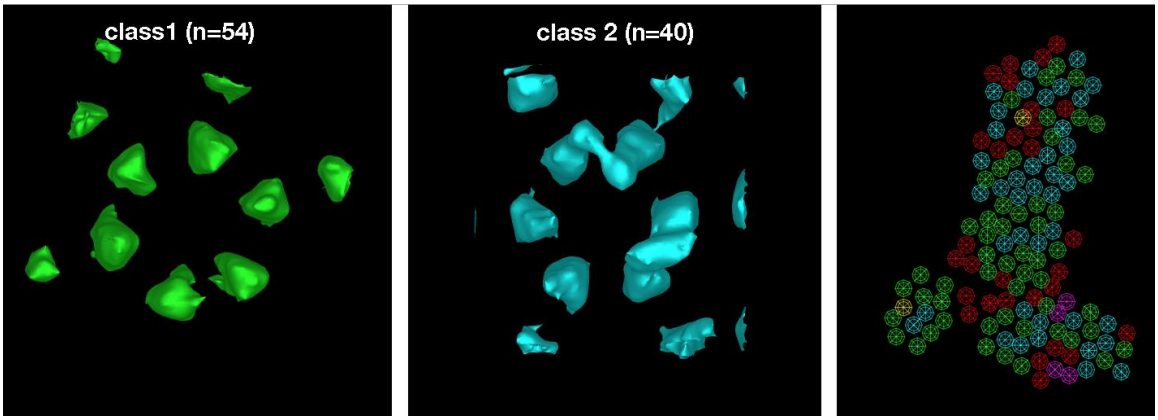

Figure 2-13. Classification of array hexagons formed by co-overexpression of Tsr, CheA, and CheW Classification by principal components analysis and k-means clustering of hexagons in the array patch shown in Figure 3 results in 4 classes. Average of class 1 (n=54) is shown in green at left, class 2 (n=40) in turquoise in the middle. Class 3 (purple, n=4) and Class 4 (yellow, n=2) represented bad particles. Organization of classes in the array patch is shown at right, with red representing particles not included in the clustering.

2.4 Discussion

Here we explored the structure and assembly of chemoreceptor arrays by imaging both native arrays and selected *in vitro* preparations that yield functional receptor-CheA-CheW complexes. We found that native arrays are not only hexagonally ordered, but a super-lattice exists of alternating CheA-filled and CheA-empty rings. When Tsr receptors are overexpressed in the absence of CheA and CheW, stable double-layered zippers form as previously observed, and the present study reveals that the receptors are still arranged as trimers-of-receptor-dimers, though packed in a non-native lattice. When receptor-containing membranes are incubated with purified CheA and CheW, isolated "functional units" (pairs of trimers-of-receptor-dimers linked by CheA dimers) and "rings" (six trimers-of-receptor-dimers linked by three CheA dimers) were found, as were clusters of rings forming small arrays, but no large, native-like arrays were observed (as expected given the low Hill coefficient reported for this type of preparation (239)). Instead, the observed small complexes and arrays are proposed to be early intermediates in the assembly of native arrays. Larger, more extended 12 nm hexagonal arrays are produced by co-overexpression of receptor, CheA, and CheW.

One of the principles that emerges from these observations and others already in the literature is that with the exception of one crystal structure of *Thermatoga* receptors, where the receptors were arranged in "hedgerows" of dimers (225), receptors always form trimers-of-dimers linked together tightly at their kinase-binding tips but splaying outwards towards their ligand-binding tips. However, the degree of splaying observed by ECT is less than that seen in the crystal structure (183, 232, 243). This same building block is seen in native arrays, zippers, reconstituted mixtures, and in cytoplasmic arrays. This structure probably forms rapidly within

cells and is highly stable, remaining intact through cell lysis and/or diverse purification/reconstitution procedures.

The second principle that emerges is that the trimers-of-receptor-dimers unit exhibits striking versatility in the kinds of contacts it can form with other trimers-of-receptor-dimers and other components of the signaling pathway. In native arrays, trimers of receptor dimers form extended hexagonal arrays anchored in the membrane at their ligand-binding tips and associating laterally through networked CheA and CheW. In the absence of CheA and CheW, trimers bind each other at their kinase-binding tips in an anti-parallel fashion to form super-stable zippers. A more recent crystal structure reveals two potential CheA and CheW binding sites along each dimer (Li *et al.*, 2013). Because there are so many possible structures that can form, while the architecture seen in cells is universally conserved (230), the assembly process within a cell must be tightly regulated.

As a final assembly principle, the effective determinant of array structure seems to be CheA and CheW. In native arrays, we find nearly complete, and highly ordered CheA occupancy. Filled hexagons containing 3 CheA dimers surround an empty hexagon containing none. This leads to a slightly higher receptor to CheA ratio in arrays (6:1) compared to the total concentration ratio in cells (3.4:1) (260). It may be that cells contain excess CheA and CheW in order to promote correct assembly. When Tsr, CheA, and CheW are decoupled from the same operon and overexpressed, the resulting arrays exhibit the same 12 nm hexagonal packing as native arrays, but we observe less-than-native CheA incorporation, suggesting that the assembly process may become defective when the precise stoichiometry and temporal control provided by the operon is disrupted. Alternatively, overexpression could activate a putative

disassembly mechanism responsible for removing CheA and destabilizing the array, thereby preventing excess array growth, as previously speculated (241). Intriguingly, *Bacillus subtilis* has been reported to have a much higher ratio of MCP to CheA than *E. coli*: approximately 23 receptor dimers to one CheA dimer (261), versus 3.4:1 for *E. coli* (260). Thus, at least in *B. subtilis,* it appears that relatively little CheA is required to nucleate a morphologically correct array with respect to receptor packing.

We imagine then that in cells, receptors are inserted into/across the membrane as they are produced and quickly dimerize. Next, receptor dimers trimerize, and then CheA dimers capture trimers-of-receptor-dimers into 6-receptor "functional units" before any off-pathway complexes form. These functional units either unite through CheW with existing arrays or link together to form CheA-filled rings, which then unite to existing arrays. Given the known interactions of CheA and CheW, both processes lead directly to the highly cooperative super-lattice of alternating CheA-filled and CheA-empty rings (Fig. 7 and supplementary movie).

The special conditions that exist within cells that enable and guide this assembly process may, however, be challenging to mimic *in vitro*. That being said, the smallest "functional unit" that displays full regulation of kinase activity is the six-receptor-dimer, one-CheA-dimer unit that also seems to be the basic building block of array assembly, and all the reconstitution protocols explored here produce such functional units. Their biochemical and biophysical properties can, therefore, be studied effectively as long as care is taken not to include a signal from non-native structures that may also be present. This can be done through CheA- or CheW-readout methods (rather than simply monitoring receptors); for instance, monitoring the effects of mutagenesis, crosslinking, or protein modification on kinase activity measures only

the effects within functional complexes (184, 246, 262, 263). Notably, certain reconstitutions have also already exhibited Hill coefficients close to those observed for cellular arrays (236), suggesting that native-like higher-order structures must be present. We hope the interplay between EM and *in vitro* reconstitution methods, together with the application of the new assembly principles revealed here, will eventually enable the production of even larger-than-cellular arrays with fully native structure for enhanced structural, biophysical, and biochemical characterization of array properties.

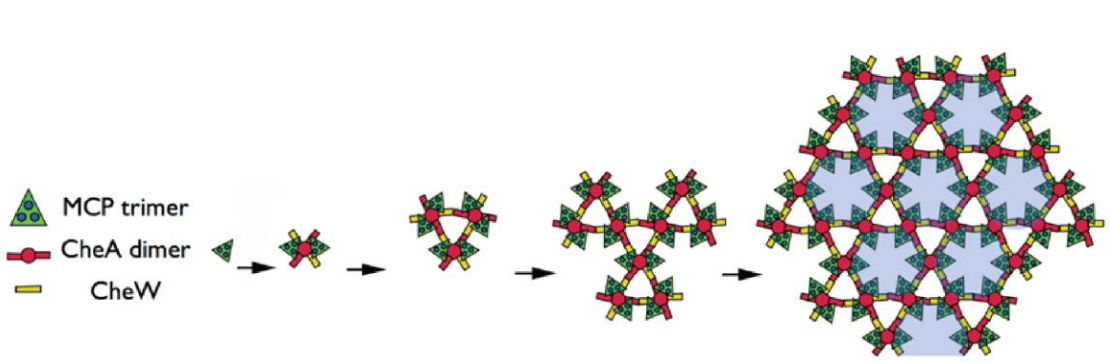

Figure 2-14. Model of array assembly Schematic showing the sequential assembly of core functional unit (two trimers-of-receptor-dimers, one CheA dimer, and two CheW monomers) forming from individual trimers-of-receptor-dimers, and subsequently coalescing into individual hexagons, which in turn assemble into the extended super-lattice. Empty hexagons without associated CheA are highlighted in blue.

2.5 Experimental

2.5.1 Bacterial Strains and Plasmids

Bacterial strains and plasmids used in this study are listed in **Table 2-1**. pCO3 was derived from pJC3 by PCR-based site-directed mutagenesis to generate tsrA413T. Strains were grown to mid-exponential phase in Tryptone Broth (TB) at 30 °C, with appropriate antibiotics. Expression of Tsr from pCO3 was induced with 250 µM IPTG. Expression of CheA and CheW was induced from pPM25 with 10 µM sodium salicylate. Strain UU2619 was lysed by incubation with 300 ng/ml penicillin for 1 h at 30 °C. Strain CO4 was lysed by treatment with 2 mg/ml lysozyme for 45 minutes at 37 °C, followed by treatment with 1 mg/ml DNase for 30 minutes at 37 °C. Samples were kept on ice until freezing for ECT.

Table 2-1. Strains used in this study

Strain	Genotype	Source
RP437	WT for chemotaxis	(264)
UU1607	(cheAW)Δ2167	(265)
UU2619	tsr-Q297E/Q311E (EEEE) Δ(tar-cheB)4346	(266)
RP8611	Rp437 derivative lacking all transmembrane chemoreceptors	(267)
HCB326	Δtsr trg::TnO ΔcheA-cheZ	(248)
CO4	(cheAW)Δ2167 pPM25(CheA CheW) pCO3(tsr-A413T)	this study

Plasmid	Relevant Features	Source
pPM25	Derivatives of pACYC184; CheA+ CheW+	(265)
pJC3	*tsr* expressed from a tac promoter	(268)
pCO3	derived from pJC3 by PCR-based site-directed mutagenesis to generate tsrA413T	this study

2.5.2 Purification of Signaling Components and Assembly *in vitro*

Tsr-containing inner membranes were prepared essentially as described (246, 269), with some modifications. Tsr expression was induced from plasmid pJC3 (268) during the mid-logarithmic phase of growth with 1 mM IPTG for 4 hours at 30 °C in HCB326; an *E. coli* strain lacking native chemotaxis proteins. Cells were collected by centrifugation (4,000 x g, 15 min), resuspended in lysis buffer (50 mM KH_2PO_4 pH 7.5, 5 mM DTT, 10 mM EDTA, 1 mM 1,10-phenanthroline, 10% glycerol, 1 mM PMSF; 25 mL per 2L), and lysed with a Constant Cell Disruption System (Constant Systems, Kennesaw, GA). Cell debris was removed by centrifugation (12,000 x g, 25 min). The collected supernatants were equilibrated with 10 mM aqueous iodoacetamide. Membranes were pelleted by ultracentrifugation (40,000 rpm, 120 min) and resuspended in a high salt buffer (~ 6mL; 50 mM KH_2HPO_4 pH 7.5, 2 M KCl, 10 mM EDTA, 1 mM 1,10-phenanthroline, 1 mM PMSF, 5 mM iodoacetamide, 10% glycerol) using a Dounce homogenizer. Membranes were isolated by ultracentrifugation (50,000 rpm, 60 min) and resuspended in 50 mM Tris pH 7.5, 5 mM EDTA, 1 mM iodoacetamide and 10% glycerol (6 mL). The suspended membranes (3 mL) were layered on top of a 70% - 30% sucrose gradient. The gradients were prepared by layering 6 mL of 70%, 60%, 50%, 40% and 30% sucrose solutions in 10 mM Tris pH 7.5 and 5 mM EDTA.

The membranes were separated by ultracentrifugation (26,000 rpm, 12 h with acceleration and deceleration profiles of 170 rpm over 4 min). Tsr containing bands were eluted from the gradient and diluted four-fold (~45 mL) with Tsr reaction buffer (50 mM HEPES pH 7.5, 50 mM KCl, 5 mM $MgCl_2$) with 1 mM PMSF. Membrane suspensions were stored at -80 °C until use. Membrane protein content was determined by a modified BCA assay (Pierce Biotechnology, Rockford, IL). Membranes typically contained 20% Tsr, determined by densitometry of Coomassie-stained SDS-PAGE gels.

To reconstitute signaling complexes, native membranes containing Tsr were combined with purified His_6-CheW and His_6-CheA (prepared as described in (246, 269)). Ternary complex components were combined as follows: 12 µM Tsr, 6 µM His_6-CheW, 2 µM His_6-CheA in Tsr reaction buffer. Samples were incubated at room temperature for 15 min then extruded through a 27-gauge needle and incubated again for 30 min at room temperature before washing. Complexes were pelleted by centrifugation (180,000 x g, 20 min) and washed with Tsr-reaction buffer (2 x 200 µL) and resuspended in Tsr reaction buffer at their original volume. Preparations were snap-frozen and stored at -80 °C

2.5.3 Transmission Electron Microscopy

Samples for electron microscopy were prepared by negative stain preparation using a two-step procedure. 2 µl of suspended sample was adsorbed on a pioloform coated 300 mesh Ni grid for 30 seconds with the excess wicked away with filter paper. A 2 µl drop of Nano-W (Nanoprobes Inc.) was placed on the sample with the excess wicked away with filter paper and allowed to dry. The negatively stained samples were viewed on a Philips CM120 at 80kV and documented with an Olympus SIS MegaView III digital camera (**Figure 2-6A**)

E. coli strains under described conditions were fixed with 2.5% glutaraldehyde and 0.05 M lysine in 0.1 M cacodylate buffer (pH 7.4) for 1h at 4 °C (1 mL). Samples were washed five times with 0.1 M cacodylate buffer. The washed cells were post-fixed with 1% w/v OsO_4 in 0.1 M cacodylate. After rinsing the fixed cells with distilled water, they were resuspended in 1% aqueous uranyl acetate for 1h and washed 5 times with water. Suspended cells were dehydrated through a graded ethanol series before being embedded in Spurr medium through intermediate 1,2-epoxypropane infiltration. Blocks were conventionally cut, stained, and examined with a Philips CM120 microscope operating under standard conditions (**Figure 2-10C**&**D**).

2.5.4 Characterization of reconstituted signaling complexes

Membrane binding assay: Preparation of reconstituted native membranes containing Tsr, H_6-CheW, and H_6-CheA were prepared as described in **2.5.2**. Membrane pellets were washed gently with 1 mg/mL BSA in 50 mM Tris pH 7.5, 50 mM KC1, 5 mM $MgCl_2$. Pellets were resuspended in SDS-PAGE loading dye with 3 mM DTT. Pelleted proteins were separated by SDS-PAGE and transferred to PVDF membranes for Western blotting. To determine the relative amounts of protein concentrations that remained in the membrane pellets after washing, the immunoblots were probed with monoclonal anti-CheA (1:2000) and developed with HRP-conjugated polyclonal secondary antibodies (goat, 1:10,000) (Jackson ImmunoResearch) and enhanced chemiluminescent substrate (ECL kit, Pierce/ThermoFisher) as recommended by the manufacturer. Western blots were visualized using a GE imageQuant.

Kinase phosphotransfer kinetics assay: Phosphotransfer reactions (26 µL total per timecourse) containing Tsr-containing native membranes (Tsr, CheA, CheW) or CheA alone were combined individually with 40 µM H_6-CheY in phosphotransfer buffer (50 mM Tris pH 8.0, 50 mM KC1, 5

mM $MgCl_2$, 0.5 mM TCEP) on ice for 1 h. A solution of 52 µM ATP and 5 µCi-γ-^{32}P-ATP was prepared. The 32-P-supplemented ATP solution was added to the protein suspensions to initiate phosphotransfer (1 mM ATP, final concentration). 3 µL aliquots were withdrawn from the reaction at 6-8 sec intervals and quenched in a prepared solution of 6X SDS-PAGE loading dye and 50 µM EDTA totaling 10 µL. Reaction time points were separated by SDS-PAGE and developed by autoradiography. Samples separated on Tris-HCl polyacrylamide gels were dried onto filter paper and exposed to phosphor screens. Phosphorimaging was performed using a Typhoon FLA 9000 imager (GE Healthcare, Piscataway, NJ), and phospho-CheY band intensity was analyzed with ImageQuant software.

2.5.5 Swim Plates

Chemotactic abilities of *E. coli* strains were measured on semisolid tryptone agar plates. Colonies were inoculated (5 µL) in the center of 0.25% (w/v) agar in TB broth from bacterial cultures whose optical density measured at λ = 600 nm were normalized (0.4-0.8). Plates were then incubated in a static 30 °C incubator overnight (16-20 hours) and photographed using a bucket of light (270). Swim plates were supplemented with inducers [IPTG, sodium salicylate] or antibiotics [ampicillin (50 µg/ml), kanamycin (25 µg/ml), chloramphenicol (25 µg/ml)] as needed.

2.5.6 Electron Cryo-Tomography (ECT)

20 µl cell culture was mixed with pelleted 100 µl colloidal gold solution, BSA treated to avoid aggregation (271). 3 µl of this cell-gold mixture was then applied to R2/2 copper Quantifoil grids (Quantifoil Micro Tools). After blotting away excess liquid using a Vitrobot (FEI), the sample was plunge-frozen in a liquid ethane-propane mixture (271, 272). Images were

collected using either an FEI Polara™ G2 (FEI Company, Hillsboro, OR) 300 kV field emission gun electron microscope at Caltech, FEI TITAN Krios (FEI Company, Hillsboro, OR) 300 kV field emission gun at UCLA, or an FEI TITAN Krios (FEI Company, Hillsboro, OR) 300 kV field emission gun with an image corrector for lens aberration correction at Janelia Farms. All microscopes were equipped with Gatan image filters (Gatan, Pleasanton, CA). Caltech and Janelia Farm microscopes were outfitted with a K2 Summit™ counting electron detector camera (Gatan, Pleasanton, CA), the UCLA microscope with a 4 megapixel CCD (Gatan, Pleasanton, CA). Data was collected using the UCSFtomo software (273) or BatchTomo (FEI Company, Hillsboro, OR) using cumulative electron doses of ~160 e/A^2 or less for each individual tilt-series. The images were CTF corrected, aligned and reconstructed using weighted back projection using the IMOD software package (274). SIRT reconstructions were calculated using TOMO3D (275). Subvolume averaging, classification and symmetrizing were done using PEET (276).

2.6 Contributions

All cryo-electron microscopy images were acquired by the Jensen lab. The Western blot in Figure 2-12 was performed by the Jensen lab. Plasmid pCO3 and strain CO4 were generated by the Jensen lab. Initial membrane preparation and protein isolation protocols were established by Dr. Margret Wong and Dr. Eric Underbakke.

2.7 Acknowledgements

We thank Dr. Sandy Parkinson for the gift of α-Tsr and α-CheA antibodies, strains, and plasmids.

Chapter 3

Synthetic Multivalent Chemoeffectors of Bacterial Chemotaxis

3.1 Abstract

The chemotaxis signaling pathway allows bacteria to sense and respond to diverse chemicals in the environment. These receptors form highly ordered lattices in the inner membrane which indicates that the interactions among chemotaxis components are an important parameter in chemotaxis based signaling. The role of array architecture during signaling is unclear. To address these questions, we developed a series of linear multivalent chemoattractant based probes to resolve and interrogate conformational changes in the chemotaxis array during signaling. Herein, we report the design and synthesis of attractant ligands based on the natural chemoattractant aspartate. Data from screens performed in the development of these ligands indicate key molecular features of aspartate involved in binding and signaling to its cognate chemoreceptor, Tar. We also demonstrate preliminarily that our aspartate ligands are effective activators of chemotaxis. Additionally, we discuss complications and future applications of these chemoattractant polymers to study bacterial chemotaxis.

3.1 Introduction

Escherichia coli possess a signal transduction system that facilitates responses to external chemical gradients in their local environment; a process termed chemotaxis. The chemotaxis sensory system is widespread throughout bacteria and archaea and can promote colonization and infection by various pathogens (197, 198). The bacterial chemotaxis pathway has been well studied, as discussed in **Chapter 2** and described elsewhere (175-178, 277). *E. coli* chemotactic behavior is governed by an operationally *simple* signal transduction pathway that facilitates the spatiotemporal sensing of chemical gradients (179). Attractants and repellents are detected by a lattice of transmembrane receptors. In *E. coli*, attractants include carbon and energy sources (e.g., glucose). These ligands are sensed either directly or indirectly by the periplasmic domain of four transmembrane receptors (chemoreceptors) that compose the chemotaxis array - Tsr, Tar, Trg, and Trp (see **Figure 2-3**). These receptors share high sequence similarity and domain organization (**Figure 3-1)** (278). As a result, these receptors self-associate at their cytoplasmic tips to form mixed trimers-of-dimers. The kinase, CheA, and scaffolding protein, CheW, associate with these trimers to form a localized extended hexagonal array (194). Ligand binding to the chemoreceptor periplasmic domain is transmitted through the receptor to activate or inhibit the autophosphorylation state of the associated kinase, CheA (184-188). Methyltransferases tailor the chemoreceptors to return bacteria to their pre-stimulus state through a process known as adaptation. This pathway provides the basis for temporal sensing and is necessary for the sensitivity of the system. Details of adaptation have been reviewed elsewhere (178, 279). Briefly, CheR and CheB respectively methylate and demethylate chemoreceptors at specific cytoplasmic located glutamate residues. CheR acts on inactive

receptors to increase receptor activity and CheB conversely acts on active receptors to reduce their activity. The combined activities of CheR and CheB modulate receptor activity to enable temporal comparisons of environmental ligand concentrations. Despite a tremendous wealth of knowledge regarding the chemotaxis pathway, the molecular level details by which ligand recognition propagates signals structurally through the chemotaxis array to control cellular behavior remains unclear.

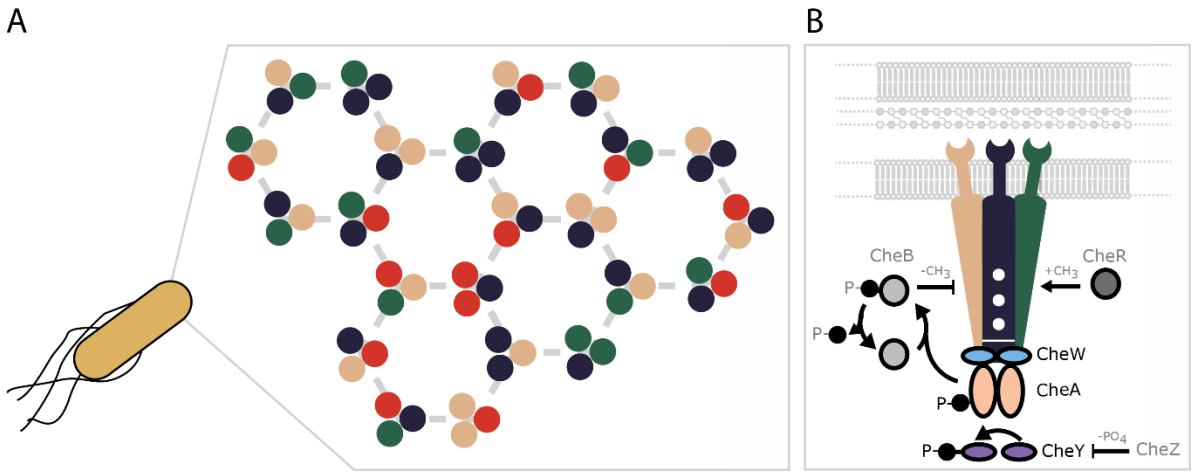

Figure 3-1. *E. coli* chemotaxis array (A) Extended hexagonal chemotaxis array of receptor trimer-of-dimers. (B) Phosphorylation flow of signaling in bacterial chemotaxis. Transmembrane chemoreceptors are arranged as trimers-of-dimers associated with a kinase, CheA, and adapter protein, CheW, at the cytoplasmic tip. Ligand binding influences CheA phosphorylation which is transferred to receiver protein CheY which interacts with the flagellar motor. CheZ is a phosphatase that modulates CheY phosphorylation levels. CheR is a methyltransferase that modifies receptors during adaptation. CheB is a demethylase and is also phosphorylated by CheA a which increases CheB activity.

Clustering or oligomerization of cell surface receptors is an important regulator of many biological processes (280-282). Altering ligand valency has been shown to manipulate clustering and responses generated by receptor oligomerization (209, 283, 284). Whether physical changes in receptor array structure are involved in chemotaxis signal transmission is controversial. Several groups have reported protein dynamics along the transmembrane

chemoreceptor including, piston-like shifts in the transmembrane domain (178, 277, 285), rotations (286), or packing instabilities in a four-helical coiled-coil region, the HAMP domain (287-290). Structural alterations in receptor arrays have also been reported in the presence of chemoeffector ligands, including microscopy based observations of polar receptor array delocalization using fluorescent antibodies raised to cytoplasmic array components (82, 291, 292) or GFP labeled receptors (293). FRET experiments using fluorescently labeled array components have reported changes in chemoreceptor dynamics during experiments of chemoreceptor ligand engagement (294-296). Contrary to these results, researchers have reported that receptor array localization is stable under activating conditions by fluorescent microscopy (297, 298) and electron cryo-tomography (ECT) (299). Recent studies have focused on the dynamics of CheA and CheW cytoplasmic rings and have revealed altered protein conformations upon activation (300). Genetic lesions at the interface of CheW and CheA were shown to cause clustering defects and block cooperativity, implicating the cytoplasmic kinase array as a conduit for chemosensory integration (265). Furthermore, this result highlights the important geometric and spatial contacts of the chemotaxis array for functional performance and bacterial viability.

Chemically defined compounds can be generated to interrogate the role of receptor spatial architecture in signal transduction. Multivalent ligands which present multiple recognition elements from a central scaffold can be used to probe the effects of clustering of cell surface receptors because of their ability to alter and perturb the spatial orientation of receptors (301). Synthetic and natural multivalent ligands derive their unique potential from the different binding modes their composition and engagement mechanism encode (**Figure**

3-2). This includes the lack of an entropic penalty for engagement of a second receptor of an oligomeric complex (chelate effect, **Figure 3-2A**). Chelate binding manifests as an increase in apparent binding affinity or so-called avidity. Apparent affinity can also be increased when a multivalent ligand rebinds the same receptor (statistical rebinding, **Figure 3-2B**). Rebinding competes with dissociation due to the increased local availability of receptor ligands. Multivalent ligands can also alter the physical location of receptors in the two-dimensional lipid membrane to cluster receptors (**Figure 3-2C**). Additionally, based on ligand composition, multivalent displays can engage different receptor types to promote or dampen signaling (**Figure 3-2D**). Given the diversity of binding modes multivalent ligand polymers can target and their ability to be systematically altered, they represent powerful tools to understand and influence biological function.

The modular design of synthetic polymers presents an opportunity to investigate what binding modes are relevant for chemotaxis array signaling or if ligands of different valency or composition can engage in different signaling modalities to affect bacterial behavior. Research from the Kiessling research group has explored the influence of multivalent ligands on chemotaxis array signaling. High-valency attractant-bearing polymers of galactose, which target the chemoreceptor Trg, were found to be more potent than their monovalent ligand counterparts (284). Engagement of Trg with synthetic multivalent galactose polymers potentiated cellular responses to serine by its receptor (Tsr) 100-fold. This result demonstrates that receptors can influence each other through array-based connectivity (209). Immuno-fluorescence microscopy based observations of arrays interacting with polymers formed a model where repellent binding stabilized chemotaxis arrays and attractant binding lead to

A Chelate Effect

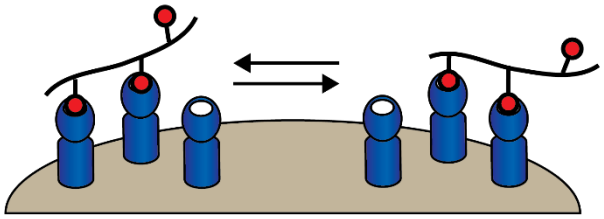

B Statistical Rebinding

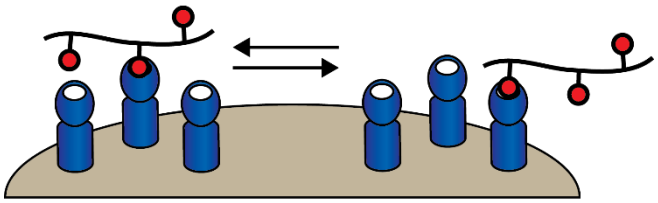

C Receptor Clustering

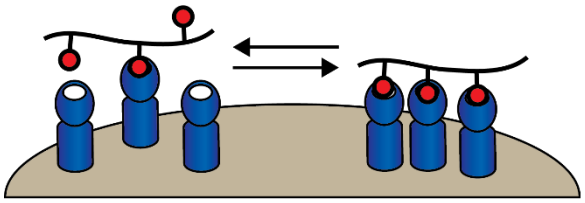

D Receptor Co-Engagement

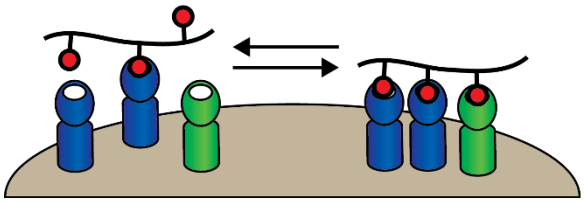

Figure 3-2. Multivalent ligands can interact with receptors through a variety of mechanisms Polymers can interact with receptors by (A) Chelate effect (B) statistical rebinding (C) Receptor clustering and (D) Receptor Co-engagement. Adapted from ref. (301)

destabilized polar chemotaxis arrays (291). In this work, High-valency multivalent polymers of leucine, which bind to Tsr as a repellent, functioned not as repellents but as attractants. Multivalent polymers of repellents where interpreted to alter receptor architecture which would induce attractant-like responses by disrupting array connectivity.

Technological advances and insights into the organization and function of chemotaxis arrays have occurred since these initial studies. Including, 1. the development of *in vivo* FRET reporter strains, which can replace autoradiographic studies, to provide real-time readouts on kinase activity (302), 2. microfluidic assays which can be run in parallel and multiplexed to provide statistical rigor and reproducibility to accumulation based assays (e.g., capillary assays) (303), 3. electron cryo-tomography visualization, which can image indivual receptors, and has examined the organization of arrays exposed to different ligands (299), and 4. sophisticated single cell tracking algorithms that can map the trajectories of hundreds of swimming cells (304). We therefore aimed to generate a system where we could leverage these advancing technologies with the potential of multivalent ligands to interrogate oligomeric protein complexes. Specifically, we wanted to explore the mechanisms by which multivalent polymers were interacting with the chemotaxis arrays to generate the responses we previously reported and were described above. Additionally, the synthetic modularity of these polymers could be leveraged to assess whether structural alterations within arrays are fundamental modes of chemotaxis signal propagation.

Previous polymers to interrogate chemoreceptor binding used the chemoattractant galactose that binds to its cognate chemoreceptor, Trg, through a periplasmic binding protein (305). The necessity for a three-part system adds complexity to the experimental design.

Additionally, Trg is a low abundance receptor whose signal integration has been demonstrated to rely on the high-abundance receptors, Tar and Tsr (306). Therefore, we set out to design a new class of direct binding multivalent chemotaxis polymers that target high-abundance receptors directly. Targeting Tsr and Tar would bypass the need for periplasmic binding receptors. The higher expression of Tsr and Tar additionally allows for increased engagement by tethered ligands. Ligands to these receptors (e.g., serine (Tsr) and aspartate (Tar)) elicit the most potent responses in chemotaxis. Here, we report the synthesis of a series of linear multivalent polymers displaying a modified aspartate by post-polymerization functionalization of polymers derived by ring-opening metathesis polymerization (ROMP). These polymers target the high abundance chemoreceptor Tar and are able to potently activate chemotaxis signaling. We propose that this class of attractants can be used to interrogate chemotaxis signaling, and efforts toward that goal are discussed. The ability to control chemotaxis is a frontier effort as many pathogenic bacteria utilize the chemotaxis system to coordinate their motility to establish infections. Development of polymers that can modify chemotactic behavior could form the basis for narrow anti-infectious agents as an alternative to antibiotics.

3.3 Results and Discussion

3.3.1 Design of a Serine and Aspartate Analog Library

Use of multivalent polymers to investigate the influence of attractants on the organization of chemoreceptor arrays necessitates attachment of protein binding epitopes that are synthetically accessible, amenable to polymerization and retain the ability to potently activate the chemotaxis pathway. Therefore, we targeted the known attractants, serine and aspartate, which are directly bound by Tsr and Tar respectively (**Figure 3-3A**&**B**). We set out to generate

a library of serine and aspartate analogs to determine possible polymer attachment positions by establishing which amino acid derivatives retain the ability to bind chemoreceptors and activate the chemotaxis pathway. Insights into the structural requirements of attractant binding were derived from the crystal structures of the periplasmic domain of *E. coli* Tar and Tsr in complex with their cognate ligands serine and aspartate (PDB: 3ATP and 4Z9J) (**Figure 3-3A**&**B**) (307) and from biochemical literature data assessing chemotaxis to amino acid analogs (308).

Structural analysis indicated that the binding pocket of Tsr is smaller than that in Tar and may also limit substitutional tolerance (**Figure 3-3A**) (307). The spatial positioning of serine **3-1** and aspartate **3-2** bound to receptors indicate that the α-carbon, -amino and -carboxyl groups are positioned at the entrance of the ligand binding pocket which may be the best entry points for substitution (**Figure 3-3A**). The α-amino group and α-carboxyl group retain similar recognition modes between Tsr and Tar. The α-amino group is coordinated by hydrogen bonding between the backbone carbonyl oxygens of Y149 and Q152 in Tar and F151, F152 and Q154 in Tsr. The α-carboxyl group of the attractant ligands is coordinated by a conserved R64 in both Tsr and Tar (**Figure 3-B**). The amino acid side chains are bound uniquely in Tsr and Tar. In Tar, the aspartate β-carboxyl group interacts with the conserved residues R69 and R73, Tsr instead utilizes N68 (**Figure 3-B**).

Capillary accumulation assays performed by Mesibov and Adler (308) examined the threshold concentrations at which various chemicals could elicit chemotaxis (**Figure 3-4**&**5**, **Table 4-1**&**2**). Here, they demonstrated that modifications to the α-amino group of serine (N-

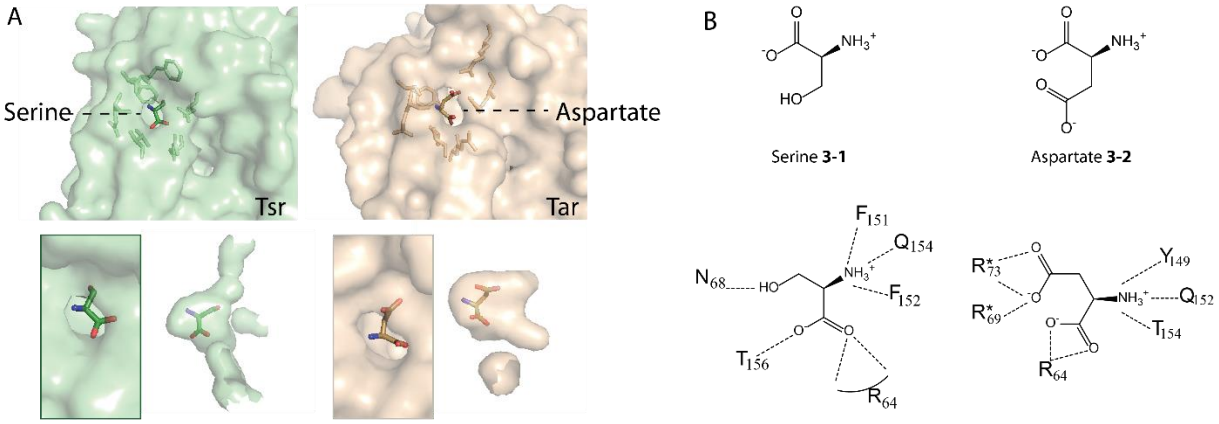

Figure 3-3. Comparison of serine and aspartate binding to Tsr and Tar (A) Surface rendering of serine and aspartate binding to Tsr and Tar based on published crystal structures PDB: 3ATP and 4Z9J (307). Inserts highlight ligand orientation in binding pocket and binding pocket size. Tsr = green, Tar = wheat. (B) Key protein residues that interact with serine and aspartate. Numbering is based on published crystal structures PDB: 3ATP and 4Z9J (307).

acetyl-L-serine **3-7** and N-methyl-L-serine **3-11)** and aspartate (N-acetyl-L-aspartate **3-18** and N- ethyl-DL-aspartate **3-24)** diminish chemotaxis sensitivity. Modifications to the α-carboxyl group of serine (L-serine-α-methylester **3-10** and Serinol **3-12)** were inhibitory but were either deleterious or neutral in aspartate (isoasparagine **3-21** and L-aspartate-α-methylester **3-15**, respectively) and inhibitory when both the α- and β-carboxylates were modified as seen in aspartate analogs (L-aspartate diamide **3-22** and DL-aspartate dimethylester **3-23**). Tar is unable to signal using β-alanine **3-25** indicating that the α-carboxylic acid is involved in signaling or required for binding. Modifications to the α-hydrogen are well tolerated in serine (α-aminoisobutyric acid, aib, **3-5** and DL-α-methyl serine **3-9**) and DL-α-methyl aspartate **3-13,** however, alterations to the β-hydrogen of aspartate were deleterious (DL-erythro-β-hydroxyaspartate **3-19** and DL-threo-β-hydroxyaspartate **3-20**). Methylation of the β-carboxylic acid or hydroxyl in aspartate **3-16** or serine **3-4** is able to elicit chemotaxis. These resides would be expected to determine ligand specificity but appear to tolerate modifications

that retain the ability to maintain hydrogen bonding. Aib **3-5** is a serine derivative that lacks the β-hydroxyl group entirely and can elicit signaling. Aib **3-5** signaling therefore indicates that the amino acid core is responsible for signaling through the receptor. Therefore we would anticipate that side chain modifications are a promising route to derivatization for retention of signaling. We would anticipate that modifications to the β-carboxylate of aspartate would be tolerated because it is coordinated by two residues and may be able to lose one of these interactions while retaining sufficient affinity for the receptor Tar.

In summary, these results indicate that the receptor contacts with the amino acid core are conserved and involved in recognition and signaling. From these results we would anticipate that aspartate can tolerate methylation of the α-carboxylic acid only if the β-carboxylic acid is left intact. A linker to the α-carbon may pose a general route to derivatization. Modifications to the β-carboxylate of both ligands were well tolerated when the ability to maintain hydrogen bonds were accommodated by either an amine or ester group. Therefore, we, acquired a library of serine and aspartate ligands, eight serine compounds (**3-1**, **3-3**, **3-5**, **3-7**, **3-7**, **3-9**, **3-10** and **3-11)** and nine aspartate compounds (**3-2**, **3-13**, **3-15**, **3-16**, **3-17**, **3-18**, **3-24** and **3-25)** for subsequent experimental analysis. The biochemical assays performed by Adler et al. (308) only assessed the threshold concentration of bacterial accumulation in capillary devices; therefore, we wanted to establish the signaling potential of these ligands in our intended *in vivo* FRET-based applications (302).

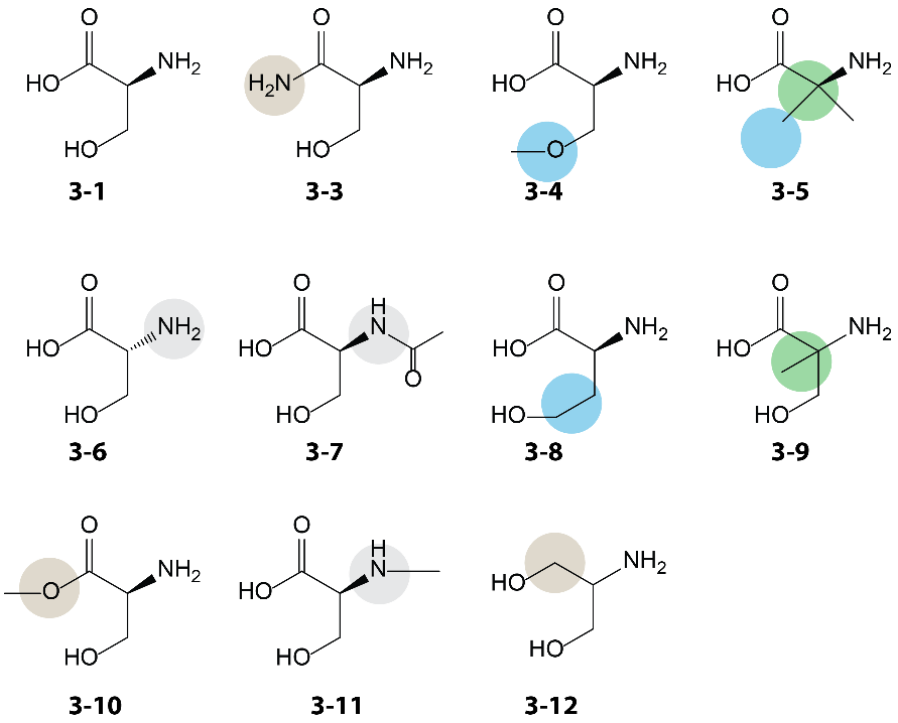

Figure 3-4. Serine and serine analogs from Table 3-1 Tan circle indicates α-carboxy modification, blue circle indicates β-hydroxyl modification, grey circle indicates α-amino modification and green circle indicates modification to the α-carbon.

Table 3-1. Threshold molarity of *E. coli* toward serine and serine analogs from ref. (308)

	Compound	Threshold molarity (μm)
3-1	L-serine	0.3
3-3	serinamide	10
3-4	L-serine-β-methylester	10
3-5	α-aminoisobutyric acid (aib)	20
3-6	D-serine	30
3-7	N-acetyl-L-serine	50
3-8	homoserine	100
3-9	DL-α-methyl serine	200
3-10	L-serine-α-methylester	200
3-11	N-methyl-L-serine	300
3-12	serinol	>100,000

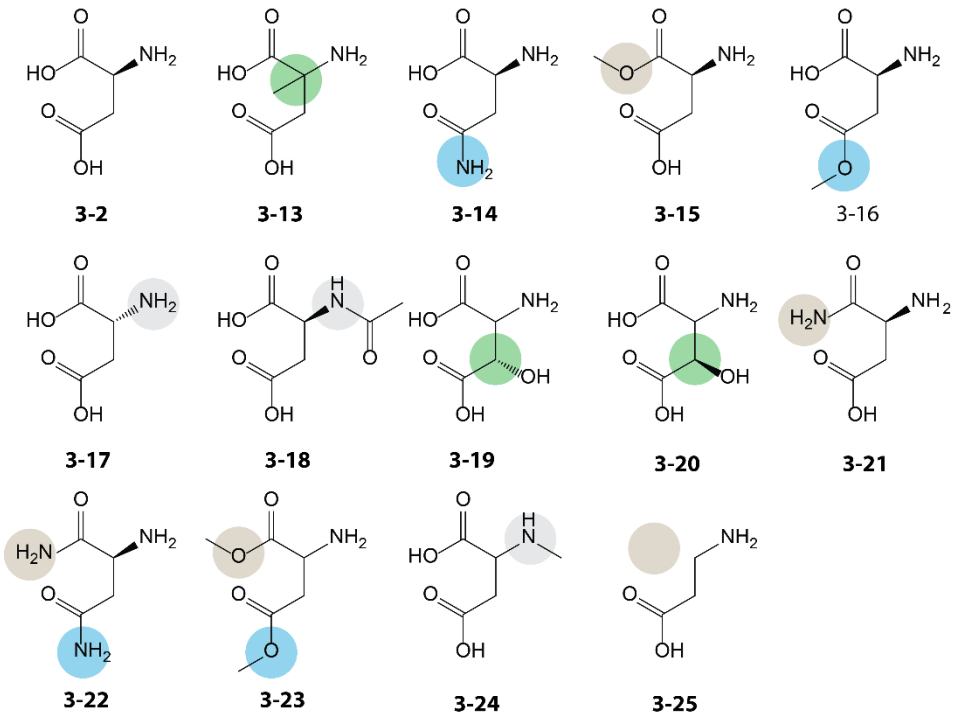

Figure 3-5. Aspartate and aspartate analogs from Table 3-2 Tan circle indicates α-carboxy modification, blue circle indicates β-hydroxyl modification, grey circle indicates amino modification and green circle indicates modification to α- and β- carbon.

Table 3-2. Threshold molarity of *E. coli* toward aspartate and aspartate analogs from ref (308)

	Compound	Threshold molarity (μm)
3-2	L-aspartate	0.06
3-13	DL-α-methyl aspartate	0.5
3-14	L-asparagine	2
3-15	L-aspartate-α-methylester	5
3-16	L-aspartate-β-methylester	5
3-17	D-aspartate	10
3-18	N-acetyl-L-aspartate	100
3-19	DL-erythro-β-hydroxyaspartate	100-500
3-20	DL-threo-β-hydroxyaspartate	100-500
3-21	isoasparagine	500
3-22	L-aspartate diamide	1000
3-23	DL-aspartate dimethylester	1000
3-24	N-methyl-DL-aspartate	1000
3-25	β-alanine	>100,000

3.3.2 Serine and Aspartate Analog Screen by *in vivo* FRET

We used an *in vivo* FRET-based assay to measure intracellular kinase activity in response to our library of serine and aspartate analogs to establish an attachment point that would facilitate polymerization to generate a multivalent attractant polymer (302). In this assay, a FRET signal is generated from the interactions of a CheY-YFP/CheZ-CFP pair in an *E. coli* FRET reporter strain with the chromosomal CheY and CheZ loci and for all five *E. coli* receptor genes deleted. These FRET reporter strains only express either Tsr or Tar and the CheY-YFP/CheZ-CFP FRET pair. At a basal rate, CheA autophosphorylation is transferred to CheY. Phosphorylation of CheY promotes binding by its cognate phosphatase, CheZ. The interaction of CheZ-CFP and CheY-YFP produces a measurable FRET signal. Attractant binding by a chemoreceptor inhibits CheA autophosphorylation, thereby decreasing the FRET signal.

We screened the aforementioned library of serine and aspartate derivatives in the described FRET strains. We first tested each compound under saturating conditions to broadly examine ligand detection by its cognate receptor. Compounds were tested in two host strains, one that expresses CheR and CheB (UU2700) and one that lacks the CheR and CheB sensory adaptation enzymes (UU2567). In UU2567 receptors converge on a two-state signaling model, where QEQE-receptors can either activate (*on*) or deactivate (*off*) CheA. The sensitivity of a ligand therefore reflects the proportion of receptors in the *on* or *off* state. At 10 mM, all compounds elicited responses in UU2700 (data not shown). In UU2567 all compounds elicited responses except aib **3-5**, N-methyl serine **3-11**, serinamide **3-3** and β-alanine **3-25** (**Figure 3-6**). The responses generated by N-acetyl serine **3-7** were complicated by possible quenching effects in both the YFP and CFP channels and not pursued further. All positive compounds were

then tested by stepwise addition and removal of the attractant at varying concentrations. The dose-response data for each attractant were fit to a multisite Hill equation to obtain $K_{1/2}$ values, the concentration that elicits half-maximal CheA kinase activity (**Table 3-3**). The modified serine compounds had $K_{1/2}$ values in the low millimolar range, and the aspartate compounds elicited responses in the low micromolar range, much closer to the natural ligand $K_{1/2}$ than the serine analogs. This indicated that Tar was more amenable to modification and therefore was more likely to respond to a polymerized ligand display. Therefore, we, focused on modification at the α- or β- carboxylic acid, α-carbon, and amino group, which displayed the lowest $K_{1/2}$ values.

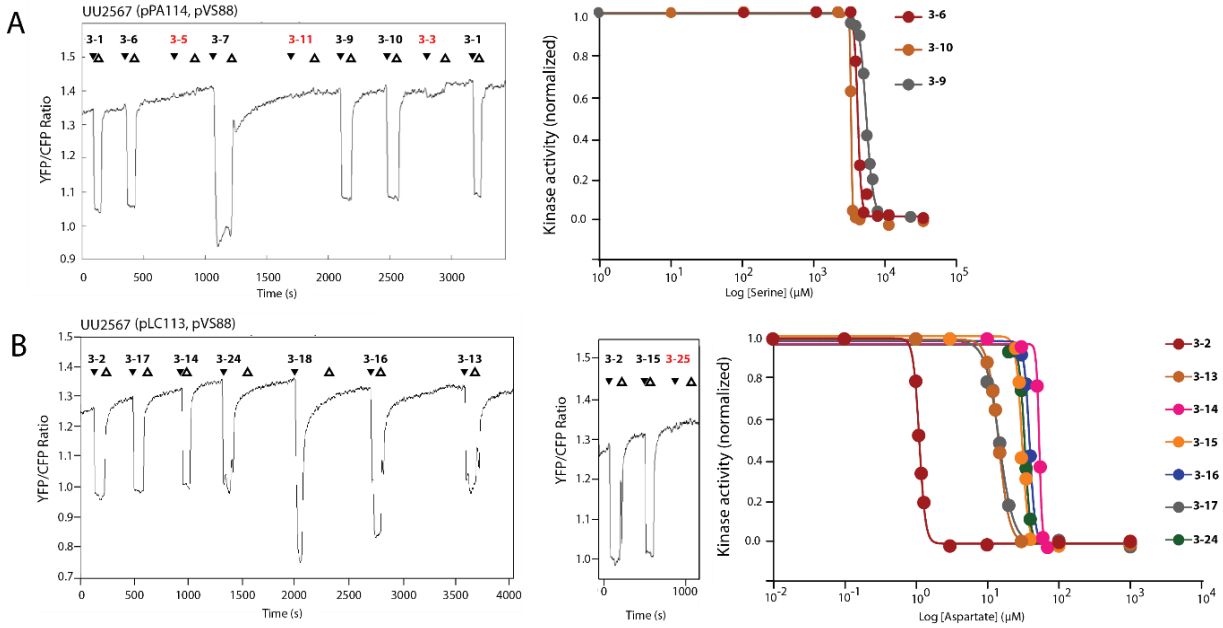

Figure 3-6. Responses of *E. coli* to serine and aspartate analogs measured by FRET (A) Responses of a Tsr- or Tar-only strain (UU2567) to saturating concentrations (10 mM) of serine and aspartate analogs measured with a CheY-YFP/CheZ-CFP FRET pair. Vectors and strains listed in **Table 3-7**. Filled arrows indicate compound addition and empty arrows indicate compound removal. Red numbered compounds did not generate responses. (B) Dose-response curves of each compound used to derive $K_{1/2}$ values.

Table 3-3. Dose-response $K_{1/2}$ values of serine and aspartate analogs

	Compound	$K_{1/2}$ (μM) (UU2567)
3-1	L-serine	18*
3-3	serinamide	No response
3-5	α-*a*minoisobutyric acid (aib)	No response
3-6	D-serine	3748 ± 17
3-7	N-acetyl-L-serine	Not determined**
3-9	DL-α-methyl serine	4883 ± 35
3-10	L-serine-α-methylester	3022 ± 4
3-11	N-methyl-L-serine	No response
	Compound	$K_{1/2}$ (μM) (UU2567)
3-2	L-aspartate	1.12 ± 0.01
3-13	DL-α-methyl aspartate	14.45 + 0.04
3-14	L-asparagine	53.31 + 0.28
3-15	L-aspartate-α-methylester	30.72 ± 0.59
3-16	L-aspartate-β-methylester	39.03 ± 0.17
3-17	D-aspartate	14.74 + 0.27
3-18	N-acetyl-L-aspartate	1081+ 75
3-24	N-methyl-DL-aspartate	33.31 + 0.24
3-25	β-alanine	No response

$K_{1/2}$ values (± SEM); *from literature **possible quenching effects both the YFP and CFP channels

3.3.3 Synthesis of a Focused Library of Polyethylene Glycol Aspartate Derivatives

Given that most of the test aspartate analogs elicited a chemotactic response more similar to that of the natural ligand, we generated a second library of aspartate analogs. In this library, we focused on structural features that would facilitate synthetic accessibility and maximal chemotactic activity. Therefore, we generated aspartates bearing a flexible polyethylene glycol (PEG) linker at either the α- or β- carboxyl group based on the results of our screening efforts described in **3.3.2**. This smaller, more refined library, was designed to discern the ability of a polymerizable monomer to stimulate chemotaxis. Addition of a PEG linker will extend the ligand from the polymer backbone which can enhance its ability to access receptors and can be systematically varied to explore how linker length influences activity to determine optimal length for activity.

We synthesized L-aspartate-α-ester-PEG$_4$-monomethyl ether **3-27**, L-aspartate-β-ester-PEG$_4$-monomethyl ether **3-28**, and L-aspartate-α-amide-PEG$_4$-azide **3-29**. To generate compounds **3-27**, **3-28** and **3-29,** we started with commercially available aspartates bearing tert-Butyloxycarbonyl (BOC) protecting groups at either the alpha- or beta- carboxylic acid. We then performed a 1-Ethyl-3-(3-dimethylaminopropyl)carbodiimide (EDC) mediated coupling to attach either a tetraethylene glycol monomethyl ether (m-PEG$_4$-OH) or a heterobifunctional O-(2-Aminoethyl)-O'-(2-azidoethyl)diethylene glycol (azido-PEG$_3$-amine). This coupling reaction generated either ester or amide linked PEG derivatives. The α-carboxylic acid group of aspartate interacts with conserved arginine side chains within the Tar receptor (**Figure 3-3**), therefore, ester or amide linked functionalization should maintain the ability to act as a hydrogen bond acceptor with this residue. Subsequent acid deprotection removed the BOC protecting groups to afford the final ester **3-27**, **3-28)** or amide **3-29** PEGylated aspartate derivatives.

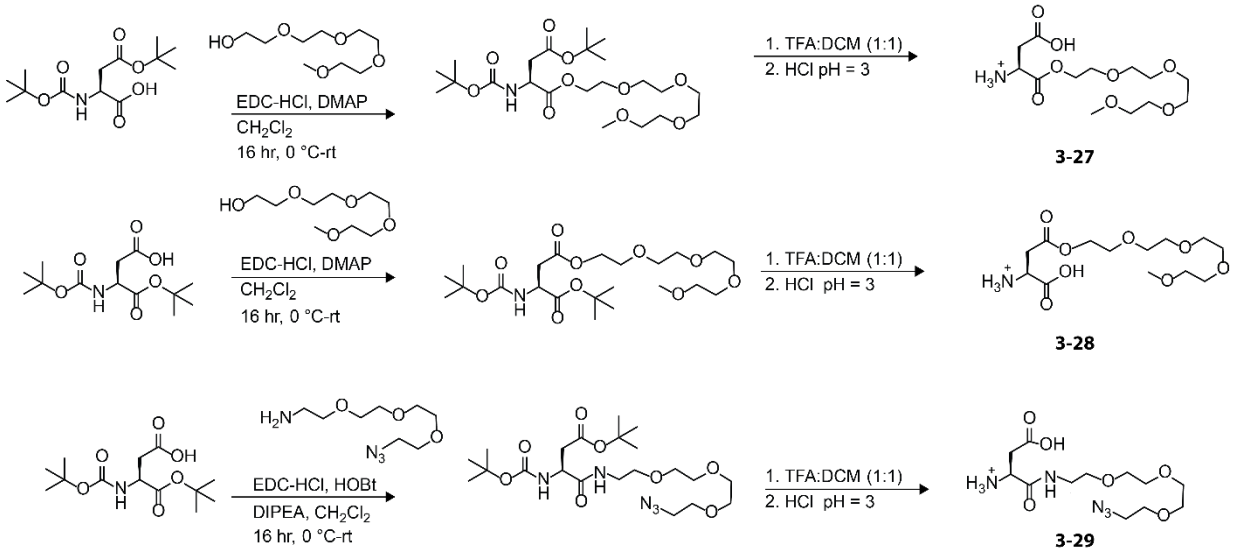

Scheme 3-1. Synthesis of aspartate PEG derivatives

3.3.4 Evaluation of a Focused Screen of Polyethylene Glycol Aspartate Derivatives

Compounds **3-2**, **3-15**, **3-16**, **3-21**, **3-27**, **3-28,** and **3-29** were evaluated using the previously described *in vivo* FRET reporter strain and by a recently developed microfluidic-based fluorescence accumulation assay (**Figure 3-7**) (303). *In vivo* FRET analysis (**Figure 3-7A, Table 3-4**) indicated that the addition of a PEG linker does not significantly affect the ability to elicit chemotaxis and that the α-carboxylic acid modified aspartate (compounds **3-15**, **3-27)** is a moderately better ligand that the β-carboxylic acid aspartate (compounds **3-16**, **3-28)**. We also tested the chemotactic responses of *E. coli* RP437 (WT) to this secondary aspartate derivative library in a microfluidic device in which the chemotactic responses to several chemicals can be measured in parallel (303). This assay generates a stable gradient along a microfluidic channel leading to a pair of terminal chambers. Bacterial cells that are stimulated by the ligand generating the gradient accumulate in these chambers and can be compared to control channels lacking attractant. Relative responses representing the sum intensity of a source containing a chemical of interest (I_x) over the sum intensity of an empty source (I_0) were plotted at the peak response concentration (**Figure 3-7B, Table 3-4**). All compounds were positive for chemotaxis except the PEG_3 derivatized α-amide aspartate **3-29**. A slightly higher response rate was seen for the α-carboxylic acid modified aspartate **3-15**, **3-27** compared to the β-carboxylic acid modified aspartate **3-16**, **3-28**.

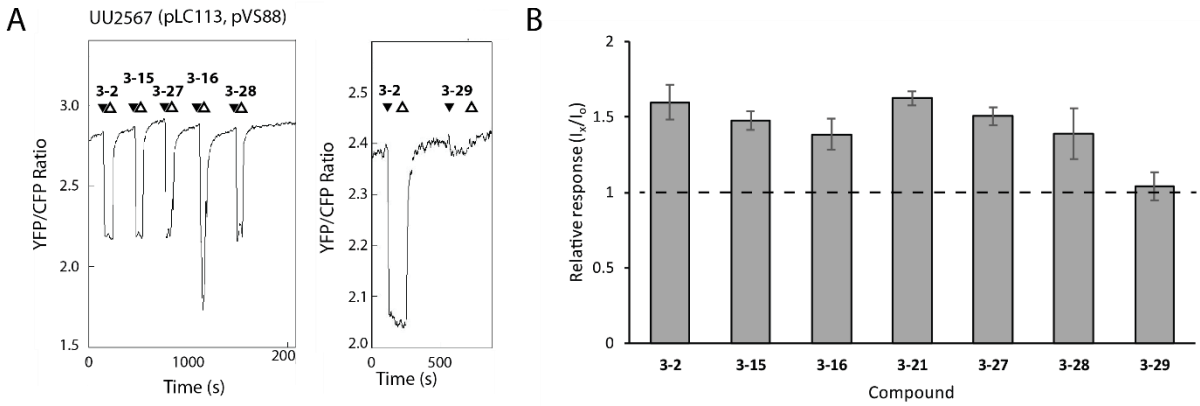

Figure 3-7. Responses of *E. coli* to serine and aspartate analogs measured by FRET and fluorescence accumulation (A) Responses of a Tar-only strain (UU2567) to saturating concentrations (10 mM) of aspartate analogs measured with a CheY-YFP/CheZ-CFP FRET pair. Vectors and strains listed in **Table 3-7** (B) Peak response concentration values from microfluidic device accumulation assays. Each value represents the mean fluorescence normalized to buffer only. Error bars indicate the SEM.

Table 3-4. Dose-response $K_{1/2}$ values and fluorescence accumulation of aspartate analogs

	Compound	UU2567 $K_{1/2}$ (μM)	Relative response (I_x/Io)
3-2	L-aspartate	1.12 ± 0.01*	1.6 ± 0.11
3-15	L-aspartate-α-methylester	30.72 ± 0.59*	1.48 ± 0.06
3-16	L-aspartate-β-methylester	39.03 ± 0.17*	1.39 ± 0.10
3-21	α-amide aspartate	Not tested	1.63 ± 0.05
3-27	L-aspartate-α-ester-PEG_4-monomethyl ether	89.03 + 1.89	1.51 ± 0.06
3-28	L-aspartate-β- ester-PEG_4-monomethyl ether	152.78 + 78	1.39 ± 0.17
3-29	L-aspartate-α-amide-peg_4-azide	No response	1.04 ± 0.09

* from **Table 3-3**; (± SEM)

3.3.5 Synthesis of a Library of Multivalent Ligands that Present an Aspartate-Based Attractant

Previous results with indirect binding polymeric chemoattractants demonstrated that multivalent polymers were more potent than their monovalent counterparts (209, 284, 292). Biochemical analysis using chemical-crosslinking indicated that polymers of varied length could alter receptor packing (291). Therefore, we generated attractant polymers of varied

length that directly bind the chemoreceptor Tar to investigate this observation further and to evaluate the consequences of receptor architecture alteration on signaling. Polymers generated by ring-opening metathesis polymerization (ROMP) offer precise control over polymer length and can be functionalized post-polymerization to display multiple epitopes (309). Such a strategy has been used by the Kiessling research group to generate polymers bearing repeating activated ester groups via the polymerization of a succinimidyl ester-substituted norbornene monomer (309). The activated ester is inert during polymerization but can be functionalized with desired amine reactive substrates affording final control over polymer composition.

Given the slightly higher chemotactic response observed for the α-carboxylic acid modified aspartate **3-27**, we pursued this compound for polymerization. Attempts to generate an amine-terminated L-aspartate-α-ester-PEG_3 ligand experienced rapid rearrangement to produce aspartate with an amide-linked PEG_3-alcohol. Therefore, we instead endeavored to produce an azide terminated L-aspartate-α-ester-PEG_3 ligand. Such a ligand could be appended to a ROMP-NHS polymer in a two-step process if polymers were first functionalized with propargylamine to generate a polymer displaying alkyne groups. A copper-catalyzed azide-alkyne [3+2] cycloaddition (CuAAC) can then be performed to functionalize alkyne bearing polymers with the L-aspartate-α-ester-PEG_4-azide ligand. CuAAC is widely used in bioconjugate chemistry owing to its chemoselectivity and efficiency (310) and has previously been applied to norbornene polymers (311, 312). Therefore, we, generated L-aspartate-α-ester-PEG_4-azide **3-31** using the same previously described EDC coupling to append a heterobifunctional O-(2-azidoethyl)triethylene glycol (azido-PEG_3-alcohol) to β-BOC protected

aspartate (**Scheme 3-2**) followed by acid deprotection. ROMP of norbornene N-hydroxysuccinimidyl ester monomers **3-32** was performed using a functional group-tolerant ruthenium carbene initiator **3-33** to access polymers with a narrow molecular weight distribution with lengths controlled by the monomer-to-initiator ratio (313). Using this approach, we prepared polymers of varied length and utilized NMR to characterize the degree of polymerization. The integration of the terminal phenyl protons relative to polymer backbone alkene protons was analyzed and indicated that polymers of an average *length* corresponding to that of an 11-mer **3-34a**, 29-mer **3-34b**, and a 56-mer **3-34c** were generated. These succinimide bearing polymers **3-34a-c** were modified with propargylamine and subsequently with aspartate ligand **3-30** by CuAAC to generate multivalent polymers of varying lengths displaying an α-ester aspartate for analysis in chemotaxis signaling assays (**Scheme 3-3**). To prevent undesired side reactions with any unreacted succinimidyl ester moieties, the functionalization reactions were terminated by backfilling with a large excess of ethanolamine. Our synthetic approach allowed the substitution levels of each pendant functional group to be determined. Specifically, the proportion of aspartate conjugated to polymer was quantified by integration of distinct ^{1}H NMR signals that arise from the generation of the triazole and the polymer backbone. We functionalized polymers with comparable aspartate density (40-50%). Specifically, the polymers were functionalized with ~5, ~11 and ~20 copies of aspartate for **3-37a**, **3-37b,** and **3-37c** respectively.

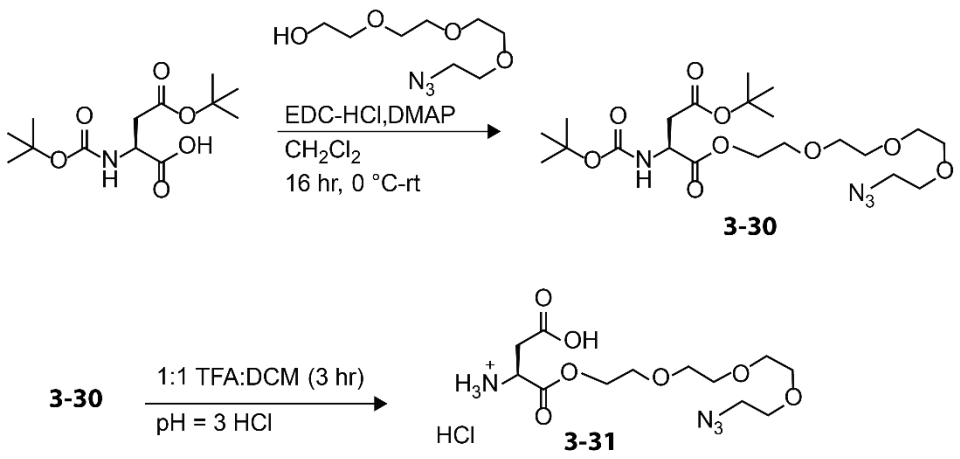

Scheme 3-2. Synthetic scheme used to prepare monomeric chemoattractant to Tar Route employed to generate aspartate ligand for polymer functionalization and evaluation as a monovalent attractant.

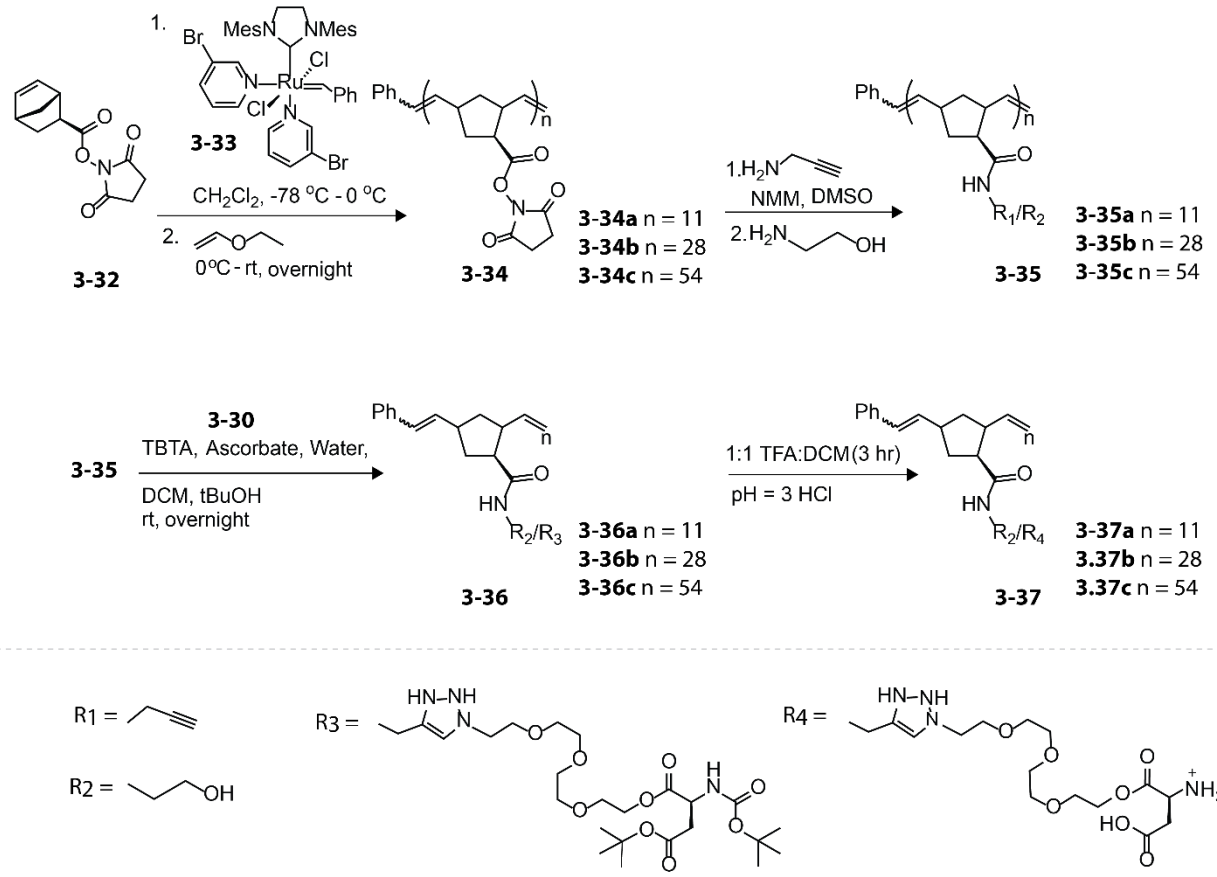

Scheme 3-3. Synthetic scheme used to prepare multivalent chemoattractants to Tar Synthetic route to polymers bearing attractants to the chemoreceptor Tar (R_4 = α-ester-PEG_3-

aspartate). Polymers of controlled length were functionalized with an aspartate derivative via a two-step post-polymerization functionalization strategy involving an alkyne linker.

3.3.6 *In vivo* Responses to Multivalent Aspartate-Based Attractants Measured by FRET

Monovalent **3-31** and multivalent aspartates **3-37a-c** were tested by *in vivo* FRET analysis to assess the effect of different length polymers on chemotaxis signaling. All compounds were evaluated in four strains; UU2567^{R-B-}, UU2700^{R+B+}, UU2869 $^{R-B-}$, which is similar to UU2567, but also carries a CheW mutation (CheW-X3, a CheW variant with amino acid replacements at three positions: CheW-R117D/E121R/F122S) that abrogates higher-order connections between receptor core signaling complexes, and UU2870 $^{R+B+}$ which also carries the same CheW mutation. In the chemotaxis array, there is a structural interaction between CheW and the P5 domain of CheA. Amino acid replacements in CheW at this interface weaken the connections between signaling units and leads to dispersed arrays and diminish cooperativity (265, 314). We would anticipate that polymers of sufficient length bearing chemoattractants should be able to cluster receptors and increase cooperativity thereby leading to more sensitive $K_{1/2}$ values and increased hill coefficients.

We observed that monovalent and multivalent displays of aspartate are effective stimulators of chemotaxis as measured by kinase activity. $K_{1/2}$ values and Hill coefficients for all prepared compounds are similar to those of aspartate alone, a potent attractant of chemotaxis. However, we did not observe enhanced potency of any polymer of any length compared to aspartate **3-3** or the monovalent aspartate ligand **3-31** in any strain examined. The following sections explore potential assay and polymer specific complications with regard to these results.

Table 3-5. Dose-response $K_{1/2}$ values and Hill coefficients of aspartate analogs in various chemotaxis strains

	UU2567^{R-B-}		UU2700^{R+B+}		UU2869$_{X3}^{R-B-}$		UU2870$_{X3}^{R+B+}$	
	$K_{1/2}$ (μM)	Hill coeff.	$K_{1/2}$ (μM)	Hill coeff.	$K_{1/2}$ (μM)	Hill coeff.	$K_{1/2}$ (μM)	Hill coeff.
L-aspartate **3-2**	0.9	18 ± 0.4	0.1	1.3 ± 0.3	0.5	2.5 ± 0.3	0.5	2.5 ± 0.2
monovalent aspartate **3-31**	0.5	20 ± 0.6	0.23	2.8 ± 0.5	0.2	2.8 ± 0.3	1.1	6.4 ± 0.5
aspartate 11-mer **3-37a**	1.1	29 ± 1.0	0.11	4.4 ± 0.8	0.9	2.3 ± 0.1	1.0	2.1 ± 0.3
aspartate 29-mer **3-37b**	2.5	35.2 ± 7.0	0.15	2.4 ± 0.2	1.1	2.4 ± 0.2	0.9	1.7 ± 0.1
aspartate 54-mer **3-37c**	2.6	17.9 ± 0.8	0.2	2.6 ± 0.2	1.2	2.1 ± 0.2	0.8	1.7 ± 0.1

± SEM

3.3.7 Assay Specific Issues With *in vivo* Responses to Multivalent Aspartate-Based Attractants

All polymers were tested in bacterial strains designed for *in vivo* FRET reporting. These strains express only a single chemoreceptor (either Tsr or Tar). These homogeneous receptor strains are used because analysis of signaling in non-homogenous arrays are complicated by the interactions between receptors of different detection specificities (e.g., Tsr and Tar) which can independently control the activity of CheA (247). In an array, a single receptor cluster which is composed of a trimer-of-dimers presents six theoretical binding sites. Given the geometric constraint of aspartate ligands on a polymer and the known modes of binding (**Figure 3-2**), it might be possible that a polymer, once bound to a single receptor, can become trapped at that cluster deactivating a single cluster redundantly and iteratively **(Figure 3-8A I**). Polymers may also interact with multiple clusters (**Figure 3-8A II**), however, given this preferred binding

mode, there are still likely unsatisfied aspartate ligands or aspartate ligands that are not engaged with receptors because of the architecture of the chemotaxis array and the geometric constraint and tethered nature of the aspartate ligands on the polymer backbone. In contrast, free aspartate ligands are able to bind to many receptors deactivating many clusters over their lifetime (**Figure 3-8A III**). In a mixed receptor system (**Figure 3-8B**), trapping may be less prevalent given the natural distribution of receptor molecules throughout the array (**Figure 3-8B I-II**). However, binding to all available aspartates may again not be geometrically favored placing such ligands at a disadvantage to the freedom contained in their monovalent counterparts (**Figure 3-8B III**). For these reasons, future studies with these polymers should also be explored in mixed- or wild-type like arrays to reduce the likelihood of potential trapping

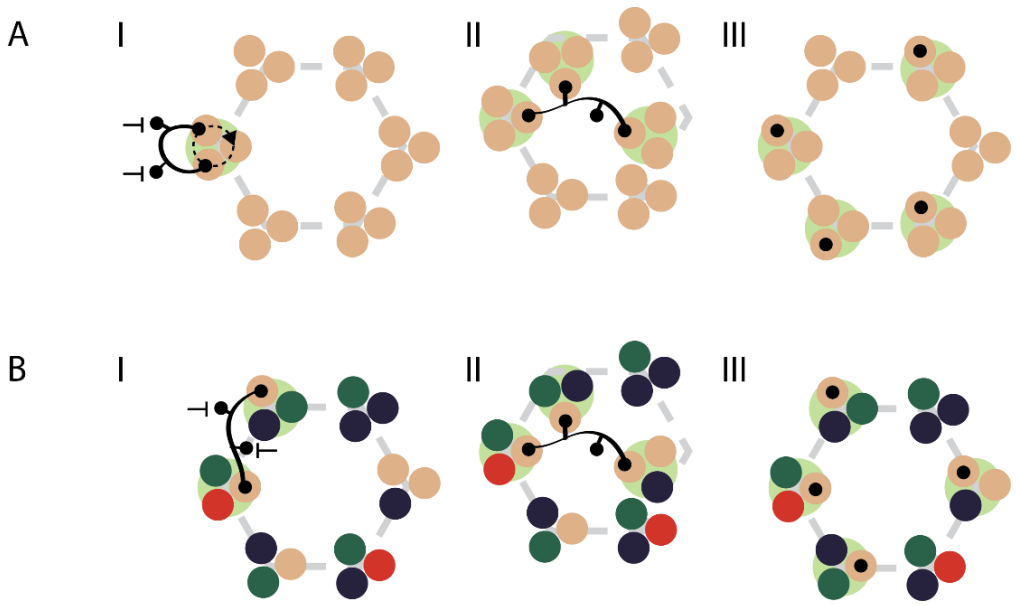

Figure 3-8. Schematic of homo- and heterogeneous chemotaxis array and ligand binding modes (A) homogeneous chemotaxis array with (I) chelate effect (II) receptor clustering and (III) monovalent binding. (B) heterogeneous chemotaxis array with (I) chelate effect (II) receptor clustering and (III) monovalent binding. Colors represent receptors with different ligand specificities. Blunt arrows highlight unbound ligands. Green circles indicated activated clusters.

of polymers. We would have anticipated that the interface mutant strains (UU2869/2879) should have benefited most from the possibility of length dependent enhancement of signaling based on the hypothetical ability of chemoattractant polymers to re-cluster the arrays. However, this was not observed. This result would only be expected if the encoded CheW mutations resulted in diffuse but intact receptor clusters. The array architecture of these interface mutant strains has not been characterized as of yet. Another complication highlighted above is that we do not know if all aspartates on a polymer can be bound. Any loss in binding would reduce the total number of clusters activated on a per aspartate basis. Exploring the effect of PEG linker length on signaling could circumvent this issue by extending these residues further from the polymer backbone thereby reducing self-sequestration and facilitating farther access to regions of the array.

In case trapping of the polymers at a single cluster is a significant complication, the data were further analyzed by normalizing the responses on a per molecule basis using the responses from UU2700. Analysis done in this way demonstrates an enhancement of the polymers over aspartate (10-fold; $K_{1/2}$ = 0.09 μM) or the monovalent aspartate derivative (20-fold; $K_{1/2}$ = 0.22 μM) alone and a 2-fold length dependent response of the polymers ($K_{1/2}$; 11-mer = 0.02 μM, 29-mer = 0.01 μM, 54-mer = 0.01 μM) (**Table 3-6**). This result inherently highlights that the responses are dependent on a strong understanding of concentration and the mechanism of ligand binding. *In vivo* FRET measurements are a population-based measurement and polymers must traverse the outer-membrane in *E. coli* to access the ligand binding domains of the transmembrane chemoreceptors which are positioned in the periplasm. Therefore, any reduction in the periplasmic availability of the polymeric ligand would reduce the effective

concentration and diminish our ability to detect receptor activation. Therefore, methods that analyze single cells or concentration independent studies should be prioritized.

Table 3-6. Dose-response $K_{1/2}$ values and Hill coefficients of aspartate in WT-all Tar strain UU2700 by concentration

	UU2700^{R+B+} [aspartate]		UU2700^{R+B+} [chemoeffector]	
	$K_{1/2}$ (μm)	Hill coeff.	$K_{1/2}$ (μm)	Hill coeff.
L-aspartate **3-2**	0.10	1.3 ± 0.3	0.10	1.3 ± 0.3
monovalent aspartate **3-31**	0.23	2.8 ± 0.5	0.23	2.6 ± 0.5
aspartate 11-mer **3-37a**	0.11	4.4 ± 0.8	0.02	4.4 ± 0.8
aspartate 29-mer **3-37b**	0.15	2.4 ± 0.2	0.01	2.4 ± 0.2
aspartate 54-mer **3-37c**	0.20	2.6 ± 0.2	0.01	2.6 ± 0.2

± SEM

Recently, elegant cell tracking algorithms have been developed that can analyze single cell swimming phenotypes. Such computational systems can bin cell behavior and monitor changes in these subpopulations in response to ligand addition (304). This would provide a readout on the fractional changes of behavioral phenotypes in response to different ligands. HOMO-FRET methods can monitor the orientation of receptors within the array using anisotropy changes of YFP-labeled receptors (296). Such experiments are performed at saturation conditions and are therefore not as sensitive to concentration. Results from these types of experiments have revealed stimulus-induced receptor dynamics. Use of polymers in these systems could reveal how multivalent ligands interact with the array and whether polymers can induce reorganization of the chemotaxis arrays. Another type of imaging that could be advantageous would be array analysis by electron cryo-tomography (ECT). Synthesis of the polymeric chemoattractant backbone could be modified to include a reporter group (e.g., a fluorophore or colloidal gold conjugate) that would be recognized in ECT to guide image

acquisition. This method would facilitate direct visualization of chemoreceptors that are ligand bound, and the reporter moiety would serve as a beacon to direct image acquisition (266).

3.3.8 Ligand Stability

In initial studies, we observed time-dependent response fluctuations with the synthesized aspartate compounds. We observed that L-aspartate **3-2** and L-aspartate-α-methylester **3-15** solution potency remained stable. However, time-dependent enhancement was observed for synthetic compounds L-aspartate-α-ester-PEG_3-azide **3-31** and polymers **3-37a-c**. Over the course of a single experiment (2 hours), the sensitivity of compound **3-31** shifted to lower $K_{1/2}$ values. This behavior was not observed for the control compound aspartate **3-2** or L-aspartate-α-methylester **3-15**. Compounds **3-2** and **3-15** were suspended directly into motility buffer to prepare stock and test solutions. Stocks of compounds **3-31** and **3-37a-c** were provided in DMSO. The potencies of **3-31** and **3-37a-c** change upon storage in buffer at room temperature, achieving maximum potency after 48 hours of mixing. Therefore, we, considered that the variability of results, uniformity of the chemotactic responses, and the observed sensitivity could have been the result of aspartate ligand decomposition to free aspartate or the result of slow compound hydration from DMSO. If hydrolysis is a component of the signal generation we have measured, earlier observations that the α-amide linked compound was not able to elicit chemotaxis could, therefore, be due to the increased hydrolytic stability of the amide. We would anticipate that even a low-level hydrolysis of 1-10% would significantly impact the resultant FRET signals, especially for adaptation deficient strains, which function as a two-state on/off system. 10% hydrolysis for a 20 μM test pulse of compound would result in 2 μM free aspartate which is above the expected $K_{1/2}$ for saturation. The inconsistency of the results

observed here for each compound ($K_{1/2}$ for **3-15** and its subsequent derivatives has been measured as 30 μM (**Table 3-3**), **3-27** 89 μM (Table **3-4**) and **3-31** 0.5 μM (**Table 3-5**). While results were initially encouraging due to the expectation of reduced but not abrogated signaling, we can not at this time rule out that they may have been the result of variation in hydrolysis extent and sample handling. Therefore, analyses should be undertaken to examine L-aspartate-α-ester stability in detail. Alternatively, other compounds that were identified in the aspartate screen that would not be prone to hydrolysis should be pursued such as the α-carbon derivatize or given the potency of asparagine, an amide linked PEG may be tolerated at the β carboxylic acid.

3.4 Conclusions

Previous results using fluorescently labeled multivalent chemotaxis ligands revealed localized chemoreceptor puncta by fluorescent microscopy in a diverse panel of chemotactic bacteria (315). These results suggested early on in chemotaxis array structure studies that chemoreceptors were localized into conserved and organized signaling systems. Signaling studies using multivalent chemoeffectors demonstrated that signaling within the chemotaxis array was integrated and that receptors performed inter-receptor communication with regards to signal output (209). Since this time powerful and sensitive techniques to interrogate chemotaxis have been advanced. This includes the ability to image chemotaxis arrays and reveal the organization of individual receptor dimers into hexagonal units by cryo-electron tomography (195, 266). Automated single-cell tracking algorithms are now available that can follow and calculate the trajectories of hundreds of cells providing statistical rigor to chemotaxis based swimming assays (304). FRET-based techniques can examine the kinase

activity and dynamics of chemotactic cells in response to ligands (314). As well as, changes in receptor orientation in response to chemotaxis ligands (296). Using these techniques, there is now a more complete picture of chemotaxis including precise and conserved geometric organization of the chemoreceptors and an understanding of how signals and noise are integrated into sensory outputs. A functional and mesoscale understanding of how array architecture, ligand binding, and signal propagation achieve chemotactic behavior are still emerging (296, 299, 300, 316). Here, we validated aspartate derivatives that can activate the chemotaxis pathway and developed a polymerizable aspartate ligand that activates chemotaxis through the receptor Tar. This tool is now poised to examine how chemotaxis signaling is altered in response to mono- or multivalent ligands. As well as, whether different polymer lengths can manipulate receptor spacing by reclustering bound chemoreceptors and how array architectural aberrations effect signaling. The ability to exogenously control chemotactic signaling could form the basis for anti-virulence strategies against pathogenic chemotactic bacteria. Such strategies have been developed that exploit quorum sensing (199) and have begun to explore chemotaxis as well (201). Our synthetic strategy toward chemotaxis ligands is modular and can be used to incorporate a wide repertoire of assay-specific reporter groups. This includes polymers that contain fluorescent reporters or dense metal reporters for correlative electron microscopy techniques which would facilitate examination of potential polymer clustering effects on receptors.

3.5 Experimental

3.5.1 Bacterial Strains

Strains used in this work are listed in **Table 3-7**.

Table 3-7. Bacterial Strains

Strain	Properties	Reference
UU2567	FRET reporter strain (R− B−) derivatives of *E. coli* K-12 strain RP437; [Δ(tar-cheZ)4211Δ(tsr)-5547 Δ(aer)-1 Δtrg-4543]	(317)
UU2700	FRET reporter strain (R+ B+) derivatives of *E. coli* K-12 strain RP437; [Δ(CheY-cheZ)1215 Δ(tar-tap)4530 Δtsr-5547 Δaer-1 Δtrg-4543]	(317)
UU2869	Similar to UU2567 but also containing CheW-X3 mutation	(265)
UU2870	Similar to UU2700 but also containing CheW-X3, a CheW variant with amino acid replacements at three positions: CheW-R117D/E121R/ F122S	(265)
Rp437	Parent strain, wt for chemotaxis; *thr-1leuB6 his-4 metF59 eda-50 rpsL136*	(264)
RP437 + dtomato	Parent strain, wt for chemotaxis; *thr-1leuB6 his-4 metF59 eda-50 rpsL136*	This work

3.5.2 Plasmids

Plasmids in this work used are listed in **Table 3-8**.

Table 3-8. Plasmids

Plasmid	Properties	Reference
Ppa114	Relative of pKG116 that carries wild-type tsr(QEQEE) under salicylate control	(268)
Pvs88	CheY-YFP and CheZ-CFP fusion proteins under IPTG control	(318)
Plc113	Relative of pACYC184 and pKMY297 that carries wild-type tar(QEQEE) under salicylate control	(268)

Ppa912	Relative of pACYC184 and pKMY297 that carries wild-type tar(QEQEE) under salicylate control; repaired G83S mutation.	
p67T1	Constitutively expressed dtomato fluorescent protein	(319)

3.5.3 Synthetic Materials and Methods

Commercially available library: Serine and aspartate compounds used in **section 3.3.2** were purchased from Sigma Aldrich and Chem Impex International without further purification.

Synthetic compounds: The protected aspartates, α-*tert*-Butyl-*N*-Boc-L-aspartate, Boc-L-aspartic acid 4-*tert*-butyl ester, used to generate PEG-derivatized aspartates were purchased from Sigma Aldrich. PEG linkers, HO-PEG_3-Ome, H2N-PEG_3-Az, and HO-PEG_3-Az, were purchased from Broadpharm. The ruthenium catalyst **3-33** and norbornene monomer **3-32** were synthesized as previously described (309, 313).

Characterization of synthetic compounds: ^1H and ^{13}C nuclear magnetic resonance (NMR) spectra were recorded on a Bruker AC+ 300a, Varian MercuryPlus 300, or Varian UNITY 500 spectrometer. Polymer NMR spectra were acquired using polymer samples in DMSO-matched NMR Microtubes (Shigemi, Inc). Chemical shifts were reported relative to trimethylsilane or residual solvent peaks in parts per million ($CHCl_3$: ^1H NMR δ 7.26, ^{13}C NMR δ 77.0; DMSO-d_6: ^1H NMR δ 2.50). Peak multiplicity is reported as singlet (s), doublet (d) doublet of doublets (dd), triplet (t), doublet of triplets (dt), etc. The degree of polymerization (DP) was determined based on the integration of the terminal phenyl protons relative to polymer backbone alkene protons. The mole fraction of conjugated aspartate ligand was determined based on the integration of the triazole protons. High-resolution electrospray ionization mass spectra (HR-MS) were obtained on a Micromass LCT (electrospray ionization, time-of-flight analyzer).

3.5.4 Synthetic Procedures

Aspartate Ligands

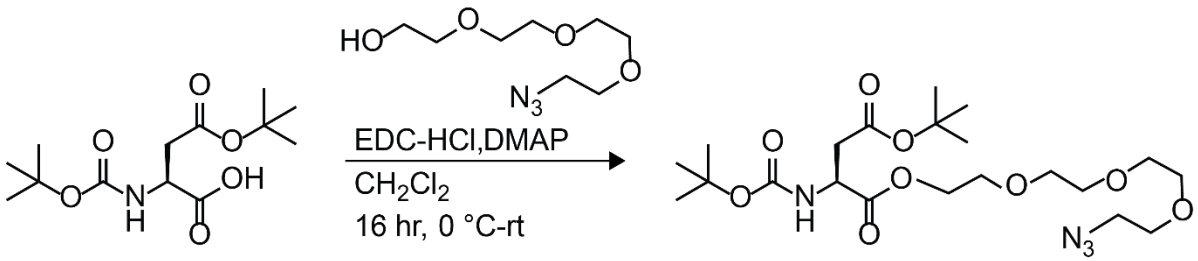

3-30

A commercially available aspartate bearing tert-Butyloxycarbonyl (BOC) protecting group at the beta- carboxylic acid (113 mg, 0.39 mmol, 1 eq) was coupled via 1-Ethyl-3-(3-dimethylaminopropyl)carbodiimide (90 mg, 0.47 mmol, 1.2 eq) to an N_3-PEG_4-alcohol (94 mg, 0.43 mmol, 1.1 eq). N_3-PEG_4-alcohol was transferred into a 10 mL flame dried round bottom flask using a syringe in 2.5 mL dry CH_2Cl_2. Next, the protected aspartate and DMAP (4.76 mg, 0.04 mmol, 0.1 eq) were added and the mixture was cooled to 0 °C. EDCI-HCl was added and the entire mixture was stirred at 0 °C for 2 h then overnight at rt for 16 h total. The final reaction mixture was concentrated *in vacuo*. Compound **3-30** was purified by column chromatography (SiO_2, 0-2% MeOH:CH_2Cl_2 in 0.5% increments). Correct fractions were combined and diluted with water and lyophilized and assessed by NMR (90% yield).

A similar procedure was used to generate the protected forms of compounds **3-27**, **3-28** and **3-29**.

Monovalent Aspartate Ligand

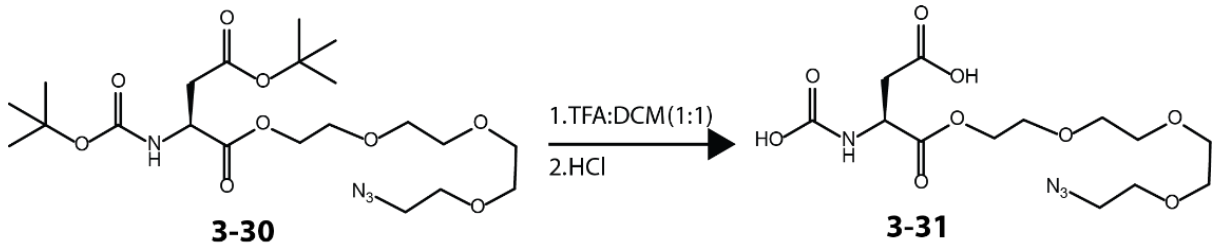

3-30 **3-31**

Compound **3-30** was stirred for 3 h at rt in 1:1 TFA:DCM (2 mL). TFA and DCM were removed by rotary evaporation and further evaporated in vacuo, then finally taken up in 5 mL HCl (pH = 3) and concentrated by lyophilization to generate **3-31**. NMR spectroscopy in DMSO-d_6 was used to confirm deprotection. Polymer stocks were prepared in DMSO (1 M) and used for subsequent experiments.

A similar procedure was used to generate the deprotected forms of compounds **3-27**, **3-28** and **3-29**.

3-27: Selected ^{1}H NMR (500 MHz, MeOD) δ (ppm): 4.4-4.35 (m, 3 H), 3.74 (t, 2 H), 3.64 (m, 10 H), 3.55 (t, 2 H), 3.36 (s, 3 H) , 3.04-3.02 (dd, 2 H, J = 3.03).

Selected ^{13}C NMR (126 MHz, MeOD) δ (ppm): 172.53, 169.36, 72.94, 71.55, 71.52, 71.49, 71.44, 71.28, 69.56, 66.68, 59.07, 50.57, 34.68.

3-28: Selected ^{1}H NMR (500 MHz, MeOD) δ (ppm): 4.38-4.30 (m, 3H), 3.73-3.71 (dt, 2 H, J = 3.73), 3.67-3.63 (m, 10 H), 3.56-3.54 (dt, 2 H, J = 3.55), 3.32-3.30 (m, 3H), 3.07-3.06 (d, 2 H, J = 3.07)

Selected ^{13}C NMR (126 MHz, MeOD) δ (ppm): 170.50, 170.47, 72.81, 71.47, 71.45, 71.36, 71.24, 69.64, 65.36, 59.06, 50.61, 35.29.

3-29: Selected ^{1}H NMR (400 MHz, MeOD) δ (ppm): 4.2-4.1 (dd, 1 H, J = 4.16 MHz), 3.70-3.65 (m, 8 H), 3.64-3.60 (d, 2 H, J = 3.63 MHz), 3.58-3.55 (t, 2 H, J = 3.57 MHz), 3.49-3.36 (m, 4 H), 2.98-2.80 (m, 2 H).

Selected ^{13}C NMR (126 MHz, MeOD) δ (ppm): 172.82, 169.21, 71.67, 71.58, 71.50, 71.25, 71.10, 70.19, 51.77, 51.13, 40.72, 36.19.

3-30: Selected ^{1}H NMR (400 MHz, MeOD) δ (ppm): 5.45 (d, 1 H, J = 5.45), 5.54 (m, 1 H), 4.34-4.25 (m, 2 H, J = 4.30), 3.70-3.64 (m, 12 H), 3.4-3.38 (t, 2 H, J = 3.39), 2.90-2.86 (dd, 1H, J = 2.88), 2.75-2.71, (dd, 2 H, J = 2.73), 1.44 (d, 18 H, J = 1.44)

Selected ^{13}C NMR (126 MHz, MeOD) δ (ppm): 171.42, 170.15, 155.53, 81.74, 80.10, 70.85, 70.82, 70.77, 70.20, 69.01, 64.77, 50.82, 50.32, 38.16, 28.46, 28.17.

3-31: Selected ^{1}H NMR (400 MHz, MeOD) δ (ppm): = 4.46-4.37 (m, 3 H), 3.78-3.76 (dt, 2 H, J = 3.77), 3.68-3.67 (d, 10 H, J = 3.68), 3.41-3.39 (dt, 2 H, J = 3.4), 3.07-3.04 (dd, 2 H, J = 3.05).

Selected ^{13}C NMR (126 MHz, MeOD) δ (ppm): 172.52, 169.38, 71.62, 71.60, 69.61, 66.72, 51.78, 50.55, 34.70.

Aspartate-Substituted Polymers

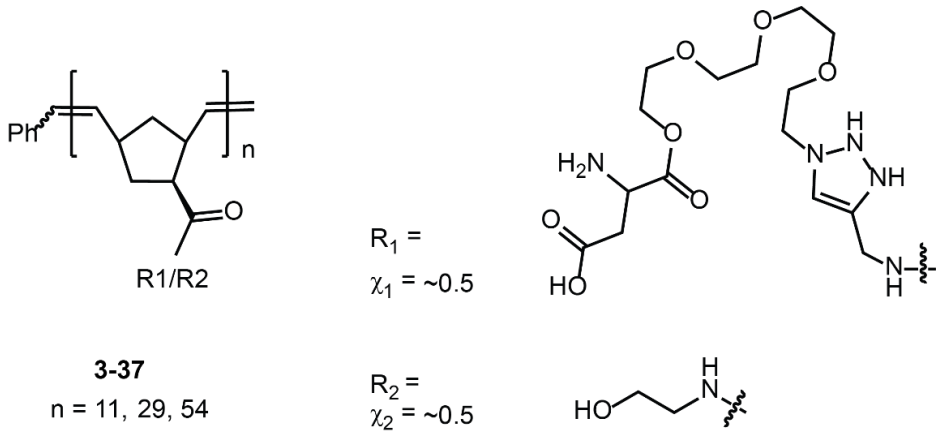

General procedure for the functionalization of aspartate substituted polymers: To an Eppendorf tube was added succinimidyl ester-substituted polymer **3-34a** (n = 11) (12.31 mg, 4.46 µmol, 1 eq), DMSO (1.2 mL), propargylamine (1.57 µL, 24.56 µmol, 5.5 eq) and N-methylmorpholine (27 µL, 245 µmol, 55 eq). The tube was capped and place on a mechanical rotator to mix for 16 h. Ethanolamine (7.41 µL, 122.8 µmol, 27.5 eq) was added and allowed to mix for 16 h. The polymer mixture was added to a 2k MWCO dialysis cassette and dialyzed into H_2O for 24 h. The sample was concentrated by lyophilization to generate **3-35a**.

Compound **3-30** was resuspended in DCM (100 mg/mL), TBTA was resuspended in DCM (0.06 M), sodium ascorbate was resuspended in water (0.1 M) and $CuSO_4$ was resuspended in water (0.1 M). Next, to an Eppendorf tube **3-35a** was added (12.5 mg, 12.2 µmol, 1 eq), compound **3-30** (711 µL, 144.8 µmol, 5 eq) and TBTA (255 µL, 14.5 µmol, 0.5 eq). This mixture was then placed on the rotovap to remove the DCM. Next, 1.9 mL of 1:1 tBuOH was added along with sodium ascorbate (145 µL, 14.5 µmol, 0.5 eq) and $CuSO_4$ (72 µL, 14.5 µmol, 0.5 eq) and stirred vigorously overnight at rt. The tBuOH was removed by rotary evaporation, and the remaining compound

was resuspended in 50:50 DMSO:water and purified over a PD10 column and eluted into water. The sample was concentrated by lyophilization to generate **3-36a**. Compound **3-36a** was stirred for 3 h at rt in 1:1 TFA:DCM (2 mL). TFA and DCM were removed by rotary evaporation and further evaporated in vacuo, then finally taken up in 5 mL HCl (pH = 3) and concentrated by lyophilization to generate **3-37a**. NMR spectroscopy in DMSO-d6 was used to determine the percent substitution. Polymer stocks were prepared in DMSO (10 mM) and used for subsequent experiments.

A similar procedure was used to prepare polymers **3-37b** and **3-37c**. Dialysis for these polymers was performed with 3.5k and 10k MWCO dialysis cassette.

Succinimidyl ester-substituted polymer (**3-34a**). Selected ^{1}H NMR (500 MHz, DMSO-d_6) δ (ppm): 7.40-7.20 (m, 5 H, phenyl), 5.70-5.10 (m, 22 H, alkene).

Succinimidyl ester-substituted polymer (**3-34b**). Selected ^{1}H NMR (500 MHz, DMSO-d_6) δ (ppm): 7.40-7.20 (m, 5 H, phenyl), 5.70-5.10 (m, 58 H, alkene).

Succinimidyl ester-substituted polymer (**3-34c**). Selected ^{1}H NMR (500 MHz, DMSO-d_6) δ (ppm): 7.40-7.20 (m, 5 H, phenyl), 5.70-5.10 (m, 109 H, alkene).

Aspartate α-ester-substituted polymer (**3-37a**). Selected ^{1}H NMR (500 MHz, DMSO-d_6) δ (ppm): 7.40-7.20 (m, 0.56 H, phenyl), 5.40-5.00 (d, 2 H, alkene), 7.80 (s, 0.45, triazole).

Aspartate α-ester-substituted polymer (**3-37b**). Selected ^{1}H NMR (500 MHz, DMSO-d_6) δ (ppm): 7.40-7.20 (m, 0.18 H, phenyl), 5.40-5.00 (d, 2 H, alkene) , 7.80 (s, 0.49, triazole).

Aspartate α-ester-substituted polymer (**3-37c**). Selected ^{1}H NMR (500 MHz, DMSO-d_6) δ (ppm): 7.40-7.20 (m, 0.12 H, phenyl), 5.40-5.00 (d, 2 H, alkene) , 7.80 (s, 0.35, triazole)

3.5.5 *In vivo* FRET Kinase Assays

The assay protocol and data analysis followed the procedures previously described in detail (297, 318, 320). Briefly, FRET signals were collected from cells expressing the reporter pair CheY-YFP and CheZ-CFP from plasmid pRZ30 and Tsr receptors from plasmid pCS53. FRET data were processed and fitted to a multisite Hill equation using KaleidaGraph 4.5 software (Synergy Software) or Prism Graphpad to obtain $K_{1/2}$ and Hill coefficient values. Absolute kinase activities were calculated from the FRET change to a saturating attractant stimulus and/or to 3 mM KCN.

3.5.6 Microfluidic Chemotaxis Assay

The assay was performed as described (303). Briefly, 1 µL of solutions of each compound were added to each source chamber and allowed to dry. After drying, the PDMS layer was inverted onto a plastic slide to seal the microfluidic channels. Fully assembled devices were placed in a vacuum for 90 min to reduce the amount of gas dissolved in the PDMS. A 120 µL drop of a dilute bacterial suspension (~ OD_{600} = 0.04) was placed over the central inlet and drawn in by the microfluidic device (~20 min). After filling, the central inlet of the device was capped with mineral oil. Fluorescent protein expressing bacterial accumulation at the ends of the microfluidic channels were measured by epifluorescence microscopy. To quantify the chemotactic response, the integrated intensity of an attractant source (I_x) was divided by the integrated intensity of an empty source (I_0) to provide relative response values (I_x /I_0

3.6 Contributions

Dr. Nitasha Bennett and Miss Cassie Jarvis prepared and characterized the ruthenium catalyst and norbornene polymer backbones. Dr. Robert Brown synthesized, characterized and supervised all ligands in this chapter. Dr. Run-zhi Lai and the Parkinson research group

performed the *in vivo* FRET analysis. John Crooks performed the microfluidic device based screen.

3.7 Acknowledgements

Special thanks to Dr. Joseph Grim who helped with early phase serine polymers that are not presented here and did not work. I would also like to acknowledge Miss Cassie Jarvis for providing helpful comments.

Chapter 4

A Fluorogenic Probe for Real-Time Imaging of Mycobacterial Growth and Division

Portions of this work have been submitted for publication:

Hodges, H.L., Brown, R.B., Crooks, J.C., Weibel, D.B. and Kiessling, L.L. 2017. A Fluorogenic Probe for Imaging Mycobacterial Growth and Division.

4.1 Abstract

Control and manipulation of bacterial populations requires an understanding of the factors that govern growth, division, and antibiotic action. Fluorescent and chemically-reactive small molecule probes of cell envelope components can visualize these processes and are advancing our knowledge of cell envelope biosynthesis (e.g. peptidoglycan production). Still, fundamental gaps remain in our understanding of the spatial and temporal dynamics of cell wall assembly. Currently available probes require steps that limit their use to static imaging. Probes that can be used for real-time imaging would advance our understanding of cell envelope construction. To this end, we synthesized a fluorogenic probe that enables continuous live cell imaging in mycobacteria and related genera. Mycobacteria possess a distinctive and complex peptidoglycan anchored lipid-rich cell envelope that protects the cell from antibiotics and host defenses. The mycolic acid membrane, a bilayer-like assembly composed of mycobacterial fatty acids, is constructed exclusively by mycolyltransferases. Our probe, QTF (quencher-trehalose-fluorophore), is an analog of the natural donor substrate of these mycolyltransferases in Corynebacteriales. Fluorescence is unleashed upon QTF processing by mycolyltransferases. QTF enables high contrast continuous imaging and the visualization of mycolyltransferase activity in live cells. QTF revealed that mycolyltransferase activity is augmented prior to cell division and localized to the septa and cell poles, especially at the old pole. In analogy to previously observed intracellular divisomes and polar elongation complexes, our demonstration of mycolyltransferase localization provides impetus to explore biosynthetic assemblies on the cell's exterior. We anticipate QTF can be exploited to detect and monitor mycobacteria in physiologically relevant environments.

4.2 Introduction

The Corynebacterineae suborder includes human pathogens that cause devastating diseases, such as *Corynebacterium diphtheriae* and *Mycobacterium tuberculosis (Mtb).* These bacteria are distinguished from other prokaryotes by the unique composition of their cell envelope, whose major constituent is the peptidoglycan-anchored mycolyl-arabinogalactan (mAG) (**Figure 1-1A**). The mAG is assembled from an eclectic set of building blocks, including a branched polysaccharide constructed from galactofuranose and arabinofuranose anchored to the peptidoglycan. Appended to this heteropolysaccharide are long chain (up to C_{90}) α-branched, β-hydroxylated lipids, known as mycolic acids, arranged in a pseudobilayer orientation (321-323). This mycolic acid membrane forms the interface of the cell with its environment and in these bacteria, forms a protective hydrophobic layer that is a permeability barrier to antibiotics and facilitates survival in host environments (324). Bacteria with this shared cell wall architecture display diversity in growth rates, cell size, and patterns of elongation and division (325-327). Modulation of these features enables pathogens to evade antibiotics and host defenses (45, 328). The importance of cell elongation and division in antibiotic function, disease latency, and microbe survival highlights the need to understand mAG biosynthesis and maintenance in cell growth and division. Many of the enzymes that construct this physical barrier have been identified, but when, where, and how they function in live cells to construct and remodel the mAG is not known.

Fluorescent reporters that can visualize cell envelope biosynthetic enzymes or their products are providing insight into cell growth and division. For example, both protein and small molecule reporters have been used to reveal that peptidoglycan (PG) biosynthesis in

mycobacteria is asymmetric, with increased synthesis occurring at the older inherited pole. This growth mechanism has been invoked to explain the observation of drug-resistance in sub-populations of *Mtb* (45, 329). Additionally, cytosolic enzymes that mediate galactan and lipid II biosynthesis (i.e., the glycosyltransferases GlfT2 or MurG) have been demonstrated to localize to a subpolar region proximal to sites of newly emerging PG. The spatial localization of these

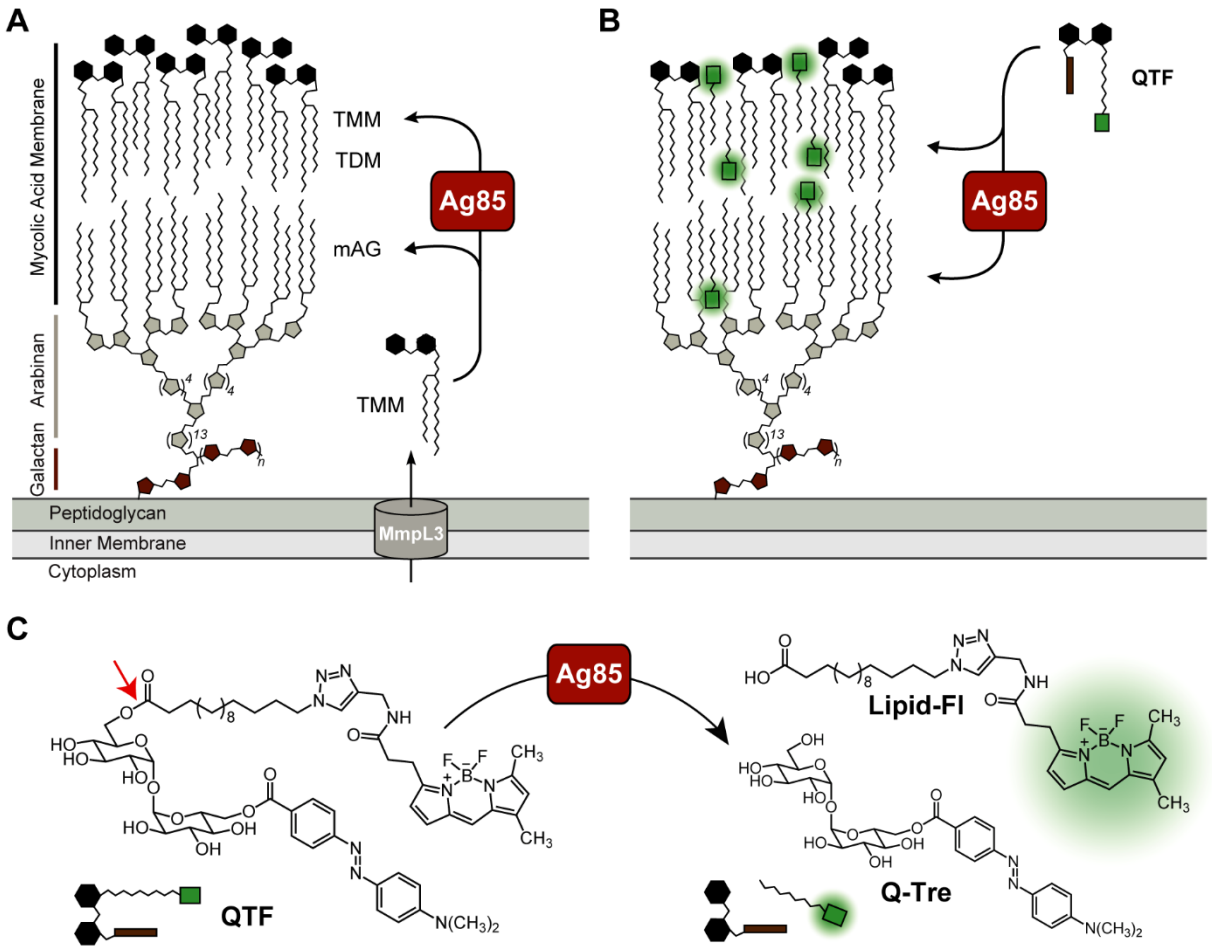

Figure 4-1. Features of QTF, a fluorogenic probe of Ag85-mediated cell wall biogenesis (A) Components of the corynebacterial cell envelope include the peptidoglycan-anchored mycolyl-arabinogalactan (mAG) complex. The mycolyltransferases, including the antigen 85 complex (Ag85) of *Mtb* construct the mycolic acid membrane by processing endogenous trehalose monomycolate (TMM) to afford TDM, mAG, TMM, or free mycolate. TMM is exported by the transporter MmpL3. (B) QTF is a TMM mimic bearing a fluorophore and quencher. QTF processing by mycolyltransferases generates a fluorescent signal. (C) Chemical structure of QTF and its products Q-Tre and Lipid-Fl generated by Ag85 cleavage.

intracellular enzymes has led to a model which suggests that they form a mycobacterial polar elongation complex (329, 330). In contrast, information is lacking regarding the activity and localization of extracellular enzymes responsible for mAG assembly and maintenance.

Several groups have used the metabolic incorporation of labeled trehalose derivatives to visualize the Corynebacterineae outer membrane (114, 331-334). These carbohydrate probes are processed through the action of trehalose metabolic proteins, including those that import trehalose as well as mycolyltransferases (114, 331-334). Mycolic acids originate in the cytoplasm, where they are synthesized, incorporated into trehalose monomycolate (TMM), and exported by a suite of proteins (**Figure 4-1A**) (335-340). On reaching the periplasm, TMM is processed by mycolyltransferases to construct the mycolic acid membrane. All bacteria known to generate a mycolate membrane produce multiple seemingly redundant mycolyltransferases (up to 11); *Mtb* possesses three active proteins, Ag85A–C (29). Mycolyltransferases carry out transesterification of TMM through an acyl-enzyme intermediate. This mycolyl-enzyme adduct persists until transfer to a mycolyl acceptor (e.g. trehalose, TMM or AG), a reaction that can afford three different products: the intercalated outer membrane glycolipid trehalose dimycolate (TDM), mycolylated cell wall arabinan (mAG), or TMM (**Figure 1-1A**). Trehalose analogs bearing fluorophores (331, 332) or possessing intermediary reactive handles (e.g., an azide or alkyne group) can be added to mycobacteria, where they are processed to generate fluorescent mycolic acids, TMM, TDM and mAG (114, 333, 334). Fluorescent or chemically reactive trehalose analogs are limited for real-time monitoring of bacterial growth. As with most small molecule probes of cell wall biosynthesis, fixing and washing steps are required because the trehalose analog precursor must be removed prior to visualization of the labeled

metabolic products. Probes that are processed by intracellular conversion pathways do not report on Ag85 activity directly. In all cases, due to the need for post-label processing, the information on the timing and location of mycolyltransferases activity is lost. As a result, fluorescent probes that report directly on mycolyltransferase activity during cell growth have been lacking.

To address this deficiency, we developed QTF (quencher-trehalose-fluorophore), a fluorogenic probe for imaging mycolyltransferase activity. QTF, an analog of the mycolyltransferase donor TMM, is hydrolyzed by mycolyltransferases to provide a real-time fluorescent readout of mycolyltransferase activity and mycolic acid membrane assembly (**Figure 4-1B-C**). Additionally, QTF specifically detects bacteria with mycolic acid membranes, even in mixed cultures. In studies of single cells of *Mycobacterium smegmatis*, we visualized cells dividing over several generations. Although mycolyltransferases are among the most abundantly secreted proteins in mycobacteria, our data reveal their activity is spatially and temporally localized.

4.3 Results

4.3.1 Fluorogenic Probe Design

To create a fluorogenic reporter of Ag85 activity, we modified the natural donor TMM with a fluorophore-quencher pair using the available structural data and postulated mycolyl transfer mechanism. Analysis of TMM structure reveals its key features: a trehalose disaccharide and two ester-linked mycolic acid chains comprised of a short α-chain and a longer β-chain (**Figure 4-2A**). The structure of Ag85B bound to trehalose determined by X-ray crystallography (PDB ID: 1F0P) indicates the 6'-hydroxyl of the disaccharide points out of the sugar binding pocket and

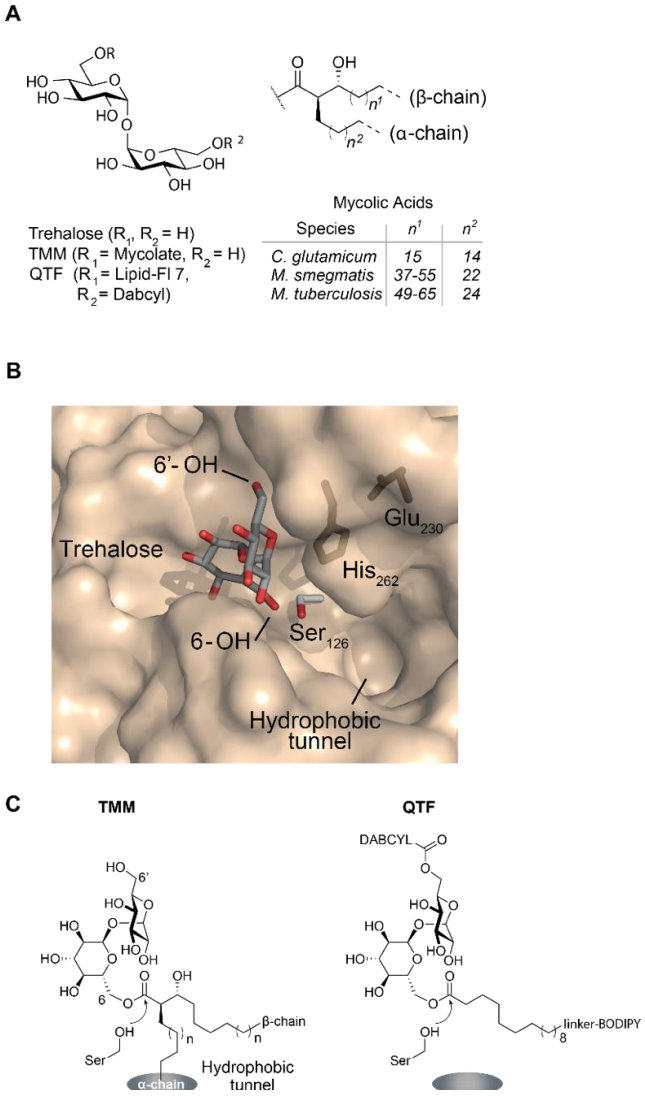

Figure 4-2. Design of fluorescence turn-on probe QTF (A) Structure of trehalose and trehalose glycolipids with average acyl chain lengths for various mycolic acid containing species. (B) Structure of the mycolyltransferase Ag85B active site showing the binding orientation of trehalose (PDB ID: 1F0P) (31). The trehalose 6-OH is proximal to the catalytic serine residue and postulated mycolate binding site, while the 6′-OH points toward the donor saccharide pocket. (C) Inferred binding orientation of mycolyl donor trehalose monomycolate (TMM) prior to enzymatic cleavage by Ag85. QTF is designed to mimic TMM binding with the DABCYL and BODIPY chromophores at the 6′-OH position and lipid terminus, respectively.

should tolerate chemical modification (**Figure 4-2B**) (331, 341). Similarly, TMM is thought to be oriented such that the shorter α-branch of the mycolic acid resides in a hydrophobic tunnel, while the longer β-chain is outside of the active site (**Figure 4-2C**). This binding mode suggested trehalose bearing a single modified lipid would orient that lipid analogously to the β-chain. We therefore reasoned that mycolyltransferases would process substrates bearing a range of non-natural lipids. Accordingly, we designed a reporter in which the hydrophobic fluorescent dye BODIPY-FL was appended to the terminus of a simplified lipid chain and the fluorescence quencher DABCYL linked to the 6'- hydroxyl through an ester (**Figure 1-2C**). DABCYL efficiently quenches the fluorescence emission of BODIPY-FL (342, 343). We anticipated that QTF would undergo processing analogous to that of TMM with nucleophilic attack by the catalytic serine residue. Formation of the fluorescent acyl-enzyme intermediate would result in the release of DABCYL-6'-trehalose, separating the FRET pair and triggering fluorescence emission (344-347).

We sought a fluorogenic probe that the mycolyltransferases would hydrolyze to avoid covalent cell envelope modification. A kinetic study using the synthetic substrate 6,6'-dihexanoyl trehalose revealed that Ag85 exhibits substantial acylhydrolase activity when acting on simple lipid linkages, orthogonal to its primary role as an acyltransferase (341). We therefore replaced the native α-branched, β-hydroxylated lipid head group of TMM with an unbranched lipid linkage in QTF, to allow the fluorescent acyl-enzyme intermediate to undergo hydrolysis rather than transfer to an *in vivo* mycolyl acceptor. The active site homology evident in the X-ray crystal structures of Ag85A-C and our own alignment of mycolyltransferase sequences (data not shown) suggests that the design of QTF should allow its broad utilization

by mycolyltransferases across genera (348-350). Thus, our modified mycolyltransferase substrate should avoid covalent modification of the cell wall with a non-natural lipid, minimize any perturbation of Ag85 function.

4.3.2 QTF properties

QTF and its predicted cleavage products were synthesized, and we characterized the photo physical properties of QTF and its predicted cleavage products (**Figure 4-3A**). We measured their relative fluorescence emission in aqueous buffer to assess the intramolecular quenching, and potential for fluorescence turn-on afforded by our probe design. An equimolar mixture of Q-Tre and Lipid-Fl show robust fluorescence at the expected wavelength for BODIPY (λ_{max} (ex) = 503 nm, λ_{max} (em) = 515 nm), whereas QTF is dark over the same region, displaying more than a 1500-fold reduction in relative fluorescence emission (**Figure 4-3B**). We calculated the quenching efficiency of QTF to be 99.9% between 10 nM – 10 µM (**Figure 4-3C**), indicating that the DABCYL chromophore is ideally positioned to facilitate effective intramolecular quenching of BODIPY fluorescence emission in QTF. Furthermore, QTF is freely soluble on dilution into aqueous buffer at all tested concentrations (up to 100 µM, 2 % DMSO), and is stable in solution for extended periods at elevated temperatures (**Figure 4-3D**). These observations together suggested that QTF possesses the necessary physical properties and intramolecular quenching efficiency for application as a fluorogenic probe.

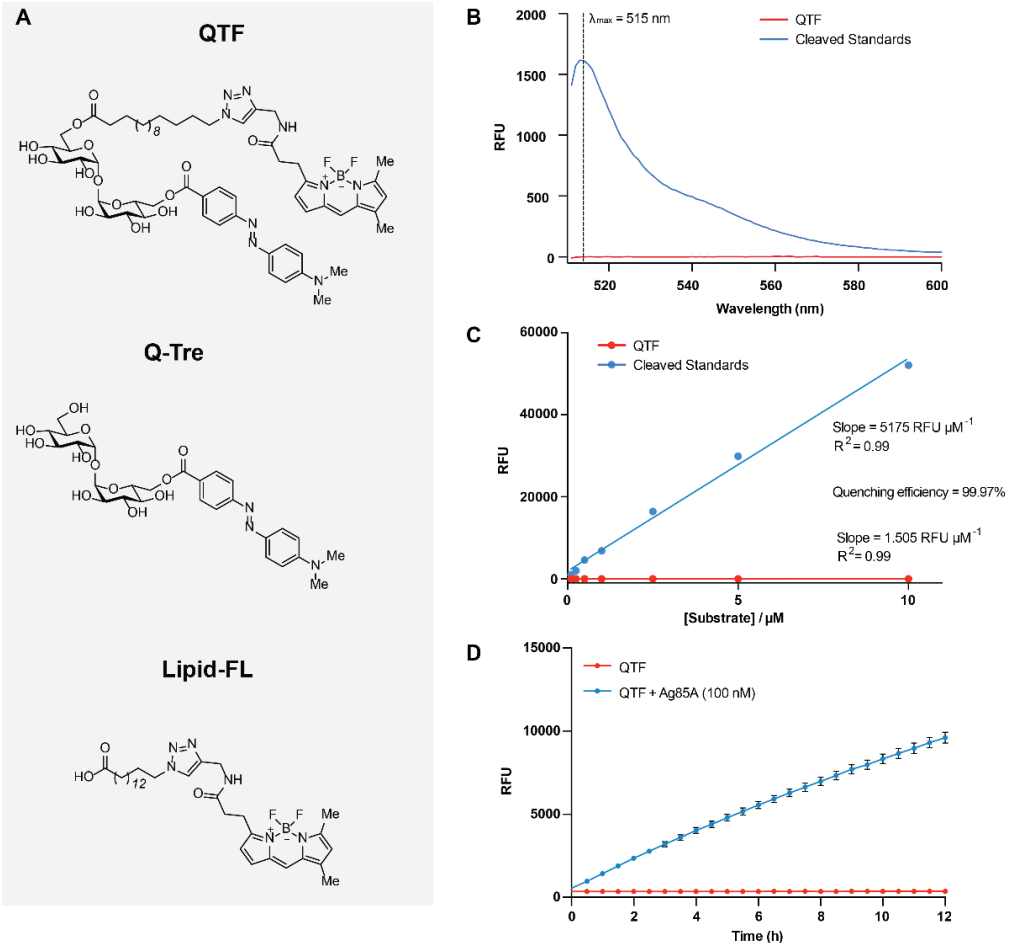

Figure 4-3. QTF properties (A) Structure of QTF and its predicted cleavage products. (B) Plot of fluorescence emission intensity versus wavelength for QTF (1 μM, red line) and an equimolar mixture of cleavage standards Q-Tre (1 μM) and Lipid-FL (1 μM) (blue line). The cleaved standard mixture is >1500-fold more fluorescent than the intact probe. (C) Plot of fluorescence emission intensity versus concentration for QTF (red line) and an equimolar mixture of the cleavage standards Q-Tre and Lipid-FL (blue line). Fluorescence increases linearly with concentration up to 10 μM in each case, and the ratio of slopes reveals that quenching is 99.97% efficient in intact QTF. (D) Plot of fluorescence emission intensity versus incubation time of QTF (1 μM, red line) for 12 h. No increase in fluorescence emission is observed, indicating spontaneous hydrolysis does not occur. For comparison, the blue line reflects the fluorescence emission generated during cleavage of QTF by Ag85A (100 nM) under otherwise identical conditions. In all figures, λ_{max} (ex) = 503 nm, λ_{max} (em) = 515 nm and aqueous NaH_2PO_4/Na_2HPO_4 buffer (20 mM, pH = 7.2) containing 2% DMSO at 37 °C.

4.3.3 QTF Processing by Mycolyltransferases

A robust increase in fluorescence occurred upon QTF exposure to Ag85A, Ag85B, or Ag8C (**Figure 4-4**, black bars), the three catalytically active mycolyltransferases of *Mtb*. This result reveals that QTF can be cleaved by all *Mtb* mycolyltransferases. QTF does not undergo spontaneous hydrolysis, as no change in fluorescence emission was observed after 20 h at 37 °C. Probe turnover without a mycolyl acceptor present to intercept the acyl-enzyme intermediate suggested that the mycolyltransferases cleaves QTF by hydrolysis. To test whether QTF processing is accelerated in the presence of a mycolyl acceptor, we assessed fluorescence upon mixing QTF, an Ag85 homolog, and trehalose (**Figure 4-4**, dark gray bars). Trehalose addition had no effect on turnover, further supporting a hydrolytic mechanism. To assess whether known Ag85 inhibitors block QTF turnover, we monitored fluorescence in the presence of tetrahydrolipstatin (THL) or ebselen. THL is a non-specific lipase inhibitor that covalently modifies catalytic serine residues, whereas ebselen is reported to disrupt the Ag85 catalytic triad through allosteric covalent modification of a non-

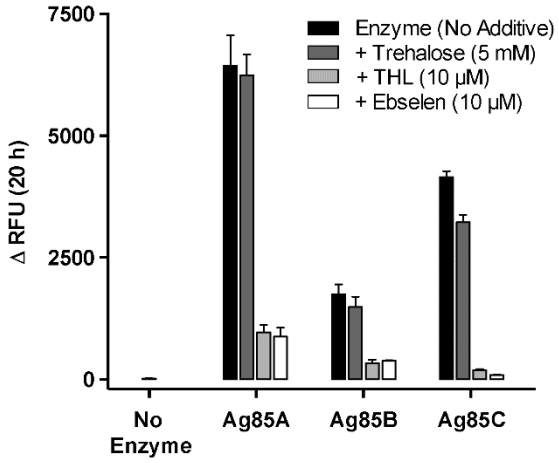

Figure 4-4. Fluorescence resulting from QTF exposure to the native Mtb mycolyltransferases Ag85A, Ag85B, and Ag85C. Fluorescence emission following incubation of QTF (1 μM) with purified *Mtb.* Ag85A, Ag85B or Ag85C (20 nM) for 20 h at 37 °C in 20 mM phosphate buffer (pH = 7.2) (black bars). Turnover was also assessed in the presence of a mycolyl acceptor (5 mM trehalose, dark gray bars) and generic mycolyltransferase inhibitors tetrahydrolipstatin (THL) (10 μM light gray) or ebselen (10 μM white). RFU = relative fluorescence units.

active site cysteine (351). Addition of either THL (**Figure 4-4**, pale gray bars) or ebselen (**Figure 4-4**, white bars) inhibited QTF processing, consistent with QTF hydrolysis mediated by the catalytic triad of Ag85.

We further examined mycolyltransferase processing of QTF by carrying out Michaelis-Menten analysis of initial reaction velocities (**Figure 4-5, Table 4-1**). The apparent K_m values for QTF (Ag85A = 107 ± 27 μM, Ag85B = 28 ± 3 μM, Ag85C = 44 ± 3 μM) are similar to the reported Michaelis constant for the natural mycolyl donor TMM (K_m = 130 μM) (352). Additionally, the apparent k_{cat} values reflect the relative activities measured by end-point analysis (**Figure 4-3**, **Figure 4-5**, **Table 4-1**). Specifically, Ag85A cleaves QTF more efficiently than Ag85C, while the activity of Ag85B is lower; these relative rankings are consistent with the known mycolyltransferase activities of these enzymes (353). Thus, the kinetic parameters of mycolyltransferase-catalyzed QTF hydrolysis are consistent with those observed for mycolyltransferase activity.

Table 4-1. Kinetic parameters for hydrolytic cleavage of QTF by purified native Ag85A, Ag85B and Ag85C from *M. tuberculosis*

Mtb Ag85 protein	K_M (app) (μM)	k_{cat} (app) (s^{-1})	k_{cat} (app) / K_M (app) (M^{-1} s^{-1})
A	107 ± 27	2.81×10^{-3}	26
B	28 ± 3	0.33×10^{-3}	12
C	44 ± 3	2.08×10^{-3}	48

Assay conditions: [Ag85] = 50 nM, [QTF] = 1–100 μM, 37 °C in 20 mM phosphate buffer (pH = 7.2)

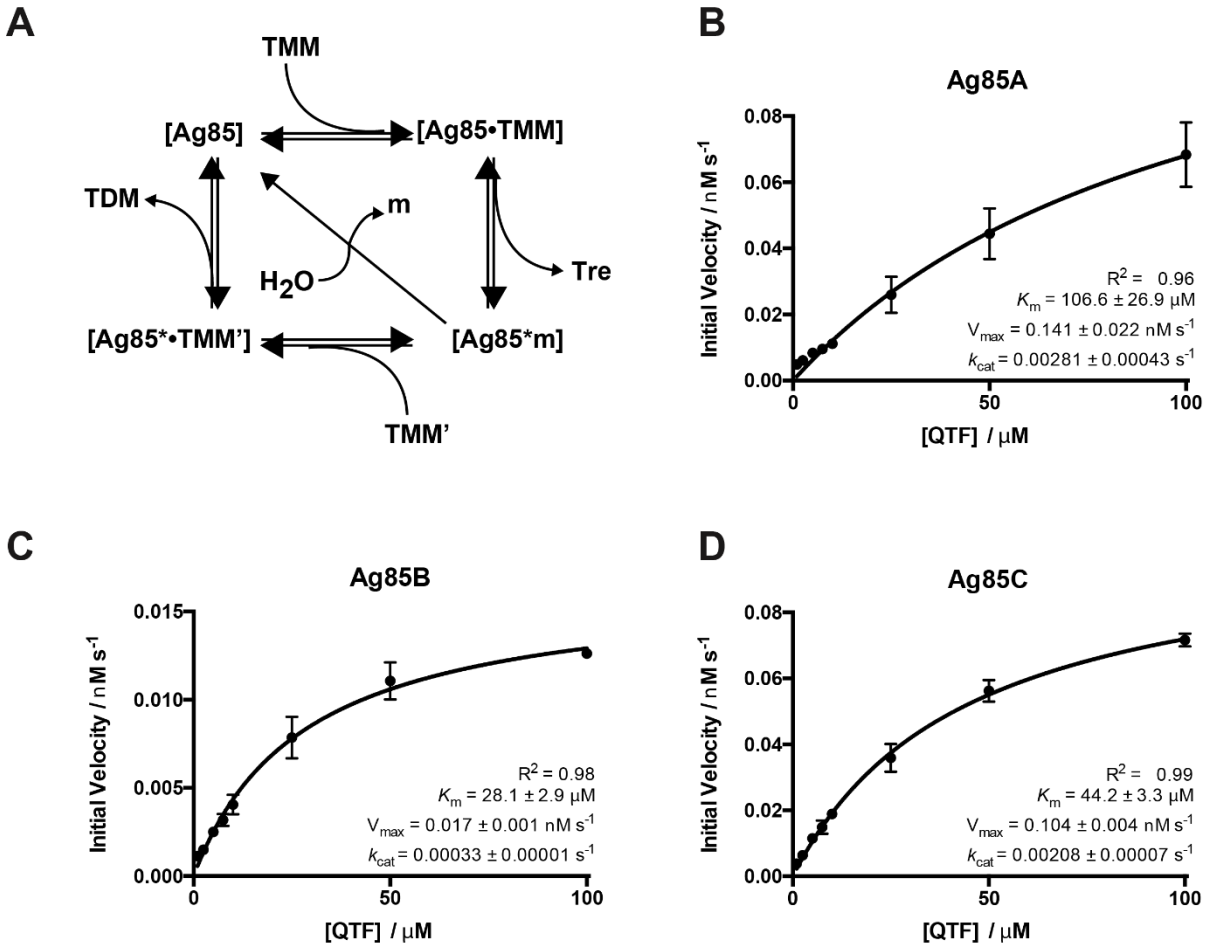

Figure 4-5. Kinetic analysis of QTF cleavage by *Mtb*. Ag85A–C (A) Ping-pong mechanism for mycolyltransferase activity including acyl hydrolase activity. Depicted for TDM formation via second acylation of a TMM substrate via TMM donor. Plots of initial reaction velocities against substrate concentration for cleavage of QTF by purified native Ag85A (B), Ag85B (C), and Ag85C (D) from *M. tuberculosis*. Fitting of the data to the Michaelis-Menten equation allowed K_m and k_{cat} to be determined for hydrolysis reaction (see **Table 4-1**). Error bars represent the standard error from three replicate experiments. Assay conditions: [Ag85] = 50 nM, [QTF] = 1–100 μM, in aqueous NaH_2PO_4/Na_2HPO_4 buffer (20 mM, pH = 7.2) containing 2% DMSO at 37 °C

4.3.4 QTF is Selectively Processed by Bacteria with Mycolic Acid Membranes

When two species that contain mycolyltransferases, *M. smegmatis* and *Corynebacterium glutamicum* were treated with QTF (1 μM), bacterial growth was unaffected (**Figure 4-6A)**, but changes in bulk fluorescence emission of more than 1000-fold were observed for each species

(**Figure 4-6B**). We compared the fluorescence resulting from these mycolyltransferase-producing organisms to *Escherichia coli* and *Bacillus subtilis*, as the latter two species serve as representative Gram-negative and Gram-positive species that lack Ag85 orthologs. When cells were cultured with QTF (1 μM) for 2 – 3 doubling times and then analyzed using flow cytometry (**Figure 4-7A**), both *M. smegmatis* and *C. glutamicum* became fluorescent. In contrast, *E. coli* and *B. subtilis* cells did not. When QTF-treated bacteria were visualized by confocal fluorescence microscopy (**Figure 4-7B)**, fluorescence was observed at the cell surface of *M. smegmatis* and *C. glutamicum*, but not *E. coli* or *B. subtilis*. Thus, QTF is a selective fluorogenic probe of mycolyltransferase-producing bacteria. To test whether QTF could be used to detect mycolyltransferase-containing organisms in a mixed cell culture, we added the probe to cultures of *B. subtilis*, *E. coli*, and *C. glutamicum* expressing cytoplasmic mCherry. The colocalization of QTF-derived fluorescence **(Figure 4-8A-B**), was observed only for *C. glutamicum*, the mycolyltransferase-producing species.

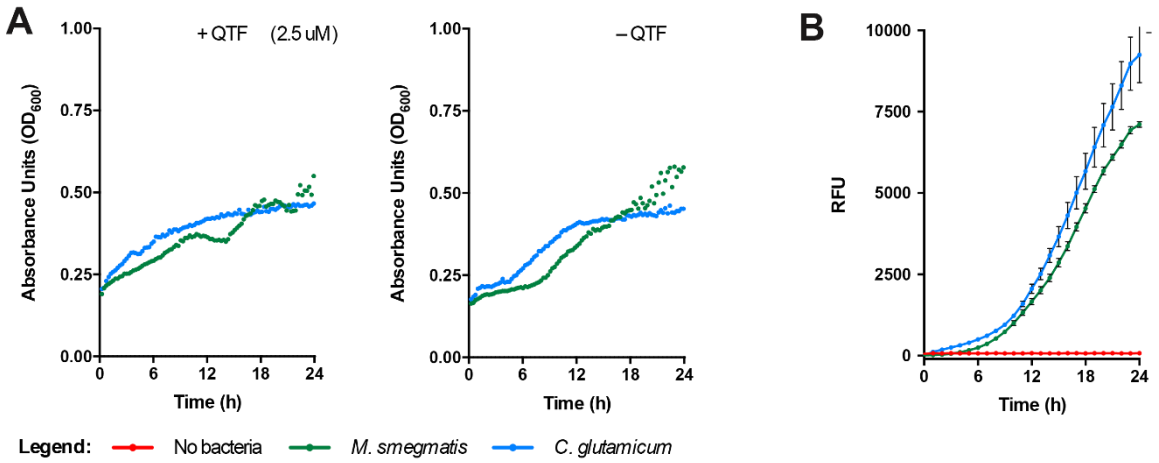

Figure 4-6. In culture growth of *M. smegmatis* and *C. glutamicum* with QTF (A) Plots of fluorescence emission intensity versus time for QTF (2.5 μM) incubated alone (red curve) or in the presence of *M. smegmatis* (green curve) or *C. glutamicum* (blue curve) bacteria. Growth of either bacteria triggers substantial increases in fluorescence. Plots of optical density versus time for the growth of *M. smegmatis* (green curve) or *C. glutamicum* (blue curve) in the

presence of QTF (2.5 µM), acquired through tandem OD_{600} absorbance measurement during the same experiment as fluorescence. (B) Growth of *M. smegmatis* (green curve) or *C. glutamicum* (blue curve) in the absence of QTF, under otherwise identical conditions as panel B, indicating QTF does not affect growth of either organism. Error bars depict the standard deviation from three replicate experiments. RFU = relative fluorescence units.

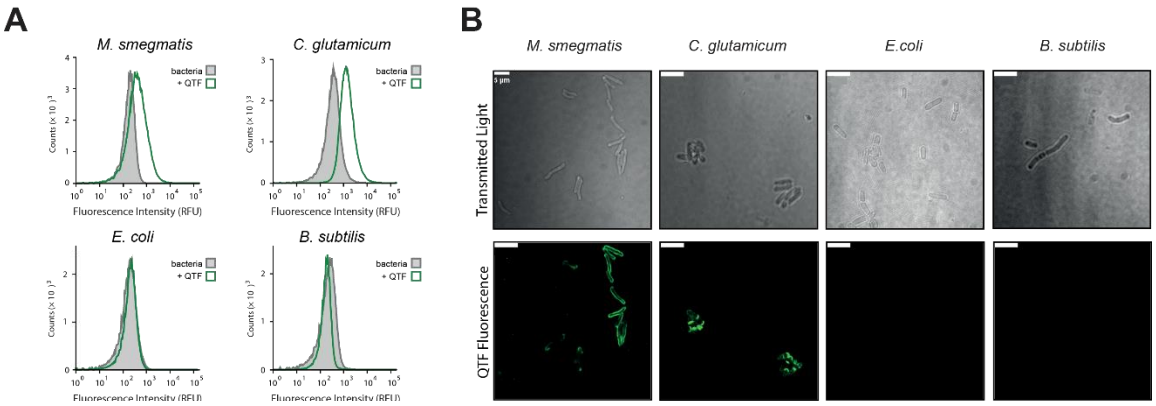

Figure 4-7. QTF processing by mycolyltransferases in live bacteria (A) Flow cytometry analysis of *M. smegmatis*, *C. glutamicum, E. coli and B. subtilis* with QTF. Cells were treated with QTF (1 µM) for 2-3 doubling times and plotted relative to untreated bacteria. Data are representative of two independent experiments. (B) Confocal fluorescence microscopy images of different bacterial species exposed to QTF (1 µM) prior to flow cytometry analysis. Scale: 5 µm.

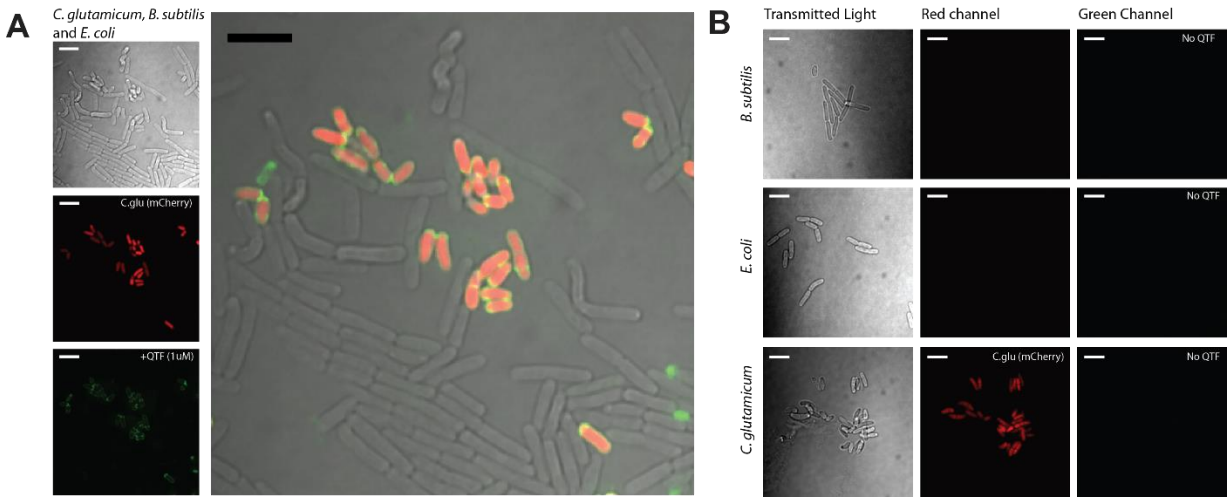

Figure 4-8. QTF selectively illuminates mycolic acid containing bacteria in mixed cultures (A) Confocal fluorescence microscopy of a mixed culture (*C. glutamicum* (red), *E. coli* and *B. subtilis)* exposed to QTF (1 µM). QTF labels mCherry-expressing *C. glutamicum* and not other bacteria that do not contain mycolic acids. scale bar: 5 µM. (B) Control images of *C.*

glutamicum, *E. coli* and *B. subtilis. C. glutamicum* is constuitively expressing mCherry and displays fluorescence in the red channel. No cells have fluorescence in the green channel. Scale bar: 5 μM.

4.3.5 QTF Processing in Live Cells

To confirm whether mycolyltransferases are responsible for QTF cleavage in live cells, we harvested culture filtrate protein (CFP) from *M. smegmatis*, which contain secreted Ag85 proteins and evaluated QTF processing (**Figure 4-9A-B**). Exposure of the CFP to QTF afforded large increases in fluorescence emission (**Figure 4-9A**). Treatment of *M. smegmatis* CFP with the Ag85 inhibitor ebselen reduced fluorescence by 63%. This reduction is consistent with mycolyltransferase-mediated probe turnover. The residual activity is likely due to inefficient inhibition of *M. smegmatis* mycolyltransferases by ebselen (332). To examine this possibility, we purified four *M. smegmatis* Ag85 homologs and measured their inhibition by ebselen (**Figure 4-9B-C**). These data indicate that ebselen is less potent against *M. smegmatis* mycolyltransferases (23 – 52% inhibition) than *M. tuberculosis* Ag85A–C (78 – 99% inhibition).

M. smegmatis CFP was subjected to analysis by non-denaturing PAGE (**Figure 4-10A**). Exposure of the gel to QTF followed by fluorescence imaging revealed only three fluorescent regions. Each band was excised and subjected to protein digest mass spectrometry analysis, which revealed the presence of at least one mycolyltransferase protein in each band (**Figure 4-10A**, **Table 4-2**). To determine the products of mycolyltransferase-catalyzed processing of QTF cleavage, the probe (100 μM) was incubated with *M. smegmatis* CFP and the resulting sample was analyzed by high-resolution MS. We detected intact QTF and its predicted cleavage standards Q-Tre and Lipid-FL (**Figure 4-10C**). No other cleavage products were detected. These

findings are consistent with thin-layer chromatography analysis of membrane extracts from whole cells treated with QTF, in which Lipid-FL was the only detectable fluorescent product recovered from *M. smegmatis* and *C. glutamicum* extracts (**Figure 4-10C**). These experiments establish QTF's selectivity for Ag85-containing organisms and that QTF is activated via mycolyltransferase-catalyzed hydrolysis in living cells.

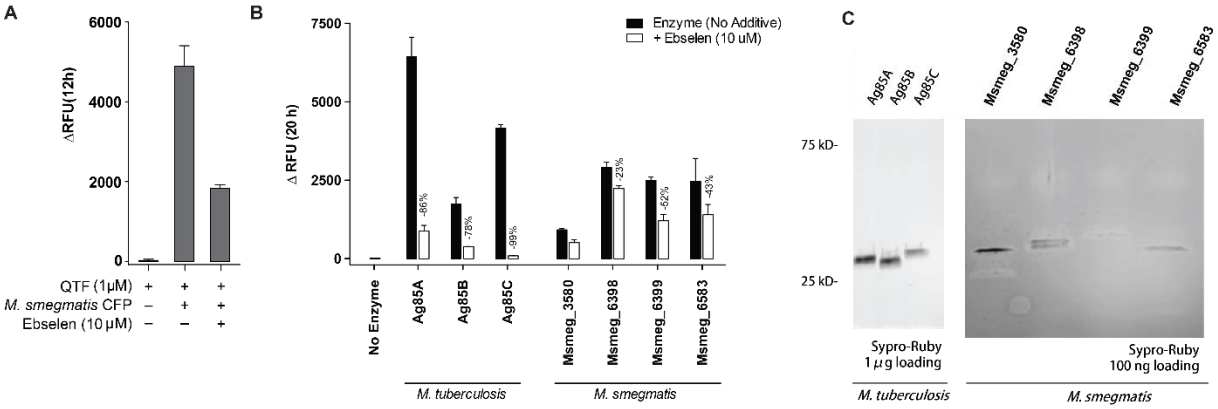

Figure 4-9. Ebselen reduces *M. smegmatis* mediated QTF turnover (A) Fluorescence emission from incubation of QTF (1 μM) with *M. smegmatis* culture filtrate protein (CFP) (200 ng). Probe turnover in the presence of ebselen (10 μM). (B) Relative increases in fluorescence emission following incubation of QTF (1 μM) with purified *M. tuberculosis* and *M. smegmatis* Ag85 proteins (20 nM). QTF is turned over by tested proteins (black bars) and inhibited following a 2 h pretreatment of each enzyme with 10 μM ebselen (white bars). Inhibition by ebselen was less effective for *M. smegmatis* proteins compared to *Mtb.* Ag85A–C. Percent reduction in QTF turnover is shown for each protein. RFU = relative fluorescence units. Standard deviation from three replicates is depicted. (C) SDS-PAGE gel demonstrating the purity of mycolyltransferases, stained with Sypro Ruby.

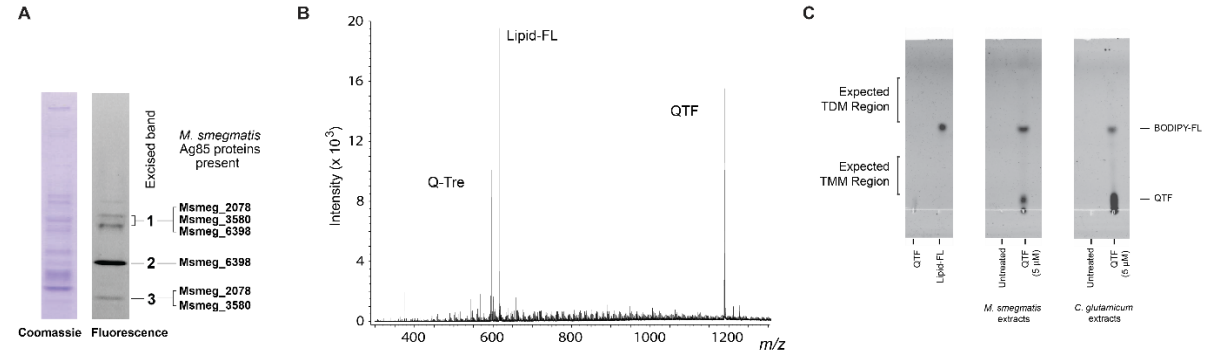

Figure 4-10. Cellular processing of QTF by mycolic acid containing bacteria (A) *M. smegmatis* CFP (9 μg) analyzed by native-PAGE (left: Coomassie stain; right: immersion in QTF solution (2.5 μM)). Fluorescent bands were excised and analyzed by protein digest mass spectrometry. Identified mycolyltransferase proteins are listed (**Table 4-2**). (B) High-resolution mass spectrometry (HRMS) analysis following exposure of QTF (50 μM) to *M. smegmatis* CFP (1 μg). Signals corresponding to QTF and predicted cleavage standards Q-Tre and Lipid-FL are labeled. (C) Fluorescence images were taken following thin-layer chromatographic (TLC) resolution of QTF and Lipid-FL standards alongside membrane extracts from *M. smegmatis* and *C. glutamicum* cells cultured with QTF (5 μM) until mid-logarithmic phase. Intact QTF and the

fluorescent cleavage product Lipid-FL were recovered in both species. No other fluorescent compounds or products were detected.

Table 4-2. *M. smegmatis* Ag85 proteins identified in extracted fluorescent bands

band no.	Protein name	accession number	% seq. coverage	Peptide sequence	Total spectrum count	Peptide id. probability	Best Mascot Ion score
1	antigen 85 (Msmeg_2078)	118473709	8.0%	ANDMWGPTE DPNSAWK	3	97.1%	35.4
1			8.0%	ANDMWGPTE DPNSAWKR	3	99.6%	23.4
1			8.0%	NDPMVQIPR	3	99.7%	32.3
1	antigen 85 (Msmeg_3580)	118467737	10.3%	NDPMVNINQL VANNTR	2	98.9%	30.2
1			10.3%	VQFQGGGPH AVYLLDGLR	2	99.7%	38.7
1	antigen 85 (Msmeg_6398)	118468744	24.5%	ADDMWGSTN DPNNAWK	5	99.1%	27.5
1			24.5%	ANDPTENVATI ANNGTR	5	99.7%	60.6
1			24.5%	FLEGFVCR	5	99.0%	28
1			24.5%	IWVYCGNGKP GELGGTDLPA K	5	99.7%	37.6
1			24.5%	VEFQSGGPGA PALYLLDGMR	5	88.9%	20.9
2	antigen 85 (MSEMG_6398)	118468744	13.4%	ANDPTENVATI ANNGTR	3	89.7%	26.4
2			13.4%	FLEGFVCR	3	99.0%	31.1
2			13.4%	VEFQSGGPGA PALYLLDGMR	3	84.5%	18.2
3	antigen 85 (Msmeg_2078)	118473709	28.6%	ANDMWGPTE DPNSAWK	16	99.7%	31.3
3			28.6%	ANDMWGPTE DPNSAWKR	16	99.7%	37.8
3			28.6%	DVAATGNAAI GLSMAGSAALI LAAYHPDR	16	98.6%	28.2
3			28.6%	ELQAMVPDLQ R	16	99.7%	51.3
3			28.6%	LVANNTR	16	90.0%	27.8

3			28.6%	NDPMVQIPR	16	99.7%	34.5
3			28.6%	VQFQSGGPGS HAVYLLDGLR	16	99.5%	20.6
3	antigen 85 (Msmeg_3580)	118467737	13.4%	GNGQDYTYK	8	99.7%	52.7
3			13.4%	NDPMVNINQL VANNTR	8	99.7%	87.7
3			13.4%	RNDPMVNINQ LVANNTR	8	84.6%	15.7
3			13.4%	VQFQGGGPH AVYLLDGLR	8	84.7%	14.9

4.3.6 Mycolyltransferase Activity is Concentrated at the Growing Poles

To examine the spatial and temporal dynamics of mycolyltransferase activity, we performed time-lapse microscopy of *M. smegmatis* exposed to QTF. We employed a microfluidic device (See **Method 4.5.14**) to maintain cells in a single focal plane for imaging and to facilitate long-term growth by perfusion of growth media containing QTF. As a result, cells could be monitored for three to four generations before crowding effects impacted the ability to distinguish specific activity of individual cells. QTF fluorescence was readily observable during growth. Moreover, because of the probe's sensitivity, even low concentrations (250 nM) afforded a robust signal with high-contrast and low-background (**Figure 4-11**). The fluorescence was localized to the septa and cell poles, with enhanced signal at the older poles (i.e., the poles inherited from the previous cell cycle) (**Figure 4-12A-B**). To examine if the fluorescence arising from mycolyltransferase activity is correlated with peptidoglycan biosynthesis, we incubated *M. smegmatis* with QTF and HCC-amino-D-alanine (HADA), a fluorescent analog of D-alanine that is incorporated into nascent peptidoglycan (77, 354). Mycolyltransferase activity (i.e., QTF-derived fluorescence) was coincident with HADA-based fluorescence. Both signals co-localized at the faster growing older pole (**Figure 4-12C**).

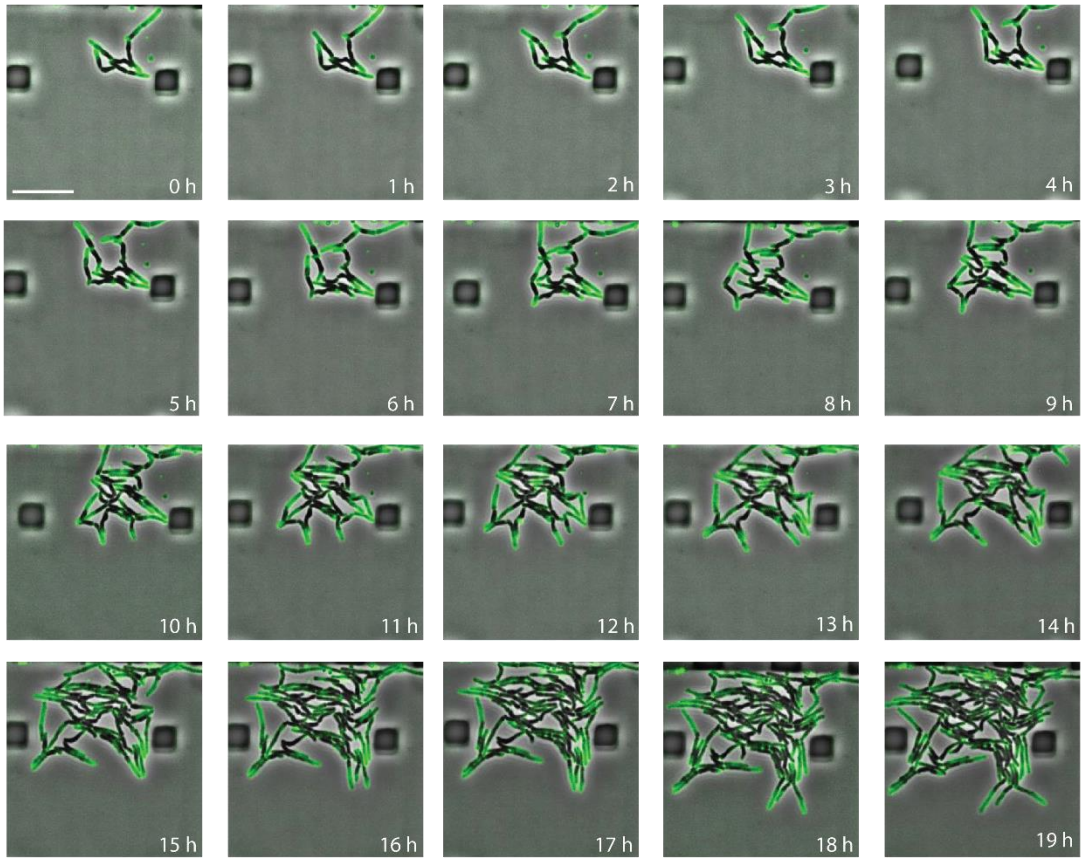

Figure 4-11. Growth of *M. smegmatis* in a microfluidic device
Still images from continuously filmed microscopic imaging of *M. smegmatis* with 250 nM QTF. Scale: 10 µm.

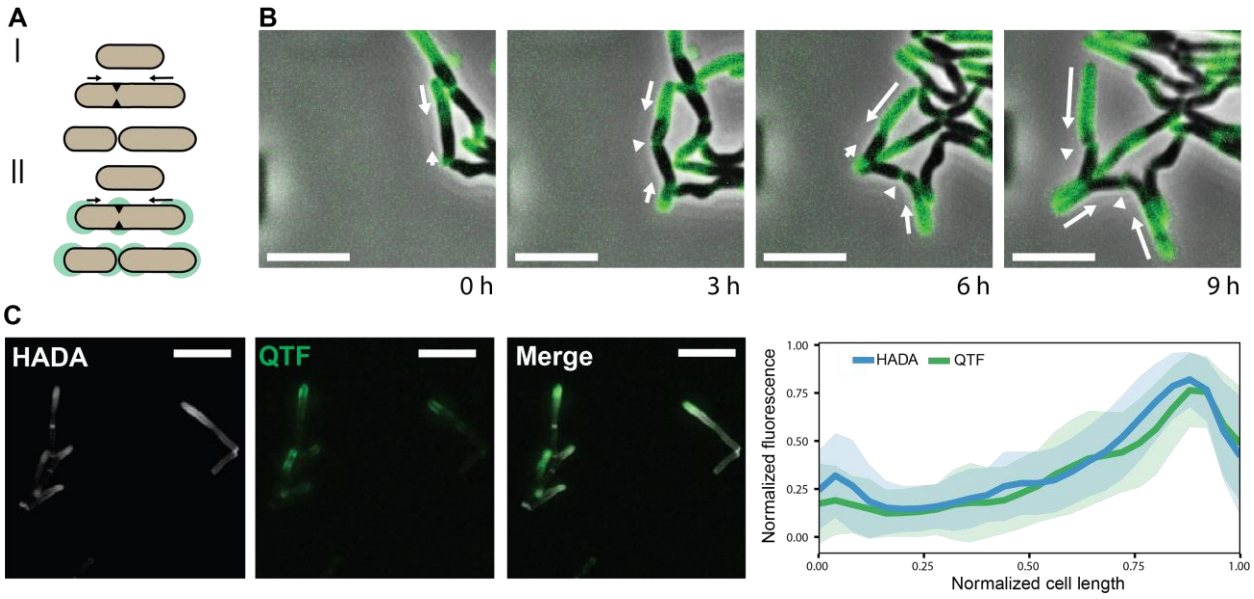

Figure 4-12. Live-cell imaging of mycolyltransferase activity during growth and division of *M. smegmatis* (A) I. Asymmetric growth model for mycobacteria II. Summary of QTF fluorescence during *M. smegmatis* growth (B) M. smegmatis was exposed to QTF (250 nM) and the sample was continuously monitored in a custom microfluidic device. White arrows depict direction and magnitude of growth. Scale: 5 µm. (C) HADA (500 µM, pulse duration of 30 m (10% of one doubling time) with 1 µM QTF. Scale: 5 µm. Colocalization analysis is reported for 71 cells. Error bars reflect standard deviations from all measured cells.

4.3.7 QTF as a Reporter of Cell Wall Assembly

Our results using QTF suggested that mycolyltransferase proteins are concentrated at the growing poles. As the cellular location of these enzymes was not known, we generated C-terminal fusions of mCherry to three *M. smegmatis* mycolyltransferases (Msmeg_3580, Msmeg_6398 and Msmeg_6399) and assessed the localization of each protein (**Figure 4-13A-C**). These studies revealed fluorescence localized to the cell envelope. Furthermore, we observed differential subcellular localizations. Msmeg_3580, Msmeg_6398 were concentrated at polar and septal regions while Msmeg_6399 was preferentially located at the septum. To confirm that the observed localization of the mCherry fusion proteins was derived from

secreted, extracellular mycolyltransferases, we first verified that mCherry fusion proteins were efficiently secreted. CFP

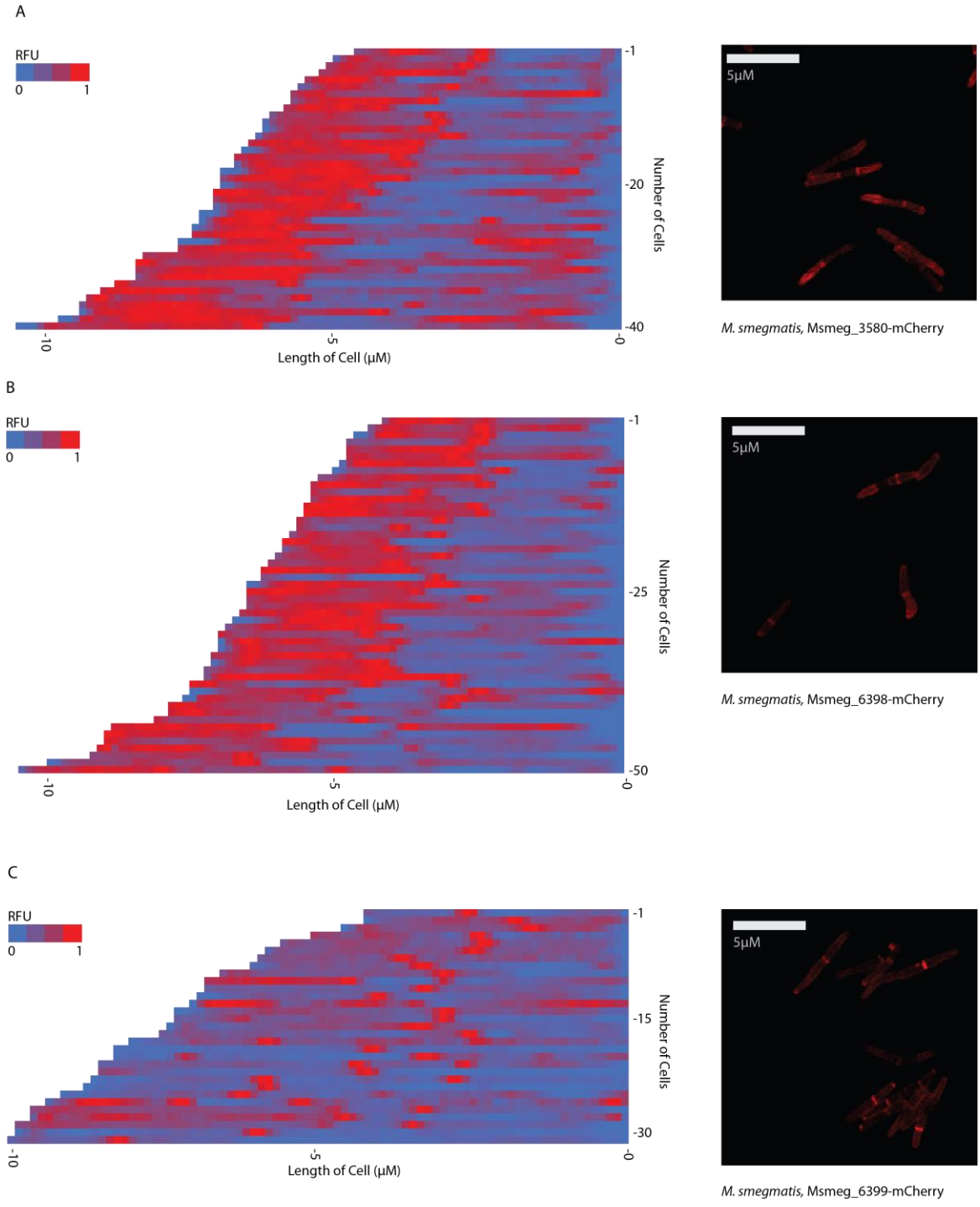

Figure 4-13. Mycolyltransferase mCherry fusions differentially localize in *M. smegmatis*
Image analysis of cell length and fluorescence distribution reveals spatial localization of (A) Msmeg_3580-mCherry (B) Msmeg_6398-mCherry and (C) Msmeg_6399-mCherry. Demograph of mCherry fluorescence, (A) N = 40 (B) N = 50 (C) N = 71, represent cells sorted by length vertically ascending, shortest (top) to longest (bottom). Fluorescence intensities are presented as heatmaps (blue to red). Note (A) asymmetric fluorescence of staining of Msmeg_3580 (mCherry) at cell poles (left). And, representative microscopy images of Msmeg_3580-mCherry expressed in *M. smegmatis* (right) (B) asymmetric fluorescence of staining of Msmeg_6398 (mCherry) at cell poles (left). And, representative microscopy images of Msmeg_6398-mCherry expressed in *M. smegmatis* (right). (C) Fluorescence of staining of Msmeg_6399 (mCherry) at cell septum (left). And, representative microscopy images of Msmeg_6399-mCherry expressed in *M. smegmatis* (right).

and cell pellets from cultures expressing mCherry-fusions Msmeg_3580, Msmeg_6398 and Msmeg_6399 were probed with an anti-mCherry antibody. Single bands at the correct molecular weight was observed and no free-mCherry protein was present indicating that observed fluorescence was from fusion proteins and that fusion proteins were able to be secreted (**Figure 4-14A**).

Next, to assess how mycolyltransferase fusion proteins were being secreted, we generated signal sequence variants of Msmeg_3580, Msmeg_6398 and Msmeg_6399. Secretion through the twin-arginine translocon (Tat) pathway can be tested by modifying the twin-arginine motif in the signal sequences. When these residues were substituted with lysine, a change that inhibits secretion through the Tat pathway (355, 356), cells remained fluorescent and exhibited the same localization patterns as observed with cells producing wild-type proteins. These experiments indicate that mycolyltransferases are likely not secreted through the Tat system but rather through the sec translocon. Cells harboring plasmids encoding mycolyltransferases lacking signal sequences entirely displayed broad cytoplasmic fluorescence but showed no localized fluorescence at the poles or septa (**Figure 4-14B**). When the strain producing

Msmeg_6398-mCherry was exposed to QTF, co-localized fluorescence emission was observed that was asymmetrically distributed at the poles (**Figure 4-15**). These findings further support our conclusion that QTF is a reporter of mycolyltransferase activity, and that extracellular mycolyltransferase activity is coincident with sites of peptidoglycan biosynthesis.

The discreet localizations that were observed for the different mycolyltransferases tested of *M. smegmatis* suggested a genetically encoded component. Therefore, after analysis of the amino-acid coding sequences for Msmeg_3580, Msmeg_6398 and Msmeg_6399 regions that were similar between Msmeg_3580 and Msemg_6398 and different in Msemg_6399 were identified (**Figure 4-16A**). A region forming an extended linker in Msmeg_6399 between Beta strand 2 and 3 (β2-β3) (**Figure 4-16B)** was targeted for alteration. This region also showed variability in other putative mycolyltransferases from other organisms with mycolic acid membranes (**Figure 4-16C).** The coding sequence from Msmeg_3580 β2-β3 linker region was substituted into the vector encoding Msmeg_6399-mCherry fusion protein at the β2-β3 linker region locus of Msmeg_6399 and assessed if localization was altered from its expected septal location. However, only septal targeting was observed indicating that this particular loop does not control localization (**Figure 16D**). The tools designed herein present a strategy to examine how localization is encoded by mycolyltransferase amino acid sequence.

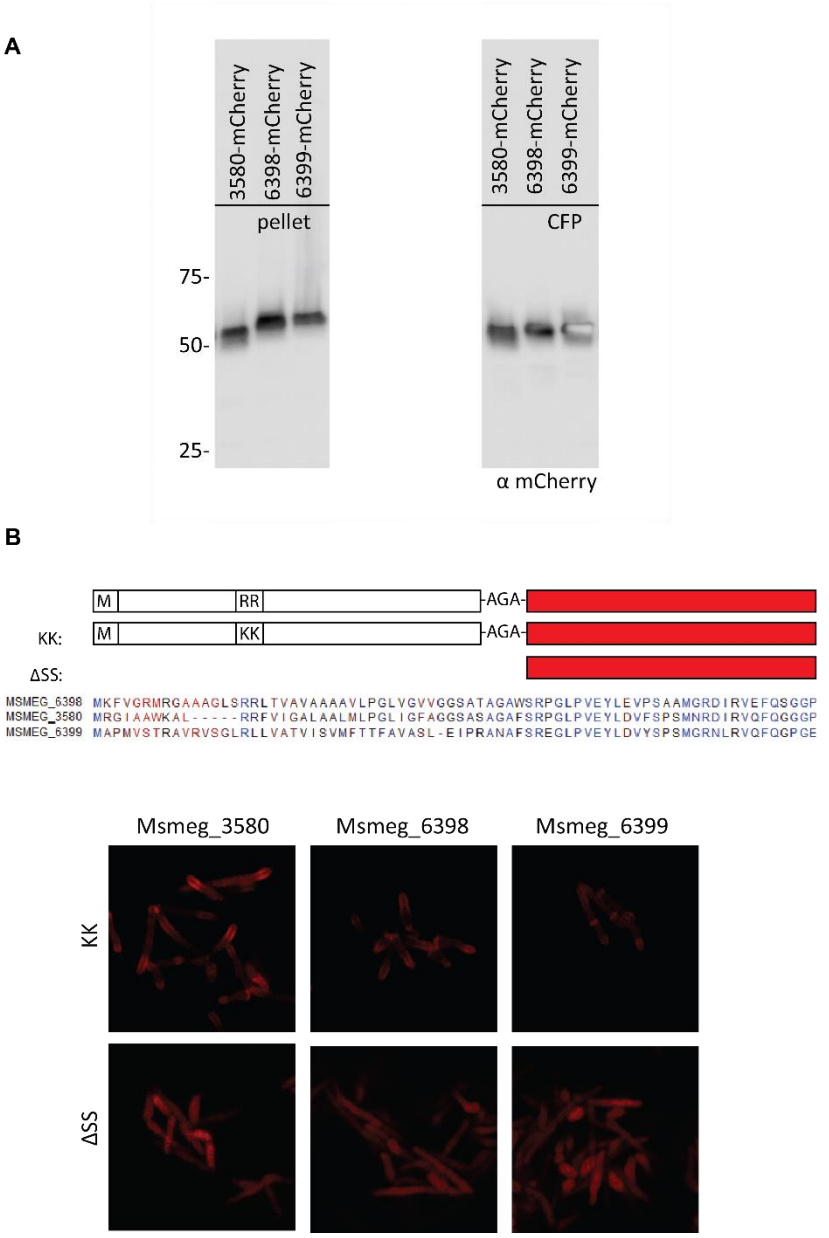

Figure 4-14. mCherry mycolyltransferase fusions are expressed intact and secreted through the sec translocon (A) Production of *M. smegmatis* Ag85 C-terminal mCherry fusion proteins. Western blot of recovered pellets and concentrated secreted protein fractions. Western blot was probed with anti-mCherry antibody. mCherry-mycolyltransferase fusion proteins are secreted and intact. (B) Schematic depicting the signal sequence variants generated for *M. smegmatis* mycolyltransferases and confocal microscopy images of *M. smegmatis* cells harboring indicated plasmids. Note polar localization of Msmeg_3580 and Msmeg_6398 mCherry fluorescence at the cell poles and Msmeg_6399 mCherry fluorescence at the cell septum in twin-lysine signal sequence variants (KK, TAT disruption), as was observed for WT signal sequences (**Figure 4-12**). Deletion of signal sequences (Δss) resulted in fluorescent cytoplasm and no observable localization.

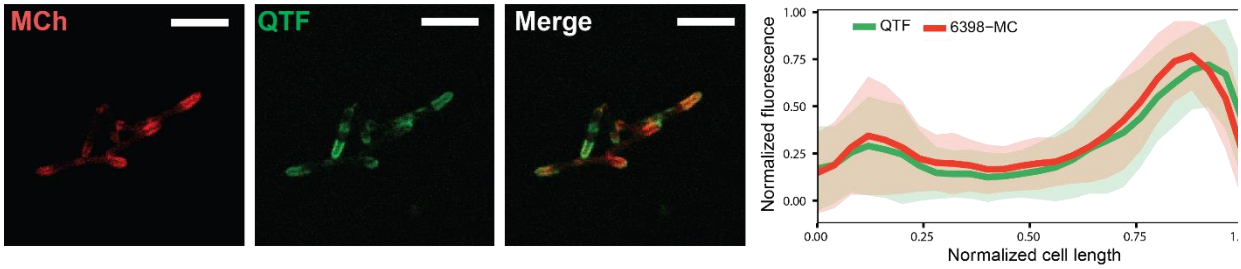

Figure 4-15. QTF indicated mycolyltransferase location *M. smegmatis* expressing an mCherry fusion to mycolyltransferase Msmeg_6398 treated with QTF (1 μM). Scale: 5 μm. Colocalization analysis is reported for 51 cells. Error bars reflect standard deviations from all measured cells.

4.4 Discussion

Most small molecule studies of cell envelope biogenesis report on peptidoglycan assembly, a process that occurs widely in bacterial species (354, 357). Probes specific to distinct classes of bacteria would serve the complementary role of enabling selective visualization and diagnosis. Mycobacteria are distinguished from other prokaryotes by the unique composition of their cell envelope, notably their mycolic acid-rich outer membrane. The mycolic acid layer is constructed by mycolyltransferases known as Ag85A–C in *M. tuberculosis*. Although mycolyltransferases are the most abundantly secreted mycobacterial proteins, whether their activity is spatially or temporally controlled is unclear (358, 359).

Chemical probes of the mycolic acid membrane lipids can label mycobacteria (114, 331, 333, 334). However, these agents were not designed to serve as real-time reporters of mycolyltransferase activity. These labeling strategies require either multiple steps that require cell fixation or use fluorophore-substituted trehalose substrates whose fluorescence signal is indistinguishable from that of their metabolic products. We envisioned complementing the

available tools with a mycolyltransferase-triggered fluorogenic probe. To this end, we synthesized QTF, a selective fluorogenic probe that obviates the need for washing and reports on mycobacterial cell wall assembly in live bacteria in real-time. Fluorescence derived from QTF is generated directly through mycolyltransferase promoted cleavage. Our data indicate this process occurs through the formation and subsequent hydrolysis of an acyl-enzyme intermediate (341). Mycolyltransferase processing of QTF yields a fluorescent lipid product, which remains at the site of its generation because of the low diffusion rates of the mycobacterial membrane (332). Mycobacteria treated with QTF exhibit fluorescence at the cell poles and cell septum, indicating that mycolyltransferase activity is localized to these sites. Thus, mycolyltransferases are abundantly secreted, yet they selectively associate with the cell envelope at the poles and septa. We also observed cell cycle-dependent mycolyltransferase activity: Mid-cell fluorescence increased only during septal formation, suggesting the localization of Ag85 to the septum is dynamic. High temporal activity at the septum is reasonable given that cytokinesis generates incipient poles in the subsequent daughter cells. Following division, we observed continued mycolyltransferase activity at both poles of the resulting daughter cells; however, the fluorescence at the new pole is markedly lower than that observed at the older inherited pole. These observations are consistent with the known sites of peptidoglycan biosynthesis detected using fluorescent peptidoglycan probes. These observations highlight that QTF can reveal temporal events in the mycobacterial cell cycle.

Our findings that mycolyltransferase activity is localized led us to examine the location of individual enzyme homologs. To this end, we generated C-terminal mCherry fusions of Msmeg_3580, Msmeg_6398 and Msmeg_6399. The resulting fluorescence aligned with that

afforded from QTF. Still, there were differences in the details of mycolyltransferase localization. Specifically, Msmeg_6399 was concentrated at the septa, while Msmeg_3580 and Msmeg_6398 exhibited septal and biased polar localization (**Figure 4-13A-C**). These findings suggest that the expression or localization of these enzymes is cell cycle-dependent and that these enzymes have distinct roles in building and maintaining the mycolic acid membrane.

Compounds that inhibit proper mycolyltransferase localization could be efficacious as deletion of a single mycolyltransferase can profoundly affect cell viability (360). Moreover, mycolyltransferases can engage in protein-protein interactions, as Msmeg_6398 has been found to interact with LprG, a lipid transport protein; this interaction could confine the enzyme within the cell envelope (361). Since mycolyltransferases are secreted, their mechanism of export could influence their localization. The *M. smegmatis* mycolyltransferases in this study are exported by the Sec translocase system, which has been reported to localize proteins at specific subcellular sites, including the cell poles (362, 363). Alternatively, it has been demonstrated that locally available pools of substrates can localize cell envelope biosynthetic proteins (364). While many encoded mycolyltransferases are seemingly redundant in mycolic acid membrane assembly, mycolyltransferases that act to mycolate proteins have been found (113). In sequence alignments of mycolyltransferases variability in the secondary trehalose binding site can indicate that a substrate other than trehalose may be used.

In vitro data obtained with QTF confirmed that the Ag85 inhibitor ebselen blocks the *Mtb* mycolyltransferases; however, we found ebselen to be poorly effective against the *M. smegmatis* orthologs. The *M. smegmatis* enzymes we tested possess the conserved cysteine residue that ebselen targets in *Mtb* Ag85 proteins; however, *M. smegmatis* also encodes an

extended linker region that directly precedes the helix (α9) that the ebselen adduct has been demonstrated to obstruct (**Figure 4-16A**) (351). The *M. smegmatis* mycolyltransferases may, therefore, be sufficiently flexible to circumvent the inhibitory effect of the ebselen adduct. Nevertheless, a major drawback of ebselen is its lack of selectivity. Ebselen functions as a general cysteine modification reagent (365). The ineffectiveness of ebselen in *M. smegmatis*, and the lack of conservation of this cysteine among mycolyltransferases from other species highlights the need for the continued development of mycolyltransferase inhibitors, especially those enzymes produced by pathogens.

QTF's ability to report on Ag85 activity provides new opportunities. The inherent sensitivity of this fluorogenic probe, together with the requisite aqueous stability and solubility render QTF an excellent screening tool. The assays we have described could readily be adapted to high-throughput screening for mycolyltransferase inhibitors. Compounds that block Ag85 activity could be powerful additions to existing anti-tubercular drug regimens. Moreover, this mycolyltransferase probe could be employed as a diagnostic tool to detect or selectively monitor mycobacteria in mixed bacterial populations. Our findings indicate that QTF can effectively be used in mixed populations to sensitively and rapidly detect mycolic acid-containing bacteria with no washing. In this way, the properties of QTF have the potential to give rise to diagnostic methods that are simple, rapid and accurate – traits that are vital for high-burden regions with limited resources.

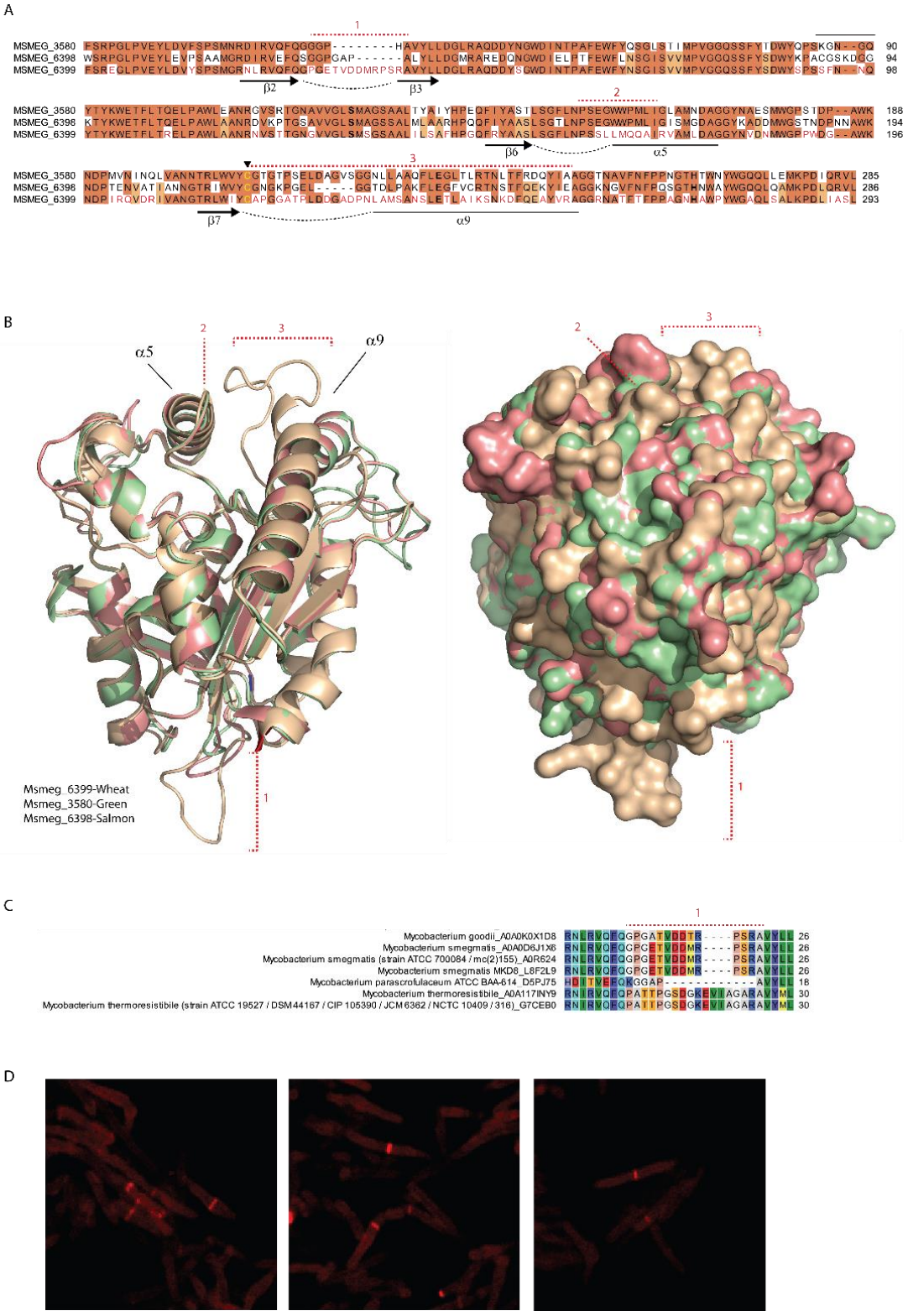

Figure 4-16. Is mycolyltransferase localization determined by protein sequence? (A) Sequence alignment of Msmeg_3580, Msmeg_6398 and Msmeg_6399. Dark orange boxes are identical residues in Msmeg_3580, light orange are identical residues in Msmeg_6398.

Highlighted by red dashed lines are three regions of sequence variability that are similar in Msemg_3580 and Msemg_6398 but different in Msemg_6399**.** Black regions below indicate protein secondary structure at these sites. Bold residues form the catalytic triad and in yellow is the cysteine targeted by ebselen. (B) Region 1 indicated in (A) encodes an extended loop region in Msemg_6399. Indicated in aligned homology models of Msmeg_3580 (green), Msmeg_6398 (salmon) and Msmeg_6399 (wheat); ribbon-diagram (left) and surface-filled (right). (C) Variability in this loop was present in other mycobacterial species as identified from sequence alignments of this region. (D) Region 1 in Msmeg_6399 (-PGETVDDMRPSRA-) was modified to match that of Msmeg_3580 (-GGPHA-) as an mCherry fusion and was found not to alter the septal localization of Msmeg_6399 by microscopy.

4.5 Experimental

4.5.1 Synthetic Procedures

Synthetic procedures and characterizations were performed by Dr. Robert Brown and are described in detail in (366).

4.5.2 General information for Biochemical Assays

Stock solutions were prepared, sterile-filtered, for all chemical reagents used in biochemical assays: QTF (5 mM in DMSO for kinetic assays, 500 µM in DMSO for all other assays), Q-Tre (1 mM in DMSO), Lipid-FL (1 mM in DMSO), trehalose (100 mM in H_2O), ebselen (1 mM in DMSO) and tetrahydrolipstatin (THL, 1 mM in DMSO). DMSO stocks were stored at –20 °C and further diluted before use, to maintain a constant 2% DMSO concentration in all assays. Ebselen was purchased from VWR and supplied by TCI America. Tetrahydrolipstatin was purchased from Sigma Aldrich and supplied by Roche. HADA, hydroxy coumarin-carbonyl-amino-D-alanine, was a kind gift from the Weibel lab, (11.8 mM in DMSO). *In vitro* assays with purified Ag85 proteins were performed in aqueous NaH_2PO_4/Na_2HPO_4 buffer (20 mM, pH = 7.2), whereas assays involving *M. smegmatis* culture filtrate proteins used aqueous NH_4HCO_3 buffer (10 mM, pH = 8.0).

For bacterial assays, the strains employed include wild type *Mycobacterium smegmatis* mc^2155, *Corynebacterium glutamicum* ATCC 13032, *Escherichia coli* K12 MG1655 and *Bacillus subtilis* 168. *M. smegmatis* was cultured in either LB liquid medium, M63 liquid medium containing 0.2% glycerol, 1 mM $MgSO_4$ and 0.02% Tween-80, or Middlebrook 7H9 liquid medium (containing 10% ADC, 0.2% glycerol and 0.05% Tween-80). *C. glutamicum*, *E. coli* and *B. subtilis* were all cultured in LB liquid medium. Generally, starter cultures were prepared by inoculating the

desired growth medium in a baffled shake flask with a single colony from a freshly-streaked agar plate. Starter cultures were incubated at 37 °C with shaking until saturation, then re-inoculated and grown to mid-logarithmic phase (determined by OD_{600} measurement on an Amersham Ultrospec 10 cell density meter), and finally diluted with additional liquid medium to the quoted optical density for each assay. When cells were induced with acetamide, 0.2%, they were grown in either M63 media or 7H9 without ADC.

4.5.3 *M. tuberculosis* Ag85 Proteins

The following reagents were obtained through BEI Resources, NIAID, NIH: Ag85A (Gene Rv3804c), Purified Native Protein from *Mycobacterium tuberculosis*, Strain H37Rv, Catalog Number: NR-14856

Ag85B (Gene Rv1886c), Purified Native Protein from *Mycobacterium tuberculosis*, Strain H37Rv, Catalog Number: NR-14857

Ag85C (Gene Rv0129c), Purified Native Protein from *Mycobacterium tuberculosis*, Strain H37Rv, Catalog Number: NR-14858

Upon receipt, lyophilized native Ag85 proteins were thawed and suspended in aqueous NaH_2PO_4/Na_2HPO_4 buffer (20 mM, pH = 7.2) to a concentration of 10 µM for storage in aliquots at –80 °C. *Mtb.* Ag85A–C proteins were thawed as needed, and further diluted with NaH_2PO_4 / Na_2HPO_4 buffer (20 mM, pH = 7.2) immediately prior to use.

4.5.4 Cloning of *M. smegmatis* Mycolyltransferase Proteins

The following mycolyltransferase proteins were produced as C-terminal mCherry or hexahistidine tag fusions; Msmeg_3580, Msmeg_6398, Msmeg_6399, Msmeg_6580. Signal

sequence truncations or signal sequence mutants were subcloned from the relevant C-terminal mCherry plasmids for Msmeg_3580, Msmeg_6398, Msmeg_6399.

Vectors encoding C-Terminal mCherry M. smegmatis mycolyltransferase fusion proteins: To generate C-terminal mCherry fusions to *M. smegmatis* Ag85 proteins, a linker-mCherry construct was codon optimized for *M. smegmatis* and ordered as a G-block from IDT with added overhangs for an isothermal reaction with a linearized Plam12 vector (Addgene, plasmid 26908) (5'-AGCTGCAGAATTCGAAG-3', 5'-TGGACTCCCTTTCTCTTATC-3') to generate a Plam12-mCherry plasmid. Each individual *M. smegmatis* Ag85 gene was amplified from isolated genomic *Mycobacterium smegmatis* mc^2155 DNA with the following primers 3580 (5'-GATAAGAGAAAGGGAGTCCATTGGTTGCCGTTATGAAGTTCATTCGAG-3', 5'-GGACCCGGACG CACGAGCACCCGCTGGATGTC-3'), 6398 (5'-GATAAGAGAAAGGGAGTCCAATGAAGTTCGTTGGG AGAATGCGCGG-3', 5'-GGACCCGGACGCACCAGCACGCGCTGCAGGTC-3'), 6399 (5'-GATAAGAG AAAGGGAGTCCAATGGCACCCATGGTGAGC-3', 5'-GGACCCGGACGCACCAGCGAAGCGATCAGG TCAG-3'), 6583 (5'-GATAAGAGAAAGGGAGTCCAGTGAAGCCCTCGTTTTTCTC-3', 5'-GGACCCGG ACGCACGAGGACCCGCAACAGATC-3'). These DNA fragments were joined with linearized a Plam12-mCherry vector (5'-GGTGCGTCCGGGTCC-3', 5'-TGGACTCCCTTTCTCTTATCGGGTG-3') by isothermal annealing with a Gibson Assembly master mix (NEB). Plasmids were transformed into DH5α *E. coli.* Vectors encoding C-terminal mCherry fusions to *M. smegmatis* Ag85 proteins were confirmed by DNA sequence analysis at the UW-Madison Biotechnology Center. Plasmids were then transformed into *Mycobacterium smegmatis* mc^2155 for homologous expression.

Signal sequence mutants of C-terminal mCherry Fusion M. smegmatis Ag85 proteins: Each C-terminal mCherry fusion vector encoding *M. smegmatis* mycolyltransferases (Msmeg_3580, Msmeg_6398, Msmeg_6399) was modified by inverse PCR such that the construct replaces twin-arginine motifs (RR) with lysine. The following primers were used: Msmeg_3580 MC KK (5′-/5phos/AAGAAATTTGTGATCGGTGCCCT-3′, 5′-/5phos/CAGGGCTTTCCATGCTG-3′), Msmeg_6398 MC KK (5′-/5phos/AAGAAACTGACGGTTGCGGTC-3', 5′-/5phos/CGACAGACCTGCCGC-3′), Msmeg_6399 MC KK (5′-/5phos/-3′, 5′-/5phos/CAGACCGGATACGCGCA-3′) Msmeg_3580MC Δss (5′-/5phos/TTTTCCCGTCCTGGTCTG-3′, 5′-/5phos/CAATGGACTCCCTTTCTCTTATCGG-3′), Msmeg_6398 MC Δss (5′-/5phos/TGGTCTCGACCCGGC-3′, 5′-/5phos/CATTGGACTCCCTTTCTCTTATCGG-3′), Msmeg_6399 MC Δss (5′-/5phos/TTTTCGCGTGAGGGCC-3', 5′-/5phos/CATTGGACTCCCTTTCTCTTATCGG-3′. Plasmids were trans-formed into DH5α *E. coli.* Vectors encoding signal sequence variants of C-terminal mCherry fusions to *M. smegmatis* Ag85 proteins were confirmed by DNA sequence analysis at the UW-Madison Biotechnology Center. Plasmids encoding the mycolyltransferase variants were then transformed into *Mycobacterium smegmatis* mc^2155 for mycolyltransferase production.

C-Terminal hexahistidine-tagged M. smegmatis mycolyltransferases: The genes encoding Msmeg_3580, Msmeg_6398, Msmeg_6399, Msmeg_6580 were amplified by inverse PCR from previously generated constructs encoding *M. smegmatis* mycolyltransferase C-terminal mCherry fusions with the following phosphorylated primers, 5'-/5phos/TAATAAAGCTGCAGAATTCGAAGCTTAT-3' and 5'-/5phos/ATGGTGGTGATGATGGTGCG

ACGCCCCGGC-3'. Template plasmid was digested with DPNI, and amplified products were self-ligated with T4 DNA ligase (Fermentas) and transformed into DH5α *E. coli*. Vectors encoding C-terminal hexahistidine tag *M. smegmatis* mycolyltransferase proteins were confirmed by DNA sequence analysis at the UW-Madison Biotechnology Center. Plasmids were then transformed into *Mycobacterium smegmatis* mc^2155 for homologous expression.

Production of M. smegmatis mycolyltransferases: *M. smegmatis* strains harboring vectors encoding C-terminal hexahistidine tag *M. smegmatis* mycolyltransferases were grown to saturation overnight in M63 liquid medium containing 0.2% glycerol, 1 mM $MgSO_4$ and 0.02% Tween-80. Cultures were diluted 1:200 in M63 liquid medium containing 0.2% glycerol, 1 mM $MgSO_4$ and 0.02% Tween-80 and induced at OD_{600} 0.2 with 0.2% acetamide for 6-10 hours at 30 °C. Cells were pelleted, and supernatants were collected and filtered through a 0.2-micron filter. Collected culture filtrates containing secreted C-terminal hexahistidine tagged mycolyltransferase proteins were concentrated with 10 kDa molecular weight filter devices at 4 °C. Concentrated protein filtrates were incubated with Prometheus Magnetic agarose derivatized with nitrilotriacetic acid (Genesee Scientific) according to manufacturer's instructions. Proteins were eluted with 500 mM imidazole and eluted proteins were subsequently dialyzed against NaH_2PO_4 / Na_2HPO_4 buffer (20 mM, pH = 7.2) in a 10 kDa dialysis cassette (Pierce). Protein concentration was determined by *NanoOrange*® Protein Quantitation. The resulting protein solutions were then diluted with NaH_2PO_4/Na_2HPO_4 buffer (20 mM, pH = 7.2) to a final concentration of 20 nM, and temporarily stored at 4 °C until use (within 48 h). Purity was assessed by polyacrylamide gel electrophoresis and staining by Sypro Ruby.

For immunoblotting, SDS/PAGE sample buffer was added to *M. smegmatis* cells lysed by bead beating or to concentrated media filtrate (3k mwco) and then samples were loaded onto a 4-15% Tris-HCl gel. Samples were then transferred onto 0.45 µm PVDF membrane (Millipore) and blocked for 2 h at rt with a solution of Tris-buffered saline and 0.1% Tween 20 (TBS-T) containing 5% nonfat milk. The membrane was exposed to rabbit polyclonal anti-mCherry (ab167453, Abcam) at 1:10000 dilution for 1 h at room temperature in TBS-T solution with 3% milk. After rinsing three times in TBS-T for 5 min, the blot was treated at rt with a 1:10000 dilution of HRP-conjugated goat anti-rabbit secondary antibody (Jackson ImmunoResearch) in TBS-T solution containing 3% milk for 1 h at rt. The membrane was washed with TBS-T and visualized with chemiluminescent substrate (ECL prime, GE) on an ImageQuant LAS 4000 (GE Healthcare).

4.5.5 Fluorescence Assays

Fluorescence measurements were acquired on a Tecan Infinite M1000 Pro microplate reader. Assays requiring only fluorescence reads were performed in Corning black 96-well half-area microplates. Assays that involve tandem fluorescence and absorbance reads were performed in Corning black 96-well clear-bottom plates. To monitor BODIPY-FL fluorescence, samples were excited at 503 nm, and detected (a minimum of 4 reads per well) at a single emission wavelength of 515 nm in QTF cleavage assays or between 510 – 600 nm when acquiring full emission spectra. Fluorimeter gain and Z-position were optimized to wells containing the lipid-FL standard. Settings were kept constant across replicates and in comparable experiments. Fluorescence emission intensities are reported in relative fluorescence units (RFU).

Emission spectra and quenching efficiency: A black 96-well half-area microplate was used to measure the fluorescence emission of a QTF concentration series. Measurements were carried out analogously with a concentration series consisting of equimolar mixtures of cleavage standards Q-Tre and Lipid-FL. Stock solutions of compounds were prepared in DMSO and transferred into wells containing aqueous NaH_2PO_4/Na_2HPO_4 buffer (20 mM, pH = 7.2), to give final concentrations of 100 nM, 250 nM, 500 nM, 1 µM, 2.5 µM, 5 µM and 10 µM for all analytes at a final well volume of 100 µL and DMSO concentration of 2%. Fluorescence emission at 515 nm following excitation at 503 nm was recorded at 37 °C for each series and plotted versus analyte concentration to determine quenching efficiency. Fluorescence emission scans (510 – 600 nm) were also acquired for the 1 µM samples.

End-point assays with Ag85 proteins: A black 96-well half-area microplate was used to measure fluorescence resulting from QTF exposure to purified *M. tuberculosis* or *M. smegmatis* mycolyltransferases proteins. Additionally, the effect of added trehalose, THL or ebselen on this fluorescence was assessed. The following stock solutions were prepared: QTF (100 µM in DMSO), ebselen (1 mM in DMSO) and THL (1 mM in DMSO), and trehalose (100 mM in H_2O). Solutions of *M. tuberculosis* Ag85A–C (400 nM) and *M. smegmatis* proteins (20 nM) in aqueous NaH_2PO_4/Na_2HPO_4 buffer (20 mM, pH = 7.2) were also prepared. Wells (n = 3) were filled with enzyme solution, phosphate buffer, and trehalose solution where appropriate (Ag85A–C wells only), followed by either DMSO (0.5 µL), THL (0.5 µL) or ebselen (0.5 µL). The total volume of all wells was 49.5 µL. Sample plates were subjected to shaking for 2 h at 37 °C before the addition of QTF stock solution (0.5 µL). All wells were at a final volume of 50 µL (phosphate buffer with

2% DMSO) with Ag85 and QTF concentrations of 20 nM and 1 μM, respectively. Each Ag85 protein was assayed with and without trehalose (5 mM), THL (10 μM), or ebselen (10 μM). Fluorescence emission at 515 nm was recorded immediately to acquire a zero-time point level and after 20 h with shaking at 37 °C.

Kinetic assays with M. tuberculosis Ag85 A–C: A black 96-well half-area microplate was used to measure initial reaction velocities for varying concentrations of QTF with a fixed concentration (1 μM) of each Ag85 isoform. Stock solutions of QTF were prepared (0.05, 0.125, 0.25, 0.375, 0.5, 1.25, 2.5 and 5 μM in DMSO), along with a solution of Ag85A, Ag85B or Ag85C (1 μM) in aqueous NaH_2PO_4/Na_2HPO_4 buffer (20 mM, pH = 7.2). Wells (n = 3) were filled with phosphate buffer (93 μL) and Ag85 solution (5 μL), and the plate incubated at 37 °C for 15 min. Reactions were initiated by the addition of 2 μL QTF solution, to give final concentrations of 50 nM Ag85, and 1, 2.5, 5, 7.5, 10, 25, 50 and 100 μM QTF. Wells were mixed thoroughly, and fluorescence emission monitored continuously for 20 min.

Plots of fluorescence (RFU) versus time (s) were generated using Microsoft Excel, and the slope of the data was used to calculate initial reaction velocities (in nM s^{-1}), after conversion from RFUs to concentration using a BODIPY-FL standard curve (10 – 500 nM). At QTF concentrations exceeding 10 μM, the measured reaction velocities were distorted by an "inner filter effect" (IFE), in which the fluorescence of the generated Lipid-FL product undergoes intramolecular quenching in the presence of high concentrations of substrate. We therefore applied Kohlbrenner's method (367) to correct the initial velocity data. After applying this correction,

the data were fit to the Michaelis-Menten equation using GraphPad Prism 6, to determine K_m (app) and k_{cat} (app) values.

In-culture bacterial growth assay: Cultures of *M. smegmatis* or *C. glutamicum* were grown in LB media to mid-logarithmic phase and diluted back to an OD_{600} of 0.05. A black 96-well clear-bottom plate was set up to monitor fluorescence in the presence of QTF during bacterial growth. Wells (n = 3) were filled with diluted bacteria (98 µL), and 2 µL of a 125 µM QTF DMSO stock solution (or 2 µL DMSO for negative control wells) was added to give a final QTF concentration of 2.5 µM, a final well volume of 100 µL, and DMSO concentration of 2%. The plate was incubated with shaking at 37 °C for 24 h, as both fluorescence emission and OD_{600} measurements were taken at 15 min intervals.

4.5.6 Flow cytometry and Fluorescence Microscopy

E. coli, *B. subtilis* and *C. glutamicum* were cultured in LB + 0.05% Tween-80. All cultures were grown at 30 °C in a shaking incubator overnight to saturation. A portion of the culture (3 mL) was then diluted to OD_{600} = 0.02 in 10 mL baffled flasks (3 independent samples) and grown to an OD_{600} of 0.2, whereupon 1 µM QTF was added to initiate labeling. Aliquots (500 µL) were removed for analysis at OD_{600} = 0.8 (2 doubling times). The *E. coli*, *B. subtilis* and *C. glutamicum* samples were pelleted and resuspended in 500 µL of 1% paraformaldehyde in PBS. Samples were fixed at rt for 30-60 min, quenched with 500 µL of 1 M lysine solution, and pelleted and resuspended in 1X PBS for analysis by flow cytometry. We also performed analysis of two control samples to establish background fluorescence values of cells alone (auto-fluorescence) or cells that were fixed and then incubated with probe (background). For the auto-fluorescence

control, each strain at OD_{600} = 0.2 was fixed in the absence of probe (-QTF). For background control experiments, each strain at OD_{600} = 0.2 was fixed (which should disrupt mycolyltransferase activity) and then exposed to QTF (1 µM for 30 m at 30 °C). These control samples were then spun to pellet the cells and resuspended once (+QTF).

M. smegmatis was cultured in 7H9 with ADC component and 0.05% Tween-80 and grown at 30 °C in a shaking incubator overnight to saturation. A portion of the culture (3 mL) was diluted to OD_{600} = 0.02 in 10 mL baffled flasks (3 independent samples) and grown to an OD_{600} of 0.2, whereupon 1 µM QTF was added to initiate labeling. 500 µL aliquots were removed for analysis at OD_{600}=1.2 (3 doubling times). We found that *M. smegmatis* cells under these conditions did remain intact after fixation. Therefore, flow cytometry of *M. smegmatis* was performed on live cells in 7H9 + ADC/Tween-80. Aliquots of *M. smegmatis* at OD_{600} = 1.2 were analyzed immediately by flow cytometry. We also performed analysis of two negative control samples to establish background fluorescence values of cells alone (auto-fluorescence) or cells that were incubated with probe and washed at incubation times insufficient for labeling (background). For auto-fluorescence controls, *M. smegmatis* at OD_{600} = 0.2 was analyzed by flow cytometry in the absence of probe (-QTF). For background control, *M. smegmatis* at OD_{600} = 0.2 were washed to remove secreted mycolyltransferases, incubated with 1 µM probe for 15 m at 30 °C then spun and resuspended once and analyzed by flow cytometry (+ QTF).

For flow cytometry, cells were diluted as necessary. Flow cytometry was performed on a BD Accuri C6 for 100,000 events with 7,000 threshold (*E. coli*, *B. subtilis* and *C. glutamicum*) or 15,000 (*M. smegmatis*). Flow cytometry analysis was performed in triplicate on three independent

cultures for each strain, representative histograms and scatter plots are shown. All flow cytometry data was processed in Flowjo (FlowJo LLC).

For analysis by microscopy, cell aliquots were taken directly from samples of *E. coli*, *B. subtilis*, *C. glutamicum* (OD_{600} = 0.8) or *M. smegmatis* (OD_{600} = 1.2) analyzed by flow cytometry. Each sample was spotted onto a glass-bottomed microwell dish (MatTek corporation) and covered with a 1% (w/v) agarose pad. Images were collected at rt with a Nikon A1 laser scanning confocal microscope (Nikon Instruments). Images were acquired with a Nikon plan apo 100/1.4 oil objective with a 1.2-AU pinhole diameter and NIS-elements C software (Nikon Instruments). Identical acquisition settings were used for samples and controls. Brightness and contrast were identically adjusted with the open-source Fiji distribution of ImageJ. Images were then converted to an RGB format to preserve normalization and then assembled into panels. Images are representative of greater than five fields of view.

4.5.7 Mixed Culture Assay

A vector encoding pEKEX2-mCherry was prepared using primers described in **Table 4-3** by isothermal annealing with a Gibson Assembly master mix (NEB) and the resulting construct was transformed into DH5α. Vectors correctly encoding pEKEX2-mCherry were confirmed by DNA sequence analysis at the UW-Madison Biotechnology Center. Plasmids were then passaged through dam-/dcm- competent *E. coli* (NEB). dam-/dcm- DNA was methylated *in vitro* by GpC Methylase (M.CviPI) (Zymo) and transformed into *C. glutamicum* for expression.

E. coli, B. subtilis and *C. glutamicum/*pEKEX2-mCherry were grown individually in LB to late logarithmic phase, OD_{600} = 0.5-1.0. Each culture was diluted and grown to OD_{600} = 0.1. Strains were mixed 1:1:2 *E. coli*: *B. subtilis*: *C. glutamicum* (the increased ratio of *C. glutamicum* employed

accounts for the slower growth rate) or maintained individually. To each sample, 1 µM QTF was added, and cells were grown for ~2 h at 37 °C. Cells were spotted without washing onto a glass-bottomed microwell dish (MatTek corporation) and covered with a 1% (w/v) agarose pad. Images were collected at room temperature with a Nikon A1 laser scanning confocal microscope (Nikon Instruments). Images were acquired with a Nikon plan apo 100/1.4 oil objective with a 1.2-AU pinhole diameter and NIS-elements C software (Nikon Instruments) with appropriate filter sets. Images were processed in the open-source Fiji distribution of ImageJ.

4.5.8 Isolation of *M. smegmatis* Culture Filtrate Proteins (CFPs)

CFPs secreted by *M. smegmatis* were isolated from cultures by growing *M. smegmatis* mc^2155 in 7H9 with 0.2% glycerol. Cells were pelleted at 3,000 x *g* and supernatants were collected and filtered through a 0.2-micron filter. CFPs were then concentrated using a membrane with a molecular weight cutoff of 10 kDa and dialyzed into NH_4HCO_3 buffer (10 mM, pH = 7.4). Protein in the isolated culture filtrate batches was quantified by BCA, aliquoted, snap frozen in liquid nitrogen, and then stored at -80 °C. Aliquots of *M. smegmatis* CFPs were thawed as needed and used immediately.

4.5.9 End Point Fluorescence Assay with *M. smegmatis* CFP

A black 96-well half-area microplate was used to measure fluorescence derived from QTF **i**n the presence of *M. smegmatis* CFP with and without ebselen. Stock solutions of QTF (100 µM in DMSO) and ebselen (1 mM in DMSO) were prepared. Three sets of wells (*n* = 3) were filled with 97 µL aqueous NH_4HCO_3 buffer (10 mM, pH = 8.0). To the first set was added 1 µL of *M. smegmatis* culture filtrate protein solution (200 µg/mL in 10 mM aqueous NH4HCO3 buffer) and

1 µL of DMSO. To the second set was added 1 µL of *M. smegmatis* CFP solution, and 1 µL of ebselen stock solution. Finally, the third set (negative control wells) was treated with 1 µL of buffer and 1 µL of DMSO. The plate was incubated with shaking for 2 h at 37 °C, then 1 µL of QTF stock solution was added to all wells, bringing the final volume to 100 µL. The final concentration of *M. smegmatis* CFP was 2µg/mL and the concentration of ebselen to 10 µM. Fluorescence emission at 515 nm was recorded immediately to acquire a zero-time point, and again after 12 h incubation at 37 °C with shaking.

4.5.10 Native-PAGE in-Gel Activity Assay

In-gel activity assays were performed by Blue Native Page Polyacrylamide Gel Electrophoresis (Invitrogen, NativePAGE™ Gel system). Briefly, CFP samples were mixed with 4x NativePage sample buffer and loaded onto a 4-16% BIS-TRIS gel. Gels were run on ice for 60 minutes at 150V and 90 minutes at 250V using 1x NativePAGE Light Blue Cathode Buffer to reduce background. Gels were rinsed with 1X PBS (pH 7.4) for 5 min to reduce background. Gels were placed on the fluorescence glass imaging surface of GE Typhoon FLA 9000 Gel Imaging Scanner and immersed in 2.5 µM QTF in 1X PBS (pH 7.4) to identify those proteins that can process QTF. Fluorescence was revealed upon scanning, and the resulting images were processed with the open-source Fiji distribution of ImageJ.

4.5.11 Identification of Proteins by Mass Spectrometry

Enzymatic "in gel" digestion : "In gel" digestion and mass spectrometric analysis were carried out at the Mass Spectrometry Facility [Biotechnology Center, UW-Madison]. The digestion was performed as outlined on the website:

http://www.biotech.wisc.edu/ServicesResearch/MassSpec/ingel.htm.

In short, Coomassie Blue R-250-stained gel bands were de-stained twice for 5 min in methanol/water/NH_4HCO_3 [50%:50%:100 mM], dehydrated for 5 min in acetonitrile/water/NH_4HCO_3 [50%:50%:25 mM], final dehydration was repeated once more for 1 min. in 100% acetonitrile, dried in a Speed-Vac for 2 min., and treated to 25 mM dithiothreitol in 25 mM NH_4HCO_3 for 30 min. at 56 °C. The samples were then subjected to the alkylating agent iodoacetamide (55 mM in 25 mM aqueous NH_4HCO_3) in darkness at rt for 30 min. After exposure, samples were washed in water (2 x 30 sec), equilibrated in 25 mM aqueous NH_4HCO_3 for 1 min., dehydrated for 5 min. in acetonitrile/water/NH_4HCO_3 [50%:50%:25 mM], exposed for 30 sec to 100% acetonitrile, dried again and treated to trypsin solution [20 µL of a solution containing 10 ng/µl trypsin Gold (Promega) in 25 mM NH_4HCO_3/0.01% ProteaseMAX w/v (Promega)]. An additional 30 µL of digestion solution [25 mM NH_4HCO_3/0.01% ProteaseMAX w/v] was added to facilitate complete rehydration for peptide extraction. The digestion was conducted for 3 h at 42 °C. Peptides generated from digestion were transferred to a new tube and acidified with 2.5% TFA [Trifluoroacetic Acid] to 0.3% final concentration. Degraded ProteaseMAX was removed via centrifugation [max speed, 10 minutes] and the peptides solid phase extracted (*ZipTip® C18* pipette tips Millipore, Billerica, MA).

NanoLC-MS/MS: Peptides were analyzed by nanoLC-MS/MS using the Agilent 1100 nanoflow system (Agilent) connected to a new generation hybrid linear ion trap-orbitrap mass spectrometer (LTQ-Orbitrap Elite™, Thermo Fisher Scientific) equipped with an EASY-Spray™ electrospray source. Peptides were separated prior to mass spectral analysis by chromatography using capillary emitter column (PepMap® C18, 3 µM, 100 Å, 150x0.075 mm,

Thermo Fisher Scientific) onto which 2 µL of extracted peptides was automatically loaded. The NanoHPLC system delivered solvents **A**: 0.1% (v/v) formic acid , and **B**: 99.9% (v/v) acetonitrile, 0.1% (v/v) formic acid at 0.50 µL/min to load the peptides (over a 30 min period) and 0.3 µL/min to elute peptides directly into the nano-electrospray with a gradual gradient from 3% (v/v) to 30% (v/v) **B** over 77 min concluding with a 5 min fast gradient from 30% (v/v) to 50% (v/v) **B** at which time a 5 min flush using 50-95% (v/v) **B** took place. As peptides eluted from the HPLC-column/electrospray source, survey MS scans were acquired in the Orbitrap with a resolution of 120,000 followed by MS2 fragmentation of 20 most intense peptides, by ion count, detected in the MS1 scan from 300 to 2000 m/z; redundancy was limited by dynamic exclusion.

Data analysis: Raw MS/MS data were converted to mgf file format using MSConvert (ProteoWizard: Open Source Software for Rapid Proteomics Tools Development). The resulting mgf files were used to search against the *M. smegmatis* acid sequence database containing a list of common contaminants (6,756 total entries) using in-house *Mascot* search engine 2.2.07 [Matrix Science] with variable methionine oxidation with asparagine and glutamine deamidation plus fixed cysteine carbamidomethylation. Peptide mass tolerance was set at 15 ppm and fragment mass at 0.6 Da. Protein annotations, significance of identification and spectral based quantification was done with the help of scaffold software (version 4.3.2, Proteome Software Inc., Portland, OR). Protein identifications were accepted if they could be established at greater than 80% probability within 1% false discovery rate and contained at least 2 identified peptides. Protein probabilities were assigned by the Protein Prophet

algorithm. Proteins that contained similar peptides and could not be differentiated based on MS/MS analysis alone were grouped to satisfy the principles of parsimony.

4.5.12 HRMS Analysis of QTF Cleavage by *M. smegmatis* CFP

To a 500 µL Eppendorf tube was added 94 µL of aqueous NH_4HCO_3 buffer (10 mM, pH = 8.0), 5 µL of *M. smegmatis* CFP solution (200 µg/mL in 10 mM aqueous NH_4HCO_3 buffer), and 1 µL of 5 mM QTF DMSO stock solution, giving final concentrations of 10 µg/mL *M. smegmatis* CFP and 50 µM QTF. To serve as a negative control, 99 µL of buffer and 1 µL of QTF solution were added to a second tube. Both samples were incubated at 37 °C with shaking for five days, then analyzed without further manipulation on an electrospray ionization-time of flight (ESI-TOF) Micromass LCT mass spectrometer in positive ion mode.

4.5.13 TLC Analysis of Lipid Extracts from QTF-treated Bacteria

Cultures (5 mL) of *M. smegmatis* in Middlebrook 7H9 liquid medium (containing 10% ADC, 0.2% glycerol and 0.05% Tween-80) and *C. glutamicum* in LB liquid medium, both at an OD_{600} of 0.2 in 12 mL aerated culture tubes, were treated with either 50 µL DMSO (for negative control cultures) or 50 µL of 5 mM QTF stock, giving final concentrations of 5 µM QTF and 1% DMSO. Bacteria were incubated at 37 °C until the culture reached an OD_{600} of 0.9 (7 h for *C. glutamicum*, 19 h for *M. smegmatis*). Bacteria were then pelleted by centrifugation (3000 x *g*, 5 min, rt), and washed three times with PBS containing 0.05% BSA. Each cell pellet was suspended in 2:1 chloroform:methanol (3 mL), transferred to a 10 mL glass culture tube equipped with a stir bar, and stirred vigorously for 16 h to extract soluble cell wall lipids. After extraction, each sample was pelleted (3000 x *g*, 5 min, rt) and washed twice with 2:1 chloroform:methanol (2 mL). The combined organic extracts were concentrated to dryness under reduced pressure, and the

residue was resuspended in THF (200 µL). A portion of each sample (15 µL) was spotted on silica gel thin layer chromatography plates. Samples were then eluted using chloroform/methanol/acetone (90:15:10) and imaged on a Typhoon FLA 9000 fluorescence scanner.

4.5.14 Microfluidic Device Fabrication and Operation

All devices were fabricated using standard soft lithography (368). Briefly, the master was patterned on a silicon wafer as three layers of SU-8 photoresist (Microchem, Newton, MA, USA) using a laser pattern generator (Heidelberg Instruments, Heidelberg, Germany). The height of each layer of photoresist was calibrated using a stylus profilometer (Tencor, Milpitas, CA, USA). The first layer was spun to a height of approximately 600 nm using SU-8 2000.5. This layer was used to pattern the bypass channels that surrounded each observation area and enabled fresh media to continuously flow across the cells during our measurements. A second layer of SU-8 2000.5 was deposited on top of the first to create a combined thickness of 1.2 µm. This layer was used to create the observation areas where cells were trapped during our measurements. Finally, a third layer of SU-8 3025 (approximately 25 µm tall) was used to create the main channel network that integrated all of the observation areas. The compound 1,1,2,2-tetradecafluorotrichlorosilane (Gelest Inc., Morristown, NJ, USA) was deposited on the master under vacuum for 4 h prior to embossing. Poly(dimethylsiloxane) (PDMS) was cast at a 10:1 ratio (base to crosslinking agent; Sylgard 184, Dow Corning, Midland, MI, USA) on the master to a depth of ~4 mm; the polymer was then cured at 100°C for 4 h. The cured PDMS replica was carefully removed from the master and trimmed to a suitable footprint. A 1 mm

diameter bore was used to punch each inlet. For final device assembly, the PDMS replica was irreversibly plasma bonded (Harrick Plasma, Ithaca, NY, USA) to a clean glass coverslip.

Prior to operating the microfluidic device, a fresh culture of *M. smegmatis* was grown from a single colony at 37 °C in 7H9 with ADC component to an absorbance at 600 nm of roughly 1 (Abs_{600} ~ 1). A portion of the culture was collected using a benchtop centrifuge (6000 RPM for 10 min) and was re-suspended in fresh media to Abs_{600} = 1 to wash the cells and standardize the cell concentration. This cell suspension was diluted 1:100 before it was flowed through the microfluidic device. Just prior to loading the cell suspension on-chip, plain fresh media was pumped through the device using a syringe pump (Harvard Apparatus, Holliston, MA, USA) until all of the channels were completely filled with liquid. Once filled, the 1:100 cell suspension was pumped through the device (at a flow rate of 50 μL/h) until the majority of the observation areas contained a small number of cells. After seeding the device with cells, fresh growth media was pumped continuously through the device at 20 μL/h and the cells were cultured on-chip for 12 h at room temperature before they were exposed to QTF. After this culturing period, QTF was added to the media at a concentration of 250 nM and was continuously supplied to the cells (at 20 μL/h) for the remainder of the experiment.

To visualize QTF dynamics, the whole microfluidic device was mounted on an inverted microscope (Nikon Ti Eclipse; Nikon Instruments Inc, Tokyo, Japan) equipped with a CoolSNAP HQ^2 camera (Photometrics, Munich, Germany). Time-lapse images were taken immediately after the addition of the probe, and images were acquired every 10 min for up to 24 h. All images were acquired through a Nikon Plan APO 100x oil immersion objective. Phase contrast and epifluorescence images were taken at every time point. All epifluorescence images were

exposed for 2 s with an appropriate filter set. To mitigate photobleaching, the fluorescence light source was attenuated to 50% of its maximum intensity. Fresh media and probe was continuously supplied to the cells throughout the time-lapse at a flow rate of 20 μL/h.

All time-lapse images were processed using a custom R script and the Imager package (369). Briefly, to both flatten and reduce background signal, we defined the background using a low-pass filter: every image was transformed with an isotropic Gaussian blur with a large kernel size (sigma = 30 px). These background images were then subtracted from each raw image. To improve contrast, pixel intensity cutoffs were defined manually, and the distribution (histogram) of pixel intensities was stretched identically for each image. Finally, the pixels were binned (2 x 2) to reduce the overall file size.

4.5.15 *M. smegmatis* HADA and QTF Microscopy and Colocalization

M. smegmatis from a single colony was grown in 7H9 with ADC component aerobically overnight at 37 °C to saturation. Cells were diluted into fresh media, and QTF was added at 1 μM final concentration when cells were at an absorbance of 0.2 at 600 nm. Cells were exposed to QTF for at least two doubling times in the presence of QTF. HADA was added at a concentration of 500 μM for 30 min (10% of the doubling time). Cells were then washed twice in 7H9 with ADC component, spotted onto a glass-bottomed microwell dish (MatTek corporation), and covered with a 1% (w/v) agarose pad. Images were collected at room temperature with a Nikon A1 laser scanning confocal microscope (Nikon Instruments). Images were acquired with a Nikon plan apo 100/1.4 oil objective with a 1.2-AU pinhole diameter and NIS-elements C software (Nikon Instruments) with appropriate filter sets. Brightness and contrast were identically adjusted within each channel with the open-source Fiji distribution of

ImageJ. To perform colocalization analysis, individual bacteria displaying QTF and/or HADA fluorescence were analyzed in the open-source Fiji distribution of ImageJ using the Plot Profile function. For each bacterium, the maximum fluorescence of each plot was collected. The maximum fluorescence levels were normalized to the highest fluorescence value and plotted against its position along the long axis of the bacterium, which was normalized to 1. The analysis was performed on the listed number of individual bacteria and expressed as mean ± SD (standard deviation). Plots were generated using R/ggplot2 (370).

M. smegmatis mCherry fusion protein microscopy: M. smegmatis harboring Ag85-mCherry fusion plasmids was cultured in M63 + 0.02% Tween-80 and induced in early logarithmic phase, OD_{600} = 0.3 with 0.2% acetamide for 6 hours at 37 °C. For analysis by microscopy, cell aliquots were spotted onto a glass-bottomed microwell dish (MatTek corporation) and covered with a 1% (w/v) agarose pad. Images were collected at room temperature with a Nikon A1 laser scanning confocal microscope (Nikon Instruments). Images were acquired with a Nikon plan apo 100/1.4 oil objective with a 1.2-AU pinhole diameter and NIS-elements C software (Nikon Instruments) with appropriate filter sets. Identical acquisition settings were used for all samples. Brightness and contrast were identically adjusted with the open-source Fiji distribution of ImageJ. Protein distribution was analyzed using the Plot Profile function in the open-source Fiji distribution of ImageJ. For each bacterium, the maximum fluorescence of each plot was collected. The maximum fluorescence levels were normalized to the highest fluorescence value and plotted against its position along the long axis of the bacterium. Heat maps were generated in Microsoft Excel for the listed number of cells analyzed (n = 30-50).

M. smegmatis Msmeg_6398-mCherry and QTF analyzed by microscopy: To image QTF colocalization with *M. smegmatis* expressing Msmeg_6398-mCherry, we used a modified agar pad method (371). Briefly, *M. smegmatis* harboring a plasmid encoding an mCherry fusion to Msmeg_6398 was grown in 7H9 without ADC and supplemented with kanamycin at 25 µg/mL aerobically overnight at 37 °C. Cells were diluted into fresh 7H9 without ADC with kanamycin at 25 µg/mL and sub-cultured to mid-logarithmic density as determined by absorbance at 600 nm (0.4-0.6). A portion of the culture (200 uL) was spotted onto a glass-bottomed microwell dish (MatTek corporation). The solution was allowed to settle for 10 min and then aspirated to leave a thin layer on cells. Molten 0.6% top agar (2 mL) in 7H9 without ADC component and supplemented with kanamycin at 25 µg/mL and 1 µM QTF was poured over MatTek dish containing cells after cooling to 37 °C. Agar was allowed to solidify, and cells were incubated at room temperature for 12-15 hours prior to imaging.

MatTek dishes containing cells were imaged with a Nikon A1 laser scanning confocal microscope (Nikon Instruments). Images were acquired with a Nikon plan apo 100/1.4 oil objective with a 1.2-AU pinhole diameter and NIS-elements C software (Nikon Instruments) using appropriate filter sets and High Sensitivity GaAsP detectors. Brightness and contrast were identically adjusted all images with the open-source Fiji distribution of ImageJ.

To perform colocalization analysis, images of individual bacteria labeled with QTF and expressing Msmeg_6398-mCherry fusion fluorescence were analyzed in the open-source Fiji distribution of ImageJ using the Plot Profile function. For each bacterium, the maximum fluorescence of each plot was collected. The maximum fluorescence levels were normalized to the highest fluorescence value and plotted against its position along the long axis of the

bacterium, which was normalized to 1. The analysis was performed on the listed number of individual bacteria and expressed as mean ± SD (standard deviation). Plots were generated using R/ggplot2 (370).

Table 4-3. Primers used in this study

Primers and Gblocks	
linker-mCherry (Msm)	5'-GATAAGAGAAAGGGAGTCCAGGTGCGTCCGGGTCCGCCGGGGCGTCGGTCT CGAAGGGCGAGGAGGACAATATGGCGATTATCAAGGAATTCATGCGGTTCAAG GTCCACATGGAAGGTTCCGTCAACGGTCATGAGTTTGAAATTGAAGGGGAGGG GGAAGGGCGGCCCTACGAGGGCACCCAGACGGCGAAACTGAAAGTGACCAAG GGGGGCCCCTTGCCGTTCGCCTGGGATATTTTGTCGCCCCAATTTATGTATGGCT CGAAAGCGTATGTGAAGCACCCAGCGGATATTCCAGATTACTTGAAGCTCAGCT TTCCCGAGGGTTTCAAATGGGAACGTGTGATGAACTTTGAAGACGGGGGGGTG GTGACCGTGACCCAGGACAGCAGCCTGCAAGACGGGGAGTTCATTTACAAAGT CAAACTCCGGGGCACGAATTTTCCGAGCGATGGGCCGGTCATGCAAAAGAAGA CGATGGGTTGGGAAGCCAGCTCCGAACGCATGTATCCGGAGGATGGGGCGCTC AAGGGCGAGATCAAGCAACGTCTGAAACTCAAGGACGGTGGCCACTACGACG CGGAGGTGAAAACGACGTACAAAGCGAAAAAGCCGGTCCAGCTGCCGGGGGC CTACAATGTGAATATTAAGCTCGATATTACGTCCCACAATGAGGATTATACCATT GTGGAACAATACGAACGCGCGGAAGGTCGTCATTCCACGGGGGGGATGGACG AGCTCTATAAGTAATAAAGCTGCAGAATTCGAAGCTT-3'
plam12 inv F	5'-AGCTGCAGAATTCGAAG-3'
plam12 inv R	5'-TGGACTCCCTTTCTCTTATC-3'
plam12 MC inv F	5'-GGTGCGTCCGGGTCC-3'
plam12 MC inv R	5'-TGGACTCCCTTTCTCTTATCGGGTG-3'
Msmeg_3580 F	5'-GATAAGAGAAAGGGAGTCCATTGGTTGCCGTTATGAAGTTCATTCGAG-3'
Msmeg_3580 R	5'-GGACCCGGACGCACGAGCACCCGCTGGATGTC-3'
Msmeg_6398 F	5'-GATAAGAGAAAGGGAGTCCAATGAAGTTCGTTGGGAGAATGCGCGG-3'
Msmeg_6398 R	5'-GGACCCGGACGCACCAGCACGCGCTGCAGGTC-3'
Msmeg_6399 F	5'-GATAAGAGAAAGGGAGTCCAATGGCACCCATGGTGAGC-3'
Msmeg_6399 R	5'-GGACCCGGACGCACCAGCGAAGCGATCAGGTCAG-3'
Msmeg_6583 F	5'-GATAAGAGAAAGGGAGTCCAGTGAAGCCCTCGTTTTTCTC-3'
Msmeg_6583 R	5'-GGACCCGGACGCACGAGGACCCGCAACAGATC-3'
H_6 F	5'-/5phos/TAATAAAGCTGCAGAATTCGAAGCTTAT-3'
H_6 R	5'-/5phos/ATGGTGGTGATGATGGTG CGACGCCCCGGC-3'
plam12 ATG-MC inv F	5'-/5phos/ATGGGTGCGTCCGGGTC-3'
plam12 ATG-MC inv R	5'-/5phos/TGGACTCCCTTTCTCTTATCGGG-3'
plam12_3580MC KK F	5'-/5phos/AAGAAATTTGTGATCGGTGCCCT-3'
plam12_3580 MC KK R	5'-/5phos/CAGGGCTTTCCATGCTG-3'
plam12_6398 MC KK F	5'-/5phos/AAGAAACTGACGGTTGCGGTC -3'
plam12_6398 MC KK R	5'-/5phos/ CGACAGACCTGCCGC-3'

plam12_6399 MC KK F	5′-/5phos/AAACTGCTGGTGGCGACAGT-3′
plam12_6399 MC KK R	5′-/5phos/CAGACCGGATACGCGCA-3′
plam12_3580MC Δss F	5′-/5phos/TTTTCCCGTCCTGGTCTG-3′
plam12_3580 MC Δss R	5′-/5phos/CAATGGACTCCCTTTCTCTTATCGG-3′
plam12_6398 MC Δss F	5′-/5phos/TGGTCTCGACCCGGC-3′
plam12_6398 MC Δss R	5′-/5phos/CATTGGACTCCCTTTCTCTTATCGG-3′
plam12_6399 MC Δss F	5′-/5phos/TTTTCGCGTGAGGGCC-3′
plam12_6399 MC Δss R	5′-/5phos/CATTGGACTCCCTTTCTCTTATCGG-3′
linker-mCherry (Cgl)	5′- GGAGCTTCTGGTTCTGCTGGAGCGTCAGTCTCGAAGGGCGAGGAGGACAATAT GGCGATTATCAAGGAATTCATGCGGTTCAAGGTCCACATGGAAGGTTCCGTCAA CGGTCATGAGTTTGAAATTGAAGGGGAGGGGGAAGGGCGGCCCTACGAGGGC ACCCAGACGGCGAAACTGAAAGTGACCAAGGGGGGCCCCTTGCCGTTCGCCTG GGATATTTTGTCGCCCCAATTTATGTATGGCTCGAAAGCGTATGTGAAGCACCC AGCGGATATTCCAGATTACTTGAAGCTCAGCTTTCCCGAGGGTTTCAAATGGGA ACGTGTGATGAACTTTGAAGACGGGGGGGTGGTGACCGTGACCCAGGACAGC AGCCTGCAAGACGGGGAGTTCATTTACAAAGTCAAACTCCGGGGCACGAATTT TCCGAGCGATGGGCCGGTCATGCAAAAGAAGACGATGGGTTGGGAAGCCAGC TCCGAACGCATGTATCCGGAGGATGGGGCGCTCAAGGGCGAGATCAAGCAAC GTCTGAAACTCAAGGACGGTGGCCACTACGACGCGGAGGTGAAAACGACGTA CAAAGCGAAAAAGCCGGTCCAGCTGCCGGGGGCCTACAATGTGAATATTAAGC TCGATATTACGTCCCACAATGAGGATTATACCATTGTGGAACAATACGAACGCG CGGAAGGTCGTCATTCCACGGGGGGGATGGACGAGCTCTATAAGTAAAAGATA TGACCATG-3′
pEKEx2 F	5′-ATTACGCCAAGCTTGCATGC-3′
pEKEx2 R	5′-CCACACATTATACGAGCCGAT-3′
Cgl-linker-mCherry F	5′- ATCGGCTCGTATAATGTGTGGGGAGCTTCTGGTTCTGC-3′
Cgl-linker-mCherry R	5′- GCATGCAAGCTTGGCGTAATCATGGTCATATCTTTTACTTATAGA-3′

Table 4-4. Plasmids used in this study

Plasmids	Properties	Source
Plam12	Kan^R; acetamidase promoter, mycobacterial origin of replication	van Kessel et al Nat Methods. 2007 Feb . 4(2):147-52
Plam12-mCherry	Plam12 with C terminus mCherry (for fusion)	this work
Plam12-ATG-mCherry	Plam12 with C terminus mCherry (for expression)	this work
plam12-3580-mCherry	Plam12 with C terminus mCherry and Msmeg_3580	this work
plam12-6398-mCherry	Plam12 with C terminus mCherry and Msmeg_6398	this work

plam12-6399-mCherry	Plam12 with C terminus mCherry and Msmeg_6399	this work
plam12-ss(kk)-3580-mCherry	Plam12 with C terminus mCherry and Msmeg_3580 and signal sequence R mutated to K	this work
plam12-ss(kk)-6398-mCherry	Plam12 with C terminus mCherry and Msmeg_6398 and signal sequence R mutated to K	this work
plam12-ss(kk)-6399-mCherry	Plam12 with C terminus mCherry and Msmeg_6399 and signal sequence R mutated to K	this work
plam12-Δss-3580-mCherry	Plam12 with C terminus mCherry and Msmeg_3580 and no signal sequence	this work
plam12-Δss-6398-mCherry	Plam12 with C terminus mCherry and Msmeg_6398 and no signal sequence	this work
plam12-Δss-6399-mCherry	Plam12 with C terminus mCherry and Msmeg_6399 and no signal sequence	this work
plam12-3580-H_6	Plam12 with C terminus 6xHis tag and Msmeg_3580	this work
plam12-6398-H_6	Plam12 with C terminus 6xHis tag and Msmeg_6398	this work
plam12-6399-H_6	Plam12 with C terminus 6xHis tag and Msmeg_6399	this work
plam12-6583-H_6	Plam12 with C terminus 6xHis tag and Msmeg_6583	this work
pEKEx2	Kan^R; pTac promoter, *E. coli* origin of replication, *C. glutamicum* origin of replication	Eikmanns, Bernhard J., et al. Gene 102.1 (1991): 93-98.
pEKEx2-mCherry	pEKEx2 expressing mCherry	this work

4.6 Contributions

QTF and cleavage standards Q-Tre and Lipid-Fl were synthesized by Dr. Robert Brown. In-gel digests and subsequent MS analysis as well as HRMS analysis was performed by the UW-Madison Biotechnology Center Mass Spectrometry/Proteomics Facility. *M. tuberculosis* Ag85 proteins were obtained through BEI Resources, NIAID, NIH. Microfluidic device was fabricated

by John Crooks and subsequent *M. smegmatis* time-lapse microscopy was performed by John Crooks.

4.7 Acknowledgements

We acknowledge experimental assistance from Dr. Elle Grevstad at the UW-Madison Biochemistry Optical Core, Dr. Dan Stevens at the UW-Madison Biophysics Instrumentation Facility and Dr. Greg Barrett-Wilt and Grzegorz Sabat at the UW-Madison Biotechnology Center Mass Spectrometry/Proteomics Facility. Plasmid pEKEx2 was kindly provided by Bernhard Eikmanns. We also acknowledge Sayaka Masuko for helpful discussion.

Chapter 5

A Glycolipid Sugar-Donor-Based Method for Cell Wall Modification of Mycobacterial Arabinan

Portions of this work have been prepared for publication:

Calabretta, P.J., Hodges, H.L., Kraft, M.B. and Kiessling, L.L. 2017. A Glycolipid Sugar-Donor-Based Method for Cell Wall Modification of Mycobacterial Arabinan

5.1 Abstract

Despite the ubiquity and importance of saccharides in biology compared to other biomolecules, there are relatively few methods to modulate their structures in cells. We sought to expand upon the library of structures that could be interrogated in bacteria through the development of a targeted chemical complementation mechanism using exogenous lipid-linked sugar donors. Utilizing a library of arabinofuranosyl phospholipids, we demonstrate incorporation of cell wall arabinose in *Corynebacterium glutamicum*. Using this method, the introduction of an isotopic label was leveraged to characterize the recovered arabinan and determine which arabinofuranosyl transferases process the exogenous lipid-linked sugar donor. Finally, microscopy of arabinan deficient cells complemented with the lipid-linked sugar donor indicated full recovery of the cell envelope. The chemical complementation method described herein should be useful for probing the function of periplasmic prokaryotic glycosyltransferases and oligosaccharyltransferases. Additionally, performing chemical complementation with non-natural arabinose donor analogs should further expand the utility of this method and provide insight into the role of the arabinan.

5.2 Introduction

The highly glycosylated surfaces of bacterial cells mediate important interactions between cells and their environment. These prominent and accessible carbohydrates affect pathogen virulence, invasion, and subversion of the immune system (81, 372). Glycans found on bacteria are exceedingly diverse in regard to the repertoire of monosaccharides involved in their construction, linkages, and modifications (163, 373). The specific composition of these glycans and their spatial organization forms the basis for molecular interactions that mediate biological responses (374-377). The specific roles of many bacterial glycans have not been determined due to either limited ability to synthesize these complex carbohydrates or a lack of tools to modulate their structures. The non-template driven nature of their biosynthesis and aforementioned structural complexity have made it difficult to predict and access bacterial glycans.

Small molecule probes including inhibitors (378) and non-natural substrates (379-382) can enable rapid perturbation of glycans *in vivo* and therefore represent powerful tools to interrogate glycan biology. Indeed, incorporation of non-natural carbohydrate substrates (383, 384) into cell surface glycans has been widely applied in mammalian cells and has allowed access to glycans containing reporter groups- including biologically or chemically reactive handles. Application of this technique has facilitated the detection (96, 332), capture, and modification of glycans to discern their cellular roles, as well as characterization of biosynthetic enzymes (385-388). However, cognate incorporation of non-natural carbohydrate substrates in bacteria has only a handful of examples (68, 96, 332, 389-392). This vast discrepancy stems from fundamental differences in mammalian and bacterial glycobiology including the diversity of

carbohydrates bacteria employ (83, 393) and how they acquire, use, and biosynthesize monosaccharides (394). Therefore, methods to improve the ability to incorporate non-natural monosaccharides in bacteria that access unique bacterial sugars and target specific bacterial polysaccharides are necessary to explore the unique roles many bacterial glycans perform. Mammalian cell metabolic incorporation strategies largely require the availability of promiscuous transporters or intracellular enzymes for deprotection of membrane permeable sugars, the presence of which are species-dependent in bacteria (384, 389). This can be accomplished in bacteria by exploiting existing salvage pathways (389) or shunting probes through the central metabolism (390). However, bacteria are adept at utilizing monosaccharides as energy sources, whereby some metabolic precursors may be able to enter multiple biosynthetic pathways (395). We envisioned an alternative method, biosynthetic incorporation, where the donor monosaccharide bypasses metabolic enzymes and is utilized directly by glycosyltransferases (**Figure 5-1**). Intervening with a sugar donor rather than a precursor would eliminate metabolic probe catabolism and subsequent incorporation into other metabolites. The most recognizable glycosyl donors, sugar nucleotides, are membrane impermeable (396). However, bacteria also utilize lipid-linked sugar donors, exploitation of glycolipids as probes for glycan incorporation would impart many advantageous properties. Therefore, we explored an alternative mode for non-natural substrate incorporation and subsequent glycan labeling and manipulation in bacteria, the use of lipid-linked sugar donors. Lipid-linked sugar donors are utilized by membrane-localized glycosyltransferases to generate cell surface glycans and oligosaccharyltransferases to transfer oligosaccharides en bloc; therefore, targeting external glycosyltransferases avoids permeability or import constraints

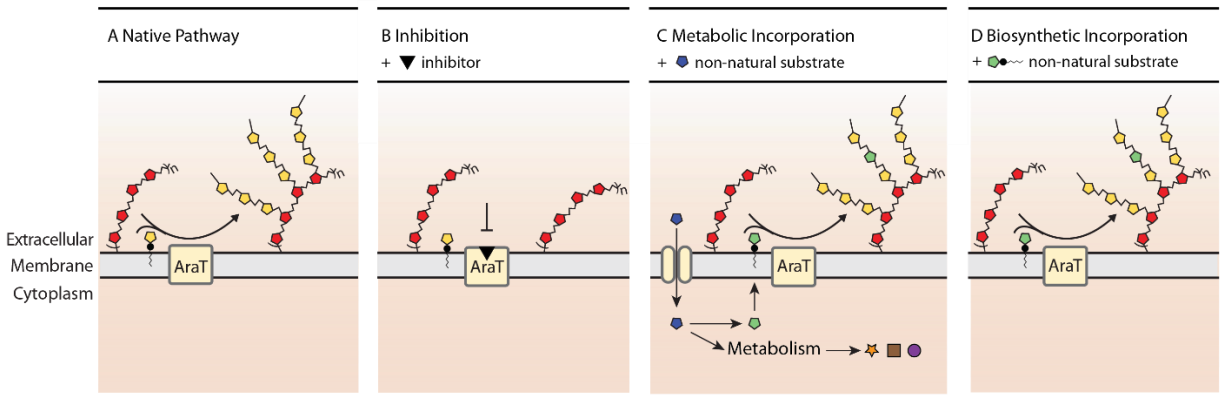

Figure 5-1. Modes of *in vivo* glycan manipulation (A) The native biosynthetic pathway can be disrupted by (B) Inhibition. Also, (C) Metabolic and (D) Biosynthetic incorporation can be used to incorporate non-natural monosaccharides into glycans. A major advantage of biosynthetic incorporation is its avoidance of central metabolism preventing probe degradation and promiscuous incorporation.

that would affect exogenously added nucleotide sugar donors. Additionally, lipid-linked sugar donors would localize to the cell membrane where they could be utilized for glycan synthesis directly. Localizing the sugar donors to their site of activity reduces overall material needs while also promoting probe incorporation over probe metabolism. Finally, the use of a committed intermediate prevents non-specific incorporation, allowing specific glycan structures to be targeted based on the identity of the sugar donor utilized and the glycosyltransferases involved.

To examine our biosynthetic incorporation strategy, we chose to explore the introduction of lipid-linked monosaccharide donors into the cell envelope of Corynebacterineae. The suborder *Corynebacterianeae* contains several important species that affect human health, most notably *Mycobacterium leprae*, *Corynebacterium diphtheriae*, and *Mycobacterium tuberculosis*. A highly-conserved feature of these bacteria is their unusual cell wall structure that complicates the treatment of infections. The mycobacterial cell wall is composed of

peptidoglycan that is decorated with linear galactan polysaccharides bearing arabinan chains at three branch points, which in turn are esterified at their termini with the inner leaflet of a mycolic acid membrane. The arabinan segment, a highly-branched polysaccharide and the focus of this work, is composed of arabinofuranose, a sugar absent from mammalian glycans. The arabinan is synthesized exclusively from the sugar donor decaprenyl phosphoryl arabinofuranose (DPA) by a series of transmembrane arabinofuranosyl transferases in a step-

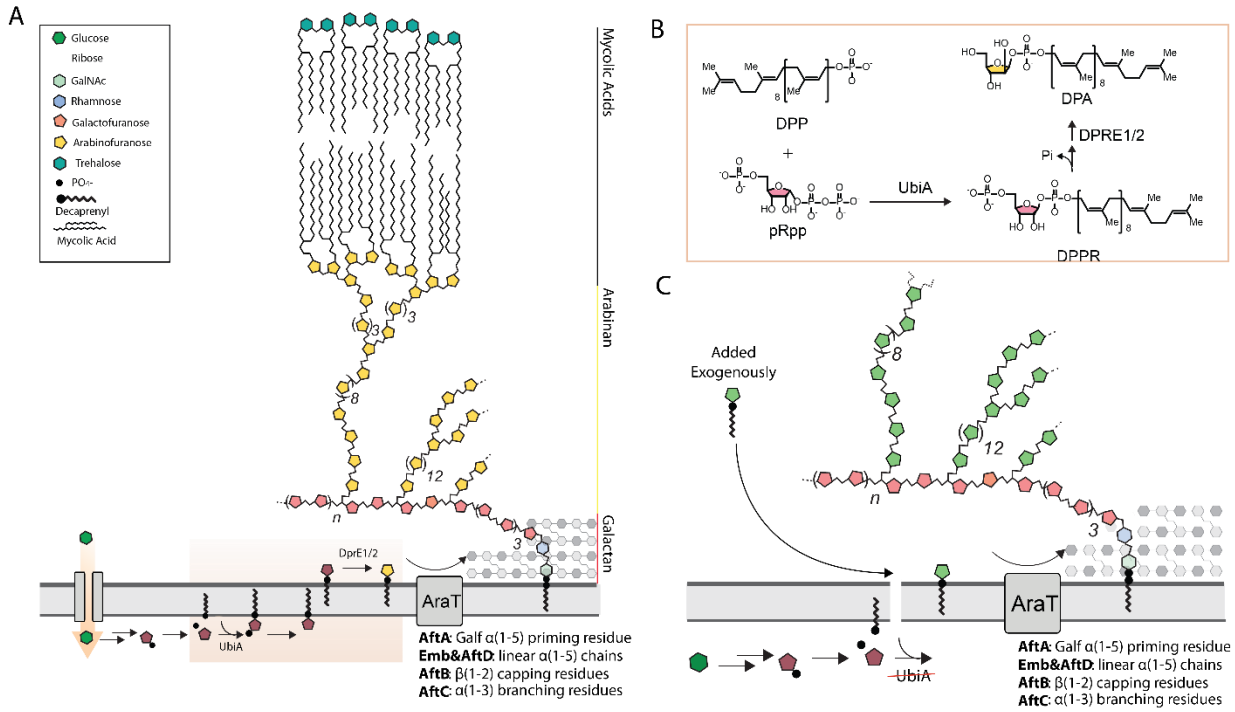

Figure 5-2. Recovery of the arabinan with analogs of decaprenyl-phosphoryl arabinofuranose (A) Components of the corynebacterial cell envelope include the mycolyl-arabinogalactan (mAG) complex. The arabinan is constructed in a step-wise fashion by arabinosyltransferases (AraTs) exclusively using the donor monosaccharide decaprenylphorphorylarabinose (DPA). DPA is generated at the plasma membrane in a five-step pathway from imported glucose. (B) UbiA is a prenyltranferase that ligates decaprenylphosphate with phosphoribosyl pyrophosphate, pRpp. A *C. glutamicum* strain lacking *ubiA* and consequently DPA and cellular arabinan has been generated and is viable. (C) Schematic depicting complementation of the arabinan using an exogenous, lipid-linked arabinose donor in *CgΔubiA* lacking arabinan which can be substituted with a supplied DPA analog.

wise fashion (**Figure 5-2A&B, Figure 5-3**) (397-402). Construction of the arabinan is initiated with AftA (NCgl0185), which transfers the first arabinofuranose (Ara*f*) residue onto the C5 galactofuranose hydroxyl of the galactan, at the 8th, 10th, and 12th residues (397). The galactan is a nominally 30 unit long peptidoglycan anchored linear carbohydrate composed of alternating β(1→5) and β(1→6) linkages of galactofuranose. Emb (NCgl0184), elaborates the linear α(1,5)-linked arabinan core. AftC (NCgl1822) is an α(1,3) transferase with a role in

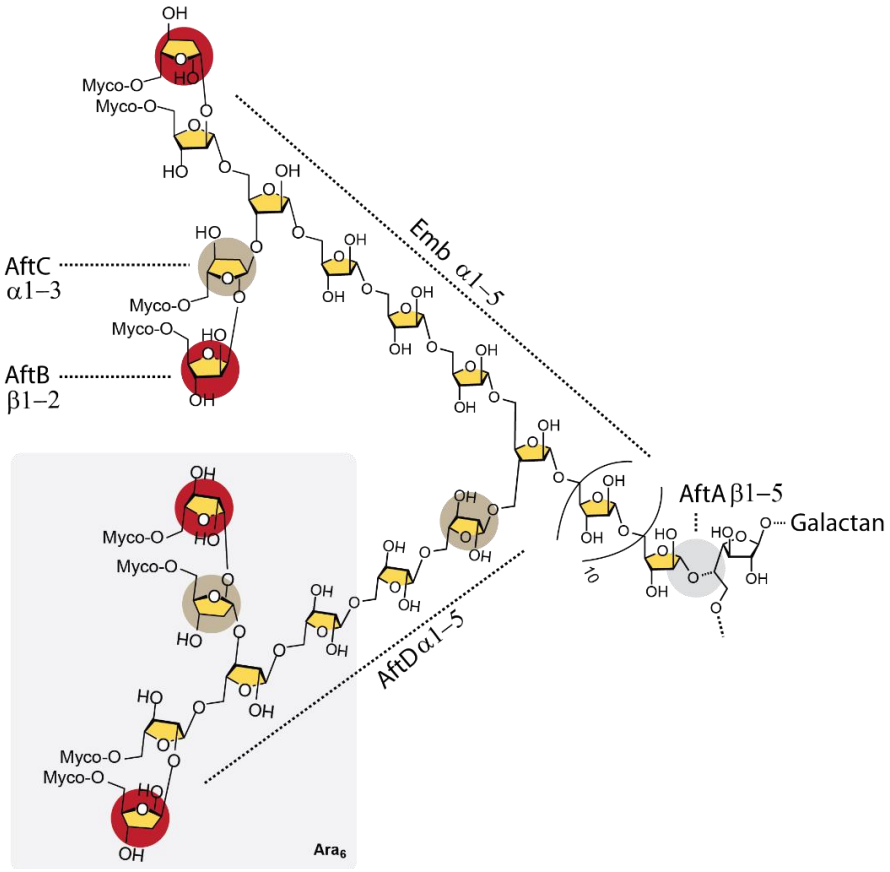

Figure 5-3. Enzymatic construction of the mycobacterial arabinan
Assigned linkages generated by AraTs are indicated as well as the terminal Ara_6 motif.

generating Ara*f* branching residues (399). AftD (NCgl2757) was recently shown to function as an α(1,5) transferase to extend the initial 3,5 branch point (403). Finally, AftB (NCgl2780), attaches a terminal β(1,2) Ara*f* residues on the non-reducing end of the arabinan (400). This

terminal residue can further be mycolylated by mycolyltransferases to form the mycolic acid membrane. A strain of *Corynebacterium glutamicum* with a disruption in *ubiA*, a decaprenyl-phosphate 5-phosphoribosyltransferase, (*CgΔubiA*) that is responsible for the commitment of ribose to form DPA is viable. *CgΔubiA* possess active AraTs and is subsequently devoid of arabinan and therefore provides a simple system for evaluating the ability to screen the exogenous delivery of DPA analogs (**Figure 5-2C**) (397). Successful biosynthetic incorporation of a DPA analogs would facilitate *in situ* assembly and manipulation of the arabinan *and* evaluation of the promiscuity of the difficult to study arabinan biosynthetic enzymes. Improved comprehension of cell wall biosynthesis in *Corynebacterianeae* could improve current understanding of mycobacterial infections and mechanisms of persistence, as well as illuminate untapped antibiotic targets.

Herein we report the recovery of cell wall arabinan via the addition of non-natural lipid-linked arabinofuranose sugar donors to *CgΔubiA*. This method of biosynthetic incorporation was leveraged to introduce carbon-13 selectively into the arabinan, allowing NMR characterization of the resulting arabinan structures. Finally, cellular envelopes were visualized by electron microscopy where we observed that treatment of the arabinan-deficient cells with our arabinofuranose sugar donors was sufficient to regenerate structurally complete native cell walls. Therefore, we demonstrate a method of biosynthetic incorporation that is a promising tool for dissecting enzymatic pathways as well as structural and functional properties of glycans.

5.3 Results

5.3.1 Design and Chemical Properties of a Synthetic Library of DPA Analogs

DPA **5-1** is a D-arabinofuranose linked by a monophosphate to a decaprenyl lipid. We developed a library of DPA analogs (**Figure 5-4**) based on a previously published synthetic route from our group (404). We installed variation in the lipid tail to investigate enzymatic recognition of decaprenyl structure by the arabinofuranosyl transferases involved in arabinan construction and to identify a DPA analog that could afford synthetic tractability and aqueous solubility. DPA lipid analogs comprised three classes: terpenoid, alkyl, and cyclic. Farnesylphosphoryl D-arabinose, FPA **5-2**, was included in the library in spite of the synthesis required since it is a known substrate of the arabinofuranosyl transferase, Aft-C (388). The diterpenes, nerylphosphoryl D-arabinose, NPA **5-3**, and (R)-citranellyl **5-4**, were included in the library to probe how different lengths and three-dimensional structures affect processing by AraTs. Octyl **5-5**, phenyloctyl **5-6**, and dodecyl **5-7** phosphoryl arabinofuranose analogs were

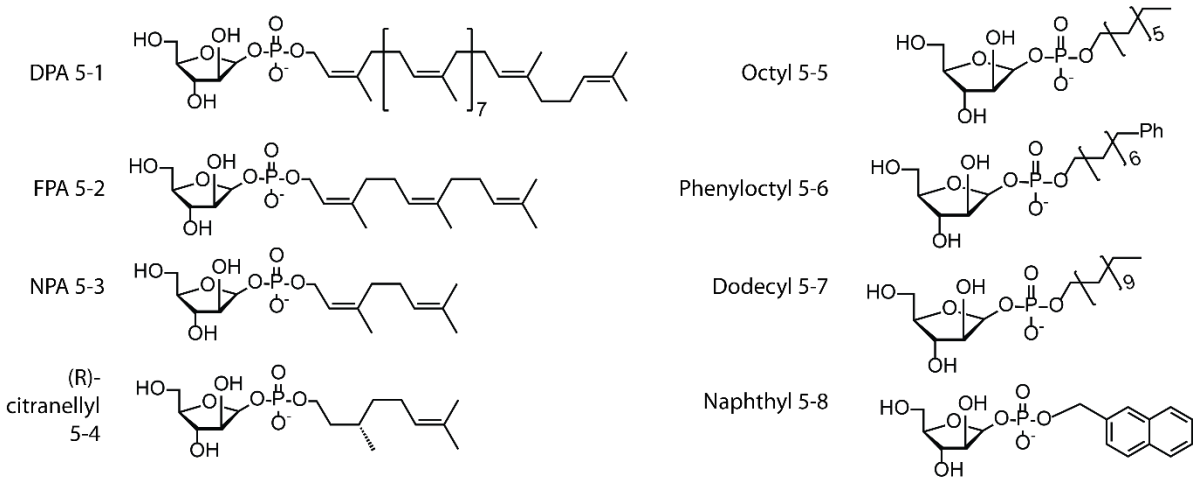

Figure 5-4. Library of DPA analogs.

included as inexpensive, commercially available lipids that likewise probed the importance of length and three-dimensional structure. Finally, the inclusion of a naphthyl analog **5-8** provided an outlier that was unlikely to act a sugar donor based on the lack of incorporation of (E)-olefin containing terpenes.

5.3.2 Recovery of Cell Wall Arabinose Using Synthetic DPA Analogs

We wanted to assess the ability of DPA analogs to be incorporated as cell wall polysaccharides by the araTs of *Cg*Δ*ubiA*. Therefore, we treated *Cg*Δ*ubiA* with our library of DPA analogs (250 μM). Cell wall composition analysis of the treated cells indicated that several of the synthetic analogs led to arabinose incorporation (**Figure 5-5**). The naphthyl analog **5-8**, as expected, did not lead to arabinose incorporation. However, the extent of arabinose incorporation showed a dependence on lipid length. The longest n-alkyl lipid analog, dodecyl phosphoryl arabinofuranose **5-8**, produced the highest amount of arabinose incorporation among the alkyl lipids. Meanwhile, the octyl analog **5-6** led to no appreciable incorporation. Similarly, FPA **5-2**, the analog bearing the longest terpene lipid, yielded higher levels of arabinose incorporation than either of the diterpene analogs. The data also suggest that the three-dimensional structure is important for effective recovery since FPA **5-2** treatment produced cells with higher arabinose content than dodecyl phosphoryl arabinofuranose **5-7** despite having lipids of similar length.

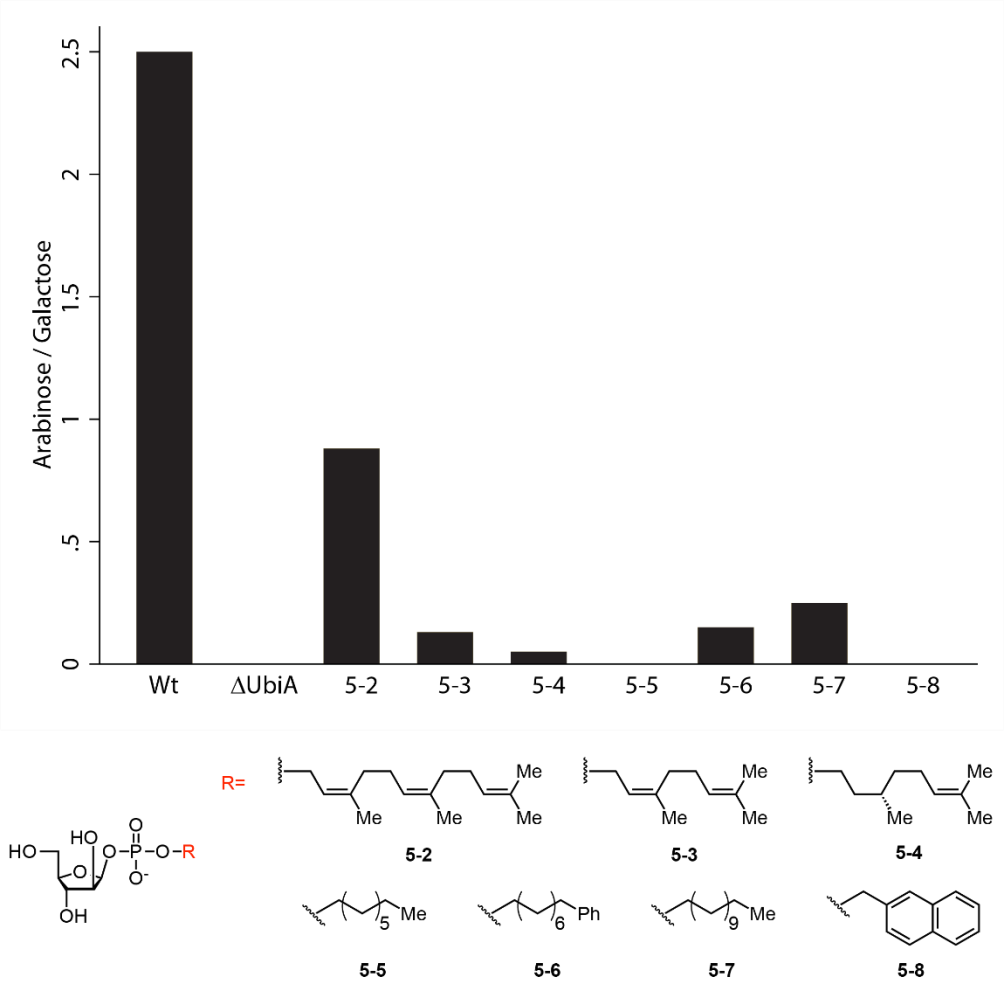

Figure 5-5. Arabinose incorporation as a function of sugar donor structure
Recovery was performed at 250 μM for each DPA analog. (Z,Z)-farnesol **5-2** produced the highest levels of arabinose incorporation.

5.3.3 Dose Dependence of Arabinose Complementation

Since FPA **5-2** led to the highest arabinose incorporation by cell wall composition analysis, we next assessed how the extent of recovery changed as a function of FPA **5-2** concentration. This was tested by varying the final concentration of FPA **5-2** in the medium during growth with *Cg*Δ*ubiA*. It was found that there was a dose dependence of arabinan recovery with FPA **5-2** (**Figure 5-6**). The extent of arabinose incorporation increased as a function of FPA **5-2**

concentration up to 500 µM; above 500 µM arabinose incorporation decreased. This concentration, 500 µM, was used in all subsequent biosynthetic incorporation experiments.

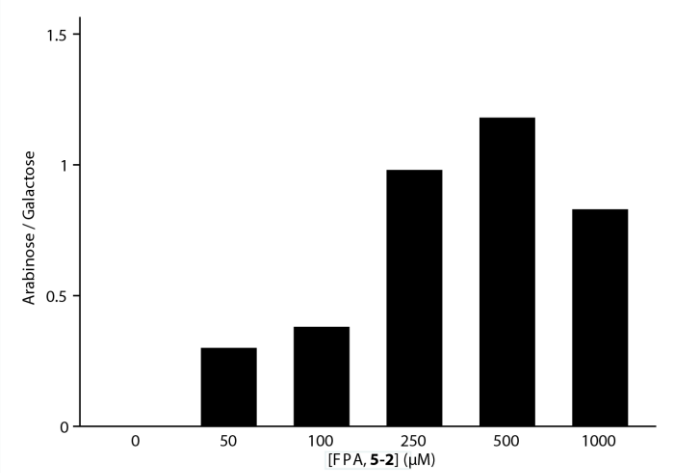

Figure 5-6 Arabinose incorporation as a function of FPA concentration
The highest amount of arabinose incorporation into the corynebacterial cell wall was observed with cells grown with 500 µM FPA **5-2**.

5.3.4 1-^{13}C-FPA

A 1-^{13}C-labeled version of FPA **5-2** was produced by the same synthetic scheme used to produce unlabeled FPA developed in the Kiessling research group (404). Labeling the anomeric position is expected to increase the signal-to-noise ratio of peaks in the anomeric region of ^{13}C NMR experiments during assignment of the arabinan structure from isolated arabinan generated by biosynthetic incorporation. *Cg*Δ*ubiA* cells treated with 1-^{13}C-FPA were analyzed by cell wall composition analysis and indicated that the extent of arabinose incorporation was comparable to FPA without the ^{13}C-label (**Figure 5-7**).

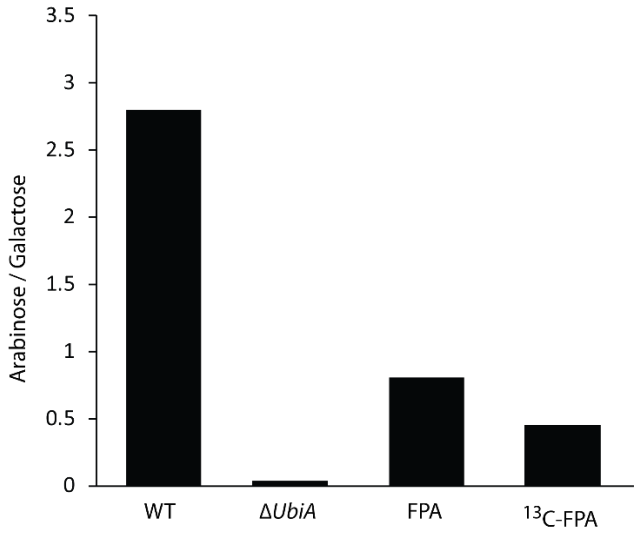

Figure 5-7. Arabinose incorporation of 1-^{13}C-FPA Presence of ^{13}C-label on FPA did not appreciably affect incorporation into the corynebacterial cell wall.

5.3.5 NMR Characterization of Arabinan after Biosynthetic incorporation of 1-^{13}C-FPA

5.3.5.1 HSQC of Arabinan from *C. glutamicum*

Intact arabinogalactan from *Mycobacterium bovis BCG* and *Mycobacterium smegmatis* has been fully characterized by Lee et al. using NMR, including 2D ^{1}H-^{13}C heteronuclear single quantum correlation (HSQC) (405). We recapitulated the HSQC characterization of arabinogalactan from *C. glutamicum* ATCC 13032. Analysis of the spectra indicates that resonances corresponding to the carbohydrate and anomeric regions are present. Analysis of the peaks indicated that relevant arabinogalactan resonances remain consistent between these species (Arabic numerals, **Figure 5-8**, **Table 5-1**).

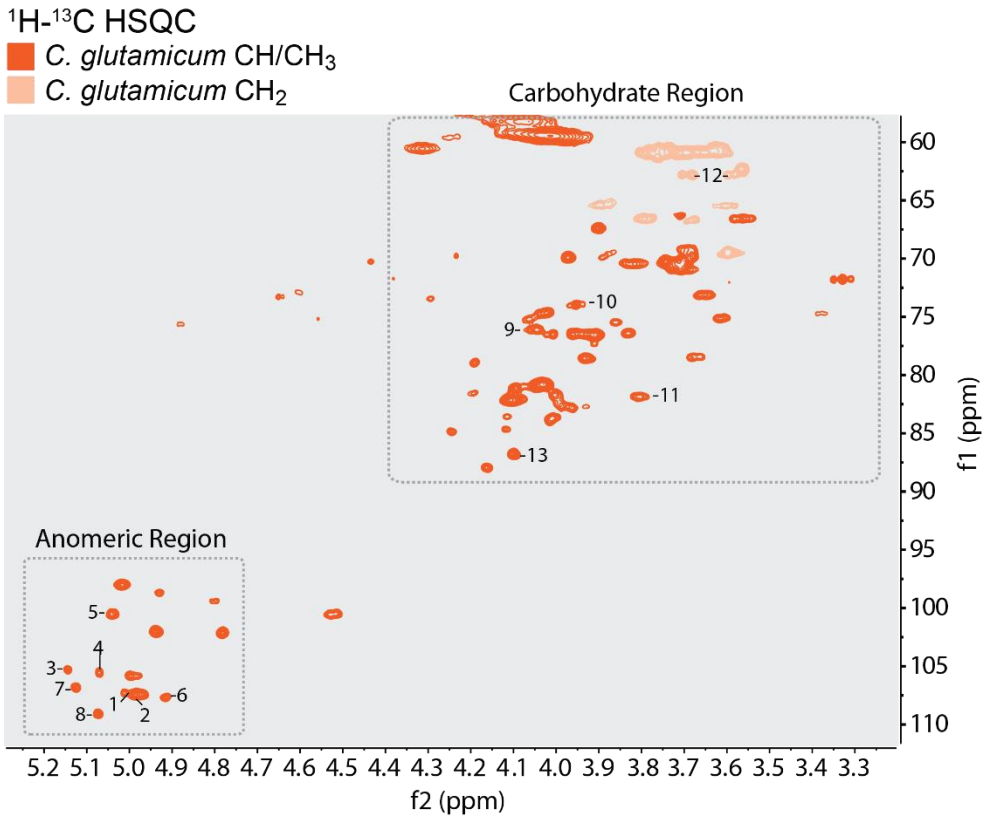

Figure 5-8. HSQC of WT *C. glutamicum*
Glycosyl residues are denoted in Arabic numerals and correspond to **Table 5-1**.

Table 5-1. Reference ^{1}H and ^{13}C chemical shift assignment of Arabinan from whole-cell *M. bovis BCG;* ref Lee et al. (405)

	Residue	^{1}H Resonance	^{13}C Resonance	Signal (this work)
1	3,5-αAra*f* (C1)	5.01	107.38	VII
2	5-αAra*f* (C1)	4.99	107.48	V
3	2-αAra*f*(→3)	5.14	105.4	I
4	2-αAra*f*(→5)	5.07	105.56	IV
5	t-β-Ara*f* (C1)	5.04	100.57	III
6	5-β-Gal*f* (C1)	4.93	107.77	VI
7	6-β-Gal*f* (C1)	5.12	106.98	II
8	5,6-β-Gal*f* (C1)	5.06*	107.13*	N.D.
9	t-β-Ara*f* (C2)	4.05	76.18	IX
10	t-β-Ara*f* (C3)	3.97	74.23	X
11	t-β-Ara*f* (C4)	3.81	81.94	XI
12	t-β-Ara*f* (C5)	3.59/3.69	62.87	XII
13	2-αAra*f* (C2)	4.10	86.93	

*estimated from literature

5.3.5.2 HSQC of 1-^{13}C-FPA Labeled Arabinogalactan from *CgΔubiA*

Next, we performed HSQC (406) of the proton, ^{1}H, and ^{13}C spectra for 1-^{13}C-FPA labeled arabinogalactan from *CgΔubiA* and compared it to the HSQC spectrum of arabinogalactan isolated from wild-type cells at natural ^{13}C abundance (**Figure 5-9A**&**B**). We assigned the anomeric proton peaks for all 6 distinct arabinofuranose linkages (**Figure 5-9B, Table 5-2)**. The assigned resonances correspond to all anticipated linkages of mature arabinogalactan and agree with those previously characterized by Lee et al. (405) (**Table 5-1).** Our ^{13}C-labeling strategy also allowed for the **5-6-β-Gal*f*** peak (**VIII)** to be identified. This peak was not visible in *C. glutamicum* WT at natural abundance likely owing to its scarcity (3 residues per galactan). This result indicated that FPA **5-2** could be processed by all AraTs to generate fully assembled arabinan.

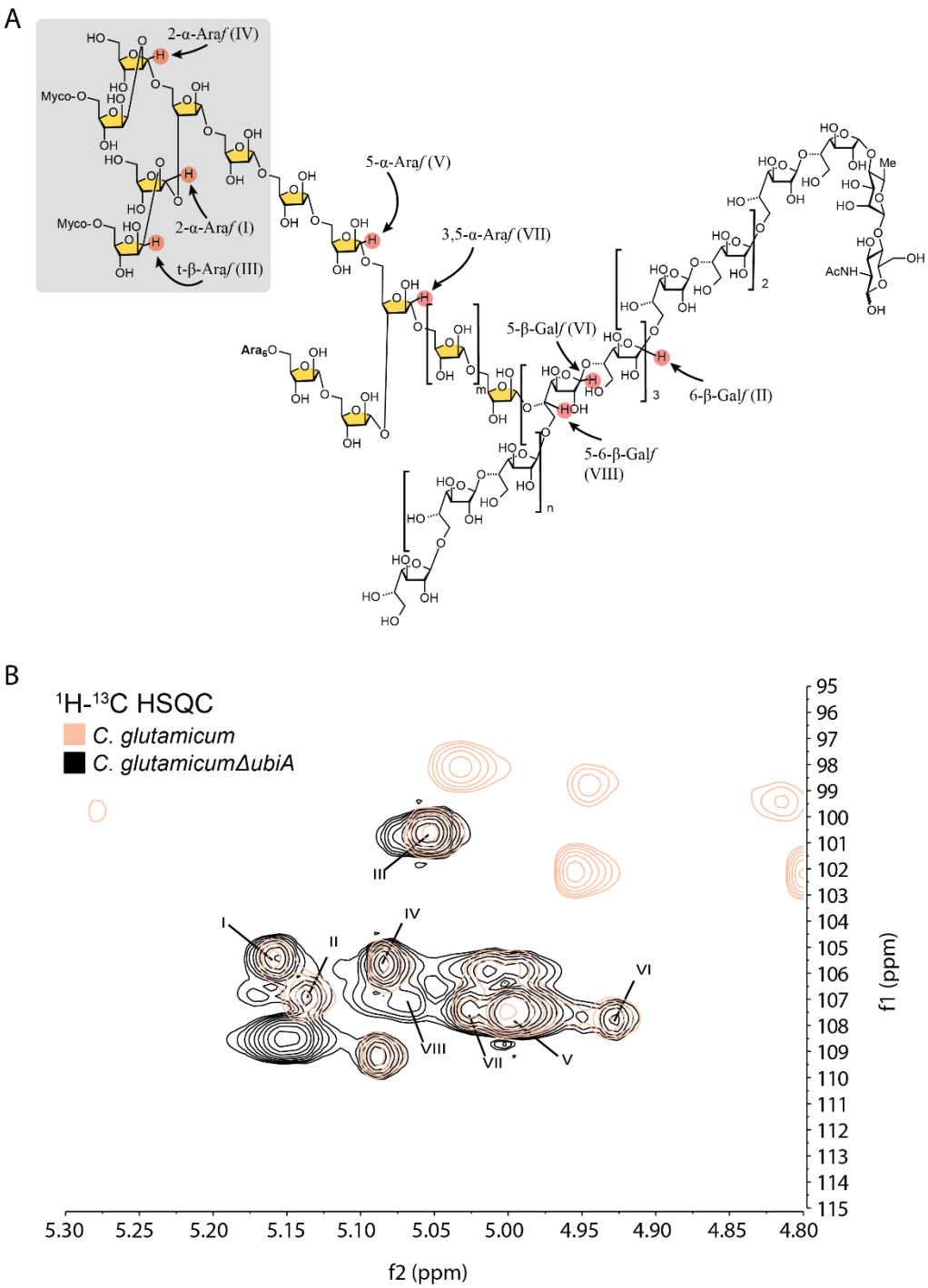

Figure 5-9. HSQC of 1-^{13}C-FPA *C. glutamicum*. The anomeric region of a ^{1}H-^{13}C HSQC spectrum of arabinogalactan *from C. glutamicum* (peach) at natural ^{13}C abundance superimposed on the ^{1}H-^{13}C HSQC spectrum of *CgΔubiA* arabinogalactan recovered with ^{1}-^{13}C-FPA (black). The spectra were recorded in D_2O at 298 K at 600MHz. All resonances corresponding to the arabinogalactan as previously characterized by Lee et al. (405) are present and tabulated in **Table 5-2.** Glycosyl residues are denoted in Roman numerals. I, 2-α-Araf *; II, 6-β-Galf; III, t-β-Araf; IV, 2-α-Araf 7; V, 5-α-Araf; VI, 5-β-Galf; VII, 3,5-α-Araf; VIII, 5,6-β-Galf;*C2 (3,5-α-Araf); 7C5 (3,5-α-Araf)

Table 5-2. ^{1}H and ^{13}C chemical shift assignment of arabinan based on the interpretation of 2D HSQC (**Figure 5-9**) with reference to **Table 5-1** (roman numerals).

Signal	Residue	^{1}H Resonance	^{13}C Resonance
I	2-α-Ara*f* *	5.16	105.44
II	6-β-Gal*f*	5.14	106.88
III	t-β-Ara*f*	5.05	100.62
IV	2-α-Ara*f* [7]	5.08	105.62
V	5-α-Ara*f*	5.00	107.48
VI	5-β-Gal*f*	4.93	107.73
VII	3,5-α-Ara*f*	5.03	107.41
VIII	5,6- β-Gal*f*	5.07	107.10

*C3 (3,5-α-Ara*f*); 7C5 (3,5-α-Ara*f*)

5.3.6 Extended NMR Characterization of the t-β-Ara*f* Residue

To further validate the formation of mature arabinan, we carried out subsequent analysis on the terminal arabinofuranose residue (t-β-Ara*f*, III) which can only be present in structurally intact arabinan. The identity of the t-β-Ara*f* residue was confirmed with 2D HSQC, total correlation spectroscopy (TOCSY) and heteronuclear multiple bond correlation (HMBC), which were used to validate the spin system of the identified t-β-Ara*f* residue and the connectivity of the glycosidic bond, respectively.

In the HSQC-TOCSY spectrum (**Figure 5-10**) five cross peaks were observed correlating to the putative anomeric resonance of the t-Araf residue. The resonances of the ring hydrogens on C2-C5 are absent as a result of the selective ^{13}C labeling from 1-^{13}C-FPA. The 1-^{13}C-FPA HSQC-TOCSY spectrum from *Cg*Δ*ubiA* was overlaid on the HSQC spectrum of arabinogalactan from wild-type cells at natural ^{13}C abundance. The five observed cross peaks are a result of mixing of the anomeric hydrogen with the other hydrogens of the t-β-Ara*f* residue. The chemical shifts

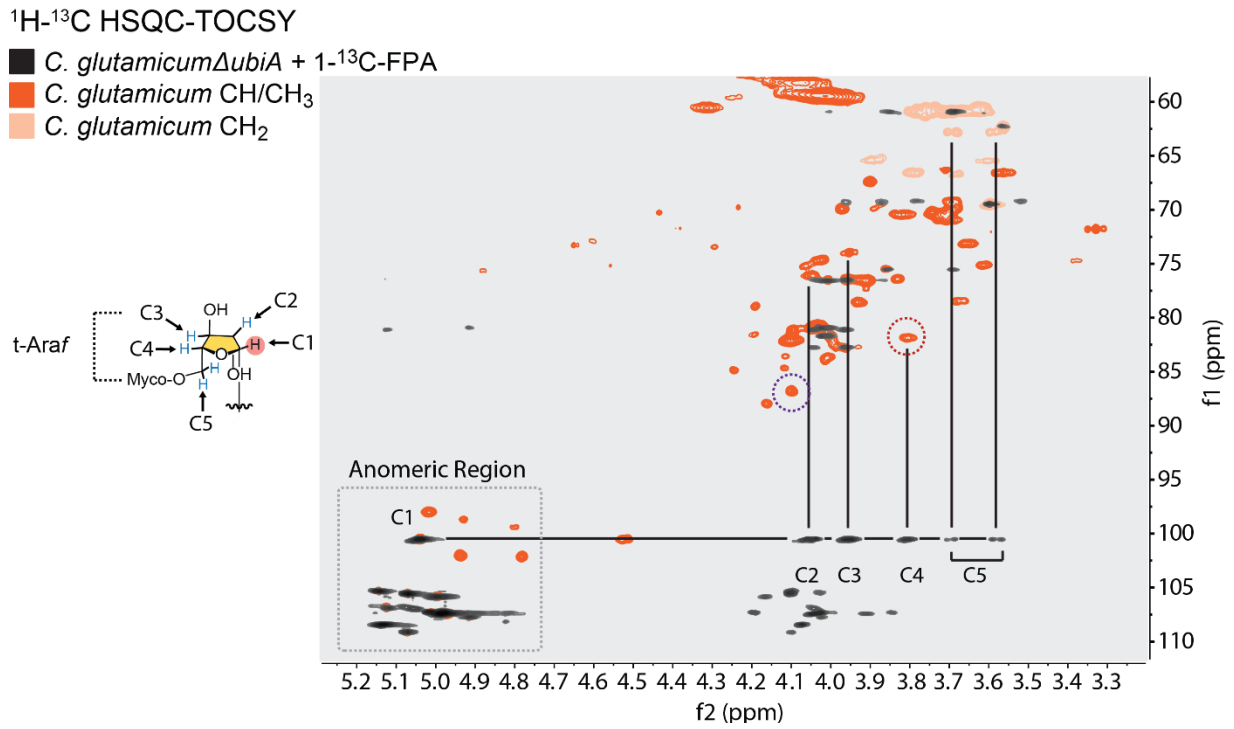

Figure 5-10. Assignment of the t-Ara*f* spin system in arabinogalactan of 1-^{13}C-FPA labeled *C. glutamicum* by HSQC-TOCSY

TOCSY peaks from 1-^{13}C-FPA labeled arabinogalactan from *CgΔubiA* (black) were correlated to resonances in the spectrum of arabinogalactan from wild-type cells at natural ^{13}C abundance (orange, CH, and CH_3; peach, CH_2). The spectra were recorded in D_2O at 298 K at 600MHz. Glycosyl residues denoted in by alphanumeric residue labeling correspond to **Table 5-3**. Purple circle denotes peak from outside spin system, also present in **Figure 5-11**. Red circle denotes peak from within spin system.

Table 5-3. ^{1}H and ^{13}C chemical shift assignment of arabinan based on the interpretation of 2D HSQC (Figure 5-10) with reference to table **5-1** (roman numerals).

Signal	Residue	^{1}H Resonance	^{13}C Resonance
III	t-β-Ara*f* (C1)	5.05	100.62
IX	t-β-Ara*f* (C2)	4.05	100.62
X	t-β-Ara*f* (C3)	3.95	100.62
XI	t-β-Ara*f* (C4)	3.81	100.63
XII	t-β-Ara*f* (C5)	3.59/3.69	100.62

on the observed TOCSY peaks in the f2 dimension are δ 4.05, 3.95, 3.81, 3.69, and 3.59 ppm, which match the resonances of the hydrogens in the t-Araf residue in previous characterizations. The observed cross peaks correlated to resonances that matched values

expected from previous characterizations of the arabinogalactan (**Table 5-1**&**3**) (405). This confirmed the identity of the assigned t-β-Ara*f*.

Further evidence for the assignment of t-β-Ara*f* was gained from HMBC experiments. Analyzing long-range carbon-proton couplings by HMBC provides information on which residues are connected and at which position. The HMBC spectrum from 1-^{13}C-FPA treated *Cg*Δ*ubiA* was overlaid on an HSQC spectrum of arabinogalactan from wild-type C. glutamicum at natural ^{13}C abundance (**Figure 5-11, Table 5-1**&**4)**. Two cross peaks developed that correlated to H1/C1 of the t-Araf. The peak at 3.80/100.63 ppm matches a resonance seen in the HSQC-TOCSY (t-β-Ara*f*(C4), red circle), suggesting it is a correlation within the terminal residue. However, the other cross peak at 4.09/100.63 ppm (purple circle) is not within the spin system. Therefore this peak is the correlation across the glycosidic bond of the terminal residue.

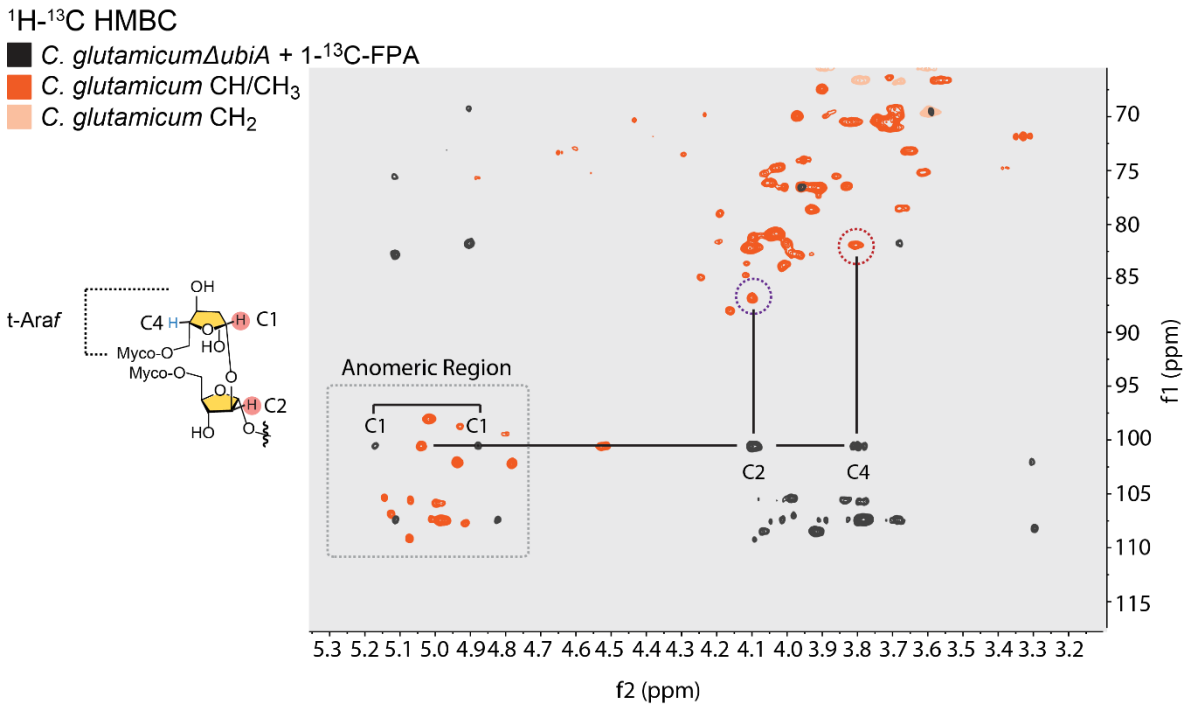

Figure 5-11. Confirmation of proper connectivity for the t-Ara*f* residue in arabinogalactan of 1-^{13}C-FPA labeled *C. glutamicum* by HMBC The correlation to the hydrogen at 4.1 ppm matches the expected chemical shifts for C-2 and H-2 of the penultimate Araf residue in the WT arabinogalactan. HMBC peaks from 1-^{13}C-FPA labeled arabinogalactan from *CgΔubiA* (black) were correlated to resonances in the spectrum of arabinogalactan from wild-type cells at natural ^{13}C abundance (orange, CH, and CH_3; peach, CH_2). Spectra were recorded in D_2O at 298 K at 600MHz. Relevant t-β-Ara*f* and 2-α-Ara*f* are labeled and listed **Table 5-4**. Purple circle denotes peak from outside spin system, also present in **Figure 5-11**. Red circle denotes peak from within spin system.

Table 5-4. ^{1}H and ^{13}C chemical shift assignment of arabinan based on the interpretation of 2D HMBC (**Figure 5-10**) with reference to table **5-1** (roman numerals).

Signal	Residue	^{1}H Resonance	^{13}C Resonance
III (split)	t-β-Ara*f* (C1)	5.17/4.88	100.63
XIII	2-α-Ara*f*(C2)	4.09	100.63
XI	t-β-Ara*f* (C4)	3.80	100.63

5.3.7 Diffusion NMR Characterization of Arabinan after Biosynthetic Incorporation of 1-^{13}C-FPA

Having previously established all necessary residues for arabinan structure. We were interested in the relative size of the recovered arabinogalactan compared with the isolated wild-type arabinogalactan. Such information could indicate if the galactan received similar levels of arabinosylation (see Figure 5-2). Fortunately, Diffusion-ordered NMR spectroscopy (DOSY), an NMR technique that provides gross measurements of molecular size, is not destructive and does not require derivatization. We obtained DOSY spectra of galactose, arabinogalactan from WT *C. glutamicum* and 1-^{13}C-FPA treated *Cg*Δ*ubiA*. DOSY analysis indicates that the arabinogalactan samples have similar diffusion coefficients, which suggests they have similar shapes and sizes.

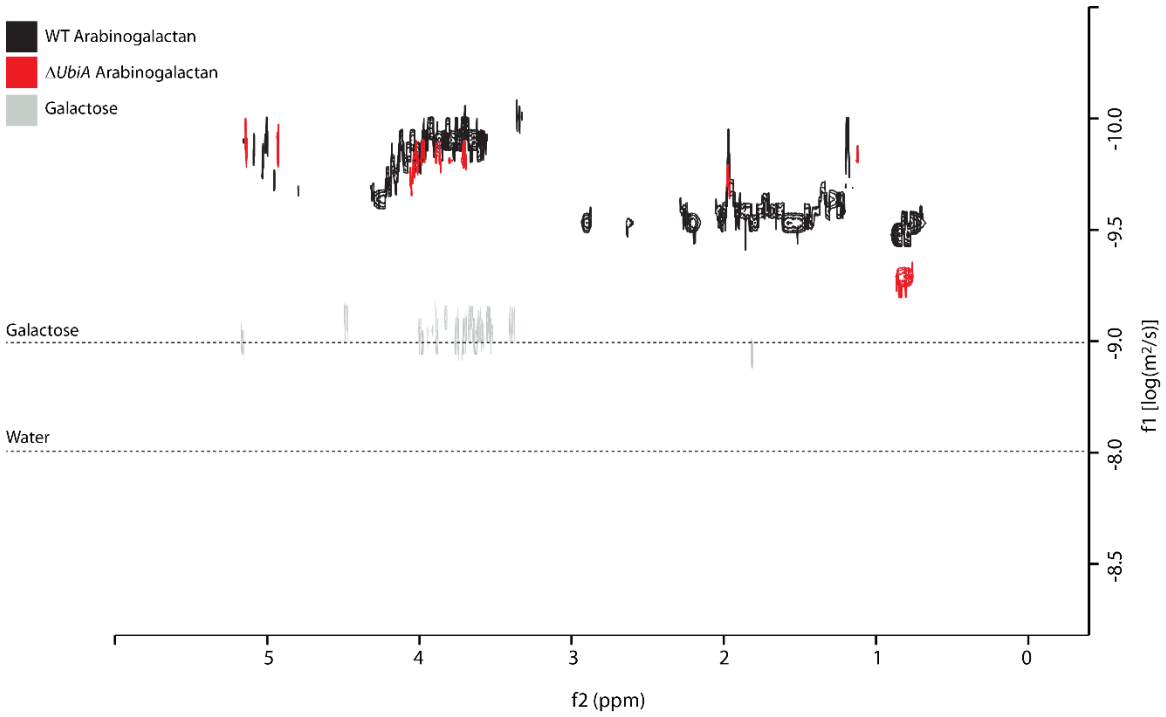

Figure 5-12. DOSY analysis of 1-^{13}C-FPA Black peaks correspond to WT *C. glutamicum* arabinogalactan. Red peaks correspond to arabinogalactan from *Cg*Δ*ubiA*. Grey peaks correspond to galactose and are indicated by a dashed line along with the peak from water. Final concentration of arabinogalactan 0.5 mg/mL

5.3.8 Full Recovery of the Corynebacterianeae Cell Wall Via Biosynthetic Incorporation of FPA

Exogenous addition of FPA was structurally characterized to contain all residues of mature *C. glutamicum* arabinan. Growth and microscopic observations revealed that *Cg*Δ*ubiA* possessed pronounced morphological defects. Electron microscopy based observation revealed only a single opaque layer which is the peptidoglycan. We anticipated that treatment of *Cg*Δ*ubiA* with FPA, given the formation of mature arabinan, should allow for mycolylation to proceed. This would be reflected in the appearance of a second opaque layer. Therefore, *Cg*Δ*ubiA* cells were treated with 500 µM FPA and visualized by electron microscopy (**Figure 5-13)**. A second dense layer, the mycolic acid membrane was observed in *Cg*Δ*ubiA* cells treated with 500 µM FPA.

Therefore, biosynthetic incorporation with FPA is sufficient to form native corynebacterial cell wall structures.

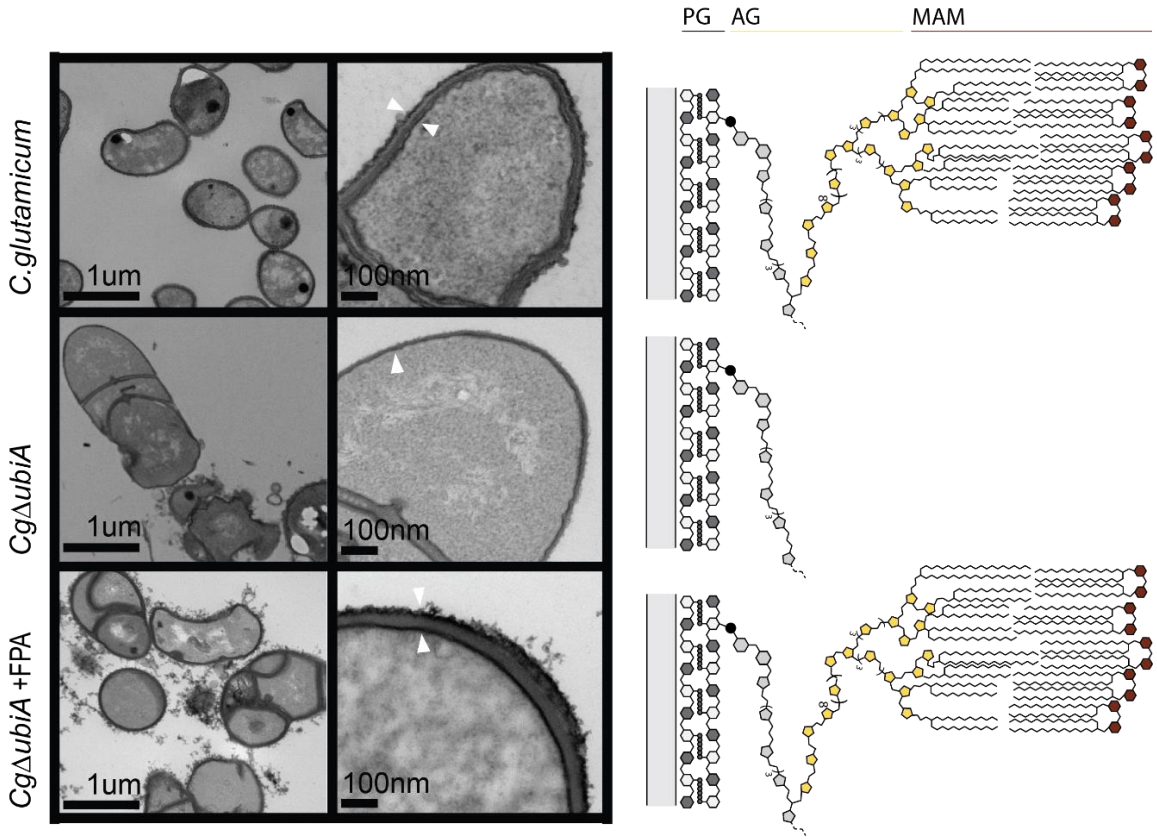

Figure 5-13. Biosynthetic incorporation of FPA can generate native cell walls Electron opaque region at the periphery the FPA treated cells, as observed by electron microscopy, indicates the recovery of the mycolic acid membrane (MAM) (*CgΔubiA* + FPA) similar to WT cells (*C. glutamicum)* and is notably absent from the arabinan-deficient mutant (*CgΔubiA*).

5.4 Discussion

We sought to demonstrate a method of bacterial glycan manipulation that expanded the scope of metabolic incorporation to include rare bacterial sugars that are synthesized de novo within cells. Towards that goal, we have demonstrated the ability to incorporate arabinose directly into the mycobacterial cell wall from synthetic lipid-linked-sugar donors. The most effective donor, FPA **5-2**, was modified to include a ^{13}C-label at the anomeric carbon to facilitate

characterization of the resultant polymer. Use of 1-^{13}C-FPA effectively labeled only arabinose containing glycans generating a 100-fold increase in signal. The complemented polymer was found to contain all the residues that would be present in natural arabinogalactan. DOSY NMR analysis confirmed that the mobility of arabinogalactan from complemented cells is equivalent to natural arabinogalactan indicating that galactan arabinosylation is equivalent. Furthermore, electron microscopy of the complemented cells revealed the mycolic acid membrane had been restored. These data indicate that FPA is a competent surrogate for DPA and that it is a substrate for all of the arabinofuranosyl transferases responsible for constructing the arabinan. The identification of an accessible DPA surrogate enables experiments with a high material cost that would otherwise not be possible. In addition, this method provides a path towards incorporation of other modifications, such as deoxygenations or inclusion of reactive handles, into the arabinose portion of the molecule, further expanding the utility of these probes.

Though the arabinan of Corynebacterineae was chosen as the focus of this study, our method should apply to other glycans in mycobacteria and corynebacteria. For example, an immunomodulatory glycolipid known as the lipoarabinomannan requires both lipid-linked mannose and lipid-linked arabinose as the sugar donors for its synthesis (407). Furthermore, the use of lipid-linked sugar donors for glycan and glycoconjugate synthesis is present in Gram-negative bacteria including some pathogenic bacteria strains. This includes the capsular polysaccharides of group B streptococci (408), group B *Neisseria meningitidis* (409), N-glycosylation of *Campylobacter jejuni* (410), and the Capsular Polysaccharide A of the gut commensal *Bacteroides fragilis* (411). In fact, several bacterial oligosaccharyltransferases are used for glycoengineering novel glycoproteins.

5.5 Experimental

5.5.1 Materials, and Instrumentation

All chemicals were purchased from Sigma Aldrich unless otherwise stated. Unlabeled DPA analogs were prepared as reported (404). 1-^{13}C-D-arabinose was purchased from Cambridge Isotope Labs (CLM-715). 1-^{13}C-(Z,Z)-farnesol was prepared following a previously published route (404). Nuclear magnetic resonance spectra were recorded on a 300 MHz spectrometer (acquired at 300 MHz for ^{1}H and 75 MHz for ^{13}C), 400 MHz spectrometer (acquired at 400 MHz for ^{1}H and 100 MHz for ^{13}C), or a 500 MHz spectrometer (acquired at 500 MHz for ^{1}H and 125 MHz for ^{13}C). Chemical shifts are reported relative to tetramethylsilane or residual solvent peaks in parts per million ($CHCl_3$: ^{1}H, 7.27, ^{13}C, 77.23; MeOH: ^{1}H, 3.31, ^{13}C, 49.15). High-resolution mass spectra (HRMS) were obtained on an electrospray ionization-time of flight (ESI-TOF) mass spectrometer.

5.5.2 Strains and Growth Conditions

Corynebacterium glutamicum ATCC 13032 and *Corynebacterium glutamicum ATCC 13032 ΔubiA* were grown at 30 °C in brain heart infusion with 9.1% sorbitol (BHIS) media. *CgΔubiA* was selected for by supplementing cultures with kanamycin to a final concentration of 25 µg/mL when appropriate.

5.5.3 Chemical Complementation of the Arabinan

Cultures of *C. glutamicum* and *CgΔubiA* were grown to saturation in BHIS media. Refresh cultures were inoculated from the saturated starter cultures and grown to late-logarithmic phase (OD_{600} = 0.6-0.8). Aliquots (1 mL) were separated into sterile 10 mL baffled flasks, and DPA analogs were added from 100 mM DMSO stocks to the desired final concentration. After

growing to saturation, cells were transferred into Eppendorf tubes and pelleted for 15 minutes at 5,000 x g. The supernatant was discarded, and the cell pellets were stored at -80 °C.

5.5.4 Mycolyl-Arabinogalactan-Peptidoglycan Complex Isolation

Cell pellets from 1 mL cultures were resuspended in lysis buffer, 2% Triton x-100 in PBS pH 7.2, and disrupted by sonication (6 x 20 sec separated by 2 min intervals) while on ice. The cell debris was pelleted by centrifugation at 15,000 x g for 15 min. The supernatant was discarded, and the pelleted material was washed three times with 2% SDS in PBS (by heating to 95 °C for 1 h before pelleting as above and discarding the supernatant). An additional 3 washes were performed with water, 80% acetone/water, and acetone. After discarding the supernatant from the final wash, the pellets were placed under vacuum overnight to remove any remaining acetone before being placed in a -20 °C freezer.

5.5.5 Alditol Acetate Preparation

The previously isolated samples of mAGP complex were taken up in 2 M trifluoroacetic acid (250 µL) and hydrolyzed at 115 °C for 2 h. The suspensions were filtered through syringe filters (Milex, PVDF, 0.2 µm) and concentrated under reduced pressure. The monosaccharide mixtures were reduced by 0.25 M $NaBD_4$ in 1 M NH_4OH in ethanol. The suspensions were filtered through syringe filters (Milex, PVDF, 0.2 µm) of 10% acetic acid/methanol and concentrated under reduced pressure. Residual borate salts were removed by evaporation with 3 x 250 µL aliquots of 10% acetic acid/ methanol under reduced pressure. The samples were dried overnight under high vacuum. The alditol samples were taken-up in a 1:1 mixture of acetic anhydride and pyridine (500 µL) and stirred at 70 °C overnight. The reactions were concentrated under reduced pressure, and residual acetic anhydride and pyridine were removed by coevaporation with

toluene. The alditol acetates were taken up in ethyl acetate (500 µL) overnight. The reactions were concentrated under reduced pressure through a plug of $MgSO_4$ and concentrated *in-vacuo*.

5.5.6 Cell Wall Composition Analysis

Alditol acetate samples were dissolved in 1:1 acetonitrile/water 200 µLand analyzed by LC-MS. Analysis was performed on Shimadzu LC-MS-2010A spectrometer fitted with a Supelco Discovery® BIO wide pore C18 column (150 mm x 2.1 mm, 5 µm pore size) eluting with a gradient from 17-23% acetonitrile in water over 25 min with a flow rate of 0.1 mL/min.

5.5.7 Preparation of Intact Arabinogalactan from Mycolyl-Arabinogalactan-Peptidoglycan for NMR Spectroscopy

Solid mAGP complex was taken up in 1 M sodium hydroxide to a final concentration of 0.1 g/mL of mAGP. The suspension was stirred for 24 h at 70 °C. The peptidoglycan was removed by vacuum filtration through a membrane filter (0.4 µm pore size) to soluble arabinogalactan in aqueous base. The solution was desalted by dialyzing into Millipore water for 24 h. The samples were lyophilized to afford fluffy off-white solids. The solids were taken up in D_2O and lyophilized three times before storage in a desiccator at -20 °C.

5.5.8 2D-NMR Spectroscopy

All 2-dimensional ^{1}H-^{13}C spectra were recorded using a Bruker Avance 600 MHz spectrometer equipped with a 5 mm TCI-F Cryoprobe at 298 K in D_2O. All experiments (heteronuclear single quantum coherence, ^{1}H-^{13}C HSQC; heteronuclear single quantum coherence-total correlation spectroscopy, ^{1}H-^{13}C HSQC-TOCSY; and heteronuclear multiple bond correlation, ^{1}H-^{13}C HMBC; diffusion ordered spectroscopy, DOSY) were performed using standard pulse sequences provided in the Bruker Software. The mixing time for the TOCSY experiment was 80 ms.

5.5.9 Electron Microscopy

Pelleted cultures grown with or without FPA were removed from the -80 °C freezer, thawed and fixed with 2.5% glutaraldehyde and 0.05 M lysine in 0.1 M cacodylate buffer (pH 7.4) containing 0.075% Ruthenium Red for 1h at 4 °C (1 mL). Samples were washed five times with 0.5mL of 0.075% ruthenium red in 0.1 M cacodylate buffer. The washed cells were post-fixed with 1% w/v OsO_4 in 0.1 M cacodylate containing 0.075% Ruthenium Red for 1h at room temperature. After rinsing the fixed cells with distilled water, they were resuspended in 1% aqueous uranyl acetate for 1h and washed 5 times with water. Suspended cells were dehydrated through a graded ethanol series before being embedded in Spurr medium through intermediate 1,2-epoxypropane infiltration. Blocks were conventionally cut, stained, and examined with a Philips CM120 microscope operating under standard conditions.

5.6 Contributions

Compounds were synthesized by Dr. Matt Kraft and Phillip Calabretta. LCMS analysis was performed by Dr. Matt Kraft and Phillip Calabretta. NMR characterizations were performed by Phillip Calabretta.

5.7 Acknowledgements

We acknowledge experimental assistance from Charles Fry and Heike Hofstetter for instruction in the application of 2D-NMR techniques at UW Madison and their tireless work to maintain a world-class facility. We also acknowledge Ben August at the UW-Madison Medical School Electron Microscope Facility.

Compiled References

1. Silhavy TJ, Kahne D, & Walker S (2010) The bacterial cell envelope. *Cold Spring Harb Perspect Biol* 2(5):a000414.

2. Kohanski MA, Dwyer DJ, & Collins JJ (2010) How antibiotics kill bacteria: from targets to networks. *Nat Rev Microbiol* 8(6):423-435.

3. Francino MP (2015) Antibiotics and the Human Gut Microbiome: Dysbioses and Accumulation of Resistances. *Front Microbiol* 6:1543.

4. Davies J & Davies D (2010) Origins and evolution of antibiotic resistance. *Microbiol Mol Biol Rev* 74(3):417-433.

5. Walsh C (2003) Where will new antibiotics come from? *Nat Rev Microbiol* 1(1):65-70.

6. Brown ED & Wright GD (2016) Antibacterial drug discovery in the resistance era. *Nature* 529(7586):336-343.

7. Park JT & Strominger JL (1957) Mode of action of penicillin. *Science* 125(3238):99-101.

8. Perkins HR (1969) The configuration of 2,6-diamino-3-hydroxypimelic acid in microbial cell walls. *Biochem J* 115(4):797-805.

9. Swoboda JG, Campbell J, Meredith TC, & Walker S (2010) Wall teichoic acid function, biosynthesis, and inhibition. *Chembiochem* 11(1):35-45.

10. Centers for Disease Control and Prevention OoID (2013) Centers for Disease Control and Prevention, Office of Infectious Disease Antibiotic resistance threats in the United States, 2013. .

11. Stanislavsky ES, Kholodkova EV, Knirel YA, & Kocharova NA (1989) Saccharides of seven Pseudomonas aeruginosa immunotypes. *FEMS Microbiol Immunol* 1(4):245-251.

12. Knirel YA, *et al.* (2011) Structure and serology of O-antigens as the basis for classification of Proteus strains. *Innate Immun* 17(1):70-96.

13. Schuchat A, *et al.* (1997) Bacterial meningitis in the United States in 1995. Active Surveillance Team. *N Engl J Med* 337(14):970-976.

14. Black S, *et al.* (2000) Efficacy, safety and immunogenicity of heptavalent pneumococcal conjugate vaccine in children. Northern California Kaiser Permanente Vaccine Study Center Group. *Pediatr Infect Dis J* 19(3):187-195.

15. Girard MP, Preziosi MP, Aguado MT, & Kieny MP (2006) A review of vaccine research and development: meningococcal disease. *Vaccine* 24(22):4692-4700.

16. Wilson MR, Zha L, & Balskus EP (2017) Natural product discovery from the human microbiome. *J Biol Chem* 292(21):8546-8552.

17. Zipperer A, *et al.* (2016) Human commensals producing a novel antibiotic impair pathogen colonization. *Nature* 535(7613):511-516.

18. Rea MC, *et al.* (2011) Effect of broad- and narrow-spectrum antimicrobials on Clostridium difficile and microbial diversity in a model of the distal colon. *Proc Natl Acad Sci U S A* 108 Suppl 1:4639-4644.

19. Farha MA, *et al.* (2013) Inhibition of WTA synthesis blocks the cooperative action of PBPs and sensitizes MRSA to beta-lactams. *ACS Chem Biol* 8(1):226-233.

20. Garcia-Fernandez E, *et al.* (2017) Membrane Microdomain Disassembly Inhibits MRSA Antibiotic Resistance. *Cell*.

21. Scheffers DJ & Pinho MG (2005) Bacterial cell wall synthesis: new insights from localization studies. *Microbiol Mol Biol Rev* 69(4):585-607.

22. Ormo M, *et al.* (1996) Crystal structure of the Aequorea victoria green fluorescent protein. *Science* 273(5280):1392-1395.

23. Yang F, Moss LG, & Phillips GN, Jr. (1996) The molecular structure of green fluorescent protein. *Nat Biotechnol* 14(10):1246-1251.

24. Miller LW, Cai Y, Sheetz MP, & Cornish VW (2005) In vivo protein labeling with trimethoprim conjugates: a flexible chemical tag. *Nat Methods* 2(4):255-257.

25. Los GV, *et al.* (2008) HaloTag: a novel protein labeling technology for cell imaging and protein analysis. *ACS Chem Biol* 3(6):373-382.

26. Gautier A, *et al.* (2008) An engineered protein tag for multiprotein labeling in living cells. *Chem Biol* 15(2):128-136.

27. Keppler A, *et al.* (2003) A general method for the covalent labeling of fusion proteins with small molecules in vivo. *Nat Biotechnol* 21(1):86-89.

28. Antos JM, *et al.* (2009) Site-specific N- and C-terminal labeling of a single polypeptide using sortases of different specificity. *J Am Chem Soc* 131(31):10800-10801.

29. Popp MW, Antos JM, Grotenbreg GM, Spooner E, & Ploegh HL (2007) Sortagging: a versatile method for protein labeling. *Nat Chem Biol* 3(11):707-708.

30. Lang K & Chin JW (2014) Cellular incorporation of unnatural amino acids and bioorthogonal labeling of proteins. *Chem Rev* 114(9):4764-4806.

31. Hinner MJ & Johnsson K (2010) How to obtain labeled proteins and what to do with them. *Curr Opin Biotechnol* 21(6):766-776.

32. Sletten EM & Bertozzi CR (2009) Bioorthogonal chemistry: fishing for selectivity in a sea of functionality. *Angew Chem Int Ed Engl* 48(38):6974-6998.

33. Landgraf D, Okumus B, Chien P, Baker TA, & Paulsson J (2012) Segregation of molecules at cell division reveals native protein localization. *Nat Methods* 9(5):480-482.

34. Margolin W (2012) The price of tags in protein localization studies. *J Bacteriol* 194(23):6369-6371.

35. Swulius MT & Jensen GJ (2012) The helical MreB cytoskeleton in Escherichia coli MC1000/pLE7 is an artifact of the N-Terminal yellow fluorescent protein tag. *J Bacteriol* 194(23):6382-6386.

36. Heo M, *et al.* (2017) Impact of fluorescent protein fusions on the bacterial flagellar motor. *Sci Rep* 7(1):12583.

37. Kocaoglu O & Carlson EE (2016) Progress and prospects for small-molecule probes of bacterial imaging. *Nat Chem Biol* 12(7):472-478.

38. Lebaron P, Catala P, & Parthuisot N (1998) Effectiveness of SYTOX Green stain for bacterial viability assessment. *Appl Environ Microbiol* 64(7):2697-2700.

39. Spahn C, Endesfelder U, & Heilemann M (2014) Super-resolution imaging of Escherichia coli nucleoids reveals highly structured and asymmetric segregation during fast growth. *J Struct Biol* 185(3):243-249.

40. Schoen I, Ries J, Klotzsch E, Ewers H, & Vogel V (2011) Binding-activated localization microscopy of DNA structures. *Nano Lett* 11(9):4008-4011.

41. Cairo CW, Key JA, & Sadek CM (2010) Fluorescent small-molecule probes of biochemistry at the plasma membrane. *Curr Opin Chem Biol* 14(1):57-63.

42. Strahl H & Errington J (2017) Bacterial Membranes: Structure, Domains, and Function. *Annu Rev Microbiol* 71:519-538.

43. Mileykovskaya E & Dowhan W (2000) Visualization of phospholipid domains in Escherichia coli by using the cardiolipin-specific fluorescent dye 10-N-nonyl acridine orange. *J Bacteriol* 182(4):1172-1175.

44. Oliver PM, *et al.* (2014) Localization of anionic phospholipids in Escherichia coli cells. *J Bacteriol* 196(19):3386-3398.

45. Aldridge BB, *et al.* (2012) Asymmetry and aging of mycobacterial cells lead to variable growth and antibiotic susceptibility. *Science* 335(6064):100-104.

46. Cameron TA, Anderson-Furgeson J, Zupan JR, Zik JJ, & Zambryski PC (2014) Peptidoglycan synthesis machinery in Agrobacterium tumefaciens during unipolar growth and cell division. *MBio* 5(3):e01219-01214.

47. Cabeen MT & Jacobs-Wagner C (2007) Skin and bones: the bacterial cytoskeleton, cell wall, and cell morphogenesis. *J Cell Biol* 179(3):381-387.

48. Cabeen MT & Jacobs-Wagner C (2005) Bacterial cell shape. *Nat Rev Microbiol* 3(8):601-610.

49. Munch D & Sahl HG (2015) Structural variations of the cell wall precursor lipid II in Gram-positive bacteria - Impact on binding and efficacy of antimicrobial peptides. *Biochim Biophys Acta* 1848(11 Pt B):3062-3071.

50. Vollmer W, Blanot D, & de Pedro MA (2008) Peptidoglycan structure and architecture. *FEMS Microbiol Rev* 32(2):149-167.

51. Sauvage E, Kerff F, Terrak M, Ayala JA, & Charlier P (2008) The penicillin-binding proteins: structure and role in peptidoglycan biosynthesis. *FEMS Microbiol Rev* 32(2):234-258.

52. Daniel RA & Errington J (2003) Control of cell morphogenesis in bacteria: two distinct ways to make a rod-shaped cell. *Cell* 113(6):767-776.

53. Tiyanont K, *et al.* (2006) Imaging peptidoglycan biosynthesis in Bacillus subtilis with fluorescent antibiotics. *Proc Natl Acad Sci U S A* 103(29):11033-11038.

54. Lunde CS, Rexer CH, Hartouni SR, Axt S, & Benton BM (2010) Fluorescence microscopy demonstrates enhanced targeting of telavancin to the division septum of Staphylococcus aureus. *Antimicrob Agents Chemother* 54(5):2198-2200.

55. Lakaye B, *et al.* (1994) Synthesis, purification and kinetic properties of fluorescein-labelled penicillins. *Biochem J* 300 (Pt 1):141-145.

56. Zhao G, Meier TI, Kahl SD, Gee KR, & Blaszczak LC (1999) BOCILLIN FL, a sensitive and commercially available reagent for detection of penicillin-binding proteins. *Antimicrob Agents Chemother* 43(5):1124-1128.

57. Kocaoglu O, *et al.* (2012) Selective penicillin-binding protein imaging probes reveal substructure in bacterial cell division. *ACS Chem Biol* 7(10):1746-1753.

58. Bindman NA & van der Donk WA (2013) A general method for fluorescent labeling of the N-termini of lanthipeptides and its application to visualize their cellular localization. *J Am Chem Soc* 135(28):10362-10371.

59. Pinho MG & Errington J (2005) Recruitment of penicillin-binding protein PBP2 to the division site of Staphylococcus aureus is dependent on its transpeptidation substrates. *Mol Microbiol* 55(3):799-807.

60. Valbuena N, *et al.* (2007) Characterization of HMW-PBPs from the rod-shaped actinomycete Corynebacterium glutamicum: peptidoglycan synthesis in cells lacking actin-like cytoskeletal structures. *Mol Microbiol* 66(3):643-657.

61. Divakaruni AV, Baida C, White CL, & Gober JW (2007) The cell shape proteins MreB and MreC control cell morphogenesis by positioning cell wall synthetic complexes. *Mol Microbiol* 66(1):174-188.

62. Gilbert Y, *et al.* (2007) Single-molecule force spectroscopy and imaging of the vancomycin/D-Ala-D-Ala interaction. *Nano Lett* 7(3):796-801.

63. Jovetic S, Zhu Y, Marcone GL, Marinelli F, & Tramper J (2010) beta-Lactam and glycopeptide antibiotics: first and last line of defense? *Trends Biotechnol* 28(12):596-604.

64. Turner RD, *et al.* (2010) Peptidoglycan architecture can specify division planes in Staphylococcus aureus. *Nat Commun* 1:26.

65. Staub I & Sieber SA (2008) Beta-lactams as selective chemical probes for the in vivo labeling of bacterial enzymes involved in cell wall biosynthesis, antibiotic resistance, and virulence. *J Am Chem Soc* 130(40):13400-13409.

66. Böttcher T, and Stephan A. Sieber. (2012) β-Lactams and β-lactones as activity-based probes in chemical biology. *MedChemComm* 3(4):408-412.

67. Scheffers DJ, Jones LJ, & Errington J (2004) Several distinct localization patterns for penicillin-binding proteins in Bacillus subtilis. *Mol Microbiol* 51(3):749-764.

68. Sadamoto R, *et al.* (2002) Cell-wall engineering of living bacteria. *J Am Chem Soc* 124(31):9018-9019.

69. Olrichs NK, *et al.* (2011) A novel in vivo cell-wall labeling approach sheds new light on peptidoglycan synthesis in Escherichia coli. *Chembiochem* 12(7):1124-1133.

70. Liang H, *et al.* (2017) Metabolic labelling of the carbohydrate core in bacterial peptidoglycan and its applications. *Nat Commun* 8:15015.

71. Lupoli TJ, *et al.* (2011) Transpeptidase-mediated incorporation of D-amino acids into bacterial peptidoglycan. *J Am Chem Soc* 133(28):10748-10751.

72. Cava F, Lam H, de Pedro MA, & Waldor MK (2011) Emerging knowledge of regulatory roles of D-amino acids in bacteria. *Cell Mol Life Sci* 68(5):817-831.

73. Siegrist MS, *et al.* (2013) (D)-Amino acid chemical reporters reveal peptidoglycan dynamics of an intracellular pathogen. *ACS Chem Biol* 8(3):500-505.

74. Kuru E, *et al.* (2012) In Situ Probing of Newly Synthesized Peptidoglycan in Live Bacteria with Fluorescent D-Amino Acids. *Angew Chem Int Ed Engl* 51(50):12519-12523.

75. Bugg TD (2013) Biosynthesis: imaging cell-wall biosynthesis live. *Nat Chem* 5(1):10-12.

76. Hsu YP, *et al.* (2017) Full color palette of fluorescent d-amino acids for in situ labeling of bacterial cell walls. *Chem Sci* 8(9):6313-6321.

77. Kuru E, Tekkam S, Hall E, Brun YV, & Van Nieuwenhze MS (2015) Synthesis of fluorescent D-amino acids and their use for probing peptidoglycan synthesis and bacterial growth in situ. *Nat Protoc* 10(1):33-52.

78. Anonymous (!!! INVALID CITATION !!! {Kuru, 2015 #84;Lebar, 2014 #86}).

79. Liechti GW, *et al.* (2014) A new metabolic cell-wall labelling method reveals peptidoglycan in Chlamydia trachomatis. *Nature* 506(7489):507-510.

80. Hudak JE, Alvarez D, Skelly A, von Andrian UH, & Kasper DL (2017) Illuminating vital surface molecules of symbionts in health and disease. *Nat Microbiol* 2:17099.

81. Comstock LE & Kasper DL (2006) Bacterial glycans: key mediators of diverse host immune responses. *Cell* 126(5):847-850.

82. Wu K, Walukiewicz HE, Glekas GD, Ordal GW, & Rao CV (2011) Attractant binding induces distinct structural changes to the polar and lateral signaling clusters in Bacillus subtilis chemotaxis. *J Biol Chem* 286(4):2587-2595.

83. Adibekian A, *et al.* (2011) Comparative bioinformatics analysis of the mammalian and bacterial glycomes. *Chemical Science* 2(2):337-344.

84. Weston A, *et al.* (1997) Biosynthetic origin of mycobacterial cell wall galactofuranosyl residues. *Tuber Lung Dis* 78(2):123-131.

85. Pedersen LL & Turco SJ (2003) Galactofuranose metabolism: a potential target for antimicrobial chemotherapy. *Cell Mol Life Sci* 60(2):259-266.

86. Heiss C, *et al.* (2013) Unusual galactofuranose modification of a capsule polysaccharide in the pathogenic yeast Cryptococcus neoformans. *J Biol Chem* 288(16):10994-11003.

87. Dumont A, Malleron A, Awwad M, Dukan S, & Vauzeilles B (2012) Click-mediated labeling of bacterial membranes through metabolic modification of the lipopolysaccharide inner core. *Angew Chem Int Ed Engl* 51(13):3143-3146.

88. Wang W, Zhu Y, & Chen X (2017) Selective Imaging of Gram-Negative and Gram-Positive Microbiotas in the Mouse Gut. *Biochemistry* 56(30):3889-3893.

89. Di Guilmi AM, *et al.* (2017) Specific and spatial labeling of choline-containing teichoic acids in Streptococcus pneumoniae by click chemistry. *Chem Commun (Camb)* 53(76):10572-10575.

90. Gehre F, *et al.* (2009) Role of teichoic acid choline moieties in the virulence of Streptococcus pneumoniae. *Infect Immun* 77(7):2824-2831.

91. Clark SE & Weiser JN (2013) Microbial modulation of host immunity with the small molecule phosphorylcholine. *Infect Immun* 81(2):392-401.

92. Young NM, Foote SJ, & Wakarchuk WW (2013) Review of phosphocholine substituents on bacterial pathogen glycans: synthesis, structures and interactions with host proteins. *Mol Immunol* 56(4):563-573.

93. Geva-Zatorsky N, *et al.* (2015) In vivo imaging and tracking of host-microbiota interactions via metabolic labeling of gut anaerobic bacteria. *Nat Med* 21(9):1091-1100.

94. Mas Pons J, *et al.* (2014) Identification of living Legionella pneumophila using species-specific metabolic lipopolysaccharide labeling. *Angew Chem Int Ed Engl* 53(5):1275-1278.

95. Whitworth GE & Imperiali B (2015) Selective biochemical labeling of Campylobacter jejuni cell-surface glycoconjugates. *Glycobiology* 25(7):756-766.

96. Backus KM, *et al.* (2011) Uptake of unnatural trehalose analogs as a reporter for Mycobacterium tuberculosis. *Nat Chem Biol* 7(4):228-235.

97. Rodriguez-Rivera FP, Zhou X, Theriot JA, & Bertozzi CR (2017) Visualization of mycobacterial membrane dynamics in live cells. *J Am Chem Soc* 139(9):3488-3495.

98. Swarts BM, *et al.* (2012) Probing the mycobacterial trehalome with bioorthogonal chemistry. *J Am Chem Soc* 134(39):16123-16126.

99. Urbanek BL, *et al.* (2014) Chemoenzymatic synthesis of trehalose analogues: rapid access to chemical probes for investigating mycobacteria. *Chembiochem* 15(14):2066-2070.

100. Rundell SR, *et al.* (2016) Deoxyfluoro-d-trehalose (FDTre) analogues as potential PET probes for imaging mycobacterial infection. *Org Biomol Chem* 14(36):8598-8609.

101. Liu F, Aubry AJ, Schoenhofen IC, Logan SM, & Tanner ME (2009) The engineering of bacteria bearing azido-pseudaminic acid-modified flagella. *Chembiochem* 10(8):1317-1320.

102. Koenigs MB, Richardson EA, & Dube DH (2009) Metabolic profiling of Helicobacter pylori glycosylation. *Mol Biosyst* 5(9):909-912.

103. Besanceney-Webler C, Jiang H, Wang W, Baughn AD, & Wu P (2011) Metabolic labeling of fucosylated glycoproteins in Bacteroidales species. *Bioorg Med Chem Lett* 21(17):4989-4992.

104. Yi W, *et al.* (2009) Remodeling bacterial polysaccharides by metabolic pathway engineering. *Proc Natl Acad Sci U S A* 106(11):4207-4212.

105. Zhang YM & Rock CO (2008) Membrane lipid homeostasis in bacteria. *Nat Rev Microbiol* 6(3):222-233.

106. Lopez D & Kolter R (2010) Functional microdomains in bacterial membranes. *Genes Dev* 24(17):1893-1902.

107. Sohlenkamp C & Geiger O (2016) Bacterial membrane lipids: diversity in structures and pathways. *FEMS Microbiol Rev* 40(1):133-159.

108. Lopez-Lara IM & Geiger O (2017) Bacterial lipid diversity. *Biochim Biophys Acta* 1862(11):1287-1299.

109. Christensen H, Garton NJ, Horobin RW, Minnikin DE, & Barer MR (1999) Lipid domains of mycobacteria studied with fluorescent molecular probes. *Mol Microbiol* 31(5):1561-1572.

110. Kumagai Y, Hirasawa T, Hayakawa K, Nagai K, & Wachi M (2005) Fluorescent phospholipid analogs as microscopic probes for detection of the mycolic acid-containing layer in Corynebacterium glutamicum: detecting alterations in the mycolic acid-containing layer following ethambutol treatment. *Biosci Biotechnol Biochem* 69(11):2051-2056.

111. Trevors JT (2003) Fluorescent probes for bacterial cytoplasmic membrane research. *J Biochem Biophys Methods* 57(2):87-103.

112. Marrakchi H, Laneelle MA, & Daffe M (2014) Mycolic acids: structures, biosynthesis, and beyond. *Chem Biol* 21(1):67-85.

113. Kavunja HW, *et al.* (2016) A chemical reporter strategy for detecting and identifying O-mycoloylated proteins in Corynebacterium. *Chem Commun (Camb)* 52(95):13795-13798.

114. Foley HN, Stewart JA, Kavunja HW, Rundell SR, & Swarts BM (2016) Bioorthogonal Chemical Reporters for Selective In Situ Probing of Mycomembrane Components in Mycobacteria. *Angewandte Chemie International Edition* 55(6):2053-2057.

115. van Teeffelen S*, et al.* (2011) The bacterial actin MreB rotates, and rotation depends on cell-wall assembly. *Proc Natl Acad Sci U S A* 108(38):15822-15827.

116. Mostafavi AZ, Lujan DK, Erickson KM, Martinez CD, & Troutman JM (2013) Fluorescent probes for investigation of isoprenoid configuration and size discrimination by bactoprenol-utilizing enzymes. *Bioorg Med Chem* 21(17):5428-5435.

117. Jankute M, Cox JA, Harrison J, & Besra GS (2015) Assembly of the Mycobacterial Cell Wall. *Annu Rev Microbiol* 69:405-423.

118. Quadri LE (2014) Biosynthesis of mycobacterial lipids by polyketide synthases and beyond. *Crit Rev Biochem Mol Biol* 49(3):179-211.

119. Xu Z, Meshcheryakov VA, Poce G, & Chng SS (2017) MmpL3 is the flippase for mycolic acids in mycobacteria. *Proc Natl Acad Sci U S A* 114(30):7993-7998.

120. Angala SK, Belardinelli JM, Huc-Claustre E, Wheat WH, & Jackson M (2014) The cell envelope glycoconjugates of Mycobacterium tuberculosis. *Crit Rev Biochem Mol Biol* 49(5):361-399.

121. Jensen MS, Costa S, Gunther-Pomorski T, & Lopez-Marques RL (2016) Cell-Based Lipid Flippase Assay Employing Fluorescent Lipid Derivatives. *Methods Mol Biol* 1377:371-382.

122. Gahlmann A & Moerner WE (2014) Exploring bacterial cell biology with single-molecule tracking and super-resolution imaging. *Nat Rev Microbiol* 12(1):9-22.

123. Schneider JP & Basler M (2016) Shedding light on biology of bacterial cells. *Philos Trans R Soc Lond B Biol Sci* 371(1707).

124. Mats G. L. Gustafsson EB, Harald F. Hess, George H. Patterson, Jennifer Lippincott-Schwartz, Michael W. Davidson (Introduction to Superresolution Microscopy. (Zeiss).

125. Tuson HH & Biteen JS (2015) Unveiling the inner workings of live bacteria using super-resolution microscopy. *Anal Chem* 87(1):42-63.

126. Cattoni DI, Fiche JB, & Nollmann M (2012) Single-molecule super-resolution imaging in bacteria. *Curr Opin Microbiol* 15(6):758-763.

127. Haas BL, Matson JS, DiRita VJ, & Biteen JS (2014) Imaging live cells at the nanometer-scale with single-molecule microscopy: obstacles and achievements in experiment optimization for microbiology. *Molecules* 19(8):12116-12149.

128. Wheeler R, Mesnage S, Boneca IG, Hobbs JK, & Foster SJ (2011) Super-resolution microscopy reveals cell wall dynamics and peptidoglycan architecture in ovococcal bacteria. *Mol Microbiol* 82(5):1096-1109.

129. Wang W, Li GW, Chen C, Xie XS, & Zhuang X (2011) Chromosome organization by a nucleoid-associated protein in live bacteria. *Science* 333(6048):1445-1449.

130. Wolff G, Hagen C, Grunewald K, & Kaufmann R (2016) Towards correlative super-resolution fluorescence and electron cryo-microscopy. *Biol Cell* 108(9):245-258.

131. Lee MK, Williams J, Twieg RJ, Rao J, & Moerner WE (2013) Enzymatic activation of nitro-aryl fluorogens in live bacterial cells for enzymatic turnover-activated localization microscopydagger. *Chem Sci* 42:220-225.

132. Zheng Q & Lavis LD (2017) Development of photostable fluorophores for molecular imaging. *Curr Opin Chem Biol* 39:32-38.

133. Wysocki LM & Lavis LD (2011) Advances in the chemistry of small molecule fluorescent probes. *Curr Opin Chem Biol* 15(6):752-759.

134. Lavis LD & Raines RT (2014) Bright building blocks for chemical biology. *ACS Chem Biol* 9(4):855-866.

135. Lavis LD & Raines RT (2008) Bright ideas for chemical biology. *ACS Chem Biol* 3(3):142-155.

136. Grimm JB, *et al.* (2016) Bright photoactivatable fluorophores for single-molecule imaging. *Nat Methods* 13(12):985-988.

137. Grimm JB, *et al.* (2016) Synthesis of a Far-Red Photoactivatable Silicon-Containing Rhodamine for Super-Resolution Microscopy. *Angew Chem Int Ed Engl* 55(5):1723-1727.

138. Grimm JB, Brown TA, English BP, Lionnet T, & Lavis LD (2017) Synthesis of Janelia Fluor HaloTag and SNAP-Tag Ligands and Their Use in Cellular Imaging Experiments. *Methods Mol Biol* 1663:179-188.

139. Grimm JB, Brown TA, Tkachuk AN, & Lavis LD (2017) General Synthetic Method for Si-Fluoresceins and Si-Rhodamines. *ACS Cent Sci* 3(9):975-985.

140. Kamariza M, Peyton Shieh, and Carolyn R. Bertozzi (2017) Imaging Mycobacterial Trehalose Glycolipids. *Methods in Enzymology*.

141. Prifti E, *et al.* (2014) A fluorogenic probe for SNAP-tagged plasma membrane proteins based on the solvatochromic molecule Nile Red. *ACS Chem Biol* 9(3):606-612.

142. Tallman KR, Levine SR, & Beatty KE (2016) Profiling Esterases in Mycobacterium tuberculosis Using Far-Red Fluorogenic Substrates. *ACS Chem Biol* 11(7):1810-1815.

143. Tallman KR, Levine SR, & Beatty KE (2016) Small-Molecule Probes Reveal Esterases with Persistent Activity in Dormant and Reactivating Mycobacterium tuberculosis. *ACS Infect Dis* 2(12):936-944.

144. Tallman KR & Beatty KE (2015) Far-red fluorogenic probes for esterase and lipase detection. *Chembiochem* 16(1):70-75.

145. Smith EL, Bertozzi CR, & Beatty KE (2014) An expanded set of fluorogenic sulfatase activity probes. *Chembiochem* 15(8):1101-1105.

146. Levine SR & Beatty KE (2016) Synthesis of a far-red fluorophore and its use as an esterase probe in living cells. *Chem Commun (Camb)* 52(9):1835-1838.

147. Mu J, *et al.* (2014) A small-molecule FRET reporter for the real-time visualization of cell-surface proteolytic enzyme functions. *Angew Chem Int Ed Engl* 53(52):14357-14362.

148. Fernandez A & Vendrell M (2016) Smart fluorescent probes for imaging macrophage activity. *Chem Soc Rev* 45(5):1182-1196.

149. Neefjes J & Dantuma NP (2004) Fluorescent probes for proteolysis: tools for drug discovery. *Nat Rev Drug Discov* 3(1):58-69.

150. Lemke EA & Schultz C (2011) Principles for designing fluorescent sensors and reporters. *Nat Chem Biol* 7(8):480-483.

151. Lim RK & Lin Q (2010) Bioorthogonal chemistry: recent progress and future directions. *Chem Commun (Camb)* 46(10):1589-1600.

152. Shih HW, Kamber DN, & Prescher JA (2014) Building better bioorthogonal reactions. *Curr Opin Chem Biol* 21:103-111.

153. Choi MG, Hwang J, Moon JO, Sung J, & Chang SK (2011) Hydrazine-selective chromogenic and fluorogenic probe based on levulinated coumarin. *Org Lett* 13(19):5260-5263.

154. Shieh P & Bertozzi CR (2014) Design strategies for bioorthogonal smart probes. *Org Biomol Chem* 12(46):9307-9320.

155. Saxon E, Armstrong JI, & Bertozzi CR (2000) A "traceless" Staudinger ligation for the chemoselective synthesis of amide bonds. *Org Lett* 2(14):2141-2143.

156. Kaewsapsak P, Esonu O, & Dube DH (2013) Recruiting the host's immune system to target Helicobacter pylori's surface glycans. *Chembiochem* 14(6):721-726.

157. Lemieux GA, De Graffenried CL, & Bertozzi CR (2003) A fluorogenic dye activated by the staudinger ligation. *J Am Chem Soc* 125(16):4708-4709.

158. Hangauer MJ & Bertozzi CR (2008) A FRET-based fluorogenic phosphine for live-cell imaging with the Staudinger ligation. *Angew Chem Int Ed Engl* 47(13):2394-2397.

159. Huisgen R (1963) Kinetics and Mechanism of 1,3-Dipolar Cycloadditions. *Angewandte Chemie International Edition in English* 2(11):633-645.

160. Tornoe CW, Christensen C, & Meldal M (2002) Peptidotriazoles on solid phase: [1,2,3]-triazoles by regiospecific copper(i)-catalyzed 1,3-dipolar cycloadditions of terminal alkynes to azides. *J Org Chem* 67(9):3057-3064.

161. Rostovtsev VV, Green LG, Fokin VV, & Sharpless KB (2002) A stepwise huisgen cycloaddition process: copper(I)-catalyzed regioselective "ligation" of azides and terminal alkynes. *Angew Chem Int Ed Engl* 41(14):2596-2599.

162. Debets MF, *et al.* (2011) Bioconjugation with strained alkenes and alkynes. *Acc Chem Res* 44(9):805-815.

163. Tra VN & Dube DH (2014) Glycans in pathogenic bacteria--potential for targeted covalent therapeutics and imaging agents. *Chem Commun (Camb)* 50(36):4659-4673.

164. Cebecauer M, Spitaler M, Serge A, & Magee AI (2010) Signalling complexes and clusters: functional advantages and methodological hurdles. *J Cell Sci* 123(Pt 3):309-320.

165. Ketchum C, Miller H, Song W, & Upadhyaya A (2014) Ligand mobility regulates B cell receptor clustering and signaling activation. *Biophys J* 106(1):26-36.

166. Hat B, Kazmierczak B, & Lipniacki T (2011) B cell activation triggered by the formation of the small receptor cluster: a computational study. *PLoS Comput Biol* 7(10):e1002197.

167. Mitchell DA, Fadden AJ, & Drickamer K (2001) A novel mechanism of carbohydrate recognition by the C-type lectins DC-SIGN and DC-SIGNR. Subunit organization and binding to multivalent ligands. *J Biol Chem* 276(31):28939-28945.

168. Alarcon B, Swamy M, van Santen HM, & Schamel WW (2006) T-cell antigen-receptor stoichiometry: pre-clustering for sensitivity. *EMBO Rep* 7(5):490-495.

169. Xia J, Zhang X, Staudinger J, & Huganir RL (1999) Clustering of AMPA receptors by the synaptic PDZ domain-containing protein PICK1. *Neuron* 22(1):179-187.

170. Abulrob A, *et al.* (2010) Nanoscale imaging of epidermal growth factor receptor clustering: effects of inhibitors. *J Biol Chem* 285(5):3145-3156.

171. Bray D, Levin MD, & Morton-Firth CJ (1998) Receptor clustering as a cellular mechanism to control sensitivity. *Nature* 393(6680):85-88.

172. Mallam AL & Marcotte EM (2017) Systems-wide Studies Uncover Commander, a Multiprotein Complex Essential to Human Development. *Cell Syst* 4(5):483-494.

173. Goretsky T, *et al.* (2016) A Cytosolic Multiprotein Complex Containing p85alpha Is Required for beta-Catenin Activation in Colitis and Colitis-associated Cancer. *J Biol Chem* 291(8):4166-4177.

174. Hazelbauer GL, Falke JJ, & Parkinson JS (2008) Bacterial chemoreceptors: high-performance signaling in networked arrays. *Trends in Biochemical Sciences* 33(1):9-19.

175. Jones CW & Armitage JP (2015) Positioning of bacterial chemoreceptors. *Trends Microbiol* 23(5):247-256.

176. Sourjik V & Wingreen NS (2012) Responding to chemical gradients: bacterial chemotaxis. *Curr Opin Cell Biol* 24(2):262-268.

177. Tu Y (2013) Quantitative modeling of bacterial chemotaxis: signal amplification and accurate adaptation. *Annu Rev Biophys* 42:337-359.

178. Parkinson JS, Hazelbauer GL, & Falke JJ (2015) Signaling and sensory adaptation in Escherichia coli chemoreceptors: 2015 update. *Trends Microbiol* 23(5):257-266.

179. Darnton NC, Turner L, Rojevsky S, & Berg HC (2007) On torque and tumbling in swimming Escherichia coli. *J Bacteriol* 189(5):1756-1764.

180. Ortega A, Zhulin IB, & Krell T (2017) Sensory Repertoire of Bacterial Chemoreceptors. *Microbiol Mol Biol Rev* 81(4).

181. Yang Y, *et al.* (2015) Relation between chemotaxis and consumption of amino acids in bacteria. *Mol Microbiol* 96(6):1272-1282.

182. Matilla MA & Krell T (2017) Chemoreceptor-based signal sensing. *Curr Opin Biotechnol* 45:8-14.

183. Kim KK, Yokota H, & Kim SH (1999) Four-helical-bundle structure of the cytoplasmic domain of a serine chemotaxis receptor. *Nature* 400(6746):787-792.

184. Miller AS, Kohout SC, Gilman KA, & Falke JJ (2006) CheA Kinase of bacterial chemotaxis: chemical mapping of four essential docking sites. *Biochemistry* 45(29):8699-8711.

185. Wang X, Vu A, Lee K, & Dahlquist FW (2012) CheA-receptor interaction sites in bacterial chemotaxis. *J Mol Biol* 422(2):282-290.

186. Li X, *et al.* (2013) The 3.2 A resolution structure of a receptor: CheA:CheW signaling complex defines overlapping binding sites and key residue interactions within bacterial chemosensory arrays. *Biochemistry* 52(22):3852-3865.

187. Vu A, Wang X, Zhou H, & Dahlquist FW (2012) The receptor-CheW binding interface in bacterial chemotaxis. *J Mol Biol* 415(4):759-767.

188. Bhatnagar J, *et al.* (2010) Structure of the ternary complex formed by a chemotaxis receptor signaling domain, the CheA histidine kinase, and the coupling protein CheW as determined by pulsed dipolar ESR spectroscopy. *Biochemistry* 49(18):3824-3841.

189. Shukla D, Zhu XY, & Matsumura P (1998) Flagellar motor-switch binding face of CheY and the biochemical basis of suppression by CheY mutants that compensate for motor-switch defects in Escherichia coli. *J Biol Chem* 273(37):23993-23999.

190. Sowa Y, *et al.* (2005) Direct observation of steps in rotation of the bacterial flagellar motor. *Nature* 437(7060):916-919.

191. Colin R & Sourjik V (2017) Emergent properties of bacterial chemotaxis pathway. *Curr Opin Microbiol* 39:24-33.

192. Berg HC (2017) The flagellar motor adapts, optimizing bacterial behavior. *Protein Sci* 26(7):1249-1251.

193. Studdert CA & Parkinson JS (2004) Crosslinking snapshots of bacterial chemoreceptor squads. *Proc. Natl. Acad. Sci. U. S. A.* 101(7):2117-2122.

194. Briegel A, *et al.* (2008) Location and architecture of the Caulobacter crescentus chemoreceptor array. *Molecular Microbiology* 69(1):30-41.

195. Briegel A, *et al.* (2009) Universal architecture of bacterial chemoreceptor arrays. *Proc Natl Acad Sci U S A* 106(40):17181-17186.

196. Wadhams GH & Armitage JP (2004) Making sense of it all: bacterial chemotaxis. *Nature Reviews: Molecular Cell Biology* 5:1024-1037.

197. Lee A, O'Rourke JL, Barrington PJ, & Trust TJ (1986) Mucus colonization as a determinant of pathogenicity in intestinal infection by Campylobacter jejuni: a mouse cecal model. *Infect Immun* 51(2):536-546.

198. Eaton KA, Morgan DR, & Krakowka S (1992) Motility as a factor in the colonisation of gnotobiotic piglets by Helicobacter pylori. *J Med Microbiol* 37(2):123-127.

199. Rasko DA & Sperandio V (2010) Anti-virulence strategies to combat bacteria-mediated disease. *Nat Rev Drug Discov* 9(2):117-128.

200. Mellbye B & Schuster M (2011) The sociomicrobiology of antivirulence drug resistance: a proof of concept. *MBio* 2(5).

201. Jain R, *et al.* (2016) Using Chemoattractants to Lure Bacteria to Contact-Killing Surfaces. *Angew Chem Int Ed Engl* 55(19):5698-5702.

202. Segall JE, Block SM, & Berg HC (1986) Temporal Comparisons in Bacterial Chemotaxis. *Proc. Natl. Acad. Sci. U. S. A.* 83(23):8987-8991.

203. Berg HC & Purcell EM (1977) Physics of chemoreception. *Biophysical Journal* 20(2):193-219.

204. Sourjik V & Berg HC (2002) Receptor sensitivity in bacterial chemotaxis. *Proc. Natl. Acad. Sci. U. S. A.* 99(1):123-127.

205. Alon U, Surette MG, Barkai N, & Leibler S (1999) Robustness in bacterial chemotaxis. *Nature* 397(6715):168-171.

206. Mao HB, Cremer PS, & Manson MD (2003) A sensitive, versatile microfluidic assay for bacterial chemotaxis. *Proc. Natl. Acad. Sci. U. S. A.* 100(9):5449-5454.

207. Mesibov R, Ordal GW, & Adler J (1973) The range of attractant concentrations for bacterial chemotaxis and the threshold and size of response over this range. Weber law and related phenomena. *J Gen Physiol* 62(2):203-223.

208. Duke TA & Bray D (1999) Heightened sensitivity of a lattice of membrane receptors. *Proc Natl Acad Sci U S A* 96(18):10104-10108.

209. Gestwicki JE & Kiessling LL (2002) Inter-receptor communication through arrays of bacterial chemoreceptors. *Nature* 415(6867):81-84.

210. Maddock JR & Shapiro L (1993) Polar location of the chemoreceptor complex in the *Escherichia coli* cell. *Science* 259(5102):1717-1723.

211. Weis RM, *et al.* (2003) Electron microscopic analysis of membrane assemblies formed by the bacterial chemotaxis receptor Tsr. *J Bacteriol* 185(12):3636-3643.

212. Ames P & Parkinson JS (2006) Conformational suppression of inter-receptor signaling defects. *Proc. Natl. Acad. Sci. U. S. A.* 103(24):9292-9297.

213. Cho HS, *et al.* (2000) NMR structure of activated CheY. *Journal of Molecular Biology* 297(3):543-551.

214. Griswold IJ & Dahlquist FW (2002) The dynamic behavior of CheW from Thermotoga maritima in solution, as determined by nuclear magnetic resonance: implications for potential protein-protein interaction sites. *Biophys. Chem.* 101:359-373.

215. Griswold IJ, *et al.* (2002) The solution structure and interactions of CheW from Thermotoga maritima. *Nat. Struct. Biol.* 9(2):121-125.

216. Li Y, Hu YF, Fu WY, Xia B, & Jin CW (2007) Solution structure of the bacterial chemotaxis adaptor protein CheW from Escherichia coli. *Biochemical and Biophysical Research Communications* 360(4):863-867.

217. Djordjevic S & Stock AM (1998) Chemotaxis receptor recognition by protein methyltransferase CheR. *Nat. Struct. Biol.* 5(6):446-450.

218. Djordjevic S, Goudreau PN, Xu QP, Stock AM, & West AH (1998) Structural basis for methylesterase CheB regulation by a phosphorylation-activated domain. *Proc. Natl. Acad. Sci. U. S. A.* 95(4):1381-1386.

219. Zhao R, Collins EJ, Bourret RB, & Silversmith RE (2002) Structure and catalytic mechanism of the *E. coli* chemotaxis phosphatase CheZ. *Nat. Struct. Biol.* 9(8):570-575.

220. Milburn MV, *et al.* (1991) Three-dimensional structures of the ligand-binding domain of the bacterial aspartate receptor with and without a ligand. *Science* 254(5036):1342-1347.

221. McEvoy MM, Hausrath AC, Randolph GB, Remington SJ, & Dahlquist FW (1998) Two binding modes reveal flexibility in kinase/response regulator interactions in the bacterial chemotaxis pathway. *Proc. Natl. Acad. Sci. U. S. A.* 95(13):7333-7338.

222. Mourey L, *et al.* (2001) Crystal structure of the CheA histidine phosphotransfer domain that mediates response regulator phosphorylation in bacterial chemotaxis. *Journal of Biological Chemistry* 276(33):31074-31082.

223. Park SY, Beel BD, Simon MI, Bilwes AM, & Crane BR (2004) In different organisms, the mode of interaction between two signaling proteins is not necessarily conserved. *Proc. Natl. Acad. Sci. U. S. A.* 101(32):11646-11651.

224. Bilwes AM, Alex LA, Crane BR, & Simon MI (1999) Structure of CheA, a signal-transducing histidine kinase. *Cell* 96(1):131-141.

225. Park SY, *et al.* (2006) Reconstruction of the chemotaxis receptor-kinase assembly. *Nat. Struct. Mol. Biol.* 13(5):400-407.

226. Tocheva EI, Li Z, & Jensen GJ (2010) Electron cryotomography. *Cold Spring Harb Perspect Biol* 2(6):a003442.

227. Oikonomou CM & Jensen GJ (2017) Cellular Electron Cryotomography: Toward Structural Biology In Situ. *Annu Rev Biochem* 86:873-896.

228. Oikonomou CM & Jensen GJ (2017) A new view into prokaryotic cell biology from electron cryotomography. *Nat Rev Microbiol* 15(2):128.

229. Li Z & Jensen GJ (2009) Electron cryotomography: a new view into microbial ultrastructure. *Curr Opin Microbiol* 12(3):333-340.

230. Briegel A, *et al.* (2009) Universal architecture of bacterial chemoreceptor arrays. *PNAS* 106(40):17181-17186.

231. Shimizu TS, *et al.* (2000) Molecular model of a lattice of signalling proteins involved in bacterial chemotaxis. *Nat. Cell Biol.* 2(11):792-796.

232. Briegel A, *et al.* (2012) Bacterial chemoreceptor arrays are hexagonally packed trimers of receptor dimers networked by rings of kinase and coupling proteins. *Proc Natl Acad Sci U S A* 109(10):3766-3771.

233. Borkovich KA, Kaplan N, Hess JF, & Simon MI (1989) Transmembrane signal transduction in bacterial chemotaxis involves ligand-dependent activation of phosphate group transfer. *Proc. Natl. Acad. Sci. U. S. A.* 86(4):1208-1212.

234. Gegner JA, Graham DR, Roth AF, & Dahlquist FW (1992) Assembly of an MCP receptor, CheW, and kinase CheA complex in the bacterial chemotaxis signal transduction pathway. *Cell* 70(6):975-982.

235. Lai RZ, *et al.* (2005) Cooperative signaling among bacterial chemoreceptors. *Biochemistry* 44(43):14298-14307.

236. Li G & Weis RM (2000) Covalent modification regulates ligand binding to receptor complexes in the chemosensory system of *Escherichia coli*. *Cell* 100:357-365.

237. Ninfa EG, Stock A, Mowbray S, & Stock J (1991) Reconstitution of the bacterial chemotaxis signal transduction system from purified components. *Journal of Biological Chemistry* 266(15):9764-9770.

238. Schuster SC, Swanson RV, Alex LA, Bourret RB, & Simon MI (1993) Assembly and Function of a Quaternary Signal-Transduction Complex Monitored by Surface-Plasmon Resonance. *Nature* 365(6444):343-347.

239. Slivka PF & Falke JJ (2012) Isolated bacterial chemosensory array possesses quasi- and ultrastable components: functional links between array stability, cooperativity, and order. *Biochemistry* 51(51):10218-10228.

240. Underbakke ES, Zhu Y, & Kiessling LL (2011) Protein Footprinting in a complex milieu: Identifying the interaction surfaces of the chemotaxis adaptor protein CheW. *Journal of Molecular Biology* 409(4):483-495.

241. Erbse AH & Falke JJ (2009) The core signaling proteins of bacterial chemotaxis assemble to form an ultrastable complex. *Biochemistry* 48(29):6975-6987.

242. Liu J, *et al.* (2012) Molecular architecture of chemoreceptor arrays revealed by cryoelectron tomography of Escherichia coli minicells. *Proc Natl Acad Sci USA* 109(23):E1481-E1488.

243. Briegel A, *et al.* (2013) The mobility of two kinase domains in the Escherichia coli chemoreceptor array varies with signaling state. *Mol Microbiol* 89:831-841.

244. Wang EA & Koshland DE, Jr. (1980) Receptor structure in the bacterial sensing system. *Proc Natl Acad Sci U S A* 77(12):7157-7161.

245. Ninfa EG, Stock A, Mowbray S, & Stock J (1991) Reconstitution of the bacterial chemotaxis signal transduction system from purified components. *J Biol Chem* 266(15):9764-9770.

246. Underbakke ES, Zhu Y, & Kiessling LL (2011) Protein footprinting in a complex milieu: identifying the interaction surfaces of the chemotaxis adaptor protein CheW. *J Mol Biol* 409(4):483-495.

247. Sourjik V & Berg HC (2004) Functional interactions between receptors in bacterial chemotaxis. *Nature* 428(6981):437-441.

248. Wolfe AJ, Conley MP, Kramer TJ, & Berg HC (1987) Reconstitution of signaling in bacterial chemotaxis. *Journal of Bacteriology* 169(5):1878-1885.

249. Rosen BP & Tsuchiya T (1979) Preparation of everted membrane vesicles from Escherichia coli for the measurement of calcium transport. *Methods in Enzymology* 56:233-241.

250. Hertzberg EL & Hinkle PC (1974) Oxidative phosphorylation and proton translocation in membrane vesciles prepared from *Escherichia coli. Biochemical and Biophysical Research Communications* 58(1):178-184.

251. Boukhvalova MS, Dahlquist FW, & Stewart RC (2002) CheW binding interactions with CheA and Tar. Importance for chemotaxis signaling in Escherichia coli. *J Biol Chem* 277(25):22251-22259.

252. Cardozo MJ, Massazza DA, Parkinson JS, & Studdert CA (2010) Disruption of chemoreceptor signalling arrays by high levels of CheW, the receptor-kinase coupling protein. *Mol Microbiol* 75(5):1171-1181.

253. Zhang P, *et al.* (2004) Direct visualization of receptor arrays in frozen-hydrated sections and plunge-frozen specimens of *E. coli* engineered to overproduce the chemotaxis receptor Tsr. *J Microsc* 216:76-83.

254. Khursigara CM, Wu X, Zhang P, Lefman J, & Subramaniam S (2008) Role of HAMP domains in chemotaxis signaling by bacterial chemoreceptors. *Proc Natl Acad Sci U S A* 105(43):16555-16560.

255. Lefman J, *et al.* (2004) Three-dimensional electron microscopic imaging of membrane invaginations in *Escherichia coli* overproducing the chemotaxis receptor Tsr. *J Bacteriol* 186(15):5052-5061.

256. Underbakke ES, Zhu YM, & Kiessling LL (2008) Isotope-coded affinity tags with tunable reactivities for protein footprinting. *Angewandte Chemie* 120:98323-99826.

257. Zhang P, Khursigara CM, Hartnell LM, & Subramaniam S (2007) Direct visualization of *Escherichia coli* chemotaxis receptor arrays using cryo-electron microscopy. *Proc Natl Acad Sci U S A* 104(10):3777-3781.

258. DeLoney-Marino CR (2013) Observing chemotaxis in Vibrio fischeri using soft agar assays in an undergraduate microbiology laboratory. *Journal of Microbiology & Biology Education: JMBE* 14(2):271.

259. Croze OA, Ferguson GP, Cates ME, & Poon WC (2011) Migration of chemotactic bacteria in soft agar: role of gel concentration. *Biophysical journal* 101(3):525-534.

260. Li M & Hazelbauer GL (2004) Cellular stoichiometry of the components of the chemotaxis signalling complex. *J Bacteriol* 186(12):3687-3694.

261. Cannistraro VJ, Glekas GD, Rao CV, & Ordal GW (2011) Cellular stoichiometry of the chemotaxis proteins in *Bacillus subtilis*. *J Bacteriol* 193:3220-3227.

262. Chervitz SA & Falke JJ (1995) Lock on/off disulfides identify the transmembrane signaling helix of the aspartate receptor. *J Biol Chem* 270:24043-24053.

263. Chervitz SA & Falke JJ (1996) Molecular mechanism of transmembrane signaling by the aspartate receptor: A model. *Proc. Natl. Acad. Sci. U. S. A.* 93(6):2545-2550.

264. Parkinson JS (1978) Complementation analysis and deletion mapping of Escherichia coli mutants defective in chemotaxis. *J Bacteriol* 135(1):45-53.

265. Pinas GE, Frank V, Vaknin A, & Parkinson JS (2016) The source of high signal cooperativity in bacterial chemosensory arrays. *Proc Natl Acad Sci U S A* 113(12):3335-3340.

266. Briegel A, *et al.* (2014) New insights into bacterial chemoreceptor array structure and assembly from electron cryotomography. *Biochemistry* 53(10):1575-1585.

267. Parkinson JS & Houts SE (1982) Isolation and behavior of Escherichia coli deletion mutants lacking chemotaxis functions. *J Bacteriol* 151(1):106-113.

268. Ames P, Studdert CA, Reiser RH, & Parkinson JS (2002) Collaborative signaling by mixed chemoreceptor teams in Escherichia coli. *Proc Natl Acad Sci U S A* 99(10):7060-7065.

269. Borkovich KA & Simon MI (1991) Coupling of receptor function to phosphate-transfer reactions in bacterial chemotaxis. *Methods in Enzymology* 200:205-214.

270. Parkinson JS (2007) [20]-A "Bucket of Light" for Viewing Bacterial Colonies in Soft Agar. *Methods in enzymology* 423:432-435.

271. Iancu CV, *et al.* (2007) Electron cryotomography sample preparation using the Vitrobot. *Nat Protoc* 1:2813-2819.

272. Tivol W, Briegel A, & Jensen GJ (2008) An Improved Cryogen for Plunge Freezing. *Microsc Micoanal* 14:375-379.

273. Zheng QS, *et al.* (2007) UCSF tomography: An integrated software suite for real-time electron microscopic tomographic data collection, alignment and reconstruction. *J Struct Biol* 157(1):138-147.

274. Kremer JR, Mastronarde DN, & McIntosh JR (1996) Computer visualization of three-dimensional data using Imod. *J. Struct. Biol.* 116:71-76.

275. Agulleiro JI & Fernandez JJ (2011) Fast tomographic reconstruction on multicore computers. *Bioinformatics* 27:582-583.

276. Nicastro D, *et al.* (2006) The molecular architecture of axonemes revealed by cryoelectron tomography. *Science* 313(5789):944-948.

277. Hazelbauer GL, Falke JJ, & Parkinson JS (2008) Bacterial chemoreceptors: high-performance signaling in networked arrays. *Trends Biochem Sci* 33(1):9-19.

278. Zhulin IB (2001) The superfamily of chemotaxis transducers: from physiology to genomics and back. *Adv Microb Physiol* 45:157-198.

279. Krembel AK, Neumann S, & Sourjik V (2015) Universal response-adaptation relation in bacterial chemotaxis. *J Bacteriol* 197(2):307-313.

280. Bray D, Levin MD, & Morton-Firth CJ (1998) Receptor clustering as a cellular mechanism to control sensitivity. *Nature* 393(6680):85-88.

281. Cochran JR, Aivazian D, Cameron TO, & Stern LJ (2001) Receptor clustering and transmembrane signaling in T cells. *Trends Biochem Sci* 26(5):304-310.

282. Leitinger B & Hogg N (2002) The involvement of lipid rafts in the regulation of integrin function. *J Cell Sci* 115(Pt 5):963-972.

283. Mammen M, Choi S-K, & Whitesides GM (1998) Polyvalent interactions in biological systems: implications for design and use of multivalent ligands and inhibitors. *Angewandte Chemie International Edition* 37(20):2754-2794.

284. Gestwicki JE, Strong LE, & Kiessling LL (2000) Tuning chemotactic responses with synthetic multivalent ligands. *Chem Biol* 7(8):583-591.

285. Falke JJ & Hazelbauer GL (2001) Transmembrane signaling in bacterial chemoreceptors. *Trends Biochem Sci* 26(4):257-265.

286. Irieda H, Homma M, Homma M, & Kawagishi I (2006) Control of chemotactic signal gain via modulation of a pre-formed receptor array. *J Biol Chem* 281(33):23880-23886.

287. Parkinson JS (2010) Signaling mechanisms of HAMP domains in chemoreceptors and sensor kinases. *Annu Rev Microbiol* 64:101-122.

288. Wright GA, Crowder RL, Draheim RR, & Manson MD (2011) Mutational analysis of the transmembrane helix 2-HAMP domain connection in the Escherichia coli aspartate chemoreceptor tar. *J Bacteriol* 193(1):82-90.

289. Hall BA, Armitage JP, & Sansom MS (2012) Mechanism of bacterial signal transduction revealed by molecular dynamics of Tsr dimers and trimers of dimers in lipid vesicles. *PLoS Comput Biol* 8(9):e1002685.

290. Koshy SS, Li X, Eyles SJ, Weis RM, & Thompson LK (2014) Hydrogen exchange differences between chemoreceptor signaling complexes localize to functionally important subdomains. *Biochemistry* 53(49):7755-7764.

291. Borrok MJ, Kolonko EM, & Kiessling LL (2008) Chemical probes of bacterial signal transduction reveal that repellents stabilize and attractants destabilize the chemoreceptor array. *ACS Chem Biol* 3(2):101-109.

292. Lamanna AC, Ordal GW, & Kiessling LL (2005) Large increases in attractant concentration disrupt the polar localization of bacterial chemoreceptors. *Mol Microbiol* 57(3):774-785.

293. Shiomi D, Banno S, Homma M, & Kawagishi I (2005) Stabilization of polar localization of a chemoreceptor via its covalent modifications and its communication with a different chemoreceptor. *J Bacteriol* 187(22):7647-7654.

294. Besschetnova TY, *et al.* (2008) Receptor density balances signal stimulation and attenuation in membrane-assembled complexes of bacterial chemotaxis signaling proteins. *Proc Natl Acad Sci U S A* 105(34):12289-12294.

295. Vaknin A & Berg HC (2007) Physical responses of bacterial chemoreceptors. *J Mol Biol* 366(5):1416-1423.

296. Frank V & Vaknin A (2013) Prolonged stimuli alter the bacterial chemosensory clusters. *Mol Microbiol* 88(3):634-644.

297. Liberman L, Berg HC, & Sourjik V (2004) Effect of chemoreceptor modification on assembly and activity of the receptor-kinase complex in Escherichia coli. *J Bacteriol* 186(19):6643-6646.

298. Homma M, Shiomi D, Homma M, & Kawagishi I (2004) Attractant binding alters arrangement of chemoreceptor dimers within its cluster at a cell pole. *Proc Natl Acad Sci U S A* 101(10):3462-3467.

299. Briegel A, Beeby M, Thanbichler M, & Jensen GJ (2011) Activated chemoreceptor arrays remain intact and hexagonally packed. *Mol Microbiol* 82(3):748-757.

300. Briegel A, *et al.* (2013) The mobility of two kinase domains in the Escherichia coli chemoreceptor array varies with signalling state. *Mol Microbiol* 89(5):831-841.

301. Kiessling LL, Gestwicki JE, & Strong LE (2000) Synthetic multivalent ligands in the exploration of cell-surface interactions. *Curr Opin Chem Biol* 4(6):696-703.

302. Sourjik V & Berg HC (2002) Receptor sensitivity in bacterial chemotaxis. *Proc Natl Acad Sci U S A* 99(1):123-127.

303. Crooks JA, Stilwell MD, Oliver PM, Zhong Z, & Weibel DB (2015) Decoding the Chemical Language of Motile Bacteria by Using High-Throughput Microfluidic Assays. *Chembiochem* 16(15):2151-2155.

304. Waite AJ, *et al.* (2016) Non-genetic diversity modulates population performance. *Mol Syst Biol* 12(12):895.

305. Neumann S, Hansen CH, Wingreen NS, & Sourjik V (2010) Differences in signalling by directly and indirectly binding ligands in bacterial chemotaxis. *EMBO J* 29(20):3484-3495.

306. Underbakke ES & Kiessling LL (2010) Classifying chemoreceptors: quantity versus quality. *EMBO J* 29(20):3435-3436.

307. Tajima H, *et al.* (2011) Ligand specificity determined by differentially arranged common ligand-binding residues in bacterial amino acid chemoreceptors Tsr and Tar. *J Biol Chem* 286(49):42200-42210.

308. Mesibov R & Adler J (1972) Chemotaxis toward amino acids in Escherichia coli. *J Bacteriol* 112(1):315-326.

309. Strong LE & Kiessling LL (1999) A general synthetic route to defined, biologically active multivalent arrays. *Journal of the American Chemical Society* 121(26):6193-6196.

310. Kolb HC, Finn MG, & Sharpless KB (2001) Click Chemistry: Diverse Chemical Function from a Few Good Reactions. *Angew Chem Int Ed Engl* 40(11):2004-2021.

311. Kluger C & Binder WH (2007) Functionalized poly (oxanorbornene)-block-copolymers: Preparation via ROMP/click-methodology. *Journal of Polymer Science Part A: Polymer Chemistry* 45(3):485-499.

312. Schaefer M, Hanik N, & Kilbinger AF (2012) ROMP copolymers for orthogonal click functionalizations. *Macromolecules* 45(17):6807-6818.

313. Choi TL & Grubbs RH (2003) Controlled living ring-opening-metathesis polymerization by a fast-initiating ruthenium catalyst. *Angew Chem Int Ed Engl* 42(15):1743-1746.

314. Frank V, Pinas GE, Cohen H, Parkinson JS, & Vaknin A (2016) Networked Chemoreceptors Benefit Bacterial Chemotaxis Performance. *MBio* 7(6).

315. Lamanna AC, *et al.* (2002) Conserved amplification of chemotactic responses through chemoreceptor interactions. *J Bacteriol* 184(18):4981-4987.

316. Cassidy CK, *et al.* (2015) CryoEM and computer simulations reveal a novel kinase conformational switch in bacterial chemotaxis signaling. *Elife* 4.

317. Lai RZ & Parkinson JS (2014) Functional suppression of HAMP domain signaling defects in the E. coli serine chemoreceptor. *J Mol Biol* 426(21):3642-3655.

318. Sourjik V, Vaknin A, Shimizu TS, & Berg HC (2007) In vivo measurement by FRET of pathway activity in bacterial chemotaxis. *Methods Enzymol* 423:365-391.

319. Singer JT, *et al.* (2010) Broad-host-range plasmids for red fluorescent protein labeling of gram-negative bacteria for use in the zebrafish model system. *Appl Environ Microbiol* 76(11):3467-3474.

320. Lai RZ, Gosink KK, & Parkinson JS (2017) Signaling Consequences of Structural Lesions that Alter the Stability of Chemoreceptor Trimers of Dimers. *J Mol Biol* 429(6):823-835.

321. Crellin PK, Luo C-Y, & Morita YS (2013) Metabolism of Plasma Membrane Lipids in Mycobacteria and Corynebacteria. *Lipid Metabolism*, ed Baez RV (InTech).

322. Brennan PJ (2003) Structure, function, and biogenesis of the cell wall of Mycobacterium tuberculosis. *Tuberculosis (Edinb)* 83(1-3):91-97.

323. Crick DC, Mahapatra S, & Brennan PJ (2001) Biosynthesis of the arabinogalactan-peptidoglycan complex of Mycobacterium tuberculosis. *Glycobiology* 11(9):107R-118R.

324. Brennan PJ & Nikaido H (1995) The Envelope of Mycobacteria. *Annual Review of Biochemistry* 64(1):29-63.

325. Kieser KJ & Rubin EJ (2014) How sisters grow apart: mycobacterial growth and division. *Nat. Rev. Microbiol.* 12(8):550-562.

326. Joyce G, *et al.* (2012) Cell division site placement and asymmetric growth in mycobacteria. *PLoS One* 7(9):e44582.

327. Botella H, *et al.* (2017) Distinct Spatiotemporal Dynamics of Peptidoglycan Synthesis between Mycobacterium smegmatis and Mycobacterium tuberculosis. *MBio* 8(5).

328. Kester JC & Fortune SM (2014) Persisters and beyond: mechanisms of phenotypic drug resistance and drug tolerance in bacteria. *Crit Rev Biochem Mol Biol* 49(2):91-101.

329. Meniche X, *et al.* (2014) Subpolar addition of new cell wall is directed by DivIVA in mycobacteria. *Proc Natl Acad Sci U S A* 111(31):E3243-3251.

330. Baumgart M, Schubert K, Bramkamp M, & Frunzke J (2016) Impact of LytR-CpsA-Psr Proteins on Cell Wall Biosynthesis in Corynebacterium glutamicum. *J Bacteriol* 198(22):3045-3059.

331. Backus KM, *et al.* (2011) Uptake of unnatural trehalose analogs as a reporter for Mycobacterium tuberculosis. *Nature Chemical Biology* 7(4):228-235.

332. Rodriguez-Rivera FP, Zhou X, Theriot JA, & Bertozzi CR (2017) Visualization of mycobacterial membrane dynamics in live cells. *Journal of the American Chemical Society* 139(9):3488-3495.

333. Swarts BM, *et al.* (2012) Probing the Mycobacterial Trehalome with Bioorthogonal Chemistry. *Journal of the American Chemical Society* 134(39):16123-16126.

334. Kavunja HW, *et al.* (2016) A chemical reporter strategy for detecting and identifying O-mycoloylated proteins in Corynebacterium. *Chemical Communications* 52(95):13795-13798.

335. Cole ST, *et al.* (1998) Deciphering the biology of Mycobacterium tuberculosis from the complete genome sequence. *Nature* 393(6685):537-544.

336. Portevin D, *et al.* (2004) A polyketide synthase catalyzes the last condensation step of mycolic acid biosynthesis in mycobacteria and related organisms. *Proceedings of the National Academy of Sciences* 101(1):314-319.

337. Gavalda S, *et al.* (The Polyketide Synthase Pks13 Catalyzes a Novel Mechanism of Lipid Transfer in Mycobacteria. *Chemistry & Biology* (0).

338. Lea-Smith DJ, *et al.* (2007) The Reductase That Catalyzes Mycolic Motif Synthesis Is Required for Efficient Attachment of Mycolic Acids to Arabinogalactan. *Journal of Biological Chemistry* 282(15):11000-11008.

339. Yamaryo-Botte Y, *et al.* (2014) Acetylation of trehalose mycolates is required for efficient MmpL-mediated membrane transport in Corynebacterineae. *ACS Chemical Biology* 10(3):734-746.

340. Tahlan K, *et al.* (2012) SQ109 Targets MmpL3, a Membrane Transporter of Trehalose Monomycolate Involved in Mycolic Acid Donation to the Cell Wall Core of Mycobacterium tuberculosis. *Antimicrobial Agents and Chemotherapy* 56(4):1797-1809.

341. Barry CS, Backus KM, Barry CE, & Davis BG (2011) ESI-MS Assay of M. tuberculosis Cell Wall Antigen 85 Enzymes Permits Substrate Profiling and Design of a Mechanism-Based Inhibitor. *Journal of the American Chemical Society* 133(34):13232-13235.

342. Rose TM & Prestwich GD (2006) Fluorogenic Phospholipids as Head Group-Selective Reporters of Phospholipase A Activity. *ACS Chemical Biology* 1(2):83-92.

343. Feng L, *et al.* (2002) A Real-Time Fluorogenic Phospholipase A2 Assay for Biochemical and Cellular Activity Measurements. *Chemistry & Biology* 9(7):795-803.

344. Watzke A, *et al.* (2008) Selective Activity-Based Probes for Cysteine Cathepsins. *Angewandte Chemie International Edition* 47(2):406-409.

345. Folk DS, Torosian JC, Hwang S, McCafferty DG, & Franz KJ (2012) Monitoring β-Secretase Activity in Living Cells with a Membrane-Anchored FRET Probe. *Angewandte Chemie International Edition* 51(43):10795-10799.

346. Pérez-López AM, Soria-Gila ML, Marsden ER, Lilienkampf A, & Bradley M (2016) Fluorogenic Substrates for In Situ Monitoring of Caspase-3 Activity in Live Cells. *PLOS ONE* 11(5):e0153209.

347. Yadav AK, *et al.* (2015) Fluorescence-Quenched Substrates for Live Cell Imaging of Human Glucocerebrosidase Activity. *Journal of the American Chemical Society* 137(3):1181-1189.

348. Ronning DR, *et al.* (2000) Crystal structure of the secreted form of antigen 85C reveals potential targets for mycobacterial drugs and vaccines. *Nat. Struct. Biol.* 7(2):141-146.

349. Anderson DH, Harth G, Horwitz MA, & Eisenberg D (2001) An interfacial mechanism and a class of inhibitors inferred from two crystal structures of the Mycobacterium tuberculosis 30 kda major secretory protein (antigen 85B), a mycolyl transferase. *Journal of Molecular Biology* 307(2):671-681.

350. Ronning DR, Vissa V, Besra GS, Belisle JT, & Sacchettini JC (2004) Mycobacterium tuberculosis Antigen 85A and 85C Structures Confirm Binding Orientation and Conserved Substrate Specificity. *Journal of Biological Chemistry* 279(35):36771-36777.

351. Favrot L, *et al.* (2013) Mechanism of inhibition of Mycobacterium tuberculosis antigen 85 by ebselen. *Nature Communications* 4.

352. Elamin AA, Stehr M, Oehlmann W, & Singh M (2009) The mycolyltransferase 85A, a putative drug target of Mycobacterium tuberculosis: development of a novel assay and quantification of glycolipid-status of the mycobacterial cell wall. *J Microbiol Methods* 79(3):358-363.

353. Belisle JT, *et al.* (1997) Role of the major antigen of Mycobacterium tuberculosis in cell wall biogenesis. *Science* 276(5317):1420-1422.

354. Kuru E, *et al.* (2012) In Situ Probing of Newly Synthesized Peptidoglycan in Live Bacteria with Fluorescent D-Amino Acids. *Angewandte Chemie International Edition* 51(50):12519-12523.

355. McDonough JA, *et al.* (2008) Identification of functional Tat signal sequences in Mycobacterium tuberculosis proteins. *J Bacteriol* 190(19):6428-6438.

356. Stanley NR, Palmer T, & Berks BC (2000) The twin arginine consensus motif of Tat signal peptides is involved in Sec-independent protein targeting in Escherichia coli. *J Biol Chem* 275(16):11591-11596.

357. Shieh P, Siegrist MS, Cullen AJ, & Bertozzi CR (2014) Imaging bacterial peptidoglycan with near-infrared fluorogenic azide probes. *Proceedings of the National Academy of Sciences* 111(15):5456-5461.

358. Dautin N, *et al.* (2017) Mycoloyltransferases: A large and major family of enzymes shaping the cell envelope of Corynebacteriales. *Biochimica et Biophysica Acta (BBA) - General Subjects* 1861(1, Part B):3581-3592.

359. Nataraj V, *et al.* (2015) Mycolic acids: deciphering and targeting the Achilles' heel of the tubercle bacillus. *Mol Microbiol* 98(1):7-16.

360. Jackson M, *et al.* (1999) Inactivation of the antigen 85C gene profoundly affects the mycolate content and alters the permeability of the Mycobacterium tuberculosis cell envelope. *Molecular Microbiology* 31(5):1573-1587.

361. Touchette MH, *et al.* (2017) A Screen for Protein-Protein Interactions in Live Mycobacteria Reveals a Functional Link between the Virulence-Associated Lipid Transporter LprG and the Mycolyltransferase Antigen 85A. *ACS Infect Dis* 3(5):336-348.

362. Tsui HC, Keen SK, Sham LT, Wayne KJ, & Winkler ME (2011) Dynamic distribution of the SecA and SecY translocase subunits and septal localization of the HtrA surface chaperone/protease during Streptococcus pneumoniae D39 cell division. *MBio* 2(5).

363. Rose P, Frobel J, Graumann PL, & Muller M (2013) Substrate-dependent assembly of the Tat translocase as observed in live Escherichia coli cells. *PLoS One* 8(8):e69488.

364. Schirner K, *et al.* (2015) Lipid-linked cell wall precursors regulate membrane association of bacterial actin MreB. *Nat Chem Biol* 11(1):38-45.

365. Azad GK & Tomar RS (2014) Ebselen, a promising antioxidant drug: mechanisms of action and targets of biological pathways. *Mol Biol Rep* 41(8):4865-4879.

366. Hodges HL, Brown, R.B., Crooks, J.C., Weibel, D.B. and Kiessling, L.L (2017) A Fluorogenic Probe for Real-Time Imaging of Mycobacterial Growth and Division. *In submission.*

367. Liu Y, *et al.* (1999) Use of a Fluorescence Plate Reader for Measuring Kinetic Parameters with Inner Filter Effect Correction. *Analytical Biochemistry* 267(2):331-335.

368. Xia Y & Whitesides G (1998) Replica molding with a polysiloxane mold provides this patterned microstructure. *Angew. Chem. Int. Ed* 37:550-575.

369. Barthelme S (2017) imager. (Github repository).

370. Hadley. W (ggplot2: An implementationof the Grammar of Graphics.

371. Joyce G, Robertson BD, & Williams KJ (2011) A modified agar pad method for mycobacterial live-cell imaging. *BMC Res Notes* 4:73.

372. Cress BF, *et al.* (2014) Masquerading microbial pathogens: capsular polysaccharides mimic host-tissue molecules. *FEMS Microbiol Rev* 38(4):660-697.

373. Herget S, *et al.* (2008) Statistical analysis of the Bacterial Carbohydrate Structure Data Base (BCSDB): characteristics and diversity of bacterial carbohydrates in comparison with mammalian glycans. *BMC Struct Biol* 8:35.

374. Hsu KL, Pilobello KT, & Mahal LK (2006) Analyzing the dynamic bacterial glycome with a lectin microarray approach. *Nat Chem Biol* 2(3):153-157.

375. Hsu KL & Mahal LK (2006) A lectin microarray approach for the rapid analysis of bacterial glycans. *Nat Protoc* 1(2):543-549.

376. Zheng RB, *et al.* (2017) Insights into Interactions of Mycobacteria with the Host Innate Immune System from a Novel Array of Synthetic Mycobacterial Glycans. *ACS Chem Biol* 12(12):2990-3002.

377. Stowell SR, *et al.* (2014) Microbial glycan microarrays define key features of host-microbial interactions. *Nat Chem Biol* 10(6):470-476.

378. Deng L, *et al.* (1995) Recognition of multiple effects of ethambutol on metabolism of mycobacterial cell envelope. *Antimicrob Agents Chemother* 39(3):694-701.

379. Dube DH & Bertozzi CR (2003) Metabolic oligosaccharide engineering as a tool for glycobiology. *Curr Opin Chem Biol* 7(5):616-625.

380. Fraser-Reid BO, Tatsuta K, & Thiem J (2001) Glycoscience : Chemistry and Chemical Biology I-III. (Springer Berlin Heidelberg,, Berlin, Heidelberg), pp 1 online resource (LVII, 2854 pages 2402 illustrations in 2853 volumes, not available separately.

381. Chang PV & Bertozzi CR (2012) Imaging beyond the proteome. *Chem Commun (Camb)* 48(71):8864-8879.

382. Sinkeldam RW, Greco NJ, & Tor Y (2010) Fluorescent analogs of biomolecular building blocks: design, properties, and applications. *Chem Rev* 110(5):2579-2619.

383. Kayser H, Ats C, Lehmann J, & Reutter W (1993) New amino sugar analogues are incorporated at different rates into glycoproteins of mouse organs. *Experientia* 49(10):885-887.

384. Jacobs CL, *et al.* (2001) Substrate Specificity of the Sialic Acid Biosynthetic Pathway. *Biochemistry* 40(43):12864-12874.

385. Martinez Farias MA, Kincaid VA, Annamalai VR, & Kiessling LL (2014) Isoprenoid Phosphonophosphates as Glycosyltransferase Acceptor Substrates. *Journal of the American Chemical Society* 136(24):8492-8495.

386. Brown CD, Rusek MS, & Kiessling LL (2012) Fluorosugar chain termination agents as probes of the sequence specificity of a carbohydrate polymerase. *J Am Chem Soc* 134(15):6552-6555.

387. Yamatsugu K, Splain RA, & Kiessling LL (2016) Fidelity and Promiscuity of a Mycobacterial Glycosyltransferase. *Journal of the American Chemical Society* 138(29):9205-9211.

388. Zhang J, *et al.* (2011) Reconstitution of functional mycobacterial arabinosyltransferase AftC proteoliposome and assessment of decaprenylphosphorylarabinose analogues as arabinofuranosyl donors. *ACS Chem Biol* 6(8):819-828.

389. Goon S, Schilling B, Tullius MV, Gibson BW, & Bertozzi CR (2003) Metabolic incorporation of unnatural sialic acids into Haemophilus ducreyi lipooligosaccharides. *Proc Natl Acad Sci U S A* 100(6):3089-3094.

390. Kolbe K, *et al.* (2017) Azido pentoses: A New Tool to Efficiently Label Mycobacterium tuberculosis Clinical Isolates. *ChemBioChem*:n/a-n/a.

391. Clark EL, *et al.* (2016) Development of Rare Bacterial Monosaccharide Analogs for Metabolic Glycan Labeling in Pathogenic Bacteria. *ACS Chemical Biology* 11(12):3365-3373.

392. Koenigs MB, Richardson EA, & Dube DH (2009) Metabolic profiling of Helicobacter pyloriglycosylation. *Molecular BioSystems* 5(9):909-912.

393. Herget S, *et al.* (2008) Statistical analysis of the Bacterial Carbohydrate Structure Data Base (BCSDB): Characteristics and diversity of bacterial carbohydrates in comparison with mammalian glycans. *BMC Structural Biology* 8:35-35.

394. Wolucka BA (2008) Biosynthesis of D-arabinose in mycobacteria – a novel bacterial pathway with implications for antimycobacterial therapy. *FEBS Journal* 275(11):2691-2711.

395. Cantarel BL, Lombard V, & Henrissat B (2012) Complex carbohydrate utilization by the healthy human microbiome. *PLoS One* 7(6):e28742.

396. Xu AM, Wang DS, Shieh P, Cao Y, & Melosh NA (2017) Direct Intracellular Delivery of Cell-Impermeable Probes of Protein Glycosylation by Using Nanostraws. *ChemBioChem* 18(7):623-628.

397. Alderwick LJ, *et al.* (2005) Deletion of Cg-emb in corynebacterianeae leads to a novel truncated cell wall arabinogalactan, whereas inactivation of Cg-ubiA results in an arabinan-deficient mutant with a cell wall galactan core. *J Biol Chem* 280(37):32362-32371.

398. Alderwick LJ, Seidel M, Sahm H, Besra GS, & Eggeling L (2006) Identification of a novel arabinofuranosyltransferase (AftA) involved in cell wall arabinan biosynthesis in Mycobacterium tuberculosis. *J Biol Chem* 281(23):15653-15661.

399. Birch HL, *et al.* (2008) Biosynthesis of mycobacterial arabinogalactan: identification of a novel alpha(1-->3) arabinofuranosyltransferase. *Mol Microbiol* 69(5):1191-1206.

400. Seidel M, *et al.* (2007) Identification of a novel arabinofuranosyltransferase AftB involved in a terminal step of cell wall arabinan biosynthesis in Corynebacterianeae, such as Corynebacterium glutamicum and Mycobacterium tuberculosis. *J Biol Chem* 282(20):14729-14740.

401. Escuyer VE, *et al.* (2001) The role of the embA and embB gene products in the biosynthesis of the terminal hexaarabinofuranosyl motif of Mycobacterium smegmatis arabinogalactan. *J Biol Chem* 276(52):48854-48862.

402. Skovierova H, *et al.* (2009) AftD, a novel essential arabinofuranosyltransferase from mycobacteria. *Glycobiology* 19(11):1235-1247.

403. Alderwick LJ, Birch, H.L., Krumbach, K., Bott, M., Eggeling, L. and Besra, G.S. (2017) AftD functions as an α1→ 5 arabinofuranosyltransferase involved in the biosynthesis of the mycobacterial cell wall core. *The Cell Surface*.

404. Kraft MB, Martinez Farias MA, & Kiessling LL (2013) Synthesis of lipid-linked arabinofuranose donors for glycosyltransferases. *J Org Chem* 78(5):2128-2133.

405. Lee RE, Li W, Chatterjee D, & Lee RE (2005) Rapid structural characterization of the arabinogalactan and lipoarabinomannan in live mycobacterial cells using 2D and 3D HR-MAS NMR: structural changes in the arabinan due to ethambutol treatment and gene mutation are observed. *Glycobiology* 15(2):139-151.

406. Bodenhausen G & Ruben DJ (1980) Natural abundance nitrogen-15 NMR by enhanced heteronuclear spectroscopy. *Chemical Physics Letters* 69(1):185-189.

407. Jankute M, Grover S, Rana AK, & Besra GS (2012) Arabinogalactan and lipoarabinomannan biosynthesis: structure, biogenesis and their potential as drug targets. *Future Microbiol* 7(1):129-147.

408. Rubens CE, Heggen LM, Haft RF, & Wessels MR (1993) Identification of cpsD, a gene essential for type III capsule expression in group B streptococci. *Mol Microbiol* 8(5):843-855.

409. Masson L & Holbein BE (1985) Role of lipid intermediate(s) in the synthesis of serogroup B Neisseria meningitidis capsular polysaccharide. *J Bacteriol* 161(3):861-867.

410. Wacker M, *et al.* (2002) N-linked glycosylation in Campylobacter jejuni and its functional transfer into E. coli. *Science* 298(5599):1790-1793.

411. Troy EB, Carey VJ, Kasper DL, & Comstock LE (2010) Orientations of the Bacteroides fragilis capsular polysaccharide biosynthesis locus promoters during symbiosis and infection. *J Bacteriol* 192(21):5832-5836.

Appendix 1. NMR Spectra

3-27

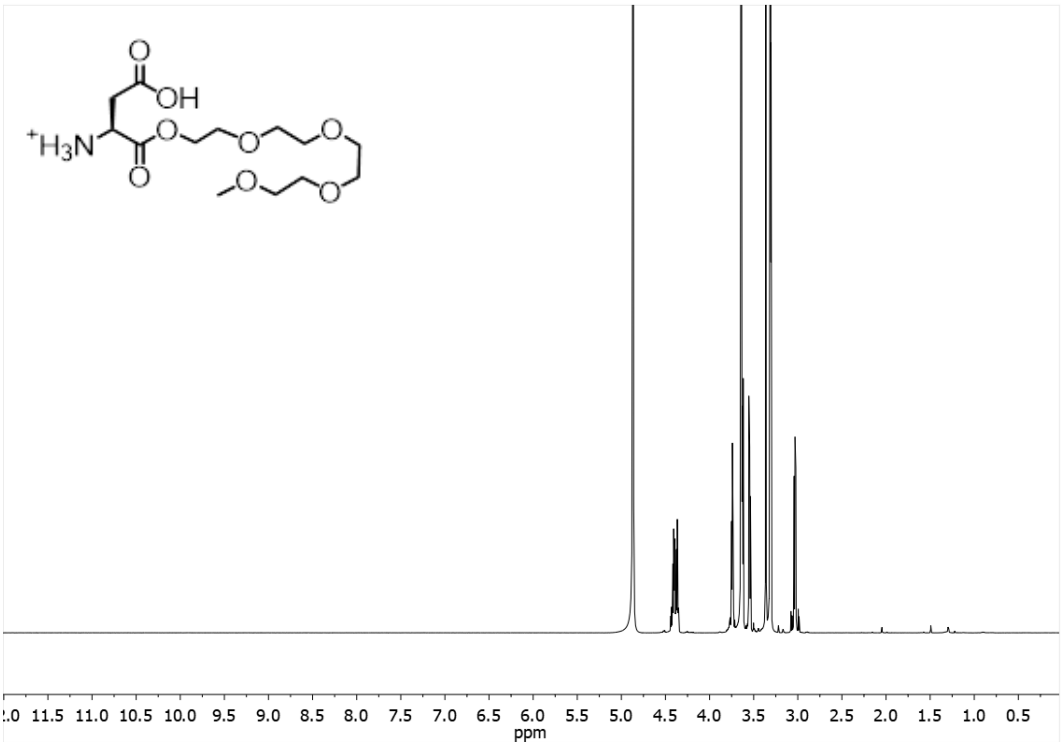
OH
+H3N
O
O
O
O
O
O
O
O
11.5 11.0 10.5 10.0 9.5 9.0 8.5 8.0 7.5 7.0 6.5 6.0 5.5 5.0 4.5 4.0 3.5 3.0 2.5 2.0 1.5 1.0 0.5
ppm

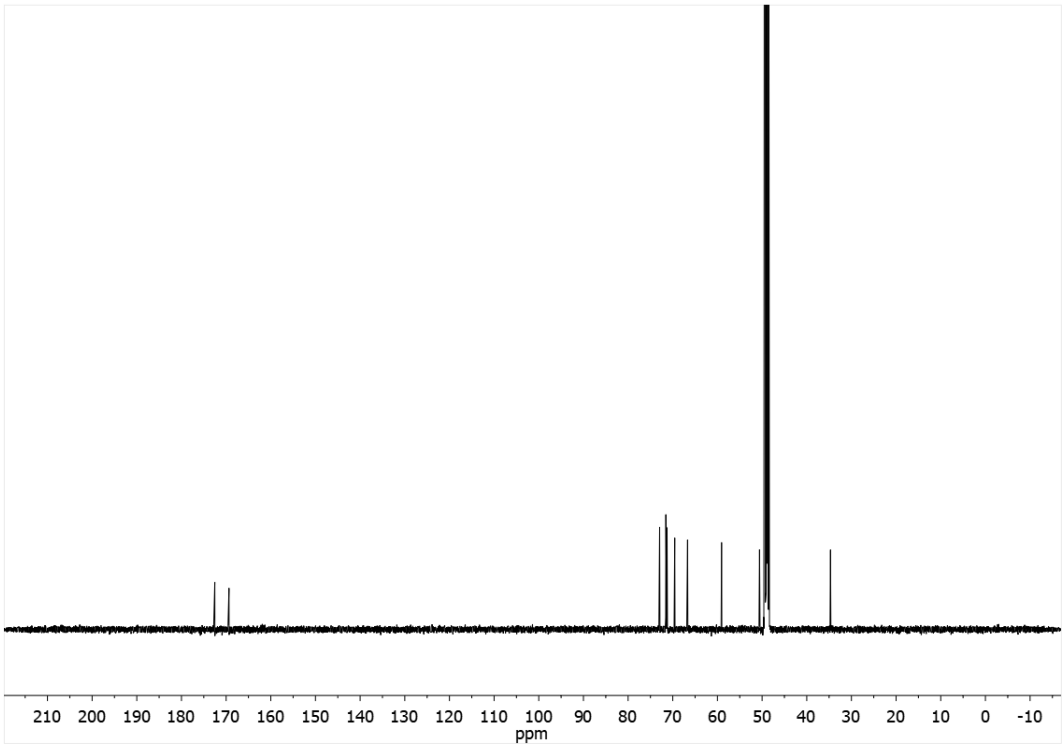
210 200 190 180 170 160 150 140 130 120 110 100 90 80 70 60 50 40 30 20 10 0 -10
ppm

3-28

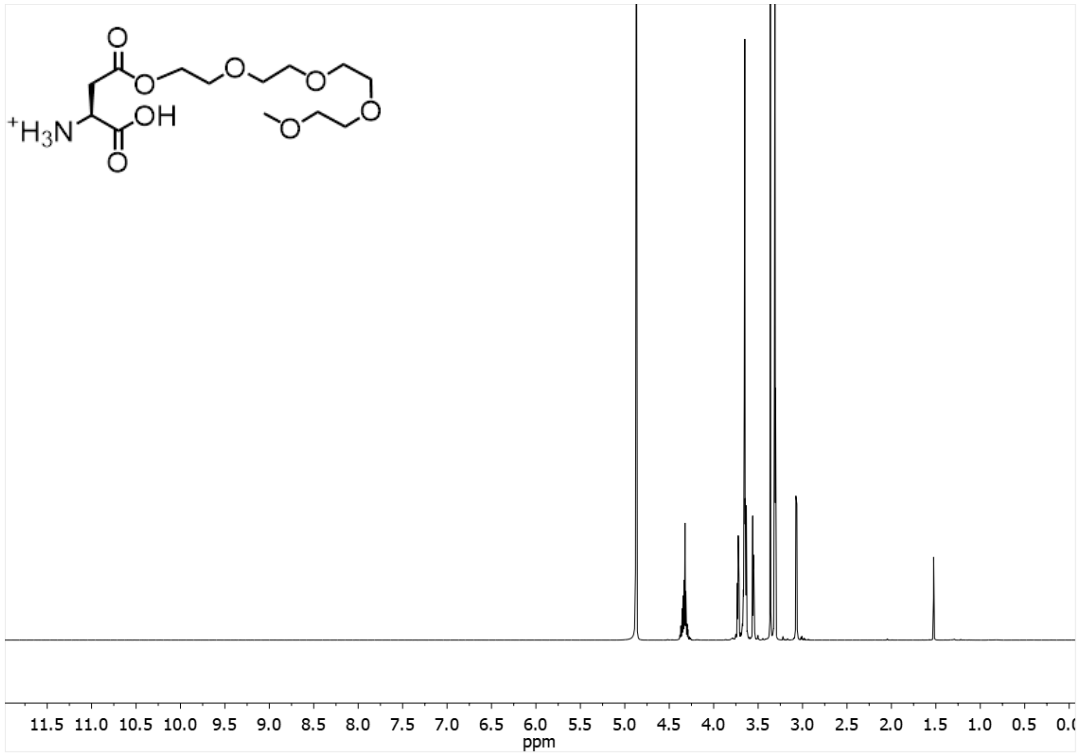
+H3N
OH
11.5 11.0 10.5 10.0 9.5 9.0 8.5 8.0 7.5 7.0 6.5 6.0 5.5 5.0 4.5 4.0 3.5 3.0 2.5 2.0 1.5 1.0 0.5
ppm

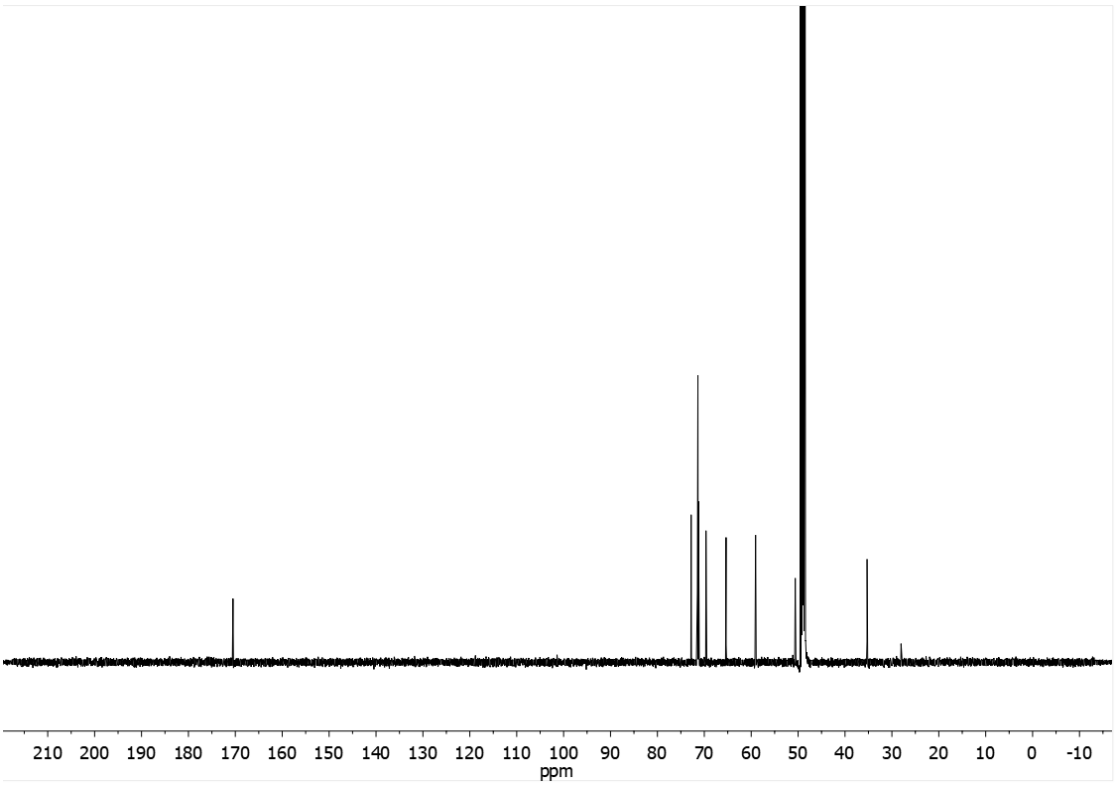
210 200 190 180 170 160 150 140 130 120 110 100 90 80 70 60 50 40 30 20 10 0 -10
ppm

3-29

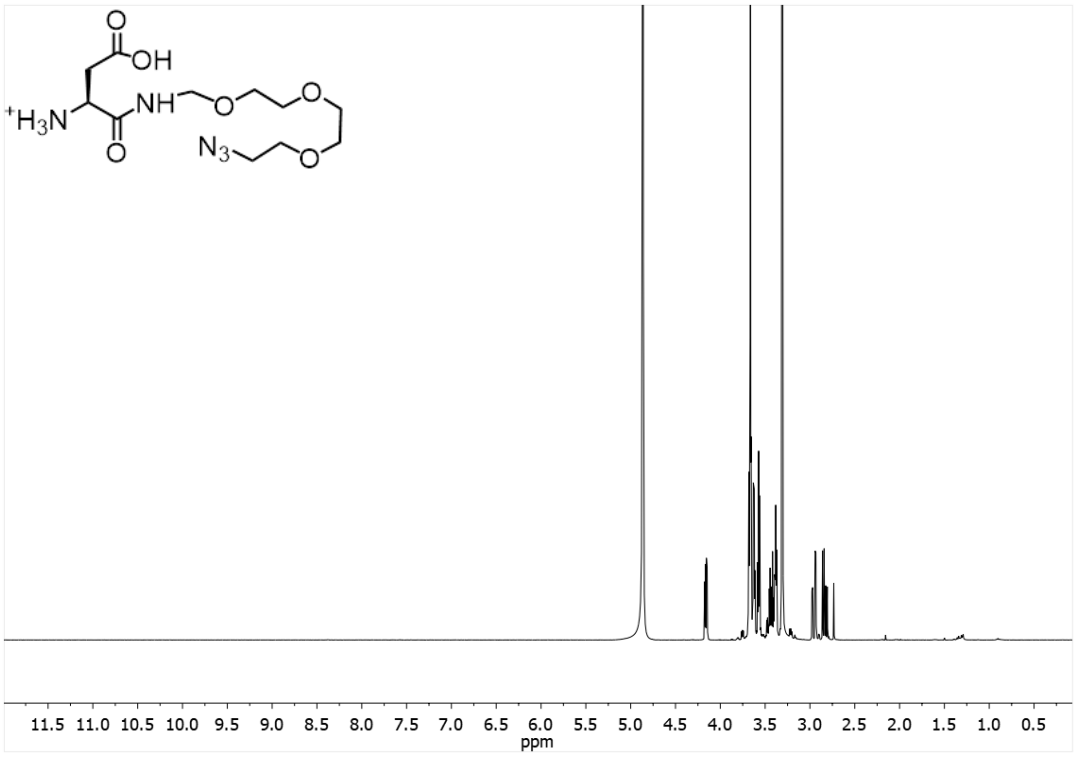
OH
NH
$^{+}H_3N$
N_3
11.5 11.0 10.5 10.0 9.5 9.0 8.5 8.0 7.5 7.0 6.5 6.0 5.5 5.0 4.5 4.0 3.5 3.0 2.5 2.0 1.5 1.0 0.5
ppm

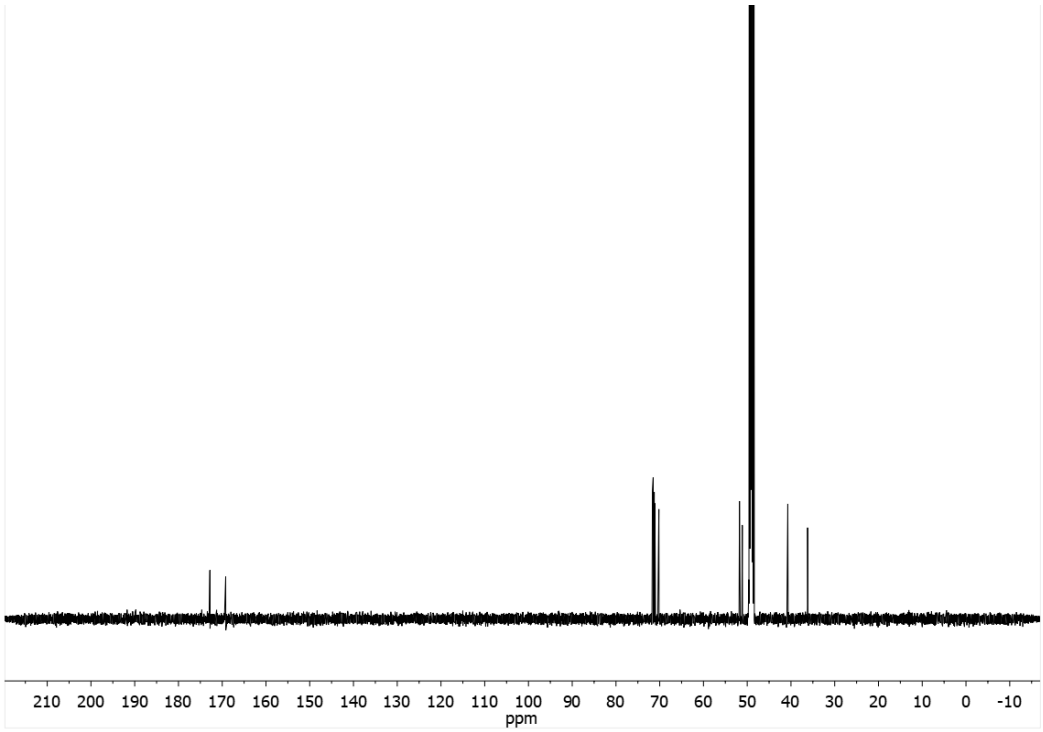
210 200 190 180 170 160 150 140 130 120 110 100 90 80 70 60 50 40 30 20 10 0 -10
ppm

3-30

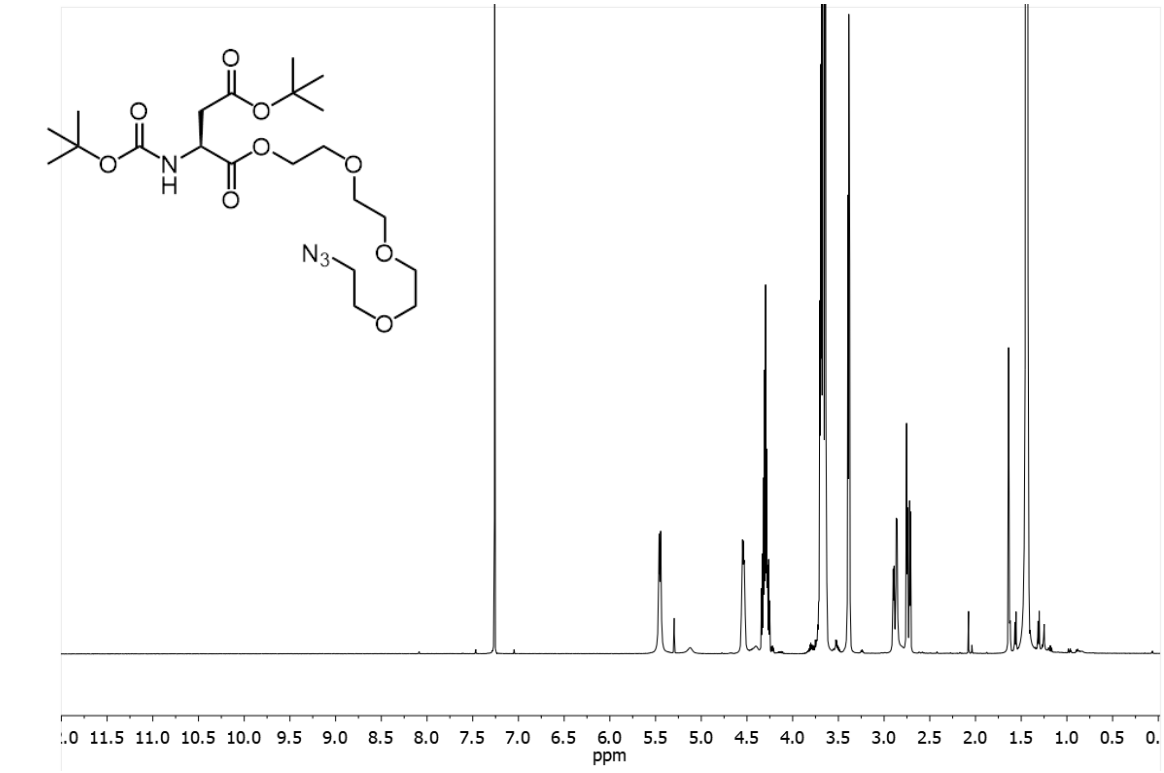

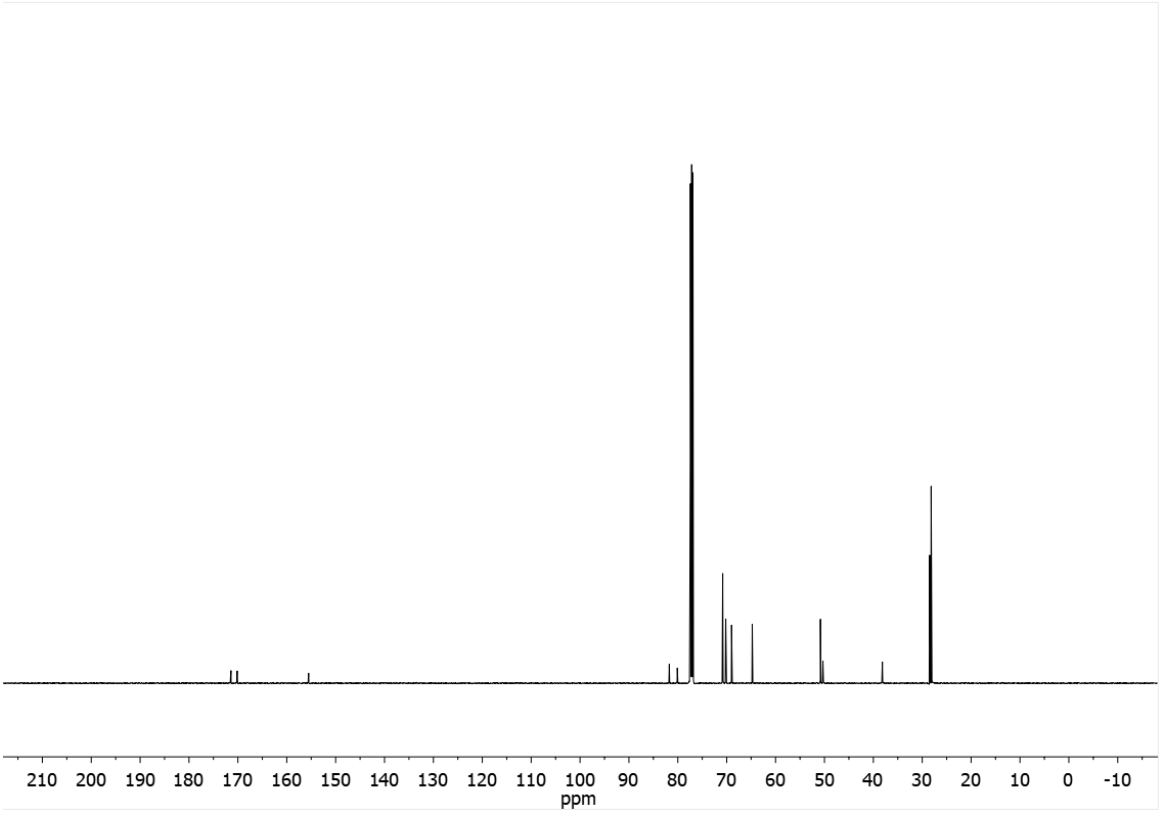

3-31

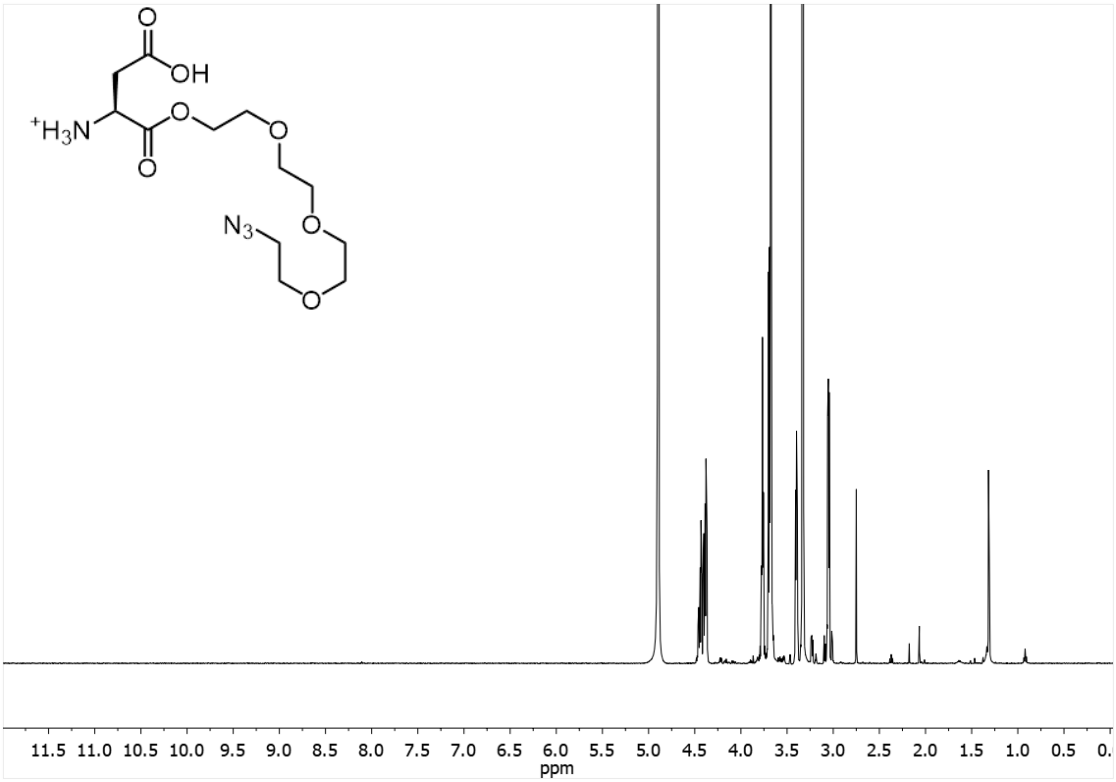
OH
+H3N
O
O
O
O
O
N3
O
O
11.5 11.0 10.5 10.0 9.5 9.0 8.5 8.0 7.5 7.0 6.5 6.0 5.5 5.0 4.5 4.0 3.5 3.0 2.5 2.0 1.5 1.0 0.5
ppm

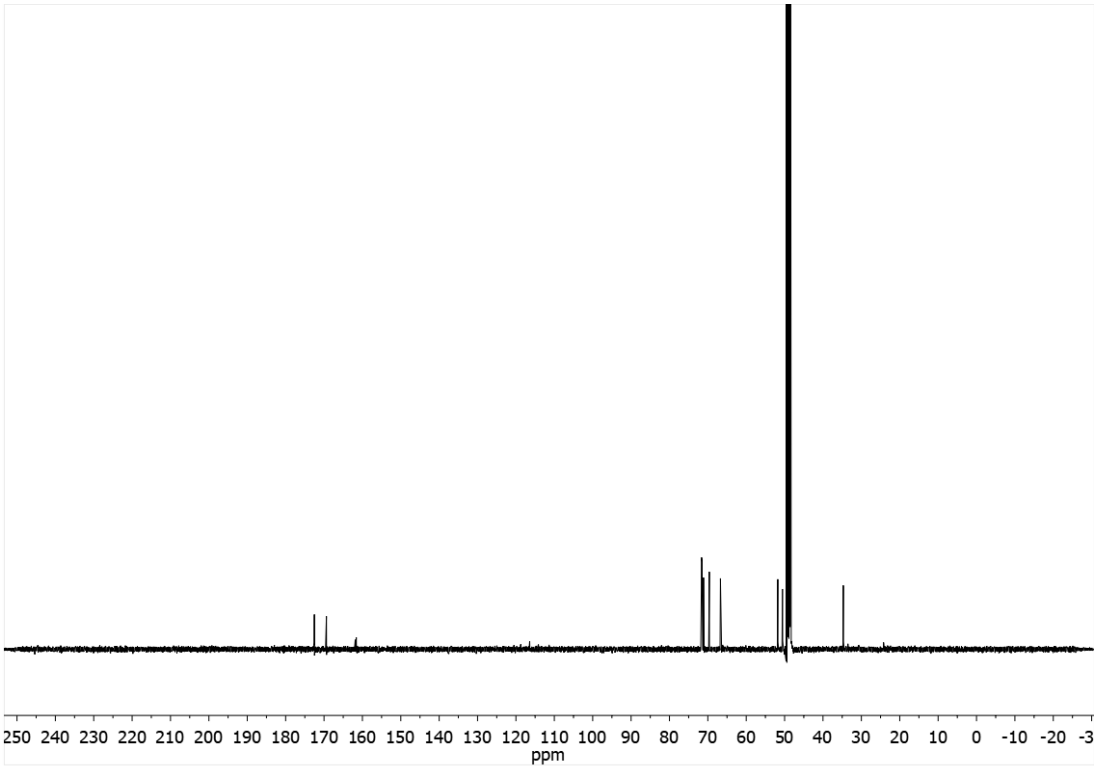
250 240 230 220 210 200 190 180 170 160 150 140 130 120 110 100 90 80 70 60 50 40 30 20 10 0 -10 -20 -3
ppm

3-34a

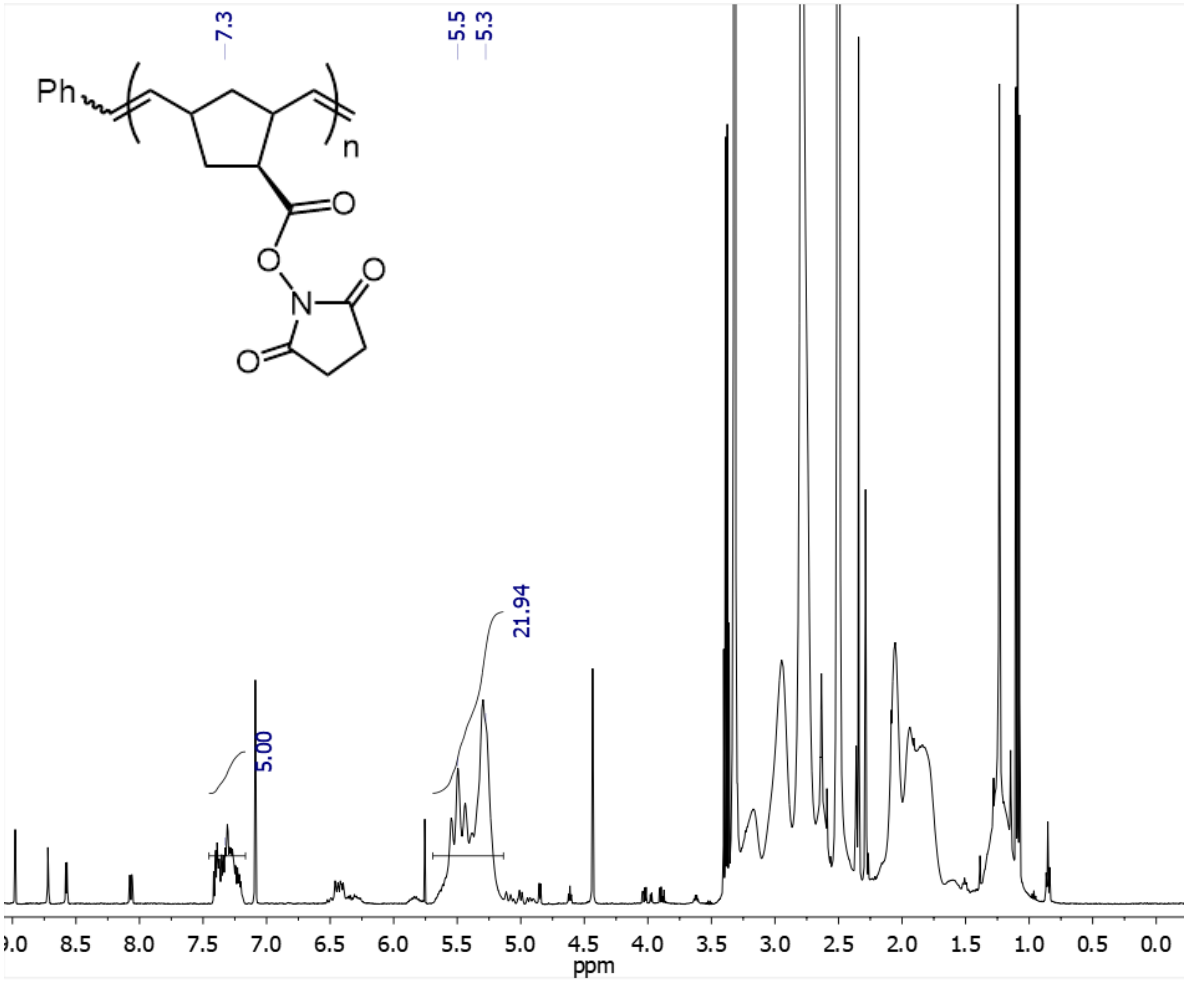
7.3
5.5
5.3
Ph
n
O
O
N
O
O
21.94
5.00
9.0
8.5
8.0
7.5
7.0
6.5
6.0
5.5
5.0
4.5
4.0
3.5
3.0
2.5
2.0
1.5
1.0
0.5
0.0
ppm

3-34b

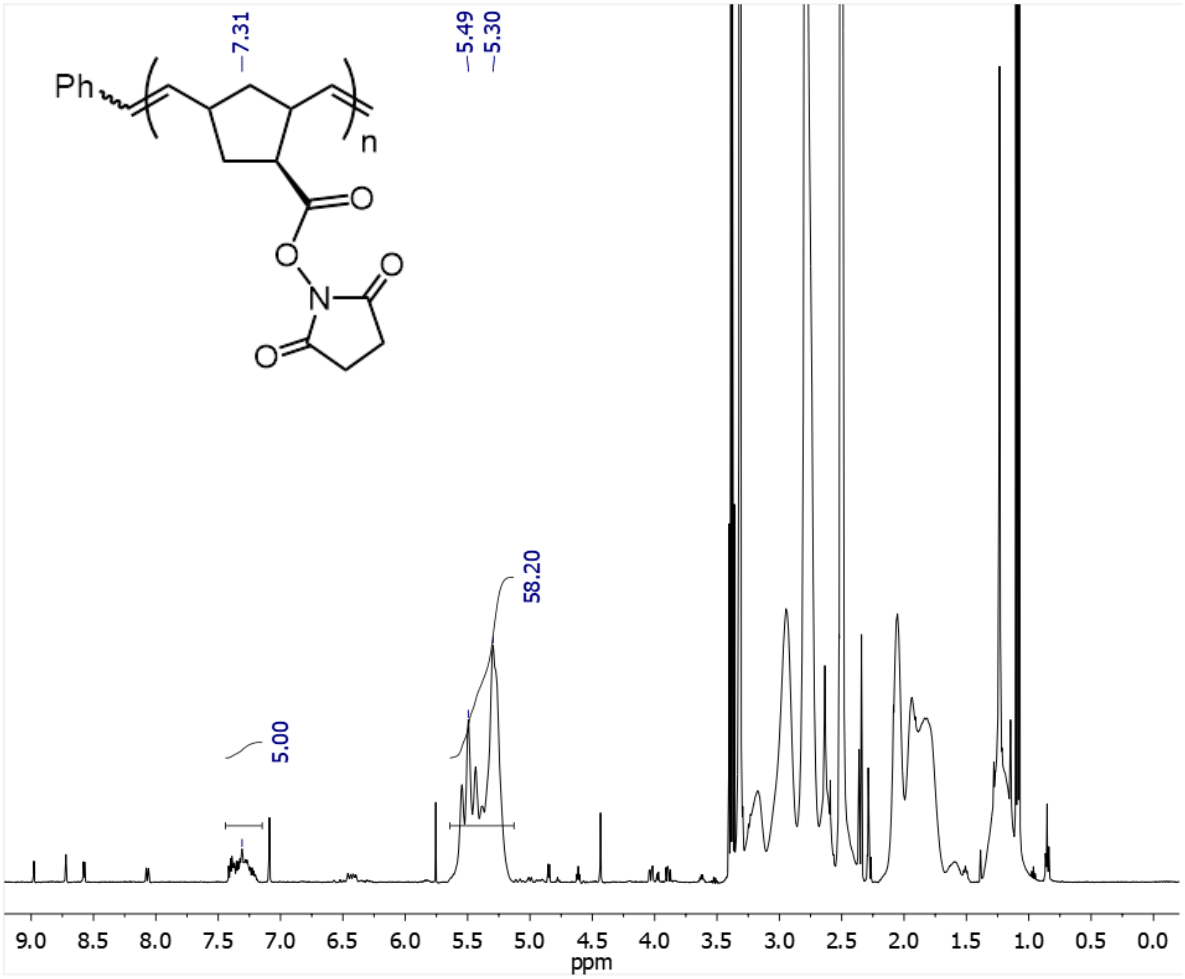
7.31
5.49
5.30
Ph
n
O
O
N
O
O
58.20
5.00
9.0
8.5
8.0
7.5
7.0
6.5
6.0
5.5
5.0
4.5
4.0
3.5
3.0
2.5
2.0
1.5
1.0
0.5
0.0
ppm

3-34c

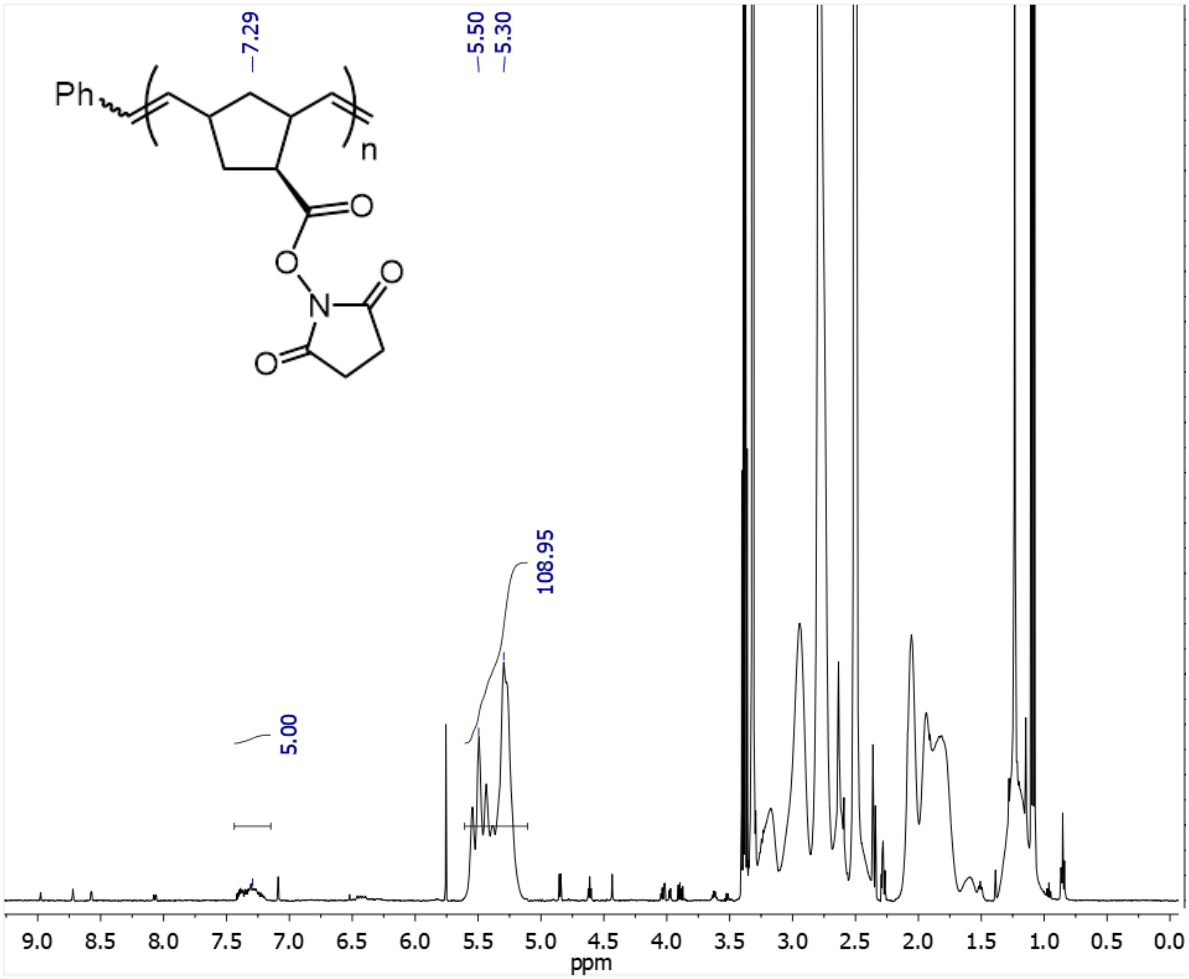
7.29
5.50
5.30
Ph
n
O
O
N
O
O
108.95
5.00
9.0 8.5 8.0 7.5 7.0 6.5 6.0 5.5 5.0 4.5 4.0 3.5 3.0 2.5 2.0 1.5 1.0 0.5 0.0
ppm

3-37a

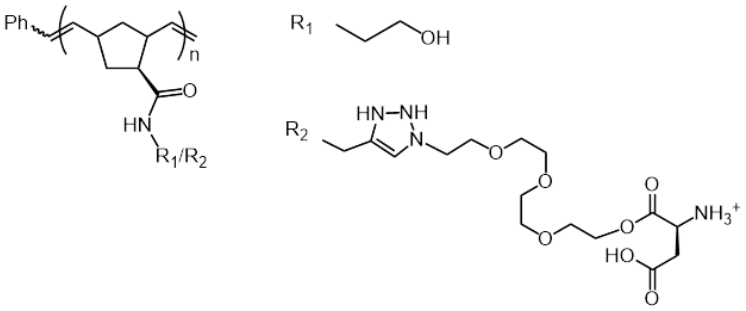
Ph
n
O
HN
R1/R2
R1
OH
R2
HN–NH
N
O
O
O
O
O
NH3+
HO
O

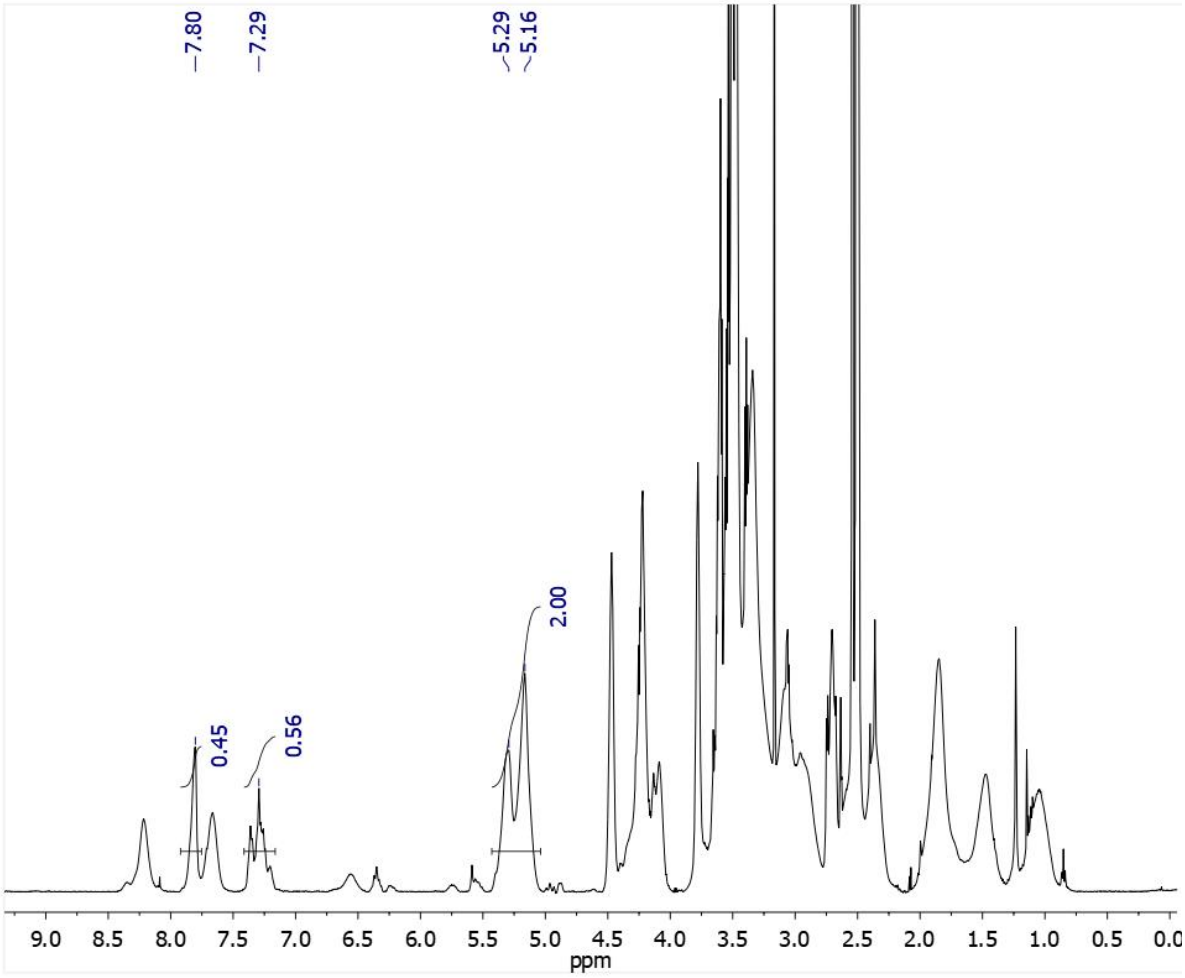
7.80
7.29
5.29
5.16
2.00
0.45
0.56
9.0
8.5
8.0
7.5
7.0
6.5
6.0
5.5
5.0
4.5
4.0
3.5
3.0
2.5
2.0
1.5
1.0
0.5
0.0
ppm

3-37b

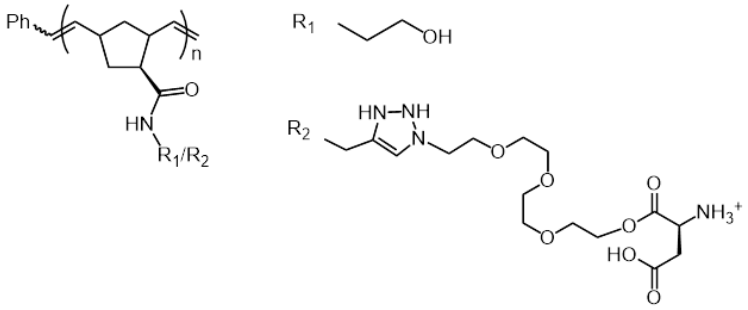
Ph
n
O
HN
R1/R2
R1
OH
HN–NH
R2
N
O
O
O
O
O
NH3+
HO
O

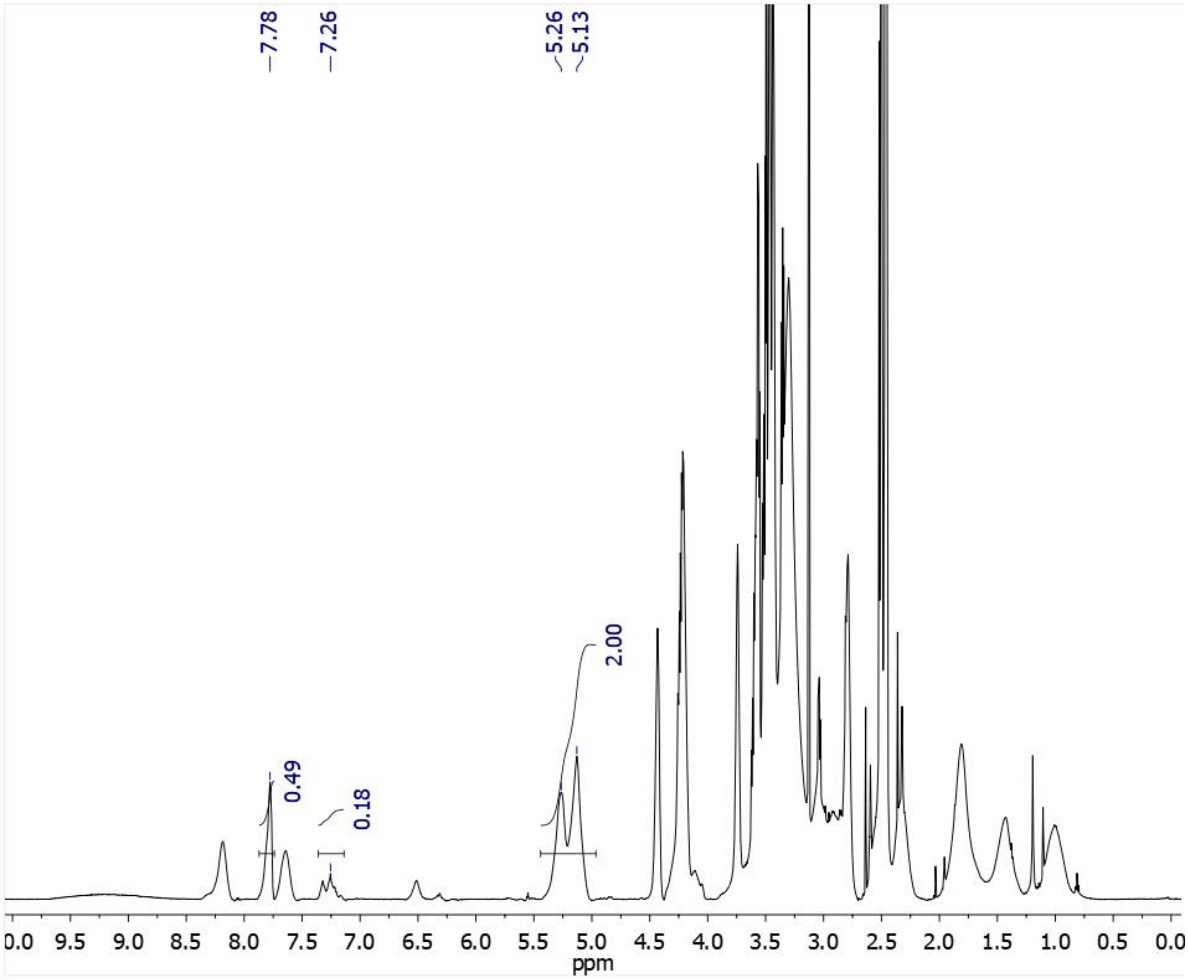
7.78
7.26
5.26
5.13
2.00
0.49
0.18
0.0 9.5 9.0 8.5 8.0 7.5 7.0 6.5 6.0 5.5 5.0 4.5 4.0 3.5 3.0 2.5 2.0 1.5 1.0 0.5 0.0
ppm

3-37c

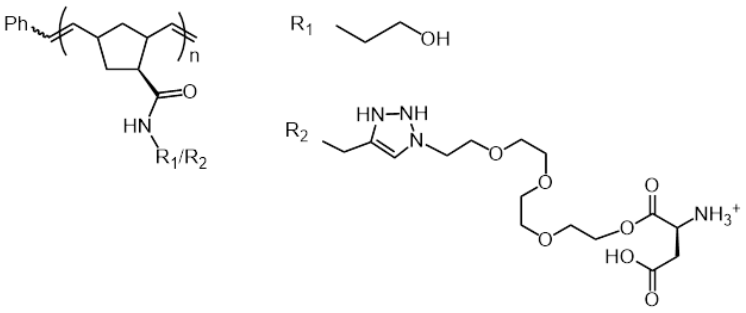
Ph
n
O
HN
R1/R2
R1
OH
R2
HN–NH
N
O
O
O
O
O
NH3+
HO
O

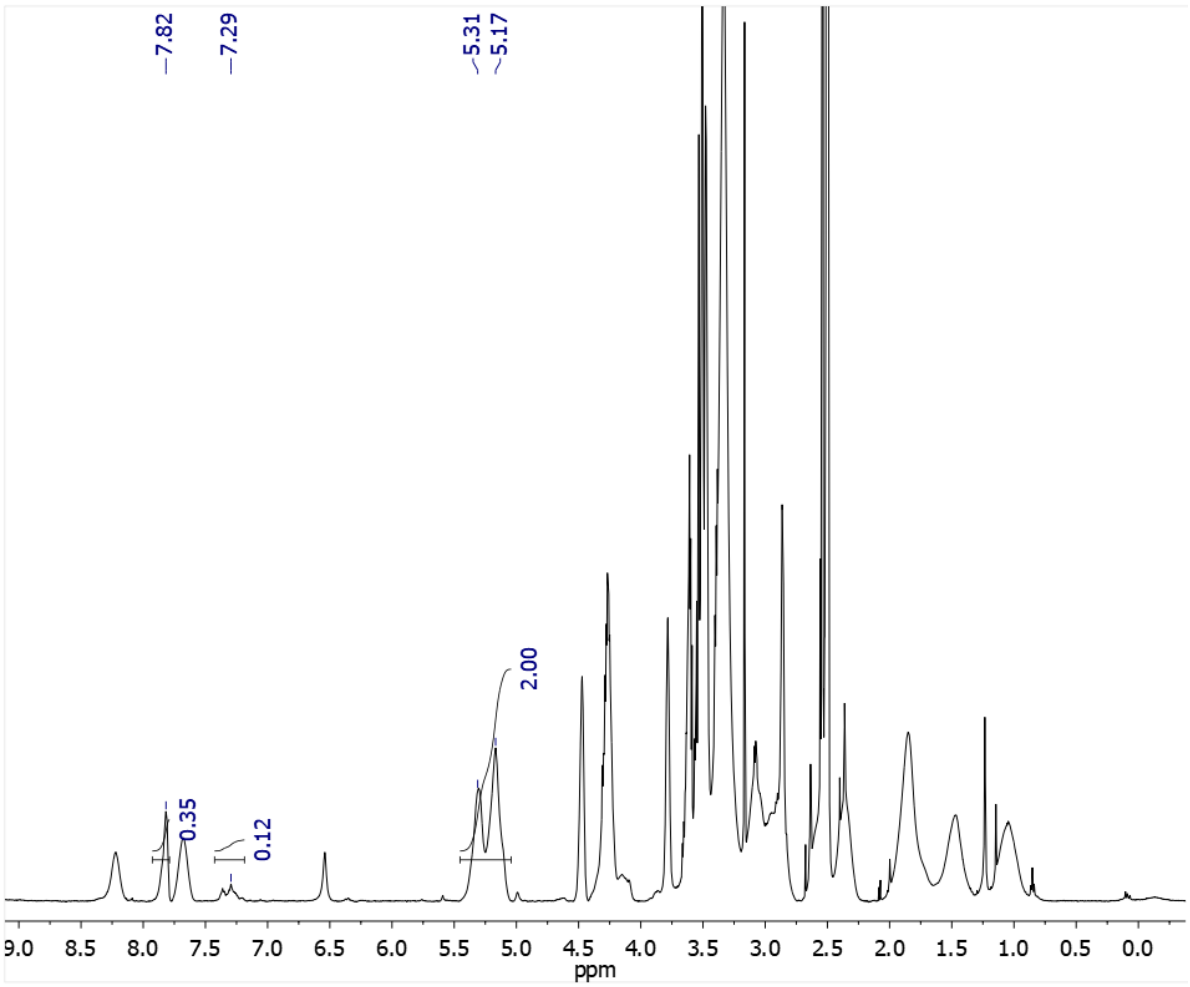
7.82
7.29
5.31
5.17
2.00
0.35
0.12
9.0
8.5
8.0
7.5
7.0
6.5
6.0
5.5
5.0
4.5
4.0
3.5
3.0
2.5
2.0
1.5
1.0
0.5
0.0
ppm